FAST PRECISE GPS POSITIONING IN THE PRESENCE OF IONOSPHERIC DELAYS

Odijk, D.

Fast precise GPS positioning in the presence of ionospheric delays

ISBN 90-804147-2-7
NUGI 816

Typesetting system: LaTeX
Printed by Optima Grafische Communicatie, The Netherlands

FAST PRECISE GPS POSITIONING IN THE PRESENCE OF IONOSPHERIC DELAYS

Proefschrift

ter verkrijging van de graad van doctor
aan de Technische Universiteit Delft,
op gezag van de Rector Magnificus prof.dr.ir. J.T. Fokkema,
voorzitter van het College voor Promoties,
in het openbaar te verdedigen
op dinsdag 17 december 2002 om 10.30 uur

door

Dennis ODIJK
geodetisch ingenieur
geboren te Utrecht

Dit proefschrift is goedgekeurd door de promotor:
Prof.dr.ir. P.J.G. Teunissen

Samenstelling promotiecommissie:

Rector Magnificus	voorzitter
Prof.dr.ir. P.J.G. Teunissen	Technische Universiteit Delft, promotor
Prof.dr.ing. K. Borre	Aalborg Universitet
Prof.dr. P.A. Cross	University College London
Prof.dr.-ing. habil. R. Klees	Technische Universiteit Delft
Prof.dr.ing. A. Kleusberg	Universität Stuttgart
Dr.ir. M.A. Salzmann	Kadaster, Apeldoorn

Dennis Odijk

Mathematical Geodesy and Positioning
Faculty of Civil Engineering and Geosciences
Delft University of Technology
Thijsseweg 11, 2629 JA Delft, The Netherlands

Support: The research for this thesis has been financially supported by the Dutch Cadastre (Kadaster) in Apeldoorn.

Keywords: Global Positioning System, relative positioning, undifferenced observables, ionosphere-weighted model, ambiguity resolution, virtual reference station

To Indah and Daniel

Contents

Abstract

Fast precise GPS positioning in the presence of ionospheric delays

This thesis deals about geodetic applications of the Global Positioning System (GPS), in which the position of the GPS receiver must be determined with cm-precision. This requires a relative measurement setup, together with an advanced processing strategy based on observations of the carrier-phase of the signal. To keep it economically interesting, this GPS technique should be based on relatively short time spans in which the satellite observations are collected. The key to precise positioning using short time spans is to take advantage of the integer property of the ambiguities of the phase observations in the processing.

The above procedure has been applied in a successful way for the last decade to applications in which the distance between the receivers is restricted to about 10 km (the so-called rapid-static and real-time kinematic GPS techniques over short distances). Above this distance, it is known that certain errors in the GPS observations start to significantly bias the computed receiver position when they are not taken care of. The aim of this research therefore is to develop a processing procedure, taking into account the errors in GPS observations due to propagation of the signals through the ionosphere, the atmospheric layer above about 80 km. Although other errors (due to troposphere and satellite orbit) are of relevance as well, the research is restricted to an improved modelling of the ionospheric error, since it is by far the largest error. For the other errors standard modelling techniques are applied in this research. Using the procedure, it should be possible to determine the desired receiver positions with cm-precision using a short time span. The research is restricted to GPS receivers with a mutual distance of a few hundred km (medium-distance baselines), located in mid-latitude regions.

To facilitate a modelling of the ionospheric error, using the theory of atmospheric refraction it is possible to decompose this error into a first-order effect, which contains the gross of the error, plus some higher-order effects and a term due to bending of the signal path. Under worst-case conditions, the first-order term may range up to about 80 m (on the GPS L2 frequency), whereas the accumulated effect of higher-order and bending terms can be up to 4 cm (for L2). For the future L5 frequency (from 2008) these effects are even larger. Fortunately, because of the

relative setup and the assumed medium distances, it is proved for this research it is allowed to neglect the higher-order and bending errors.

In the procedure a stochastic modelling of the first-order ionospheric errors (referred to as ionospheric delays) is chosen. This means that the ionospheric delays are not modelled as completely unknown parameters, but that stochastic prior information is incorporated by means of ionospheric pseudo-observations. This model is referred to as the ionosphere-weighted model: The weight of the ionospheric information can be tuned by the a priori standard deviation of the pseudo-observations. When this standard deviation is chosen zero, the ionosphere-weighted model reduces to the ionosphere-fixed model, which is the usual processing model for short-distance baselines (for which the ionospheric delays may be neglected). On the other hand, with an infinitely large ionospheric standard deviation, the model will be equivalent to the ionosphere-float model, in which the ionospheric delays are assumed as completely unknown parameters. This latter model is closely related to the ionosphere-free combination, for which it is known that it cannot be used to achieve fast positioning results. It is shown that the ionosphere-weighted model is only suitable for fast ambiguity resolution (and consequently positioning), when the ionospheric standard deviation is small. This requires very precise a priori ionospheric information.

The developed procedure consists of three steps. It is required that a user collects GPS observations in the vicinity of a network of permanent GPS stations. In the first step, the observations at the network stations are processed simultaneously using the ionosphere-weighted model. Since in this research the goal is precise positioning within the shortest time span possible, i.e. instantaneous or single-epoch positioning, it is required that the network data is also processed instantaneously. To make instantaneous resolution of the network ambiguities possible, the sample values of the ionospheric pseudo-observations are temporal predictions based on estimates of previous epochs. Test computations using a network with a station spacing of more than 100 km demonstrated that in this way high network ambiguity success rates (close to 100%) can be obtained. In the second step, precise ambiguity-fixed network ionospheric delays are spatially interpolated at the approximate location of the user's receiver. In the procedure for this purpose the concept of virtual reference station (VRS) observations is used. In this concept the network estimates (ionospheric delays and other parameters) are transformed to VRS observations, which should correspond to the data a real receiver would have collected at the user's location. The processing of the user's observations relative to this VRS is the third step of the procedure. Because of the presence of possible residual ionospheric delays also in this step the ionosphere-weighted model is applied. The difference with the application in the network processing is that the sample values of the pseudo-observations are now taken zero, and the ionospheric standard deviation is computed as a function of the distance to the closest real network station. Using this, test computations demonstrated that instantaneous ambiguity success rates of 90% are feasible. When the ionosphere-fixed model would be applied, the success rates would not be higher than about 60%.

Samenvatting

Snelle precieze GPS-puntsbepaling in de aanwezigheid van ionosferische vertragingen

Dit proefschrift heeft betrekking op geodetische toepassingen van het Global Positioning System (GPS), waarbij de ontvangerpositie moet worden bepaald met cm-precisie. Dit vereist een relatieve meetopzet in combinatie met een geavanceerde verwerkingsstrategie gebaseerd op waarnemingen van de fase van de draaggolf van het signaal. Om het economisch interessant te houden, moet de GPS-techniek zijn gebaseerd op relatief korte tijdspannes (maximaal een paar minuten) waarin de satellietwaarnemingen worden verzameld. De sleutel tot precieze puntsbepaling in korte tijdspannes ligt in het in de verwerking gebruikmaken van de geheeltallige eigenschap van de meerduidigheden waarmee de fasewaarnemingen zijn behept.

De bovenstaande procedure is het afgelopen decennium met succes toegepast in landmeetkundige toepassingen waarbij de afstand tussen de GPS ontvangers werd beperkt tot pakweg 10 km (de zogenaamde snel-statische en real-time kinematische GPS technieken over korte afstanden). Het is bekend dat boven deze afstand bepaalde fouten in de GPS-waarnemingen de berekende ontvangerpositie significant beïnvloeden indien er geen rekening mee wordt gehouden. Het doel van dit onderzoek is daarom het ontwikkelen van een verwerkingsprocedure waarin rekening wordt gehouden met fouten in GPS-waarnemingen tengevolge van voortplanting door de ionosfeer, de atmosferische laag hoger dan ongeveer 80 km. Hoewel andere fouten (als gevolg van de troposfeer en de satellietbanen) ook een rol spelen, is het onderzoek beperkt tot de ionosferische fout, aangezien dit de grootste fout is. Voor de andere fouten worden in dit onderzoek standaard modelleringstechnieken toegepast. Met behulp van de procedure moet het mogelijk zijn om de gewenste ontvangerposities te bepalen met cm-precisie in een korte tijdspanne. Overigens is het onderzoek beperkt tot GPS ontvangers welke een onderlinge afstand hebben van maximaal een paar honderd km (zogenaamde middellange basislijnen), en welke zijn gelegen op middelbare breedten op aarde.

Om de ionosferische fout te modelleren is gebruik gemaakt van de atmosferische refractietheorie. Uit deze theorie blijkt dat de fout kan worden opgesplitst in een eerste-orde effect, welke het gros van de fout bevat, plus enkele hogere-orde effec-

ten en een term als gevolg van de kromming van het signaalpad. Onder de slechtst denkbare omstandigheden kan het eerste-orde effect tot zo'n 80 m reiken (op de GPS L2-frequentie), terwijl het geaccumuleerde effect van hogere-orde en krommingstermen zo'n 4 cm kan zijn (voor L2). Voor de toekomstige L5-frequentie (vanaf 2008) zullen deze effecten zelfs nog groter zijn. Gelukkig blijkt uit simulatieberekeningen dat voor dit onderzoek de hogere-orde en krommingseffecten mogen worden verwaarloosd, vanwege de relatieve meetopzet en de veronderstelde middellange basislijnen.

Voor de vewerkingsprocedure is gekozen voor een stochastische modellering van de eerste-orde ionosferische fouten (ionosferische vertragingen). Dit houdt niet alleen in dat de ionosferische fouten zijn gemodelleerd als onbekende parameters, maar dat stochastische a priori informatie wordt meegenomen in de vorm van ionosferische pseudo-waarnemingen. Dit model is bekend als het ionosfeer-gewogen model: Het gewicht van de ionosferische informatie kan worden afgestemd d.m.v. de standaardafwijking van de pseudo-waarnemingen. Wanneer deze standaardafwijking wordt gelijkgesteld aan nul reduceert het ionosfeer-gewogen model tot het zogenaamde ionosfeer-afwezig model, het gebruikelijke model voor de verwerking van data van korte basislijnen, waarin de ionosferische vertragingen mogen worden verwaarloosd. Aan de andere kant leidt een oneindig grote ionosferische standaardafwijking tot het ionosfeer-aanwezig model, waarin de ionosferische vertragingen als volledig onbekende parameters worden verondersteld. Laatstgenoemd model is gerelateerd aan de ionosfeervrije combinatie, waarvan bekend is dat het niet geschikt is om toegepast te worden om snelle puntsbepalingsresultaten te behalen. Het ionosfeer-gewogen model is daarentegen geschikt voor snelle meerduidigheidsschatting en dientengevolge precieze puntsbepaling, maar alleen met een voldoende kleine ionosferische standaardafwijking. Afhankelijk of troposferische vertragingen wel of niet worden geschat, mag deze standaardafwijking een paar mm tot een paar cm zijn. Dit leidt tot de behoefte aan zeer precieze a priori ionosferische informatie.

De ontwikkelde procedure bestaat uit drie stappen. Voor de procedure is het noodzakelijk dat een gebruiker GPS-metingen verzamelt in de nabijheid van een netwerk van permanente GPS-stations. In de eerste stap worden de waarnemingen van alleen de netwerkstations verwerkt volgens het ionosfeer-gewogen model. Aangezien in dit onderzoek de snelst mogelijke vorm van precieze puntsbepaling tot doel heeft, d.w.z. instantane of enkele-epoche puntsbepaling, dient de netwerkverwerking ook instantaan te worden uitgevoerd. Om de netwerkmeerduidigheden instantaan te kunnen schatten, zijn de sample waarden van de ionosferische pseudo-waarnemingen voorspellingen in tijd gebaseerd op schattingen uit voorgaande epochen epochen. Testberekeningen tonen aan dat op deze manier zeer hoge meerduidigheidssucceskansen (dichtbij 100%) haalbaar zijn netwerken waarbij de stations een gemiddelde onderlinge afstand hebben van meer dan 100 km. In de tweede stap van de procedure worden de ionosferische vertragingen welke zijn geschat met de geheeltallige netwerkmeerduidigheden vastgehouden, ruimtelijk geïnterpoleerd naar de locatie van de gebruikersontvanger. Voor dit doel wordt in de procedure het concept van het virtuele referentiestation (VRS)

gebruikt. In plaats van expliciete ionosferische correcties krijgt de gebruiker VRS-waarnemingen, welke zoveel mogelijk zouden moeten overeenkomen met de data een echte ontvanger zou hebben verzameld op de virtuele locatie. De gezamenlijke verwerking van deze virtuele waarnemingen en de gebruikerswaarnemingen vormt de derde stap van de procedure. Vanwege mogelijke residuele ionosferische vertragingen (de interpolatie is nooit perfect) wordt ook in deze stap het ionosfeer-gewogen model toegepast. Het verschil met de toepassing in de netwerkverwerking ligt erin dat voor de sample waarden van de pseudo-waarnemingen nu nul wordt genomen, terwijl hun standaardafwijking wordt berekend als functie van de afstand tot het dichtstbijzijnde echte netwerkstation. Testberekeningen tonen aan dat met deze methode instantane succeskansen van 90% haalbaar zijn voor het oplossen van de geheeltallige meerduidigheden in de verwerking van de gebruiker. Wanneer het ionosfeer-afwezig model daarentegen zou worden toegepast, zouden de succeskansen niet hoger zijn dan pakweg 60%.

Curriculum vitae

Dennis Odijk was born in Utrecht, the Netherlands, on June 12th 1970. From 1982 to 1988 he fulfilled his pre-university education at Cals College in Nieuwegein. After that, he started his study in geodetic engineering at the Delft University of Technology, which he finished in 1994 with a thesis on the quality analysis of the (passive) Dutch GPS base network (GPS-kernnet). In the same year he worked at the Survey Department of Rijkswaterstaat on the initiation of the active GPS control network in the Netherlands (AGRS.NL), and in 1995 he left the field of geodesy to fulfil his military duties. In 1996 he returned to Delft University of Technology to start his PhD studies at the department of Mathematical Geodesy and Positioning (MGP) on fast GPS positioning in the context of significant ionospheric delays. During this research, he worked for half a year as a visiting fellow at the Satellite Navigation And Positioning (SNAP) group of Prof. C. Rizos at the University of New South Wales in Sydney, Australia (2000). While writing his PhD thesis, in late 2001 he started working as a research associate at the department of MGP on the modelling of land subsidence.

Acknowledgements

The Dutch Cadastre (Kadaster) is gratefully acknowledged for their financial support to carry out my PhD research. Especially I would like to thank Joop van Buren from the Cadastre to let me do my research with a lot of freedom. The Cadastre (in cooperation with the Survey Department of Rijkswaterstaat) also provided the AGRS.NL data used in some numerical examples.

The Southern California Integrated GPS Network and its sponsors, the W.M. Keck Foundation, NASA, NSF, USGS and SCEC, are acknowledged for providing the SCIGN data used in this thesis.

Besides, this thesis could not be realized without the support of many persons. In the first place, I would like to thank my supervisor, Prof. Peter Teunissen, for letting me finish this thesis and for the discussions with him during my research and his valuable suggestions to improve the manuscript.

I am indebted to Prof. Chris Rizos and Dr. Shaowei Han for giving me the opportunity to work in their Satellite Navigation and Positioning (SNAP) group at the University of New South Wales in Australia for half a year. The atmosphere within their group is an example for other groups.

Many current and former colleagues at the department of Mathematical Geodesy and Positioning (MGP) have directly or indirectly contributed to this thesis. Frank Kleijer and Peter Joosten are thanked for their discussions and for critically reading some early versions of the manuscript. They also helped me when I had problems with *Matlab*$^{\text{TM}}$. Dr. Paul de Jonge is acknowledged for teaching me to work with the *GPSveQ* software and Dr. Hans van der Marel for the cooperation during the development of the *Virint* software. Dr. Christian Tiberius and Niels Jonkman are acknowledged for using their knowledge of GPS, especially at the beginning of my PhD studies. I am grateful to Dr. Ramon Hanssen for lending me his LaTeX stylefile, which is, in an adapted version, used for this thesis.

Finally, I would like to express my deepest gratitude to my wife Indah, for being patient all those weekends and evenings when I was away, despite our busy life the past year with little Daniel.

Chapter 1

Introduction

1.1 Background

In order to apply the Global Positioning System (GPS) for surveying purposes in an economic manner, relatively short observation time spans are required. The key to precise GPS positioning is to use carrier-phase observations in a relative measurement setup, such that the unknown phase ambiguities become quantities that are known to be *integer*-valued, instead of real-valued. Using non-standard estimation techniques the integer ambiguities can be determined and be fixed in another standard adjustment, in which the coordinate parameters can be estimated with cm-precision.

The above procedure is currently in a successful way applied to *rapid-static* and *real-time kinematic* (RTK) GPS surveying. For these type of applications the receiver positions need to be determined in a few minutes or even instantaneously, i.e. using just one epoch of data. However, the distance between the reference receiver and the receiver for which its position needs to be determined, is usually restricted to about 10 km. Above this distance, it is known that errors due to propagation through the atmosphere (ionosphere and troposphere) and orbit errors become significantly present in relative GPS observations, since these errors tend to decorrelate with the distance.

The *ionospheric errors* dominantly contribute to the atmospheric errors. In the ionosphere, an atmospheric layer above about 80 km altitude, many molecules are split into charged particles due to incoming radiation from the Sun. Mainly the negatively charged particles, the free electrons, influence the GPS signals. As a consequence, the range from satellite to receiver becomes longer than the geometric range. It is known that the effect of these ionospheric delays can be estimated (or eliminated; the ionosphere-free combination) from dual-frequency measurements, since the ionosphere is a dispersive medium. This is the strategy which is usually applied for the processing of baselines which may be up to a few thousands of km. This approach is unfortunately not suitable for fast GPS applications, since the integer ambiguities cannot be resolved quickly. Another problem is that in the

last years the ionospheric errors have generally increased, and as a consequence it is even not automatically allowed to neglect them in the processing of the mentioned short baselines (< 10 km). This general increase is due to the recent (2001) maximum of the *solar cycle*. One solar cycle takes about 11 years and therefore the low level of ionospheric activity as in 1996 is not expected before 2005.

1.2 Research objective and limitations

The *objective* of this research is to develop (and implement) an efficient procedure to process relative GPS observations, which properly takes the errors due to the ionosphere into account. The estimation of the receiver coordinate parameters, the parameters of interest, should fulfil two important requirements in this strategy. It should namely be estimated i) Using a *short time span* of data (*fast*), and ii) With high *geodetic* precision (cm-level or better).

In the research the following limitations should be taken care of:

- In this thesis with *fast* it is aimed at the shortest time span possible: Instantaneous or single-epoch processing, allowing real-time applications. Besides this, for instantaneous positioning it is not necessary to keep the GPS signal locked, since the ambiguities are re-estimated for each epoch, see e.g. [Tiberius, 1998] and [Bock et al., 2000]. For surveying applications instantaneous positioning is an attractive method allowing an increased productivity, since the surveyor does not have to wait before moving to another point to be determined. Since coordinate parameters are estimated each observation epoch, the technique is also very suitable for the positioning of moving vehicles. In fact, in case of instantaneous positioning the difference between static and kinematic applications disappears.

- Concerning the ionospheric errors, the research is restricted to *mid-latitude* regions. It is known that the ionosphere is more active in equatorial and auroral regions and consequently the errors in GPS observations collected in those regions are larger and more variable, in general. The developed procedure is however not suitable for these regions.

- Another restriction is that the distance between GPS receivers is not allowed to be unlimited. The research is restricted to baselines which are at maximum a few hundred km long. These types of baselines may be assigned as *medium (distance)* GPS baselines. These distances are typical when the positioning is carried out relative to one or more reference stations of a *permanent GPS network*, which have been set up in many countries in the last decade as part of the geometric infrastructure.

- Concerning the desired precision of the receiver position, this only holds for the horizontal components, since the *height*-component can be estimated with a lower accuracy, which is not necessarily caused by the ionosphere. This is first of all due to the worse geometry of the GPS satellites with

respect to the receiver in the height direction. Second, *tropospheric errors* in the GPS observations could play a significant role in the determination of the height. The troposphere is the atmospheric layer between the Earth's surface and the ionosphere. This research is however not primarily focussed on improving the tropospheric modelling for GPS applications.

- With respect to the positions of the GPS *satellites*, these are assumed to be sufficiently known in this research (using the precise orbits of the IGS), so it is not tried to improve them in the processing.

1.3 Outline of the thesis

This thesis consists of seven chapters. Each chapter is outlined as follows:

- In Chap. 2 the mathematical model for the processing of relative GPS phase and code observations is reviewed. For the sake of simplicity the errors due to the atmospheric propagation are neglected in this chapter, since these will be introduced later on in the thesis.

- Chapter 3 describes the general way of solving the mathematical model for applications as formulated in the objective. A crucial and non-trivial step of this procedure is the resolution of the integer phase ambiguities.

- Before extending the GPS model for the atmospheric errors, in Chap. 4 the physical backgrounds are reviewed of the propagation of the GPS signals through the atmosphere, with the main focus on the ionospheric propagation. Attention is paid to the for precise GPS application relevant aspects: The size and the variability of the effects, in absolute as well as in relative sense. Besides the first-order effect, also ionospheric higher-order and bending effects are discussed.

- Based on the results of Chap. 4, in Chap. 5 the mathematical model as was set up in Chap. 2 is extended to account for the atmospheric biases. For the ionospheric delays this is done in the most general way: Treating the ionospheric delays (on each epoch) as stochastic variables. The resulting model is referred to as the ionosphere-weighted GPS model. For this model, in this chapter also planning computations are described, which include an analysis of the expected precision of the parameters of interest and an evaluation of ambiguity success rates, performed without the collection of real observations.

- In Chap. 6 this ionosphere-weighted model is applied for fast positioning. Use is made of the network-concept: Ionospheric delays are precisely and rapidly estimated from a surrounding network of GPS reference stations and made available to users operating within the coverage of the network. For this purpose in this thesis the idea of *virtual reference stations* (VRS) is used. Experimental results are shown for some case studies.

- Finally, in Chap. 7 the conclusions of this thesis are summarized and recommendations are given for further research.

1.4 Contributions of this research

The contributions of the research as conducted for this thesis can be summarized as follows:

- A systematic and consistent setup is presented for the relative GPS model, which is based on *undifferenced* phase and code observables, rather than the more common single- or double-differenced observables. A plea for this undifferenced approach is that estimates for the clock parameters become available. In a differenced approach they would be eliminated. For the generation of VRS data as discussed in this thesis, this is essential. In this thesis it is explicitly shown how VRS observables are derived from undifferenced estimates of the (permanent) network parameters. Another advantage of an undifferenced model is that for clock parameters it is possible to incorporate a priori models. A third advantage is that the undifferenced GPS model can be easily extended to include observations from other satellite positioning systems, such as the Russian *Glonass* or the future European *Galileo* system.

- For this undifferenced model *closed-form expressions* have been derived. Using these expressions one may already get insight in the way various factors contribute to the solution and precision of the model, without collecting real observations. These closed-form expressions are also used to investigate the impact of a proposed *third GPS frequency*.

- The *ionospheric error* in GPS observations is analyzed from a geometric point of view. Not only the *first-order* effect is taken into account, but also the *higher-order* and *bending* effects. These latter effects are silently neglected in most of the literature, but in this thesis a quantification is given whether this is really allowed.

- It is shown that the *ionosphere-weighted* model is a very suitable basis for network-based positioning. Intrinsically the same model can be applied for both network and user's processing. Also, in both models (for network and user's processing) a similar approach for *ambiguity resolution* is used: The optimal integer least-squares technique as implemented in the LAMBDA method.

1.5 Software implementation

For this research the *GPSveQ* software is extended and/or modified. *GPSveQ* is the in-house GPS processing software of the Department of Mathematical Geodesy and Positioning and was originally developed by *P.J. de Jonge*, see [De Jonge, 1998].

It is based on undifferenced observation equations.

Besides this, the program *Virint* has been written (in cooperation with *H. van der Marel*), in which the undifferenced estimates from a *GPSveQ* network processing are transformed to VRS observations.

Chapter 2

Setting up the precise relative GPS model

2.1 Introduction

In this chapter the mathematical model for the adjustment of precise relative GPS observations is derived. Although in many GPS/geodesy books, such as for example [Hofmann-Wellenhof et al., 2001], [Teunissen and Kleusberg, 1998] and [Misra and Enge, 2001], a good description of GPS models is given, the precise relative GPS model derived in this chapter is the basis of the research committed for this thesis. The model is set up in a very general way: It is meant to be applicable for a multiple of *observables* (phase and code), *receivers*, *satellites*, *epochs* and, with respect to the proposed GPS modernization from a dual- to a triple-frequency system (in 2008), also for a multiple of *frequencies*. The emphasis is on the design matrix and estimable parameters in case of a model which uses *undifferenced* observables, instead of the more traditional single- or double-differenced observables. The argumentation for an undifferenced approach was given in Chap. 1.

The chapter starts in Sect. 2.2 with a short physical description of the GPS signals. This description facilitates the comprehension of the two basic observables in precise GPS applications: The code (or pseudo-range) observable and the (carrier-) phase observable, which are both explained in Sect. 2.3. These observables may be applied to a various type of GPS processing models, which can generally be divided into models for *positioning* applications and models for *non-positioning* applications. See Sect. 2.4 for a detailed discussion. These latter type of models are discussed here, since in this thesis the parameters of interest are not always positions or coordinates. For both types of models in Sect. 2.5 the fundamental observation equations are presented and the mathematical models, consisting of a functional and a stochastic part, are derived in Sects. 2.6, 2.7 and 2.8. For these undifferenced models a number of rank deficiencies have to be removed to obtain a full-rank functional model. Section 2.7 describes step-by-step how this can be done. For the sake of simplicity, in this chapter it is assumed that biases in the GPS observations due to *atmospheric propagation* are absent. In the following chapters the models will be extended for these systematic errors. Section 2.8 gives

a brief summary on the stochastic model of the GPS phase and code observables. After deriving and discussing the functional and stochastic models, in Sect. 2.9 the undifferenced GPS model is related to the mathematical model in terms of *double-differenced* observables. Finally, Sect. 2.10 ends the chapter with some concluding remarks.

2.2 GPS signals

In this section background information is given on the GPS signals. First some basic wave propagation theory is discussed and it is described how the GPS signals fit into this. After that a closer look is taken at the codes and carriers of the GPS signals.

2.2.1 Electro-magnetic waves

A GPS signal consists of *electro-magnetic* (EM) waves. An EM-wave is defined as a self-propagating wave with both electric and magnetic field components. Although these EM-waves are spherical, far from the transmitter, the GPS satellite, it is possible to approximate the spherical wave by a *plane wavefront*. An expression for the sinusoidal electric field of the plane wave, denoted as $E(r,t)$, propagating in *free space* (vacuum), reads:

$$\boxed{E(r,t) \;=\; E_0 \exp\{\Im\, 2\pi\varphi(r,t)\}} \tag{2.1}$$

where:

$E(r,t)$	:	electric field vector [Volt/m]
r	:	position vector (w.r.t. origin in transmitter) [m]
t	:	time [s]
E_0	:	amplitude [Volt/m]
$\varphi(r,t)$	:	phase [cyc]
$\Im \;=\; \sqrt{-1}$	:	imaginary number

For the magnetic field of the wave, denoted by $H(r,t)$, a similar expression can be set up. This vector is, like the electric field vector, perpendicular to the propagation direction of the wave (see Fig. 2.1). Besides, both fields oscillate perpendicular to each other. Such a wave is called a *transversal* wave. In free space, the EM-wave propagates with the *velocity of light*, which is by definition $c = 299{,}792{,}458$ m/s. In the case of GPS however, the signals have to pass the atmosphere, and therefore their propagation velocity is not equal to the velocity of light in free space.

The space- and time-varying *phase* of the wave can be written as follows:

$$\boxed{\varphi(r,t) \;=\; ft \;-\; (1/\lambda)j^T r \;+\; \varphi(t_0)} \tag{2.2}$$

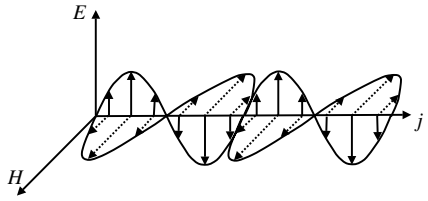

Fig. 2.1. Linearly polarized wave

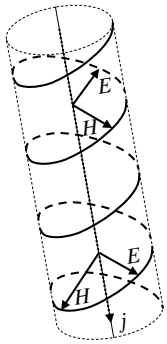

Fig. 2.2. Right-handed circularly polarized wave

where:

f	:	frequency [Hz $= \mathrm{s}^{-1}$]
$\lambda = c/f$	:	wavelength [m]
$\jmath$	:	vector of propagation direction (unit vector: $\|\jmath\| = 1$) [-]
$\varphi(t_0)$	:	initial phase (phase at origin in transmitter, $r = 0$) [cyc]

A plane wavefront is a plane of *constant phase* at a certain time epoch, denoted as $t = t_i$, which is perpendicular to the propagation direction $\jmath$ of the wave. The *polarization* of a wave is the mode of vibration in the plane of constant phase. An unpolarized wave (such as natural light) vibrates in all directions. However EM-signals may be polarized, and different types of polarization exist. For example, the polarization of the wave in Fig. 2.1 is *linear*: The direction of the electric field is constant in time (it varies only in amplitude). Other types of polarization are elliptical, circular, etc. GPS signals are (right-handed) *circularly* polarized waves: The electric field makes a spiral movement from transmitter to receiver, see Fig. 2.2. The reason of this choice of polarization is that the GPS signals have to pass the atmosphere, see Chap. 4.

The discussed EM-waves act in case of GPS as *carrier* waves. This means that information (the *code*) is added onto these waves. This is called *modulation*. Modulation can be carried out via the amplitude, frequency, or the phase of the carrier wave. For GPS the modulation technique is the *binary bi-phase modulation*, see e.g. [Langley, 1998] for a description of this technique.

Due to the modulation with the codes, the GPS signal can be considered as a result from the superposition of a *group*, a packet of waves, which are centered on the carrier frequency. Dependent on the medium, the velocity of this group may differ from the velocity of the wave's phase. Hence, we distinguish between the *group velocity* and the *phase velocity* of a signal. Note that the phase and group

velocity are equivalent in free space.

2.2.2 GPS codes and carriers

The current GPS satellites broadcast their signals on two frequencies: L1 (at 1575.42 MHz) and L2 (at 1227.60 MHz). Both carriers are derived from the same (atomic) clock driven oscillator with a frequency of 10.23 MHz. The carrier waves on L1 and L2 are modulated by a *Precision* (P) code, and only the L1 carrier is modulated by the *Coarse/Acquisition* (C/A) code. Both measurements of the code (pseudo-range) and of the much more precise phase of the carrier wave may act as GPS observables. The codes are also referred to as *Pseudo Random Noise* (PRN) codes, and are different for each GPS satellite.

Although the P-code is much more precise than the C/A-code, the P-code is encrypted to the (for civilian users) secret Y-code because of security reasons. This is called *Anti-Spoofing* (A-S). The C/A-code is on the contrary available for *all* GPS users. Using an encrypted signal for measurements without knowing the complete code is referred to as a (semi-) codeless technique. Many (geodetic) GPS receivers employ special techniques to reconstruct the P-code, resulting in observables which are less precise than the original P-code observables, but still more precise than the C/A-code observable.

2.2.3 GPS modernization

At the moment of writing this thesis, there are plans to modernize the GPS signals, see e.g. [Shaw et al., 2000] and [Eissfeller et al., 2001]. The first plan is to add a third frequency to the current dual-frequency system. This L5 frequency (at 1176.45 MHz) is expected to be transmitted by the GPS satellites from 2005. A new code will be modulated onto this L5 signal. Table 2.1 gives an overview of the GPS frequencies. Besides a third frequency, from 2003 the L2 carrier wave will, like the L1 signal, be modulated with the civil C/A code. For military users a new Military (M) code will be added to the current P-code (for both L1 and L2 signals).

Table 2.1. Overview of current and future GPS carrier waves

carrier signal	frequency (MHz)	wavelength (cm)
L1	$154 \times 10.23 = 1575.42$	19.03
L2	$120 \times 10.23 = 1227.60$	24.42
L5 (from 2005)	$115 \times 10.23 = 1176.45$	25.48

2.3 GPS code and phase observables

For precise GPS applications both code and phase of the GPS signal are used as observable. Both observable types are unfortunately not an unbiased function of the geometric distance between satellite and receiver. They contain several bias terms, which are discussed in this section.

2.3.1 Code or pseudo-range observable

The GPS code observable on epoch t_i at the carrier with frequency j is derived from the difference between the time the signal is received at receiver r time and the time at which the signal is transmitted at satellite s, which is the time of reception diminished with the signal travel time:

$$\vartheta^s_{r,j}(t_i) \;=\; c\left[t_r(t_i) \;-\; t^s(t_i - \tau^s_{g,r,j}(t_i))\right] \tag{2.3}$$

where:

$\vartheta^s_{r,j}$	:	code observable [m]
t_i	:	time of observation (GPS time) [s]
c	:	velocity of light [m/s]
t_r	:	time of reception in receiver [s]
t^s	:	time of transmission from satellite [s]
$\tau^s_{g,r,j}$	:	code travel time [s]

Note that the travel time for the code is the *group* travel time of the signal, and to emphasize this subscript g is used.

Due to instabilities in the receiver clock the receiver time is not equal to GPS time, but it contains an offset:

$$t_r(t_i) \;=\; t_i \;+\; dt_r(t_i) \tag{2.4}$$

The offset dt_r is called the *receiver clock error*. Also, satellite time is not equal to GPS time, there is a *satellite clock error*, denoted by dt^s, such that the time of transmission of the signal can be written as:

$$t^s(t_i - \tau^s_{g,r,j}(t_i)) \;=\; t_i - \tau^s_{g,r,j}(t_i) \;+\; dt^s(t_i - \tau^s_{g,r,j}(t_i)) \tag{2.5}$$

Using Eqs. (2.4) and (2.5), the code observable can be rewritten as:

$$\begin{aligned} \vartheta^s_{r,j}(t_i) &= c\left[(t_i + dt_r(t_i)) - \left\{t_i - \tau^s_{g,r,j}(t_i) + dt^s(t_i - \tau^s_{g,r,j}(t_i))\right\}\right] \\ &= c\left[dt_r(t_i) + \tau^s_{g,r,j}(t_i) - dt^s(t_i - \tau^s_{g,r,j}(t_i))\right] \end{aligned} \tag{2.6}$$

Multiplication of the travel time of the group of the signal, denoted by $\tau^s_{g,r,j}$, with the velocity of light is unfortunately not equal to the geometric straight distance between receiver and satellite. This is caused by systematic effects as *atmospheric refraction*, *instrumental delays* (in the receiver and satellite) and other non-random effects such as *multipath*. So for the travel time of a code observation we may write:

$$\begin{aligned} \tau^s_{g,r,j}(t_i) &= d^s_{,j}(t_i - \tau^s_{g,r,j}(t_i)) + \\ &\quad \tfrac{1}{c}\left[\rho^s_r(t_i - \tau^s_{g,r,j}(t_i)) + da^s_{r,j}(t_i) + dm^s_{r,j}(t_i)\right] \;+\; d_{r,j}(t_i) \end{aligned} \tag{2.7}$$

where:

$d_{r,j}$	:	instrumental code delay in receiver [s] (travel time between reception and correlation in receiver)
$d^s_{,j}$	:	instrumental code delay in satellite [s] (travel time between generation and transmission in satellite)
ρ^s_r	:	geometric distance between satellite and receiver [m]
$da^s_{r,j}$	:	atmospheric code error [m]
$dm^s_{g,r,j}$	:	sum of other (non-random) code errors [m]

Note that in Eq. (2.7) it has been assumed that the receiver delays are equal for all satellites and that the satellite delays are equal for all receivers. Inserting Eq. (2.7) into Eq. (2.6), for the code observable we obtain the following expression:

$$\begin{array}{rcl} \vartheta^s_{r,j}(t_i) & = & \rho^s_r(t_i - \tau^s_{g,r,j}(t_i)) + da^s_{r,j}(t_i) + dm^s_{r,j}(t_i) + \\ & & c\left[dt_r(t_i) + d_{r,j}(t_i) - dt^s(t_i - \tau^s_{g,r,j}(t_i)) + d^s_{,j}(t_i - \tau^s_{g,r,j}(t_i))\right] \end{array} \tag{2.8}$$

2.3.2 Carrier-phase observable

The GPS (carrier-) phase observable as function of the geometric distance is obtained in a similar way as the code observable. It is obtained by taking the difference between the phase of the generated signal in the receiver at reception time and the phase of the generated signal in the satellite at transmission time. Only the *fractional* phase can be measured in this way, so in the difference an *integer number* of full cycles is unknown. This *phase ambiguity* is time-constant due to uninterrupted tracking of the satellite (in case no cycle slips are present in the data, which is assumed here). So the phase observable can be written as:

$$\varphi^s_{r,j}(t_i) \;=\; [f_j t_r(t_i) + \varphi_{r,j}(t_0)] \;-\; \left[f_j t^s(t_i - \tau^s_{\phi,r,j}(t_i)) + \varphi^s_{,j}(t_0)\right] \;+\; N^s_{r,j} \tag{2.9}$$

where:

$\varphi^s_{r,j}$	:	phase observable [cyc]
f_j	:	carrier frequency [s^{-1}]
$\varphi_{r,j}(t_0)$	:	initial phase in the receiver [cyc]
$\varphi^s_{,j}(t_0)$	:	initial phase in the satellite [cyc]
$\tau^s_{\phi,r,j}$	:	phase travel time [s]
$N^s_{r,j}$	:	integer phase ambiguity [cyc]

Note that the phase is expressed in *cycles*. To distinguish between phase travel time and code travel time, the subscript ϕ is used here.

Like in the case of the code observable, both receiver and satellite time differ

from GPS time and therefore one has to account for *receiver and satellite clock errors*. This leads to the following expression for the phase observable:

$$\begin{aligned} \varphi^s_{r,j}(t_i) &= f_j \left[dt_r(t_i) + \tau^s_{\phi,r,j}(t_i) - dt^s(t_i - \tau^s_{\phi,r,j}(t_i)) \right] + \\ & \quad \left[\varphi_{r,j}(t_0) - \varphi^s_{,j}(t_0) + N^s_{r,j} \right] \end{aligned} \tag{2.10}$$

Similar to the travel time of the code observable in Eq. (2.7), for the signal travel time of the phase observable we may write:

$$\begin{aligned} \tau^s_{\phi,r,j}(t_i) &= \delta^s_{,j}(t_i - \tau^s_{\phi,r,j}(t_i)) + \\ & \quad \tfrac{1}{c} \left[\rho^s_r(t_i - \tau^s_{\phi,r,j}(t_i)) + \delta a^s_{r,j}(t_i) + \delta m^s_{r,j}(t_i) \right] + \delta_{r,j}(t_i) \end{aligned} \tag{2.11}$$

where:

$\delta_{r,j}$	:	instrumental phase delay in receiver [s] (travel time between reception and correlation in receiver)
$\delta^s_{,j}$	:	instrumental phase delay in satellite [s] (travel time between generation and transmission in satellite)
$\delta a^s_{r,j}$	:	atmospheric phase error [m]
$\delta m^s_{r,j}$	:	sum of other (non-random) phase errors [m]

Inserting Eq. (2.11) into Eq. (2.10), results in the following expression for the carrier-phase observable:

$$\boxed{\begin{aligned} \varphi^s_{r,j}(t_i) &= \tfrac{1}{\lambda_j} \left[\rho^s_r(t_i - \tau^s_{\phi,r,j}(t_i)) + \delta a^s_{r,j}(t_i) + \delta m^s_{r,j}(t_i) \right] + \\ & \quad f_j \left[dt_r(t_i) + \delta_{r,j}(t_i) - dt^s(t_i - \tau^s_{\phi,r,j}(t_i)) + \delta^s_{,j}(t_i - \tau^s_{\phi,r,j}(t_i)) \right] + \\ & \quad \varphi_{r,j}(t_0) - \varphi^s_{,j}(t_0) + N^s_{r,j} \end{aligned}} \tag{2.12}$$

2.4 GPS processing models

The in the previous section derived expressions for the code and phase observables, Eq. (2.8) and Eq. (2.12), constitute the basis of a mathematical model for the processing of the observations. This processing (or adjustment) is based on a least-squares estimation of the parameters involved.

The parameters of interest do not always have to be the receiver coordinates, but for some applications these may be, for example, the atmospheric or the clock parameters, which appear as biases of the geometric distance in the expressions of the previous section. In this thesis it is distinguished between models which solve for positions or coordinates (*positioning* models) on the one hand, and models that solve for the receiver-satellite ranges (*non-positioning* models) on the other hand.

2.4.1 Positioning or geometry-based models

In order to solve for position parameters, the GPS phase and code expressions as derived in the previous section need to be *linearized*, since the receiver-satellite

ranges are a non-linear function of the receiver coordinates. The models based on the linearized observation equations are known as *geometry-based* models, since the receiver-satellite geometry plays an important role. This geometry-based model can be applied for processing the data of a single receiver only (*absolute* positioning), or for a multiple number of receivers simultaneously (*relative* positioning).

Absolute positioning, traditionally used for navigation applications, has resulted in a ten times better coordinate precision since *Selective Availability* has been turned off in May 2000, but this precision (at 10 m level) is still insufficient for high-precision geodetic applications, in which mm-cm precision is required. This poor precision is due to the use of *code* data, which have a precision at dm-level. The concept of *Precise Point Positioning* (PPP; see e.g. [Zumberge et al., 1997]), does not only use the code, but also the more precise phase observations (which have mm precision). To fully exploit this high precision, one should however properly take the biases in the observations into account.

Although the precision using this PPP technique (dm-level) is better than of the traditional navigation solution, for precise geodetic applications this is still insufficient. Hence in this research the traditional *relative* approach is used for precise positioning. In this approach phase and code observations from one or more receivers to one satellite must be collected *simultaneously*. As a consequence, in the processing some important biases are significantly reduced or even fully eliminated. Besides this, with a relative approach advanced processing strategies are possible.

2.4.2 Non-positioning or geometry-free models

In case one is not interested in position parameters, the original phase and code observation equations may also form the basis of a processing model. A type of non-positioning model which has been subject to a lot of research in the recent past is the *geometry-free* model (see e.g. [Teunissen, 1996] and [Jonkman, 1998b]), in which the model is solved for the original receiver-satellite ranges. In contrast to the geometry-based model for this model the receiver-satellite geometry does *not* play a role.

Like the geometry-based model, the geometry-free model can be used for either *absolute* or *relative* applications. An absolute application is described in [De Jong, 1998], in which the geometry-free model is used to process observations from only one single receiver to one single satellite, in order to detect cycle slips and outliers in the data (*integrity monitoring*). Relative applications of the geometry-free model are described in, among others, [Jonkman, 1998a] and [Jonkman, 1998b].

In this thesis for the geometry-free model a more general version is used than is described in the mentioned literature. To the common GPS phase and code observables a so-called *pseudo-observable* is added for each receiver-satellite range

parameter, such that it becomes possible to incorporate a priori information on these ranges. This a priori range information can be computed from the approximate receiver and satellite positions. In this way the receiver-satellite ranges become become *stochastic* variables.

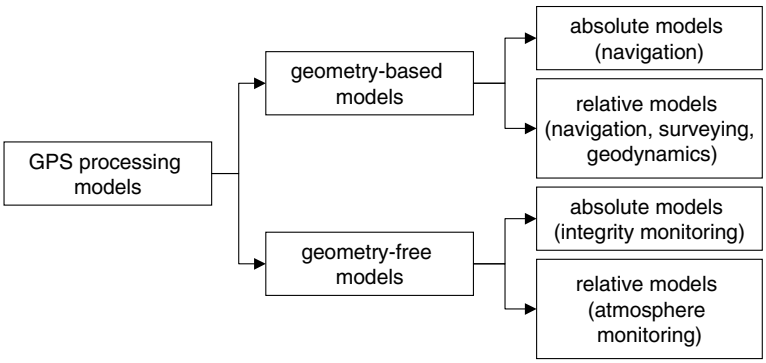

Fig. 2.3. Types of GPS processing models and their applications

2.5 GPS observation equations

In this section the fundamental GPS observation equations are given, using the expressions for the phase and code observable as derived in Sect. 2.3. Two types of observation equations can be distinguished: The original equations for non-positioning applications, and the linearized equations for solving the position parameters. Before giving these observation equations, some simplifications are carried out on the expressions for the phase and code observable from Sect. 2.3.

2.5.1 Simplifications

Evaluation of signal travel time

From the expression for the travel time of the code observable, Eq. (2.7), and the travel time for the phase observable, Eq. (2.11), it is known that the receiver-satellite range contributes much more to this travel time than the instrumental delays and atmospheric terms. The difference between the travel times of different observation types and frequencies turns out to be less than 10^{-7} s (on a maximum travel time of maximal 0.1 s), see [Tiberius, 1998]. Hence, when it concerns the evaluation of the time of departure of the signal, it is allowed to assume the signal travel times of group, phase and all frequencies *equal*:

$$t_i - \tau^s_{g,r,j}(t_i) \;=\; t_i - \tau^s_{\phi,r,j}(t_i) \;=\; t_i - \tau^s_r(t_i) \tag{2.13}$$

The receiver-satellite range may thus be assumed equally for each observable type. This range is denoted as follows:

$$\boxed{\rho_r^s(t_i - \tau_{g,r,j}^s(t_i)) \;=\; \rho_r^s(t_i - \tau_{\phi,r,j}^s(t_i)) \;=\; \rho_r^s(t_i - \tau_r^s(t_i))} \tag{2.14}$$

Observable- and frequency-dependent clock errors

In Sect. 2.3 receiver and satellite clock errors were introduced that are independent of the observable type. Besides, the introduced instrumental or hardware delays were different for each observable type and frequency. In a least-squares estimation it is however not possible to separate these clock errors and instrumental delays and only lumped combinations are estimable, which are denoted as:

$$\boxed{\begin{array}{lcl} dt_{r,j}(t_i) & = & dt_r(t_i) + d_{r,j}(t_i) \\ dt_{,j}^s(t_i) & = & dt^s(t_i - \tau_r^s(t_i)) - d_{,j}^s(t_i - \tau_r^s(t_i)) \\ \delta t_{r,j}(t_i) & = & dt_r(t_i) + \delta_{r,j}(t_i) \\ \delta t_{,j}^s(t_i) & = & dt^s(t_i - \tau_r^s(t_i)) - \delta_{,j}^s(t_i - \tau_r^s(t_i)) \end{array}} \tag{2.15}$$

Because of this lumping, the receiver and satellite clock errors become observable- and frequency-dependent variables.

Non-integer phase ambiguity

Like the clock error terms, also the initial phases of the signal and the integer phase ambiguity are only estimable when lumped together:

$$\boxed{M_{r,j}^s \;=\; \left[\varphi_{r,j}(t_0) - \varphi_{,j}^s(t_0) + N_{r,j}^s\right]} \tag{2.16}$$

This resulting ambiguity $M_{r,j}^s$ is a *non-integer*, whereas the ambiguity $N_{r,j}^s$ is an integer.

Other non-random errors

In Eqs. (2.12) and (2.8) all other non-random errors, like e.g. multipath, were included in $dm_{r,j}^s(t_i)$ (for code) and $\delta m_{r,j}^s(t_i)$ (for phase). From now on, it is assumed that these unmodelled errors may be neglected:

$$\boxed{dm_{r,j}^s(t_i) \;=\; \delta m_{r,j}^s(t_i) \;=\; 0} \tag{2.17}$$

Random errors or noise

Since GPS observations are stochastic, one needs to account for random errors or observation noise in the observation equations. For the code observable these random errors are denoted as $\epsilon_{p_{r,j}^s}(t_i)$ and for the phase observable as $\epsilon_{\phi_{r,j}^s}(t_i)$. In case of the geometry-free model, in which besides the phase and code observables pseudo-observables for the ranges are used, the random errors in these pseudo-observables are denoted by $\epsilon_{\rho_{r,p}^s}(t_i)$. Note that the subscript p is used to distinguish

the range *pseudo-observable* from the range *parameter*. The mean of all these random errors is zero:

$$\begin{array}{lcll} E\{\epsilon_{\phi^s_{r,j}}(t_i)\} & = & 0 & \\ E\{\epsilon_{p^s_{r,j}}(t_i)\} & = & 0 & \\ E\{\epsilon_{\rho^s_{r,p}}(t_i)\} & = & 0 & \text{(geometry-free model only)} \end{array} \tag{2.18}$$

A priori phase and code corrections

When available, the GPS observations may be corrected a priori. For example, they may be corrected using known phase center variations, satellite clock models, atmospheric models, phase wind-up model, etc. The sum of these a priori corrections for the phase observations is denoted as $\phi^s_{r,j}(t_i)^c$, whereas for the code observations it is denoted as $p^s_{r,j}(t_i)^c$. Note that both sums are expressed in meters. When also the phase observations are expressed in lengths, we obtain for the a priori corrected phase and code observables, denoted as respectively $\phi^s_{r,j}(t_i)$ and $p^s_{r,j}(t_i)$:

$$\begin{array}{lcl} \phi^s_{r,j}(t_i) & = & \lambda_j \varphi^s_{r,j}(t_i) \; - \; \phi^s_{r,j}(t_i)^c \\ p^s_{r,j}(t_i) & = & \vartheta^s_{r,j}(t_i) \; - \; p^s_{r,j}(t_i)^c \end{array} \tag{2.19}$$

Epoch notation

A last simplification in the phase and code expressions concerns the notation of the epoch, t_i, which from now on is abbreviated as i.

2.5.2 Non-positioning observation equations

Taking into account the simplifications in the previous subsection, the observation equations for non-positioning applications, in which phase, code and range pseudo-observables are used, can be given as follows (in units of length) for epoch i:

$$\begin{array}{lcl} \phi^s_{r,j}(i) & = & \rho^s_r(i) + c\delta t_{r,j}(i) - c\delta t^s_{,j}(i) + \delta a^s_{r,j}(i) + \lambda_j M^s_{r,j} + \epsilon_{\phi^s_{r,j}}(i) \\ p^s_{r,j}(i) & = & \rho^s_r(i) + cdt_{r,j}(i) - cdt^s_{,j}(i) + da^s_{r,j}(i) + \epsilon_{p^s_{r,j}}(i) \\ \rho^s_{r,p}(i) & = & \rho^s_r(i) + \epsilon_{\rho^s_{r,p}}(i) \end{array} \tag{2.20}$$

2.5.3 Positioning observation equations

Linearized observation equations

For positioning applications the phase and code observation equations need to be linearized with respect to the receiver position(s). The basis of this linearization is given by:

$$\rho^s_r(i) \; = \; \|r^s(i) \; - \; r_r(i)\| \tag{2.21}$$

where $r_r(i) \; = \; [x_r(i), y_r(i), z_r(i)]^T$ denotes the receiver coordinates and $r^s(i) = [x^s(i), y^s(i), z^s(i)]^T$ the satellite coordinates on epoch i. It is emphasized here that

this epoch i used for the satellite coordinates (and also the satellite clock in Eq. (2.20)) is not quite correct; for these parameters it should strictly be the epoch *minus the signal travel time* as explained in Eqs. (2.14) and (2.15). Although the *GPSveQ* software takes this effect into account, in this thesis we simply use the epoch of measurement in the receiver for all time-dependent variables, because of notational convenience. After linearization, the linearized observation equations read:

$$\boxed{\begin{array}{rcl} \Delta\phi^s_{r,j}(i) & = & -u^s_r(i)^{0T}\Delta r_r(i) + u^s_r(i)^{0T}\Delta r^s(i) + c\delta t_{r,j}(i) - c\delta t^s_{,j}(i) + \\ & & \delta a^s_{r,j}(i) + \lambda_j M^s_{r,j} + \epsilon_{\phi^s_{r,j}}(i) \\ \Delta p^s_{r,j}(i) & = & -u^s_r(i)^{0T}\Delta r_r(i) + u^s_r(i)^{0T}\Delta r^s(i) + cdt_{r,j}(i) - cdt^s_{,j}(i) + \\ & & da^s_{r,j}(i) + \epsilon_{p^s_{r,j}}(i) \end{array}} \tag{2.22}$$

Computation of approximate values

In the linearized observation equations $\Delta r_r(i)$ and $\Delta r^s(i)$ denote the increments of the receiver respectively satellite positions:

$$\begin{array}{rcl} \Delta r_r(i) & = & r_r(i) \; - \; r_r(i)^0 \\ \Delta r^s(i) & = & r^s(i) \; - \; r^s(i)^0 \end{array} \tag{2.23}$$

where $r_r(i)^0$ and $r^s(i)^0$ are *approximate values*. In GPS applications the approximate receiver position is usually available (the receiver itself computes a code solution all the time). In Sect. 2.5.4 more is said about the computation of the approximate satellite positions. The approximate receiver and satellite positions are also required to compute the vector $u^s_r(i)^0$, which is the approximate *unit direction vector* from receiver to satellite. It is computed as follows:

$$u^s_r(i)^0 \; = \; \frac{r^s_r(i)^0}{\|r^s_r(i)^0\|} \; = \; \frac{r^s(i)^0 - r_r(i)^0}{\rho^s_r(i)^0} \tag{2.24}$$

Note that for the other parameters in the linearized observation equations no increments appear. For these parameters it has been implicitly assumed that their approximate values are zero:

$$\begin{array}{rcl} dt_{r,j}(i)^0 & = & 0 \\ dt^s_{,j}(i)^0 & = & 0 \\ da^s_{r,j}(i)^0 & = & 0 \\ \delta t_{r,j}(i)^0 & = & 0 \\ \delta t^s_{,j}(i)^0 & = & 0 \\ \delta a^s_{r,j}(i)^0 & = & 0 \\ M^{s0}_{r,j} & = & 0 \end{array} \tag{2.25}$$

In the case that one wants to use approximate values for these parameters, increments for these parameters should be used in the observation equations. This may be the case when the a priori values of the unknown parameters are not precise enough, and an *iteration* procedure is necessary in the adjustment.

Observed-minus-computed observations

The incremental phase and code observables in the linearized observation equations, are obtained by subtracting the computed observations, denoted as $\phi^s_{r,j}(i)^0$ and $p^s_{r,j}(i)^0$, from the real observations. They are also referred to as the *observed-minus-computed* observations:

$$\begin{aligned} \Delta\phi^s_{r,j}(i) &= \phi^s_{r,j}(i) - \phi^s_{r,j}(i)^0 \\ \Delta p^s_{r,j}(i) &= p^s_{r,j}(i) - p^s_{r,j}(i)^0 \end{aligned} \tag{2.26}$$

Note that when no iterations are carried out, the computed observations are only based on the approximated receiver-satellite range, since the approximate values for all other parameters are zero:

$$\begin{aligned} \phi^s_{r,j}(i)^0 &= \rho^s_r(i)^0 \\ p^s_{r,j}(i)^0 &= \rho^s_r(i)^0 \end{aligned} \tag{2.27}$$

2.5.4 Computation of the satellite positions

As mentioned, for both geometry-based and geometry-free models a priori values for the satellite positions are required to compute the approximate receiver-satellite ranges. These satellite positions can be computed using the *broadcast ephemerides* in the satellite's navigation message or, much more precise, using *precise ephemerides* as computed and made available by the International GPS Service (IGS). In Table 2.2 the availability and accuracy of the different available orbit products is shown.

Table 2.2. Accuracy of GPS satellite positions (after [Neilan et al., 2000])

orbits	availability	accuracy
broadcast ephemerides	real-time	5 m
IGS ultra-rapid (predicted)	near real-time	20 cm
IGS rapid	17 hours	10 cm
IGS final	10 days	5 cm

2.6 General mathematical model

The linear or linearized observation equations from the previous section form the basis of a mathematical model for the least-squares estimation of the unknown parameters. This mathematical model, also known as the *Gauss-Markov model*, is discussed in its general form in the first subsection. For GPS applications it is advantageous to partition this model for temporal and non-temporal parameters, which is the topic of the remaining part of this section.

2.6.1 Gauss-Markov model

The general Gauss-Markov model can mathematically be given as:

$$\boxed{E\{y\} = Ax; \quad D\{y\} = Q_y} \tag{2.28}$$

where:

$E\{\cdot\}$	:	mathematical expectation operator
$D\{\cdot\}$	:	mathematical dispersion operator
y	:	vector of observables
x	:	vector of parameters
A	:	design matrix
Q_y	:	variance-covariance (vc-) matrix of the observables

The first part, in which the relations of the observables and the parameters are described, is called the *functional* model and the second part, describing the noise characteristics of the observables, is called the *stochastic* model.

2.6.2 Partitioning of the mathematical model

In case of GPS applications, the parameter vector x can be partitioned into two parts: A part for the parameters which are assumed to be *constant* in time (denoted as x_I), and a part for the time-varying or *temporal* parameters (denoted as x_{II}). As a consequence, the design matrix A is partitioned as follows:

$$A \;=\; [A_I,\; A_{II}]\,; \qquad x \;=\; \left[x_I^T,\; x_{II}^T\right]^T \tag{2.29}$$

In case of (traditional) *static* positioning applications the non-temporal parameters are formed by the coordinate components and the phase ambiguities. The other parameters (clocks, atmospheric biases) are all temporal. In case of (true) *kinematic* positioning applications however, at each observation epoch new receiver coordinate parameters are introduced, such that only the ambiguities remain as non-temporal parameters. Also, in case of *non-positioning* applications the only non-temporal parameters are the phase ambiguities, since the receiver-satellite ranges change with time. Note that in case of *instantaneous* or single-epoch processing (the shortest time span possible) the difference between non-temporal and temporal parameters disappears, since all parameters are estimated again for each observation epoch (including the phase ambiguities). For instantaneous processing there is also no distinction between static and kinematic applications.

When a *multiple of epochs* is involved in the mathematical model, in this research it is assumed that for the geometry-based model the non-temporal parameters are formed by the phase ambiguities plus receiver coordinates. All other parameters are temporally assumed. In case of the geometry-free model the only non-temporal parameters are the ambiguities. This classification is primarily meant for surveying applications, in which the receiver for which the position needs to be determined is assumed to be static during the time span.

When the *sampling interval* between two consecutive epochs is constant and denoted as $\Delta t = t_i - t_{i-1}$, and the number of epochs is denoted as k, it is said that the observations are collected during a *time span* with length $(k-1)\Delta t$. The observable vector for these k epochs can then be written as:

$$y = [y(1), \ldots, y(k)]^T \tag{2.30}$$

with the variance-covariance (vc-) matrix of the observables:

$$Q_y = \begin{bmatrix} Q_{y(1)} & \cdots & Q_{y(1)y(k)} \\ \vdots & \ddots & \vdots \\ Q_{y(k)y(1)} & \cdots & Q_{y(k)} \end{bmatrix} \tag{2.31}$$

Like the observables, the temporal parameters x_{II} are also parameterized for k epochs:

$$x_{II} = [x_{II}(1), \ldots, x_{II}(k)]^T \tag{2.32}$$

The design matrix parts A_I and A_{II} can be given as:

$$\begin{aligned} A_I &= \left[A_I(1)^T, \ldots, A_I(k)^T\right]^T \\ A_{II} &= \begin{bmatrix} A_{II}(1) & & \\ & \ddots & \\ & & A_{II}(k) \end{bmatrix} = \text{blkdiag}\left[A_{II}(1), \ldots, A_{II}(k)\right] \end{aligned} \tag{2.33}$$

where 'blkdiag' stands for a *block-diagonal* matrix, which is used to shorten the notation (it is in fact the matrix counterpart of the scalar 'diag'). In the following sections the functional and stochastic models for the geometry-based and the geometry-free models are derived in more detail.

2.7 The functional model without atmospheric errors

In this section the functional model parts of the geometry-based model and the geometry-free model are derived. For each model, the following functional model elements are set up: $y(i)$, $A_I(i)$, $A_{II}(i)$, x_I, $x_{II}(i)$. It is not trivial to set up the design matrix parts $A_I(i)$ and $A_{II}(i)$, since for a processing based on the original, undifferenced observables, they contain many *rank deficiencies*. This means that not all the original parameters can be estimated individually, but only lumped combinations of them. To distinct between the geometry-based and geometry-free models, the first model will be referred to using the superscript gb, whereas for the second model the superscript gf is reserved.

Both the geometry-based and geometry-free functional models derived in this section are valid for a multiple of receivers, collecting phase and code observations

from a multiple of satellites, at a multiple of frequencies. Hence, the model applies not only to the current single- and dual-frequency applications, but also to a modernized triple-frequency system. In the following derivations it is for the sake of simplicity assumed that all satellites are tracked by all receivers during all epochs, but in the *GPSveQ* software this is not a necessary condition, since in practice satellites rise and set, receivers may malfunction for some epochs, or there is signal loss-of-lock.

Another important assumption for the derivation of the models in this section is that the errors in the observations due to *atmospheric propagation* may be *neglected*:

$$\boxed{da^s_{r,j}(i) \;=\; \delta a^s_{r,j}(i) \;=\; 0} \tag{2.34}$$

This is of course an unrealistic assumption, but it is used for the time being to focus on the basic rank deficiencies. In the forthcoming chapters this assumption will be relaxed.

2.7.1 The rank-deficient functional model

In this subsection the vector of observables and the rank-deficient design matrix parts are presented, for both the geometry-based and geometry-free models. To emphasize the rank-deficient design matrix parts and corresponding parameters, an apostrophe (') is used.

Geometry-based model

In case of the geometry-based model, the vector of observables $y(i)$, for phase and code data, reads for j frequencies:

$$\boxed{y^{gb}(i) = \begin{bmatrix} \Phi^{gb}(i) \\ P^{gb}(i) \end{bmatrix} = \begin{bmatrix} \left[\Phi^{gb}_1(i)^T,\ \ldots,\ \Phi^{gb}_j(i)^T\right]^T \\ \left[P^{gb}_1(i)^T,\ \ldots,\ P^{gb}_j(i)^T\right]^T \end{bmatrix}} \tag{2.35}$$

The vector $y^{gb}(i)$ contains the 'observed-minus-computed' observations. It is assumed that on each GPS frequency nm phase and nm code observations have been collected, where n denotes the number of receivers and m the number of satellites:

$$\boxed{\begin{array}{rcl} \Phi^{gb}_j(i) & = & \left[\left(\Delta\phi^1_{1,j}(i), \ldots, \Delta\phi^m_{1,j}(i)\right),\ \ldots,\ \left(\Delta\phi^1_{n,j}(i), \ldots, \Delta\phi^m_{n,j}(i)\right)\right]^T \\ P^{gb}_j(i) & = & \left[\left(\Delta p^1_{1,j}(i), \ldots, \Delta p^m_{1,j}(i)\right),\ \ldots,\ \left(\Delta p^1_{n,j}(i), \ldots, \Delta p^m_{n,j}(i)\right)\right]^T \end{array}} \tag{2.36}$$

The rank-deficient design matrix corresponding to the non-temporal parameters will be denoted as $A^{gb'}_I(i)$, while the part corresponding to the temporal parameters

will be denoted as $A_{II}^{gb'}(i)$. They both read:

$$\begin{aligned} A_{I}^{gb'}(i) &= \left[\begin{pmatrix} e_j \\ e_j \end{pmatrix} \otimes \mathcal{A}'(i) \quad \begin{pmatrix} \Lambda \\ 0 \end{pmatrix} \otimes I_{nm} \right] \\ A_{II}^{gb'}(i) &= \left[\begin{pmatrix} I_j & \\ & I_j \end{pmatrix} \otimes \mathcal{D}' \quad \begin{pmatrix} e_j \\ e_j \end{pmatrix} \otimes \mathcal{H}'(i) \right] \end{aligned} \tag{2.37}$$

For a compact notation, the matrix *Kronecker product* (denoted by the symbol $\otimes$) has been used. For its definition and properties, see App. A.

In these rank-deficient design matrices, the sub-matrices $\mathcal{A}'(i)$, $\mathcal{H}'(i)$ and $\mathcal{D}'$ denote the parts for respectively the receiver positions, satellite positions and (receiver and satellite) clock errors. They read:

$$\begin{aligned} \mathcal{A}'(i) &= \underbrace{\text{blkdiag}\left[G_1(i),\ \ldots,\ G_n(i)\right]}_{nm\times 3n} && \text{(receiver positions)} \\ \mathcal{H}'(i) &= \underbrace{\left[H_1(i)^T,\ \ldots,\ H_n(i)^T\right]^T}_{nm\times 3m} && \text{(satellite positions)} \\ \mathcal{D}' &= \underbrace{\left[I_n \otimes e_m \quad -e_n \otimes I_m\right]}_{nm\times(n+m)} && \text{(receiver and satellite clock errors)} \end{aligned} \tag{2.38}$$

Both matrices $G_r(i)$ and $H_r(i)$ contain the receiver-satellite unit vectors. They read for $r = 1, \ldots, n$:

$$\boxed{\begin{aligned} G_r(i) &= \underbrace{\left[-u_r^1(i)^0,\ \ldots,\ -u_r^m(i)^0\right]^T}_{m\times 3} \\ H_r(i) &= \underbrace{\text{blkdiag}\left[-u_r^1(i)^0,\ \ldots,\ -u_r^m(i)^0\right]^T}_{m\times 3m} \end{aligned}} \tag{2.39}$$

The sub-matrix Λ in the design matrix part of the phase ambiguities is a diagonal matrix with GPS wavelengths, since the phase observable is expressed in meters, rather than cycles. It reads:

$$\boxed{\Lambda = \underbrace{\text{diag}\left(\lambda_1,\ \ldots,\ \lambda_j\right)}_{j\times j}} \tag{2.40}$$

The vector of unknown parameters is split into a non-temporal part x'_I and a temporal part $x'_{II}(i)$, conform the structure of the design matrix:

$$\begin{aligned} x_I^{gb'} &= \left[g'^T,\ \left(a_1'^T, \ldots, a_j'^T\right)\right]^T \\ x_{II}^{gb'}(i) &= \left[\left(\alpha'_1(i)^T, \ldots, \alpha'_j(i)^T\right),\ \left(\beta'_1(i)^T, \ldots, \beta'_j(i)^T\right),\ o'(i)^T\right]^T \end{aligned} \tag{2.41}$$

The non-temporal parameters, the receiver positions and the phase ambiguities, are stored in g' resp. in a'_j:

$$\begin{aligned} g' &= \left[\Delta r_1^T,\ \ldots,\ \Delta r_n^T\right]^T \\ a'_j &= \left[\left(M_{1,j}^1,\ \ldots,\ M_{1,j}^m\right),\ \ldots,\ \left(M_{n,j}^1,\ \ldots,\ M_{n,j}^m\right)\right]^T \end{aligned}$$

The temporal parameters are the phase clock and code clock error terms, stored in $\alpha'_j(i)$ resp. $\beta'_j(i)$, and the satellite positions, which are stored in $o'(i)$:

$$\begin{aligned} \alpha'_j(i) &= \left[\left(c\delta t_{1,j}(i),\ \ldots,\ c\delta t_{n,j}(i)\right),\ \left(c\delta t_{,j}^1(i),\ \ldots,\ c\delta t_{,j}^m(i)\right)\right]^T \\ \beta'_j(i) &= \left[\left(cdt_{1,j}(i),\ \ldots,\ cdt_{n,j}(i)\right),\ \left(cdt_{,j}^1(i),\ \ldots,\ cdt_{,j}^m(i)\right)\right]^T \\ o'(i) &= \left[\Delta r^1(i)^T,\ \ldots,\ \Delta r^m(i)^T\right]^T \end{aligned} \tag{2.42}$$

Geometry-free model

In case of the geometry-free model, the vector of observables $y^{gf}(i)$, for phase and code data plus range pseudo-observations, reads:

$$\boxed{y^{gf}(i) = \begin{bmatrix} \begin{pmatrix} \Phi^{gf}(i) \\ P^{gf}(i) \end{pmatrix} \\ \rho_p(i) \end{bmatrix} = \begin{bmatrix} \begin{pmatrix} \left[\Phi_1^{gf}(i)^T,\ \ldots,\ \Phi_j^{gf}(i)^T\right]^T \\ \left[P_1^{gf}(i)^T,\ \ldots,\ P_j^{gf}(i)^T\right]^T \end{pmatrix} \\ \rho_p(i) \end{bmatrix}} \tag{2.43}$$

For the geometry-free model the original observations appear in the observable vector:

$$\boxed{\begin{aligned} \Phi_j^{gf}(i) &= \left[\left(\phi_{1,j}^1(i),\ldots,\phi_{1,j}^m(i)\right),\ \ldots,\ \left(\phi_{n,j}^1(i),\ldots,\phi_{n,j}^m(i)\right)\right]^T \\ P_j^{gf}(i) &= \left[\left(p_{1,j}^1(i),\ldots,p_{1,j}^m(i)\right),\ \ldots,\ \left(p_{n,j}^1(i),\ldots,p_{n,j}^m(i)\right)\right]^T \\ \rho_p(i) &= \left[\left(\rho_{1,p}^1(i),\ldots,\rho_{1,p}^m(i)\right),\ \ldots,\ \left(\rho_{n,p}^1(i),\ldots,\rho_{n,p}^m(i)\right)\right]^T \end{aligned}} \tag{2.44}$$

Note that the sample values of the range pseudo-observables are computed from the a priori satellite and receiver positions.

Like for the geometry-based model, the parameter vector is split into a non-temporal part x'_I and a temporal part $x'_{II}(i)$. Their partial design matrices read:

$$\begin{aligned} A_I^{gf'}(i) &= \begin{bmatrix} \begin{pmatrix} \Lambda \\ 0 \end{pmatrix} \\ 0 \end{bmatrix} \otimes I_{nm} \\ A_{II}^{gf'}(i) &= \begin{bmatrix} \begin{bmatrix} \begin{pmatrix} I_j & \\ & I_j \end{pmatrix} \\ 0 \end{bmatrix} \otimes \mathcal{D}' & \begin{bmatrix} \begin{pmatrix} e_j \\ e_j \end{pmatrix} \\ 1 \end{bmatrix} \otimes I_{nm} \end{bmatrix} \end{aligned} \tag{2.45}$$

For this model the non-temporal parameters are the phase ambiguities. All other

parameters, which are the phase and code clock errors and the ranges receiver-satellite, are temporal parameters:

$$\begin{array}{rcl} x_I^{gf'} & = & \left[a_1'^T, \ldots, a_j'^T\right]^T \\ x_{II}^{gf'}(i) & = & \left[\left(\alpha_1'(i)^T, \ldots, \alpha_j'(i)^T\right),\ \left(\beta_1'(i)^T, \ldots, \beta_j'(i)^T\right),\ \rho(i)^T\right]^T \end{array} \tag{2.46}$$

2.7.2 Rank deficiencies and ways to remove them

To solve the mathematical model uniquely, the rank deficiencies in the columns of the design matrix must be eliminated. The design matrix can be made of full rank by lumping the parameters together (in fact a parameter transformation is performed), which corresponds to the well-known *S-basis* techniques as developed by [Baarda, 1973] and [Teunissen, 1984]. In this section the rank deficiencies in the geometry-based and geometry-free models are identified and eliminated. This will be done in a step-by-step approach, since it is allowed to solve the rank deficiencies individually. Some rank deficiencies are the same for both models and in that case they are discussed just once. Other rank deficiencies are model-specific, which is emphasized in the text. Note that in this subsection the rank deficiencies are removed in one particular way, and this choice determines the estimable parameter solutions. One should realize that it is also possible to solve them in other ways, from which other estimable parameter solutions follow.

Step 1: Receiver and satellite clocks

A first rank deficiency can be identified when the design matrix columns for the receiver and satellite clock biases are considered, see Eq. (2.38):

$$\mathcal{D}' = \underbrace{[I_n \otimes e_m, \quad -e_n \otimes I_m]}_{nm \times (n+m)} \tag{2.47}$$

This submatrix has a rank deficiency of 1. It can be solved by subtracting the clock error of the first (pivot) receiver from every other clock error. The full-rank matrix, denoted by $\mathcal{D}$, becomes:

$$\boxed{\mathcal{D} = \underbrace{[C_n \otimes e_m, \quad -e_n \otimes I_m]}_{nm \times (n-1+m)}, \quad \text{where } C_n = \underbrace{\begin{bmatrix} 0_{1\times(n-1)} \\ I_{n-1} \end{bmatrix}}_{n \times (n-1)}} \tag{2.48}$$

For the receiver clock parameters this implies that the clock of the first receiver is removed and the following set of reparameterized clock errors remains:

$$\begin{array}{rcl} \alpha"(i) & = & [([c\delta t_{2,j}(i) - c\delta t_{1,j}(i)],\ \ldots,\ [c\delta t_{n,j}(i) - c\delta t_{1,j}(i)]) \\ & & \left([c\delta t_{,j}^1(i) - c\delta t_{1,j}(i)],\ \ldots,\ [c\delta t_{,j}^m(i) - c\delta t_{1,j}(i)]\right)\big]^T \\ \beta"(i) & = & [([cdt_{2,j}(i) - cdt_{1,j}(i)],\ \ldots,\ [cdt_{n,j}(i) - cdt_{1,j}(i)]) \\ & & \left([cdt_{,j}^1(i) - cdt_{1,j}(i)],\ \ldots,\ [cdt_{,j}^m(i) - cdt_{1,j}(i)]\right)\big]^T \end{array}$$

In fact, *relative* receiver and satellite clock errors become estimable.

Step 2: Phase satellite clocks and ambiguities

A second rank deficiency is present in the design matrix columns of the reparameterized satellite clock parameters of the phase observables and the ambiguities (for one frequency j):

$$\underbrace{[-e_n \otimes I_m, \quad \lambda_j I_n \otimes I_m]}_{nm \times (n+1)m} \tag{2.49}$$

The rank deficiency of this matrix is m. It can be eliminated by subtracting the m ambiguities of the first (pivot) receiver from all other parameters. The resulting full-rank matrix becomes:

$$\underbrace{[-e_n \otimes I_m, \quad \lambda_j C_n \otimes I_m]}_{nm \times nm} \tag{2.50}$$

As a consequence, the reparameterized phase satellite clocks and ambiguities become:

$$\begin{aligned}&[\underbrace{[c\delta t^1_{,j}(i) - c\delta t_{1,j}(i) - \lambda_j M^1_{1,j}]}_{c\delta t^1_{1,j}(i)}, \ \ldots, \ \underbrace{[c\delta t^m_{,j}(i) - c\delta t_{1,j}(i) - \lambda_j M^m_{1,j}]}_{c\delta t^m_{1,j}(i)}]^T \\ &\left[\left(M^1_{12,j}, \ \ldots, \ M^m_{12,j}\right), \ \ldots, \ \left(M^1_{1n,j}, \ \ldots, \ M^m_{1n,j}\right)\right]^T\end{aligned}$$

These reparameterized ambiguities are better known as (between-receiver) *single-differenced* ambiguities. Note that the *code* satellite clock parameters remain unchanged in this step. They read:

$$[\underbrace{[cdt^1_{,j}(i) - cdt_{1,j}(i)]}_{cdt^1_{1,j}(i)}, \ \ldots, \ \underbrace{[cdt^m_{,j}(i) - cdt_{1,j}(i)]}_{cdt^m_{1,j}(i)}]^T$$

Step 3: Phase receiver clocks and ambiguities

A next rank deficiency can be identified by considering the design matrix columns of the reparametrized phase receiver clock parameters and the reparameterized ambiguities (for one frequency j):

$$\underbrace{[C_n \otimes e_m, \quad \lambda_j C_n \otimes I_m]}_{nm \times (n-1)(m+1)} \tag{2.51}$$

The rank deficiency is of size $(n-1)$. It can be removed by adding the single-differenced ambiguities corresponding to the first (or pivot) satellite to the receiver clock parameters and by subtracting the same terms from the ambiguity parameters. The full-rank matrix becomes:

$$\underbrace{[C_n \otimes e_m, \quad \lambda_j C_n \otimes C_m]}_{nm \times (n-1)m} \tag{2.52}$$

From now on the Kronecker product of C_n with C_m will be denoted by $\mathcal{C}$:

$$\boxed{\mathcal{C} \;=\; C_n \otimes C_m} \tag{2.53}$$

Removing the single-differenced ambiguities corresponding to the first (pivot) satellite, the following vectors of reparametrized receiver clock and ambiguity parameters remain:

$$\underbrace{[[c\delta t_{2,j}(i) - c\delta t_{1,j}(i) + \lambda_j M^1_{12,j}]}_{c\delta t_{12,j}(i)},\; \ldots,\; \underbrace{[c\delta t_{n,j}(i) - c\delta t_{1,j}(i) + \lambda_j M^1_{1n,j}]]}_{c\delta t_{1n,j}(i)}{}^T$$
$$\left[\left(M^{12}_{12,j},\; \ldots,\; M^{1m}_{12,j}\right),\; \ldots,\; \left(M^{12}_{1n,j},\; \ldots,\; M^{1m}_{1n,j}\right)\right]^T$$

In this step, due to the reparametrization, the single-differenced ambiguities have become *double-differenced* ambiguities instead, which turns out to be very crucial for *fast* GPS applications (see Chap. 3). Note that after this step the *code* receiver clock parameters remain unchanged. They read:

$$\underbrace{[[cdt_{2,j}(i) - cdt_{1,j}(i)]}_{cdt_{12,j}(i)},\; \ldots,\; \underbrace{[cdt_{n,j}(i) - cdt_{1,j}(i)]]}_{cdt_{1n,j}(i)}{}^T \tag{2.54}$$

Step 4: Satellite positions and satellite clocks (geometry-based model only)

Consider the partial design matrices of the satellite positions and satellite clocks:

$$\left[\; \begin{pmatrix} e_j \\ e_j \end{pmatrix} \otimes \begin{pmatrix} H_1(i) \\ \vdots \\ H_n(i) \end{pmatrix} \quad \begin{pmatrix} e_j \\ e_j \end{pmatrix} \otimes \begin{pmatrix} -I_m \\ \vdots \\ -I_m \end{pmatrix} \;\right] \tag{2.55}$$

These partial design matrices do however not contain a *real* rank deficiency. In the type of GPS applications discussed in this thesis the distances between the receivers are quite short compared to the distance from the receivers to a certain satellite (about 20,200 km). This means that the unit vectors $u^s_r(i)^0$ to a certain satellite become approximately *parallel* vectors for all receivers in the network:

$$H_1(i) \;\approx\; H_2(i) \;\approx\; \ldots \;\approx\; H_n(i) \tag{2.56}$$

In the limiting case, when $H_1(i) = H_2(i) = \ldots = H_n(i) \equiv \tilde{H}(i)$, a real rank deficiency arises in the design matrix, between the columns of the satellite positions and those of the satellite clock parameters. Therefore, for the relative GPS applications in this thesis, the satellite positions are not parameterized at all, but held *fixed* in the adjustment:

$$\boxed{\Delta r^s(i) \;=\; 0, \quad s = 1, \ldots, m} \tag{2.57}$$

For precise relative GPS applications the satellite positions should be computed from precise IGS orbits, see Sect. 2.5.4. These orbits are so precise, such that the effect of the uncertainty in the satellite positions may be neglected for the relative GPS applications described in this thesis (see e.g. [Teunissen and Kleusberg, 1998]).

Step 5: Receiver positions and satellite clocks (geometry-based model only)

Similar to the previous (near-) rank deficiency, another near rank deficiency arises for short to medium-distance applications, since the partial design matrices for the receiver positions become approximately equal:

$$G_1(i) \;\approx\; G_2(i) \;\approx\; \ldots \;\approx\; G_n(i) \tag{2.58}$$

Like in step 4, in the limiting case, when $G_1(i) = G_2(i) = \ldots = G_n(i) \equiv \tilde{G}(i)$, a real rank deficiency arises between the columns of the receiver positions and those of the satellite clock parameters. This rank deficiency is of size 3 and it is solved by assuming the coordinates of the first (pivot) receiver to be known:

$$\boxed{\Delta r_1 \;=\; 0} \tag{2.59}$$

Because of this assumption, the position increments of the other receivers can be parameterized with respect to the pivot receiver, such that *relative* positions are estimable:

$$\Delta r_{1r} \;=\; \Delta r_r \;-\; \Delta r_1 \;=\; \Delta r_r, \quad r = 2, \ldots, n \tag{2.60}$$

The resulting partial design matrix for these receiver positions reads:

$$\boxed{\mathcal{A}(i) \;=\; \underbrace{\begin{bmatrix} 0_{m\times 3(n-1)} \\ \text{blkdiag}\,[G_2(i),\; \ldots,\; G_n(i)] \end{bmatrix}}_{nm\times 3(n-1)}} \tag{2.61}$$

2.7.3 The full-rank functional model

Having identified and removed the rank deficiencies, Table 2.3 summarizes the full-rank functional model elements for the geometry-based and geometry-free models. Some estimable parameters are the same for both models, and they are given below the second bold horizontal line in the table.

Inclusion of code data

In this context, note that the inclusion of the *code* observations in both geometry-based and geometry-free models is not strictly required for solving the model, at least, when more than one observation epoch is used. The code observations are included here, since they are usually available and strengthen the model. In the absence of code data, the rank deficiencies in the design matrices are not altered, and hence the phase-only model is obtained by leaving out the code observables and code-specific parameters from the partial design matrices in Table 2.3. In the case of *instantaneous* GPS applications however, it is absolutely required that code data are included in the model (this is discussed later on in this section).

Redundancy aspects

Using the full-rank model, the *redundancy* of the model can be computed. The redundancy of a model is the number of observations minus the number of es-

Table 2.3. Undifferenced partial design matrices and estimable parameters

	`geometry-based model`	`geometry-free model`
$A_I(i)$	$\left[\begin{pmatrix} e_j \\ e_j \end{pmatrix} \otimes \mathcal{A}(i) \quad \begin{pmatrix} \Lambda \\ 0 \end{pmatrix} \otimes \mathcal{C} \right]$	$\left[\begin{pmatrix} \Lambda \\ 0 \\ 0 \end{pmatrix} \right] \otimes \mathcal{C}$
$A_{II}(i)$	$\left[\begin{pmatrix} I_j & \\ & I_j \end{pmatrix} \otimes \mathcal{D} \right]$	$\left[\left[\begin{pmatrix} I_j & \\ & I_j \\ 0 & \end{pmatrix} \right] \otimes \mathcal{D} \left[\begin{pmatrix} e_j \\ e_j \\ 1 \end{pmatrix} \right] \otimes I_{nm} \right]$
x_I	$\left[g^T,\ \left(a_1^T,\ \ldots,\ a_j^T \right) \right]^T$	$\left[a_1^T,\ \ldots,\ a_j^T \right]^T$
$x_{II}(i)$	$\left[\left(\alpha_1^T(i), \ldots, \alpha_j^T(i) \right), \left(\beta_1^T(i), \ldots, \beta_j^T(i) \right) \right]^T$	$\left[\left(\alpha_1^T(i), \ldots, \alpha_j^T(i) \right), \left(\beta_1^T(i), \ldots, \beta_j^T(i) \right), \rho(i)^T \right]^T$

g	$= \left[\Delta r_{12}^T,\ \ldots,\ \Delta r_{1n}^T \right]^T$	$3(n-1)$ `coordinates`
a_j	$= \left[\left(M_{12,j}^{12},\ \ldots,\ M_{12,j}^{1m} \right),\ \ldots,\ \left(M_{1n,j}^{12},\ \ldots,\ M_{1n,j}^{1m} \right) \right]^T$	$j(n-1)(m-1)$ `ambiguities`
$\alpha_j(i)$	$= \left[\left(c\delta t_{12,j}(i),\ \ldots,\ c\delta t_{1n,j}(i) \right),\ \left(c\delta t_{1,j}^1(i),\ \ldots,\ c\delta t_{1,j}^m(i) \right) \right]^T$	$j(n-1+m)$ `phase clocks`
$\beta_j(i)$	$= \left[\left(cdt_{12,j}(i),\ \ldots,\ cdt_{1n,j}(i) \right),\ \left(cdt_{1,j}^1(i),\ \ldots,\ cdt_{1,j}^m(i) \right) \right]^T$	$j(n-1+m)$ `code clocks`
$\rho(i)$	$= \left[\left(\rho_1^1(i),\ \ldots,\ \rho_1^m(i) \right),\ \ldots,\ \left(\rho_n^1(i),\ \ldots,\ \rho_n^m(i) \right) \right]^T$	nm `ranges`

timable parameters. When there is redundancy in a model, it is possible to derive *statistical hypotheses* to test for errors and other model mis-specifications, see [Teunissen, 2000c]. For the geometry-based and geometry-free GPS models, in Table 2.4 the redundancy is given as function of the number of receivers n, satellites m, frequencies j, and observation epochs k. This is done for the case that both phase and code observations are included in the model, as well as for the case in which only phase observations are used.

Table 2.4. Redundancy of the geometry-based and geometry-free models

	`phase and code`	`phase-only`
`geometry-based model`	$(n-1)[(m-1)j(2k-1)-3]$	$(n-1)[(m-1)j(k-1)-3]$
`geometry-free model`	$(n-1)(m-1)j(2k-1)$	$(n-1)(m-1)j(k-1)$

To actually have redundancy in the models, the following requirements with respect to the number of receivers, satellites, epochs and frequencies should be met. To process relative GPS data, the number of *receivers* should be at least two. When $n = 2$, the measurement setup is usually referred to as a *single-baseline*. The minimum number of *satellites* differs for the geometry-based and the geometry-free models. For the geometry-free model, a number of $m = 2$ satellites is already sufficient, so -if desired- the processing can be carried out for each receiver-satellite pair *individually*. When the receiver-satellite geometry is incorporated into the model, the model is solvable with $m = 4$ satellites, but the redundancy becomes zero in case of single-frequency data. In that case the minimum number should

be $m = 5$. The minimum number of *epochs* for which the GPS data is collected should be at least one, provided that both phase and code observations are used. In case of phase-only, at least two epochs should be used. When $k = 1$, the shortest time span possible, we speak of *instantaneous* or *single-epoch* processing. Concerning the minimum number of *frequencies*, both the geometry-based and geometry-free models (in the absence of atmospheric errors) are already solvable with *single-frequency* GPS data ($j = 1$).

2.8 The stochastic model

Besides the functional model, in a least-squares adjustment of the GPS observations, the stochastic model plays an important role. This stochastic model describes the statistical properties of the observables in the form of a *variance-covariance matrix*. The GPS code and phase observables are stochastic variables because of (random) noise in the observations and (non-random) noise due to biases which are not modelled in the functional model. It is evident that this uncertainty should be adequately modelled, since the quality of the estimated parameters (precision and reliability), and also the statistical testing results, depend for a large amount on these a priori assumptions. In this section the stochastic model which is used in this thesis is described.

2.8.1 The stochastic properties of GPS observables

It is well known that the noise of the phase observations is much less than that of the code observations, but the vc-matrix of the GPS observables is still not well known. Therefore, a common approach is to assume the phase and code observables to be *normally distributed* and uncorrelated, with a constant standard deviation for both code observables (e.g. 30 cm) and both phase observables (e.g. 3 mm). Because of this lack of knowledge, the research to the stochastic properties of the GPS observables has received increasing attention in the recent past. Below a summary is given containing the most important findings from the recent literature. An important conclusion which can be drawn is that the stochastic properties turn out to be very *receiver-specific* and observable-type dependent.

Normally distributed observables

In GPS data processing it is very common to assume the observables to be normally distributed, but it is rarely verified whether this is really the case. From experiments described in [Tiberius, 1998] and [Tiberius and Borre, 1999] it is concluded that normality (fortunately) seems to be a reasonable assumption for GPS phase and code observations.

Accuracy of each observable type

[Bona, 2000b] concluded from zero-baseline experiments (where the influence of atmospheric delays, orbit errors and multipath is eliminated) that the phase stan-

dard deviations are better than the often assumed 3 mm. It was claimed that they have an accuarcy at sub-mm level or even better, and that the L2 standard deviation is typically larger than the L1 standard deviation, because of Anti-Spoofing encryption (see cross-correlation, below). The code standard deviations seem to be even better than 10 cm. In the presence of multipath however, the observations can be biased, and since multipath can hardly be captured in the functional model, it will be lumped with the noise of the observations. As a consequence, the phase standard deviations, when estimated from the data, may be about 3 mm, whereas the code standard deviations can be up to 60 cm for a low elevation satellite [Bona, 2000a].

Satellite-elevation dependency

Since the signals from low-elevation satellites are generally weaker than signals from higher satellites, various researchers concluded that the standard deviation is a function of the elevation angle at which the satellite is observed, see e.g. [Euler and Goad, 1991], [Gerdan, 1995], [Jin, 1996] and more recently, [Tiberius, 1999] and [Barnes, 2000]. From the latter article it follows that it is possible to model this elevation dependency with the same function for every observable type, but the coefficients of this function seem to differ extremely per observable type and per receiver.

Cross-correlation

In Sect. 2.2.2 it was already mentioned that under Anti-Spoofing (A-S) the known P-code is replaced by the unknown Y-code and the receiver has to apply a reconstruction technique to derive the observations on L2. This may cause correlation between the L1 and L2 observables. Note that this only concerns correlation between the *phase* observations on L1 and L2, or correlation between the *code* observations on L1 and L2. Correlation between phase and code seems to be practically absent. For more information, see [Bona, 2000b].

Time-correlation

Time-correlation is present in GPS observations, especially for code observations. This is probably caused by internal receiver filtering for reducing the noise and the effect of multipath on the code observations. However, the time-correlation seems to be very little (the lag is smaller than 20 s in general) [Bona, 2000b]. So when a sampling interval of e.g. 30 s is used, the GPS observations seem to be essentially *white-noise* (uncorrelated in time). In [Borre and Tiberius, 2000] it is concluded that time-correlation turns out to be significant for 5 Hz data (one sample per 0.2 s). Note that in case of instantaneous applications, possible time-correlation does not play a role, since the processing is conducted for each epoch individually.

2.8.2 The structure of the variance-covariance matrix

The stochastic model of the GPS observables used in the research for this thesis is restricted to the possibilities in the *GPSveQ* software. Although the vc-matrix which is specified in the current version of this software is more sophisticated than the original model as described in [De Jonge, 1998], it is still impossible to incorporate all statistical properties as mentioned in the previous subsection. The components of the observable vc-matrix in the current version of *GPSveQ* are summarized below.

Uncorrelated observables in time

It is *not* possible to model time-correlation in the vc-matrix, since this does not fit into the algorithm in which the normal equations in *GPSveQ* are solved (see Chap. 5). Instead of the general vc-matrix as given in Eq. (2.31), the following block-diagonal vc-matrix is implemented, which is uncorrelated in time:

$$\boxed{Q_y \;=\; \text{blkdiag}\left[Q_{y(1)},\; \ldots,\; Q_{y(k)}\right]} \tag{2.62}$$

Epoch-specific parts

The epoch-specific vc-matrix $Q_{y(i)}$ depends on whether the geometry-based or geometry-free model is used:

$$\boxed{Q_{y(i)} \;=\; \begin{cases} \text{blkdiag}\left[Q_\phi,\; Q_p\right] \otimes Q(i) & \text{(geometry-based model)} \\ \text{blkdiag}\left[\left(Q_\phi,\; Q_p\right),\; \sigma_\rho^2\right] \otimes Q(i) & \text{(geometry-free model)} \end{cases}} \tag{2.63}$$

In this vc-matrix per epoch Q_ϕ and Q_p denote the parts specific for the phase respectively code observables, σ_ρ^2 the variance factor of the range pseudo-observables in case of the geometry-free model, and $Q(i)$ the part which is similar for each observable type. Note that only when $Q(i) = I_{nm}$, the matrices Q_ϕ, Q_p may be referred to as phase and code *vc-matrices*. When this does not hold, one should speak of *cofactor matrices*. Also, when $Q(i) = I_{nm}$, σ_ρ^2 may be called a *variance*. Otherwise it should be referred to as *variance factor*.

By tuning the size of σ_ρ in the geometry-free vc-matrix, the weight of the *range pseudo-observables* in the least-squares adjustment can be controlled. In this context two extreme situations can be distinguished. When the weight is taken as an *infinitely large* value, in the adjustment the ranges become completely *known* quantities. Using a *infinitely small* or zero weight on the other hand, the range parameters become completely *unknown* parameters. The first weight should be taken in the case one would have ultimately precise ranges available. The processing model becomes in that case a so-called *range-fixed* model, since no parameters for the ranges are solved. In the second case, when the weight is zero, the geometry-free model reduces to the so-called *range-float* model, for which no a priori range

information at all is included. Note that this range-float model corresponds to the traditional geometry-free model as described in the literature.

Observable-type specific parts

The observable-type specific parts of the vc-matrix read for phase and code respectively on j frequencies:

$$Q_\phi = \begin{bmatrix} \sigma^2_{\phi_1} & \dots & \sigma_{\phi_1\phi_j} \\ \vdots & \ddots & \vdots \\ \sigma_{\phi_j\phi_1} & \dots & \sigma^2_{\phi_j} \end{bmatrix}; \quad Q_p = \begin{bmatrix} \sigma^2_{p_1} & \dots & \sigma_{p_1p_j} \\ \vdots & \ddots & \vdots \\ \sigma_{p_jp_1} & \dots & \sigma^2_{p_j} \end{bmatrix} \tag{2.64}$$

where $\sigma^2_{\phi_1}$ and $\sigma^2_{\phi_j}$ denote the a priori variance factors of the phase observables on the different frequencies, whereas $\sigma_{\phi_1\phi_j}$ denotes the covariance factor between the different frequencies. The factors $\sigma^2_{p_1}$, $\sigma^2_{p_j}$ and $\sigma_{p_1p_j}$ denote their code counterparts. Only when $Q(i) = I_{nm}$ they may be referred to as variances and covariances.

Receiver/satellite-specific part

For n receivers and m satellites, the matrix $Q(i)$, which is equally assumed for all observables, reads:

$$Q(i) \;=\; \text{blkdiag}\left[Q_1(i),\; \dots,\; Q_n(i)\right] \tag{2.65}$$

where $Q_r(i),\ r = 1,\dots,n$ models the satellite-dependent precision effects per receiver. Through this part possible *satellite-elevation dependency* can be taken into account:

$$Q_r(i) \;=\; \text{diag}\left(\left[q^1_r(i)\right]^2,\; \dots,\; \left[q^m_r(i)\right]^2\right) \tag{2.66}$$

where $q^s_r(i)$ is a chosen elevation-dependent function for the standard deviation. This may for example be an exponential function as used in [Euler and Goad, 1991]. When no elevation-dependent function is specified, it is by default assumed that $Q_r(i) = I_m$.

2.9 Undifferenced vs. double-differenced model

In the previous sections the mathematical model for *undifferenced* GPS observation equations was derived. In this section it is shown that this undifferenced model can be transformed to a model with *double-differenced* observation equations, the model which is often applied in practice. However, the information content in the original undifferenced observations is only preserved in this transformation when *all* n receivers track the *same* m satellites, which is not always the case in practice. For example, in the case that not all receivers in the network track the same number of satellites, in the double-differenced model some observations cannot be used, while in the undifferenced model they are included. In that case the use of the double-differenced model results in a loss of information. See for

a more elaborate discussion on this topic, [De Jonge, 1998]. In this section it is however assumed that all n receivers track the same m satellites. It is shown how in that situation the double-differenced versions of the design matrix, vc-matrix and estimable parameters are derived, for both the geometry-based and the geometry-free models.

2.9.1 Transformation matrix

The transformation from undifferenced to double-differenced model is carried out by pre-multiplying the undifferenced model on each observation epoch with the following transformation matrix:

$$\boxed{\Upsilon(i) \;=\; \begin{cases} \text{blkdiag}\left[I_j,\ I_j\right] \otimes \left[D_n^T \otimes D_m^T\right] & \text{(geometry-based model)} \\ \text{blkdiag}\left[\left(I_j,\ I_j\right),\ 1\right] \otimes \left[D_n^T \otimes D_m^T\right] & \text{(geometry-free model)} \end{cases}} \tag{2.67}$$

In these transformation matrices the $(n-1)\times n$ matrix D_n^T denotes the *difference operator for receivers* and the $(m-1)\times m$ matrix D_m^T the *difference operator for satellites*. The structure of these difference operators depends on the way the observables are differenced. For example, when the first receiver and the first satellite are selected as pivots, the respective difference operators read:

$$\boxed{D_n^T = \left[-e_{n-1},\ I_{n-1}\right];\qquad D_m^T = \left[-e_{m-1},\ I_{m-1}\right]} \tag{2.68}$$

Throughout this thesis we will adopt for the difference operators the structure as in Eq. (2.68).

As can be seen, both difference operators D_n and D_m are not of full rank, which implies that transformation matrix Υ is also not of full rank. So when going from the undifferenced to the double-differenced model, it seems that the information content in the original undifferenced observations is lost. In App. B it is shown that this is fortunately not the case.

2.9.2 Double-differenced observables and vc-matrix

DD observables

After the transformation, the DD observable vector reads as follows:

$$\boxed{y^{dd}(i) \;=\; \Upsilon(i)y(i) \;=\; \begin{cases} \begin{bmatrix} \left[\Phi_1^{gb,dd}(i)^T,\ \ldots,\ \Phi_j^{gb,dd}(i)^T\right]^T \\ \left[P_1^{gb,dd}(i)^T,\ \ldots,\ P_j^{gb,dd}(i)^T\right]^T \end{bmatrix} & \text{(geom.-based)} \\ \begin{bmatrix} \left[\Phi_1^{gf,dd}(i)^T,\ \ldots,\ \Phi_j^{gf,dd}(i)^T\right]^T \\ \left[P_1^{gf,dd}(i)^T,\ \ldots,\ P_j^{gf,dd}(i)^T\right]^T \\ \rho_p^{dd}(i) \end{bmatrix} & \text{(geom.-free)} \end{cases}}$$

(2.69)

In case of the geometry-based model the transformed observables are in fact the *observed-minus-computed* DD observables:

$$\begin{aligned} \Phi_j^{gb,dd}(i) &= \left[\left(\Delta\phi_{12,j}^{12}(i),\ldots,\Delta\phi_{12,j}^{1m}(i)\right),\ \ldots,\ \left(\Delta\phi_{1n,j}^{12}(i),\ldots,\Delta\phi_{1n,j}^{1m}(i)\right)\right]^T \\ P_j^{gb,dd}(i) &= \left[\left(\Delta p_{12,j}^{12}(i),\ldots,\Delta p_{12,j}^{1m}(i)\right),\ \ldots,\ \left(\Delta p_{1n,j}^{12}(i),\ldots,\Delta p_{1n,j}^{1m}(i)\right)\right]^T \end{aligned}$$

For the geometry-free model, double-differences of the *original* observables are used:

$$\begin{aligned} \Phi_j^{gf,dd}(i) &= \left[\left(\phi_{12,j}^{12}(i),\ldots,\phi_{12,j}^{1m}(i)\right),\ \ldots,\ \left(\phi_{1n,j}^{12}(i),\ldots,\phi_{1n,j}^{1m}(i)\right)\right]^T \\ P_j^{gf,dd}(i) &= \left[\left(p_{12,j}^{12}(i),\ldots,p_{12,j}^{1m}(i)\right),\ \ldots,\ \left(p_{1n,j}^{12}(i),\ldots,p_{1n,j}^{1m}(i)\right)\right]^T \\ \rho_p^{dd}(i) &= \left[\left(\rho_{12,p}^{12}(i),\ldots,\rho_{12,p}^{1m}(i)\right),\ \ldots,\ \left(\rho_{1n,p}^{12}(i),\ldots,\rho_{1n,p}^{1m}(i)\right)\right]^T \end{aligned}$$

DD vc-matrix

To obtain the vc-matrix of the DD observables, we need to apply the propagation law of variances to the undifferenced vc-matrix:

$$Q_{y(i)}^{dd} = \Upsilon(i) Q_{y(i)} \Upsilon(i)^T = \begin{cases} \text{blkdiag}\left[Q_\phi,\ Q_p\right] \otimes Q^{dd}(i) & \text{(geom.-based)} \\ \text{blkdiag}\left[\left(Q_\phi,\ Q_p\right),\ \sigma_\rho^2\right] \otimes Q^{dd}(i) & \text{(geom.-free)} \end{cases} \tag{2.70}$$

From this it can be seen that the differencing only influences the receiver/satellite specific part of the vc-matrix. This part is denoted as $Q^{dd}(i)$ and is obtained from the original matrix $Q(i)$ as follows:

$$\begin{aligned} Q^{dd}(i) &= \left[D_n^T \otimes D_m^T\right] Q(i) \left[D_n \otimes D_m\right] \\ &= \begin{bmatrix} D_m^T\left[Q_1(i)+Q_2(i)\right]D_m & \cdots & D_m^T Q_1(i) D_m \\ \vdots & \ddots & \vdots \\ D_m^T Q_1(i) D_m & \cdots & D_m^T\left[Q_1(i)+Q_n(i)\right]D_m \end{bmatrix} \end{aligned} \tag{2.71}$$

From the resulting vc-matrix it can be seen that the DD observables between different receivers become correlated (the off-diagonal matrices $D_m^T Q_1(i) D_m$). This is called *inter-station correlation* due to double-differencing. Moreover, all matrices on the main diagonal and off-diagonal are double-differenced for satellites, which implies that also *inter-satellite correlation* has arisen. Both inter-station and inter-satellite correlation are also referred to as *mathematical correlation*. When all observations from all receivers to all satellites are assumed to have the same precision, $Q(i) = I_{nm}$, the matrix $Q^{dd}(i)$ reduces to a very simple form:

$$Q^{dd}(i) = \left(D_n^T D_n\right) \otimes \left(D_m^T D_m\right) \tag{2.72}$$

2.9.3 Double-differenced design matrix and parameters

Due to the transformation the partial design matrices for the *geometry-based model* become as follows:

$$\left[\begin{pmatrix} e_j \\ e_j \end{pmatrix} \otimes \mathcal{A}^{dd}(i) \quad \begin{pmatrix} \Lambda \\ 0 \end{pmatrix} \otimes \mathcal{C}^{dd} \right] \text{ and } \left[\begin{pmatrix} I_j & \\ & I_j \end{pmatrix} \otimes \mathcal{D}^{dd} \right] \tag{2.73}$$

Their transformed counterparts of the *geometry-free model* read:

$$\left[\begin{pmatrix} \Lambda \\ 0 \\ 0 \end{pmatrix} \right] \otimes \mathcal{C}^{dd} \text{ and } \left[\left[\begin{pmatrix} I_j & \\ & I_j \\ 0 & \end{pmatrix} \right] \otimes \mathcal{D}^{dd} \quad \left[\begin{pmatrix} e_j \\ e_j \\ 1 \end{pmatrix} \right] \otimes \left[D_n^T \otimes D_m^T \right] \right] \tag{2.74}$$

It is possible to further simplify the matrices in Eq. (2.73) and Eq. (2.74) which have a superscript *dd*:

- Using Eq. (2.61), the DD partial design matrix for the *receiver position* parameters becomes:

$$\mathcal{A}^{dd}(i) \;=\; \left[D_n^T \otimes D_m^T \right] \mathcal{A}(i) \;=\; \text{blkdiag}\left[D_m^T G_2(i),\; \ldots,\; D_m^T G_n(i) \right] \tag{2.75}$$

- Using Eq. (2.53), the DD partial design matrix for the *ambiguity* parameters reduces to the identity matrix, such that each individual DD ambiguity can be assigned to one individual DD phase observable:

$$\begin{aligned} \mathcal{C}^{dd} \;=\; \left[D_n^T \otimes D_m^T \right] \mathcal{C} \;&=\; \left[D_n^T \otimes D_m^T \right] \left[C_n \otimes C_m \right] \\ &=\; \left[D_n^T C_n \right] \otimes \left[D_m^T C_m \right] \\ &=\; I_{n-1} \otimes I_{m-1} \\ &=\; I_{(n-1)(m-1)} \end{aligned} \tag{2.76}$$

- Another consequence of the double-differencing is that all *clock parameters* are eliminated from the model, since, using Eq. (2.48), it holds that:

$$\begin{aligned} \mathcal{D}^{dd} \;&=\; \left[D_n^T \otimes D_m^T \right] \mathcal{D} \\ &=\; \left[D_n^T C_n \otimes D_m^T e_m \quad - D_n^T e_n \otimes D_m^T I_m \right] \\ &=\; 0 \end{aligned} \tag{2.77}$$

- In the transformed temporal design matrix part of the geometry-free model the columns of the range parameters become rank-deficient (since $\left[D_n^T \otimes D_m^T \right]$ is not of full rank), and therefore the original undifferenced range parameters are transformed to the following DD range parameters:

$$\begin{aligned} \rho^{dd}(i) \;&=\; \left[D_n^T \otimes D_m^T \right] \rho(i) \\ &=\; \left[\left(\rho_{12}^{12}(i) \ldots \rho_{12}^{1m}(i) \right) \;\ldots\; \left(\rho_{1n}^{12}(i) \ldots \rho_{1n}^{1m}(i) \right) \right]^T \end{aligned} \tag{2.78}$$

Table 2.5 summarizes the full-rank partial design matrices and estimable parameters of the resulting double-differenced model. Note that in case of the geometry-based model only the coordinates and ambiguity parameters remain as non-temporal parameters. All temporal parameters are eliminated.

Table 2.5. Double-differenced partial design matrices and estimable parameters

	geometry-based model	geometry-free model
$A_I^{dd}(i)$	$\left[\begin{pmatrix} e_j \\ e_j \end{pmatrix} \otimes \mathcal{A}^{dd}(i) \quad \begin{pmatrix} \Lambda \\ 0 \end{pmatrix} \otimes I_{(n-1)(m-1)} \right]$	$\left[\begin{pmatrix} \Lambda \\ 0 \\ 0 \end{pmatrix} \right] \otimes I_{(n-1)(m-1)}$
$A_{II}^{dd}(i)$	-	$\left[\begin{pmatrix} e_j \\ e_j \\ 1 \end{pmatrix} \right] \otimes I_{(n-1)(m-1)}$
x_I^{dd}	$\left[g^T,\ \left(a_1^T,\ \ldots,\ a_j^T\right)\right]^T$	$\left[a_1^T,\ \ldots,\ a_j^T\right]^T$
$x_{II}^{dd}(i)$	-	$\rho^{dd}(i)$
g	$= \left[\Delta r_{12}^T,\ \ldots,\ \Delta r_{1n}^T\right]^T$	$3(n-1)$ coordinates
a_j	$= \left[\left(M_{12,j}^{12},\ \ldots,\ M_{12,j}^{1m}\right),\ \ldots,\ \left(M_{1n,j}^{12},\ \ldots,\ M_{1n,j}^{1m}\right)\right]^T$	$j(n-1)(m-1)$ ambiguities
$\rho^{dd}(i)$	$= \left[\left(\rho_{12}^{12}(i),\ \ldots,\ \rho_{12}^{1m}(i)\right),\ \ldots,\ \left(\rho_{1n}^{12}(i),\ \ldots,\ \rho_{1n}^{1m}(i)\right)\right]^T$	$(n-1)(m-1)$ ranges

2.10 Concluding remarks

In this chapter the mathematical model for the processing of code (pseudo-range) and carrier-phase observations for precise relative GPS applications has been set up. For the sake of simplicity, the errors in the GPS observations due to atmospheric propagation were neglected for the time being. Two types of relative GPS models were described: The positioning (geometry-based) model and the non-positioning (geometry-free) model. In the latter type of model the original receiver-satellite ranges are solved, instead of the receiver coordinates. For both types of models the full-rank functional and stochastic parts were derived, based on undifferenced observables. It was shown that under certain assumptions, there is a one-to-one relation between this undifferenced model and the in practice often used double-differenced model.

Chapter 3

Procedure for solving the GPS model

3.1 Introduction

In Chap. 2 the mathematical model for precise relative GPS applications was derived. In this chapter the focus is on the procedure to solve the parameters of interest, using GPS data of *short* observation time spans. In case of the geometry-based model, these parameters of interest are the receiver positions. To solve these parameters with sufficient geodetic precision (cm-level or better), the receiver-satellite geometry has to change significantly. Usually this will take quite a long observation time span, since the geometry changes only slowly. When however a short time span of data is used, for example only a single epoch, the precision of the coordinate parameters is predominantly governed by the precision of the code observations (which lies at dm-level). So although precise phase observations are used, the resulting coordinate precision is poor. This poor precision is caused by the presence of the *ambiguities* in the phase data. However, for fast precise GPS applications the presence of these ambiguities is exploited. This can be explained as follows. In the previous chapter it was shown that for the GPS model the phase ambiguities are estimable as double-difference (DD) ambiguities in the processing. From their nature these DD ambiguities are *integer*-valued (instead of real-valued), since by double-differencing the initial phases of the signal are eliminated. In the processing it is this integer property that needs to be addressed: When the ambiguities can be *resolved* at their correct integer values, in a subsequent adjustment the ambiguities disappear as unknown parameters and the parameters of interest can be estimated with high precision from precise *unambiguous* phase data.

The above procedure for solving the GPS model, in fact a three-step procedure, is explained in more detail in Sect. 3.3. The non-trivial ambiguity resolution step of this procedure is discussed in detail in the sections following. Many approaches are possible for estimating the integer solution, however not all of them are admissible. The criteria for admissibility plus some admissible integer estimators are treated in Sect. 3.4. One of these admissible estimators is the integer least-squares estimator, which is mechanized in the *LAMBDA method* for ambiguity resolution [De Jonge and Tiberius, 1996]. As part of the *GPSveQ* software, this LAMBDA

method is used for all the ambiguity resolution problems in this thesis. Its principle is described in detail in this chapter. An important component of this method is the efficient *decorrelating* ambiguity transformation which is described in Sect. 3.5. Besides the estimation part, an important aspect of ambiguity resolution is the judgement of the quality of the integer solution, which is discussed in Sect. 3.6. Since the estimated integer ambiguities are stochastic variables, before fixing them (i.e. to consider them as deterministic quantities) in order to obtain precise position parameters, one has to be sure that the obtained solution is the correct one with sufficient probability. Therefore, in Sect. 3.7 a for fast GPS applications important planning tool is reviewed, to infer whether it is likely that the correct ambiguities will be estimated. This is the *ambiguity success rate*, which can be computed without collecting real data, but purely based on the functional and stochastic assumptions in the mathematical model. Section 3.8 finally gives the concluding remarks of this chapter.

3.2 Integer property of the DD ambiguities

In this section the integer property of the estimable ambiguities in the GPS relative model is proved. Recall from Eq. (2.16) that the *non-integer* phase ambiguity for a certain receiver-satellite combination reads as follows:

$$M^s_{r,j} \;=\; \varphi_{r,j}(t_0) - \varphi^s_{,j}(t_0) + N^s_{r,j} \tag{3.1}$$

with $\varphi_{r,j}(t_0)$ the initial phase of the signal generated in the receiver, $\varphi^s_{,j}(t_0)$ the initial phase of the signal generated in the satellite and $N^s_{r,j}$ the integer ambiguity. When for n receivers and m satellites the following vectors are defined,

$$\begin{array}{lcl} M_j & = & \left[\left(M^1_{1,j},\ \ldots,\ M^m_{1,j}\right),\ \ldots,\ \left(M^1_{n,j},\ \ldots,\ M^m_{n,j}\right)\right]^T \\ \Psi_{r,j} & = & \left[\varphi_{1,j}(t_0),\ \ldots,\ \varphi_{n,j}(t_0)\right]^T \\ \Psi^s_j & = & \left[\varphi^1_{,j}(t_0),\ \ldots,\ \varphi^m_{,j}(t_0)\right]^T \\ N_j & = & \left[\left(N^1_{1,j},\ \ldots,\ N^m_{1,j}\right),\ \ldots,\ \left(N^1_{n,j},\ \ldots,\ N^m_{n,j}\right)\right]^T \end{array} \tag{3.2}$$

then the vector of non-integer ambiguities, M_j, can be decomposed as follows:

$$M_j \;=\; \left[I_n \otimes e_m,\ \ -e_n \otimes I_m,\ \ I_n \otimes I_m\right] \left[\begin{array}{c} \Psi_{r,j} \\ \Psi^s_j \\ N_j \end{array}\right] \tag{3.3}$$

From Table 2.3 in Chap. 2 note that the vector of estimable double-difference ambiguities reads as follows:

$$a_j \;=\; \left[\left(M^{12}_{12,j},\ \ldots,\ M^{1m}_{12,j}\right),\ \ldots,\ \left(M^{12}_{1n,j},\ \ldots,\ M^{1m}_{1n,j}\right)\right]^T \tag{3.4}$$

This double-difference vector a_j can be obtained from its undifferenced counterpart M_j by application of the difference operators D^T_n and D^T_m, as defined in Sect. 2.9.

Using Eq. (3.3), the vector of DD ambiguities a_j can then be rewritten as:

$$\begin{aligned} a_j &= \left[D_n^T \otimes D_m^T\right] M_j \\ &= \left[D_n^T \otimes \underbrace{D_m^T e_m}_{0},\ \underbrace{-D_n^T e_n}_{0} \otimes D_m^T,\ D_n^T \otimes D_m^T\right] \begin{bmatrix} \Psi_{r,j} \\ \Psi_j^s \\ N_j \end{bmatrix} \\ &= \left[D_n^T \otimes D_m^T\right] N_j \end{aligned} \tag{3.5}$$

So the initial phases become eliminated, as due the double-differencing. From this it follows that, since the undifferenced ambiguities stored in N_j are integer-valued, the estimable double-difference ambiguities are also integer:

$$\boxed{N_j \in Z^{nm} \ \Rightarrow\ a_j \in Z^{(n-1)(m-1)}} \tag{3.6}$$

3.3 Three-step processing procedure

The integer property of the DD ambiguities is included as a constraint to the model of GPS observation equations which was set up in Chap. 2. In a very general form, the extended Gauss-Markov model reads:

$$\boxed{E\{y\} = A_1 a + A_2 b, \qquad y \in R^l,\ \ a \in Z^q,\ \ b \in R^p; \quad D\{y\} = Q_y} \tag{3.7}$$

In this model the observable vector y has dimension l. The parameter vector is decomposed into two parts: a, the $q \times 1$ vector of integer-valued DD ambiguities, and b, the $p \times 1$ vector of all the remaining real-valued parameters. Note that $q = j(n-1)(m-1)$ for j frequencies, n receivers and m satellites.

The least-squares criterion for solving the linear model (3.7) reads:

$$\min_{a,b} \|y - A_1 a - A_2 b\|^2_{Q_y}, \qquad y \in R^l,\ \ a \in Z^q,\ \ b \in R^p \tag{3.8}$$

To account for the integer constraint $a \in Z^q$, this function to be minimized can be decomposed into a sum-of-squares [Teunissen and Kleusberg, 1998]:

$$\boxed{\|y - A_1 a - A_2 b\|^2_{Q_y} \ =\ \underbrace{\|\hat{\epsilon}\|^2_{Q_y}}_{1} \ +\ \underbrace{\|\hat{a} - a\|^2_{Q_{\hat{a}}}}_{2} \ +\ \underbrace{\|\hat{b}_{|a} - b\|^2_{Q_{\hat{b}|a}}}_{3}} \tag{3.9}$$

where $\|\cdot\|^2_Q = (\cdot)^T Q^{-1} (\cdot)$ and $\hat{b}_{|a}$ denotes the least-squares solution of b conditioned on a. So the original minimization problem is transformed to *three* individual minimization problems. The solutions of these three problems are referred to as the *float solution*, *ambiguity resolution* and the *fixed solution*. In the following subsections it will be explained how these three solutions can be computed. Besides this *estimation* procedure, a procedure is outlined to *validate* the solutions.

3.3.1 Estimation procedure

Float solution

The first squared norm, $\|\hat{\epsilon}\|^2_{Q_y}$, is the squared norm of the least-squares residuals, when there would be *no* integer constraints at all on the ambiguities. It is obtained through solving the following 'standard' least-squares minimization problem:

$$\min_{a,b} \; = \; \|y - A_1 a - A_2 b\|^2_{Q_y}, \quad a \in R^q, \; b \in R^p \tag{3.10}$$

The least-squares solution of this problem, the real-valued parameter estimates plus their vc-matrix, reads symbolically:

$$\boxed{\begin{bmatrix} \hat{a} \\ \hat{b} \end{bmatrix}; \quad \begin{bmatrix} Q_{\hat{a}} & Q_{\hat{a}\hat{b}} \\ Q_{\hat{b}\hat{a}} & Q_{\hat{b}} \end{bmatrix}} \tag{3.11}$$

Note that the ambiguity-float solution is denoted by a 'hat'-sign.

Ambiguity resolution

The second squared norm to be minimized is however a *non-standard* minimization problem, because of the imposed integer constraints:

$$\min_{a} \|\hat{a} - a\|^2_{Q_{\hat{a}}}, \quad a \in Z^q \tag{3.12}$$

The solution is obtained by a *mapping function* F of the space of reals to the space of integers:

$$\boxed{\check{a} \; = \; F(\hat{a}); \quad F: \; R^q \rightarrow Z^q} \tag{3.13}$$

Note that the integer solution is denoted by a 'check'-sign.

Fixed solution

Eventually, after the correct integer ambiguities have been resolved, another standard minimization problem is solved to obtain the improved solution of the parameters of interest:

$$\min_{b} \|\hat{b}_{|a} - b\|^2_{Q_{\hat{b}|\hat{a}}}, \quad b \in R^p \tag{3.14}$$

The solution of this problem is the least-squares estimate of the real-valued parameters b conditioned at the integer-valued ambiguity estimate $\check{a}$:

$$\boxed{\hat{b}_{|\check{a}} \; = \; \hat{b} - Q_{\hat{b}\hat{a}} Q^{-1}_{\hat{a}} (\hat{a} - \check{a}) \; \doteq \; \check{b}} \tag{3.15}$$

For the precision description of these estimates, in GPS practice often the following vc-matrix is computed:

$$\boxed{Q_{\hat{b}|\hat{a}} \; = \; Q_{\hat{b}} - Q_{\hat{b}\hat{a}} Q^{-1}_{\hat{a}} Q_{\hat{a}\hat{b}}} \tag{3.16}$$

And from this latter equation the beneficial effect of ambiguity resolution can easily be seen, since it holds that $Q_{\hat{b}|\hat{a}} \leq Q_{\hat{b}}$. To this 'ambiguity-fixed' vc-matrix however a comment can be made. It is namely computed assuming that the integer estimated ambiguities are *non-stochastic* or deterministic quantities. From a theoretical point of view this is not correct, since the integer ambiguities are, like other parameters, estimated from *stochastic* observables. Therefore, before using the vc-matrix in Eq. (3.16) for the precision description of the fixed parameters, one should have confidence in the *quality* of the integer ambiguity solution, as obtained in step 2. In the ambiguity estimation step one is always able to compute an integer least-squares solution, whether it is of poor quality or not. This quality inference is unfortunately a non-trivial issue, since the integer ambiguities are of the discrete-type instead of the continuous-type, for which the traditional quality control theory based on the vc-matrix of the estimated parameters applies. However, much progress has been made in the recent past to develop a new theory to infer the the quality of integer parameters. Section 3.6 describes in full detail the state-of-the-art.

3.3.2 Validation procedure

Besides an estimation part, a GPS data processing strategy should contain a procedure to *validate* the obtained solutions, since errors in the observations may bias the estimated parameters. In the float solution step, *cycle slips* and/or *outliers* in the phase and code observations may bias the solution seriously when they are not accounted for. In the ambiguity resolution step one may test whether the integer solution is sufficient likely. In the fixed solution step a possible test is whether the integer ambiguity solution fits the model.

A validation procedure should be carried out by means of statistical *hypothesis testing*, in which a set of alternative hypotheses are tested against a null-hypothesis, see [Teunissen, 2000c]. The null-hypothesis is the mathematical model as formulated in Eq. (3.7):

$$\boxed{H_0: \quad E\{y\} = A_1 a + A_2 b, \quad a \in Z^q,\ b \in R^p} \tag{3.17}$$

However, because of the integer constraints imposed on the ambiguities, $a \in Z^q$, it is not yet possible to use *rigorous* test statistics based on this null-hypothesis, since the distribution of the resulting test statistic is still unknown. Although significant progress is made, see e.g. [Teunissen, 2002], research is still going on. In the mean time, in GPS practice and also in the *GPSveQ* software two other hypothesis are considered:

$$\begin{array}{lll} H_{\hat{0}} & : & E\{y\} = A_1 a + A_2 b, \quad a \in R^q,\ b \in R^p \\ H_{\check{0}} & : & E\{y\} = A_1 a + A_2 b, \quad a = \check{a}, \quad b \in R^p \end{array} \tag{3.18}$$

In the first hypothesis, $H_{\hat{0}}$, it is assumed that the ambiguities are *real*-valued instead of integers, whereas in the second hypothesis, $H_{\check{0}}$, the estimated integer ambiguity solution is assumed to be the *correct* one. In the following subsections

tests are described in which the two hypothesis above are confronted with other alternative hypothesis. These tests are implemented in the *GPSveQ* software.

Overall model tests

The *overall model test* (OMT) is a general test on the validity of the model. The null-hypothesis is tested against the most general alternative hypothesis one can think of:

$$H_A \;:\; E\{y\} \;\in\; R^l \tag{3.19}$$

The test statistic is computed from the squared norm of least-squares residuals. In the *GPSveQ* software, two overall model tests are carried out. In the first one, the hypotheses $H_{\hat{0}}$ (see Eq. (3.18)) and H_A are confronted with each other. The resulting *float OMT* reads:

$$\text{reject } H_{\hat{0}} \text{ if } \;\hat{\sigma}^2 \;=\; \frac{\|\hat{\epsilon}\|^2_{Q_y}}{l-q-p} \;>\; F_\alpha(l-q-p,\infty) \tag{3.20}$$

where $\|\hat{\epsilon}\|^2_{Q_y} = \|y - A_1\hat{a} - A_2\hat{b}\|^2_{Q_y}$. $F_\alpha(l-q-p,\infty)$ denotes the critical value for a level of significance α and $l-q-p$ the degrees of freedom. The test statistic, denoted by $\hat{\sigma}^2$, has a Fisher-distribution. In the second overall model test, the hypothesis $H_{\check{0}}$ is confronted with H_A. The *fixed OMT* reads:

$$\text{reject } H_{\check{0}} \text{ if } \;\check{\sigma}^2 \;=\; \frac{\|\check{\epsilon}\|^2_{Q_y}}{l-p} \;>\; F_\alpha(l-p,\infty) \tag{3.21}$$

where $\|\check{\epsilon}\|^2_{Q_y} \;=\; \|\hat{\epsilon}\|^2_{Q_y} + \|\hat{a} - \check{a}\|^2_{Q_{\hat{a}}} \;=\; \|y - A_1\check{a} - A_2\check{b}\|^2_{Q_y}$.

Outlier tests

Another important test in GPS data processing is a test in which each *individual* observation is tested on a single blunder or outlier. This procedure of systematic testing of all observations is also known as *data-snooping* [Baarda, 1968]. For both float and fixed models these tests can be carried out. In the first case $H_{\hat{0}}$ is confronted with $H_{\hat{A}}$ and in the second case $H_{\check{0}}$ is confronted with $H_{\check{A}}$, where these alternative hypotheses are defined as:

$$\begin{array}{lcl} H_{\hat{A}} \;:\; E\{y\} \;=\; A_1 a + A_2 b + C_y^o\nabla, & a \in R^q,\; b \in R^p,\; \nabla \in R^1 \\ H_{\check{A}} \;:\; E\{y\} \;=\; A_1 a + A_2 b + C_y^o\nabla, & a = \check{a},\quad b \in R^p,\; \nabla \in R^1 \end{array} \tag{3.22}$$

So in these alternative hypotheses the functional model is extended with $C_y^o\nabla$ to account for the outlier. Since these tests are one-dimensional, they are well known as the *w-test* statistics which have a normal distribution.

Cycle-slip tests (phase-only)

Besides the outlier test, another one-dimensional w-test, though only applied to the phase observations, is the test on cycle slips. A cycle slip is a sudden jump

in the phase ambiguity with an unknown number of cycles. For the ambiguity it means that it does not remain constant during the complete time span. A cycle slip can be caused by, among others, a loss-of-lock of the GPS signal. This cycle-slip test is only carried out for the float model, since in the fixed model the ambiguities do not appear anymore as unknown parameters. The null hypothesis for the float model $H_{\hat{0}}$ is confronted with the following alternative hypothesis $H_{\hat{A}}$:

$$H_{\hat{A}}: \quad E\{y\} \;=\; A_1 a + A_2 b + C_y^s \nabla, \quad a \in R^q,\ b \in R^p,\ \nabla \in R^1 \tag{3.23}$$

Note that since cycle slips can only take on integer values, in fact we should use a hypothesis with $\nabla \in Z^1$, instead of the alternative hypothesis in Eq. (3.23). This is however not done for the same reason as given before.

Ambiguity tests

It is also possible to test both the hypotheses $H_{\hat{0}}$ and $H_{\check{0}}$ in Eq. (3.18) against *each other*. It tests whether the estimated ambiguity solution is sufficient likely to be accepted as integer solution, instead of as real-valued solution. It is therefore referred to as the ambiguity *acceptance* test. It can be proved that this test statistic is a *weighted average* of the fixed and float OMT statistics, $\hat{\sigma}^2$ and $\check{\sigma}^2$ (see Eq. (3.20) and Eq. (3.21)). The corresponding test reads [Teunissen and Kleusberg, 1998]:

$$\text{reject } H_{\hat{0}} \text{ if } \quad \left[\frac{l-p}{q}\check{\sigma}^2 - \frac{l-q-p}{q}\hat{\sigma}^2\right] \;=\; \frac{\|\hat{a}-\check{a}\|^2_{Q_{\hat{a}}}}{q} \;>\; F_\alpha(q,\infty) \tag{3.24}$$

Besides this ambiguity acceptance test, in GPS practice often a second ambiguity test is performed, which tests the likelihood of the integer solution $\check{a}$ versus its *second best* candidate $\check{a}'$, that is the integer candidate closest to the integer solution (in the metric of $Q_{\hat{a}}$). Like for the best candidate, also for this second best candidate an alternative hypothesis can be set up, which is denoted by $H_{\check{0}'}$:

$$H_{\check{0}'}: \quad E\{y\} \;=\; A_1 a + A_2 b, \quad a = \check{a}', \quad b \in R^p \tag{3.25}$$

Also for the second best candidate an acceptance test can be carried out, in which the hypothesis above $H_{\check{0}'}$ is confronted with $H_{\hat{0}}$. The test reads in this case:

$$\text{reject } H_{\hat{0}} \text{ if } \quad \frac{\|\hat{a}-\check{a}'\|^2_{Q_{\hat{a}}}}{q} \;>\; F_{\alpha'}(q,\infty) \tag{3.26}$$

Combining both acceptance tests in Eq. (3.24) and Eq. (3.26), leads to the ambiguity *discrimination* test, which says that $\check{a}$ is more likely than $\check{a}'$ if

$$\frac{\|\hat{a}-\check{a}'\|^2_{Q_{\hat{a}}}}{q} \;>\; F_{\alpha'}(q,\infty) \;\geq\; F_\alpha(q,\infty) \tag{3.27}$$

where $F_{\alpha'}(q,\infty)$ has to be sufficiently larger than $F_\alpha(q,\infty)$.

3.4 Admissible integer ambiguity estimators

In the previous section the integer estimation was symbolized by a function F that maps the q-dimensional space of reals to the q-dimensional space of integers. Many choices for this function F are possible to compute the integer solution from its float counterpart, however not all of them are *admissible*. In this section the admissible integer estimators are classified. To do so, first a subset S_z of the space of reals R^q is defined, for which the ambiguity vectors x are mapped to a certain integer vector z:

$$S_z \;=\; \{x \in R^q \mid z \;=\; F(x)\}\,, \quad z \in Z^q \tag{3.28}$$

The subset S_z is referred to as the *pull-in region* of z [Jonkman, 1998a]. Thus, when the float solution 'lies' inside the pull-in region of integer z, the integer solution is equal to z:

$$\boxed{\hat{a} \in S_z \;\Leftrightarrow\; \breve{a} = z} \tag{3.29}$$

To be *admissible*, the pull-in region of an integer estimator should fulfil the following criteria [Teunissen, 1999a]:

$$\begin{array}{ll} 1. & \bigcup_{z\in Z^q} S_z = R^q \quad \text{(no gaps)} \\ 2. & S_{z_1} \bigcap S_{z_2} = 0 \;\; \forall\; z_1, z_2 \in Z^q,\; z_1 \neq z_2 \quad \text{(no overlaps)} \\ 3. & S_z \;=\; z + S_0 \;\; \forall\; z \in Z^q \quad \text{(integer remove-restore)} \end{array} \tag{3.30}$$

These criteria are motivated as follows. First, all pull-in regions together should cover the complete q-dimensional space of reals. If there would be *gaps*, not every float ambiguity vector can be assigned to an integer solution. Second, two distinct pull-in regions should not *overlap* each other, such that a float solution can be mapped to only one pull-in region. The third criterium is that when the float solution is translated by an integer amount z, the corresponding integer solution is also translated by the same amount. This implies that it is allowed to use the *integer-remove-restore* technique: $F(\hat{a}-z)+z = F(\hat{a})$. For the pull-in regions this means that they are translated copies of each other.

Three integer estimators which fulfil the above three criteria are: The *integer rounding*, *integer bootstrapping* and *integer least-squares* estimators, which are explained in the following subsections. For this purpose, the float ambiguity solution, consisting of a vector with estimates plus vc-matrix, is written as:

$$\hat{a} \;=\; \begin{bmatrix} \hat{a}_1 \\ \hat{a}_2 \\ \vdots \\ \hat{a}_q \end{bmatrix} ; \quad Q_{\hat{a}} \;=\; \begin{bmatrix} \sigma^2_{\hat{a}_1} & \sigma_{\hat{a}_1\hat{a}_2} & \cdots & \sigma_{\hat{a}_1\hat{a}_q} \\ \sigma_{\hat{a}_2\hat{a}_1} & \sigma^2_{\hat{a}_2} & \cdots & \sigma_{\hat{a}_2\hat{a}_q} \\ \vdots & \vdots & \ddots & \vdots \\ \sigma_{\hat{a}_q\hat{a}_1} & \sigma_{\hat{a}_q\hat{a}_2} & \cdots & \sigma^2_{\hat{a}_q} \end{bmatrix} \tag{3.31}$$

3.4.1 Integer rounding

The simplest integer estimator one can think of is *rounding* the entries of the float ambiguity solution to their nearest integer values. The integer estimation

procedure is therefore trivial:

$$\breve{a}_R = \begin{bmatrix} \breve{a}_{R,1} \\ \breve{a}_{R,2} \\ \vdots \\ \breve{a}_{R,q} \end{bmatrix} = \begin{bmatrix} nint\,(\hat{a}_1) \\ nint\,(\hat{a}_2) \\ \vdots \\ nint\,(\hat{a}_q) \end{bmatrix} \tag{3.32}$$

where $nint(\cdot)$ denotes the rounding-to-the-nearest-integer operator. Using this rounding operator it easily follows that a float vector is mapped to a certain integer vector when the absolute value of the difference between each component is at most $\frac{1}{2}$. Hence, the pull-in region for integer rounding in R^q is an q-dimensional *cube*, centered at the grid-point and which has all sides of length 1 [Teunissen, 1998a].

Although the integer rounding technique is an admissible integer estimator, in general the solution will *not* satisfy the minimization criterium as formulated in Eq. (3.12), since the estimator does not take the ambiguity correlation into account. This will only be the case when there is no correlation between the ambiguities, i.e. when the ambiguity vc-matrix $Q_{\hat{a}}$ is a *diagonal matrix*.

3.4.2 Integer bootstrapping (sequential conditional rounding)

An integer estimator which takes *some* of the correlation between the float ambiguities into account, is the so-called integer *bootstrapping* estimator. The integer solution is computed from the float solution as follows. The first ambiguity ($\hat{a}_1$) is simply rounded to its nearest integer. After that, the real-valued estimates of the remaining ambiguities are corrected by virtue of their correlation with the first ambiguity. In a next step, the second (corrected) ambiguity is rounded to its nearest integer, etc. etc. The algorithm reads mathematically [Teunissen, 1998b]:

$$\breve{a}_B = \begin{bmatrix} \breve{a}_{B,1} \\ \breve{a}_{B,2} \\ \vdots \\ \breve{a}_{B,q} \end{bmatrix} = \begin{bmatrix} nint\,(\hat{a}_1) \\ nint\left(\hat{a}_2 - \sigma_{\hat{a}_2\hat{a}_1}\sigma_{\hat{a}_1}^{-2}\,(\hat{a}_1 - \breve{a}_{B,1})\right) \\ \vdots \\ nint\left(\hat{a}_q - \sum_{i=1}^{q-1}\sigma_{\hat{a}_q\hat{a}_{i|I}}\sigma_{\hat{a}_{i|I}}^{-2}\left(\hat{a}_{i|I} - \breve{a}_{B,i}\right)\right) \end{bmatrix} \tag{3.33}$$

where $I = 1, \ldots, i-1$. Note that the integer solution depends on with which ambiguity the bootstrapping is started. This integer bootstrapping technique is also known as the *sequential conditional integer rounding* technique. Note that using this estimator, a float vector is mapped to a certain integer vector when the absolute value of the difference between the conditional ambiguity and the integer component is at most $\frac{1}{2}$.

Although the integer bootstrapping technique is an admissible integer estimator and takes some of the ambiguity correlation into account, like in the case of the rounding estimator, the solution will in general *not* satisfy the minimization criterium as formulated in Eq. (3.12).

3.4.3 Integer least-squares search

The *integer least-squares* estimator is the only estimator which is completely based on the minimization criterium in Eq. (3.12):

$$\boxed{\min_{a \in Z^q} (\hat{a} - a)^T Q_{\hat{a}}^{-1} (\hat{a} - a)} \tag{3.34}$$

Because of the appearance of the vc-matrix $Q_{\hat{a}}$, the integer least-squares estimator takes all correlation between the ambiguities into account. In contrast to rounding and bootstrapping, the integer least-squares solution, denoted as $\breve{a}_{LSQ}$, is at *shortest* distance of the float solution, in the metric of the vc-matrix $Q_{\hat{a}}$.

Due to the dimension of the ambiguity vector (which can for example be as large as $q = 2(5-1)(10-1) = 72$ for a network consisting of 5 receivers, tracking dual-frequency data of 10 satellites), in practice it is a non-trivial task to solve the above minimization problem. Therefore the aim is to *decorrelate* $Q_{\hat{a}}$ such that the minimization problem reduces to a *sum* of q integer least-squares problems. For this purpose the following decorrelation is chosen [Teunissen, 1993]:

$$\boxed{(\hat{a}' - a) \;=\; L^{-1}(\hat{a} - a)} \tag{3.35}$$

where $\hat{a}'$ denotes the decorrelated ambiguities and L is the lower triangular matrix following from an LDL^T-decomposition of the ambiguity vc-matrix $Q_{\hat{a}}$. This matrix L has the following structure:

$$L \;=\; \begin{bmatrix} 1 & & & \\ \frac{\sigma_{\hat{a}_2\hat{a}_1}}{\sigma^2_{\hat{a}_1}} & 1 & & \\ \vdots & \ddots & \ddots & \\ \frac{\sigma_{\hat{a}_q\hat{a}_1}}{\sigma^2_{\hat{a}_1}} & \cdots & \frac{\sigma_{\hat{a}_q\hat{a}_{q-1}|1,\ldots,q-2}}{\sigma^2_{\hat{a}_{q-1}|1,\ldots,q-2}} & 1 \end{bmatrix} \tag{3.36}$$

The matrix D, which is a diagonal matrix, is constructed as follows:

$$D \;=\; \mathrm{diag}(\sigma^2_{\hat{a}_1},\; \sigma^2_{\hat{a}_{2|1}},\; \ldots,\; \sigma^2_{\hat{a}_{q|Q}}) \tag{3.37}$$

In both matrices elements appear, which are known as *conditional (co-) variances* and are denoted as $\sigma^2_{\hat{a}_{i|I}}$, where $I = 1, \ldots, i-1$. The conditional variances are computed as follows:

$$\sigma^2_{\hat{a}_{i|I}} \;=\; \sigma^2_{\hat{a}_i} - \sum_{j=1}^{i-1} \sigma^2_{\hat{a}_j\hat{a}_{j|J}} \sigma^{-2}_{\hat{a}_{j|J}}, \quad \text{where } J = 1, \ldots, j-1 \tag{3.38}$$

Using this concept, the decorrelated float ambiguity vector $\hat{a}'$ consists of so-called *sequential conditional* ambiguities, having the diagonal matrix D as vc-matrix:

$$\hat{a}' \;=\; \begin{bmatrix} \hat{a}_1 \\ \hat{a}_{2|1} \\ \vdots \\ \hat{a}_{q|Q} \end{bmatrix} \;=\; \begin{bmatrix} \hat{a}_1 \\ \hat{a}_2 - \sigma_{\hat{a}_2\hat{a}_1}\sigma^{-2}_{\hat{a}_1}(\hat{a}_1 - a_1) \\ \vdots \\ \hat{a}_q - \sum_{i=1}^{q-1} \sigma_{\hat{a}_q\hat{a}_{i|I}}\sigma^{-2}_{\hat{a}_{i|I}}\left(\hat{a}_{i|I} - a_i\right) \end{bmatrix}; \quad Q_{\hat{a}'} \;=\; D \tag{3.39}$$

Note the close similarity of these conditional ambiguities with the bootstrapped ambiguities in Eq. (3.33). Using this decorrelation, it follows that the inverse ambiguity vc-matrix reads as $Q_{\hat{a}}^{-1} = L^{-T}D^{-1}L^{-1}$, such that the squared norm in the minimization problem in Eq. (3.34) boils down to a sum of q squares:

$$\begin{array}{rcl}(\hat{a}-a)^T Q_{\hat{a}}^{-1}(\hat{a}-a) & = & (\hat{a}'-a)^T L^T L^{-T} D^{-1} L^{-1} L(\hat{a}'-a) \\ & = & (\hat{a}'-a)^T D^{-1}(\hat{a}'-a) \\ & = & \sum_{i=1}^{q}(\hat{a}_{i|I}-a_i)^2 / \, \sigma^2_{\hat{a}_{i|I}}\end{array} \tag{3.40}$$

In order to avoid a search through the *complete* space of integers Z^q, it is possible to enumerate a smaller search space that still contains the integer least-squares solution. This *ambiguity search space*, in fact a hyper-ellipsoid centered at $\hat{a}$ of which its shape governed by the vc-matrix $Q_{\hat{a}}$, is bounded as follows:

$$(\hat{a}-a)^T Q_{\hat{a}}^{-1}(\hat{a}-a) \;\leq\; \chi^2 \tag{3.41}$$

where the factor χ^2 is a certain positive constant. This χ^2 should be chosen sufficiently large, such that the search space contains at least *one* integer vector. A way to precisely set the χ^2 is by using the integer bootstrapped solution [Teunissen, 2001a]:

$$\chi^2 \;=\; (\hat{a}-\check{a}_B)^T Q_{\hat{a}}^{-1}(\hat{a}-\check{a}_B) \tag{3.42}$$

Using this search space concept and Eq. (3.40) it follows that the q integer ambiguities, which together form the solution, are bounded as follows:

$$\boxed{\begin{array}{rcl}\left(\hat{a}_1-a_1\right)^2 & \leq & \sigma^2_{\hat{a}_1}\chi^2 \\ \left(\hat{a}_{2|1}-a_2\right)^2 & \leq & \sigma^2_{\hat{a}_{2|1}}\left[\chi^2-\left(\hat{a}_1-a_1\right)^2/\sigma^2_{\hat{a}_1}\right] \\ & \vdots & \\ \left(\hat{a}_{q|Q}-a_q\right)^2 & \leq & \sigma^2_{\hat{a}_{q|Q}}\left[\chi^2-\sum_{i=1}^{q-1}\left(\hat{a}_{i|I}-a_i\right)^2/\sigma^2_{\hat{a}_{i|I}}\right]\end{array}} \tag{3.43}$$

Using Eq. (3.43), the *candidate* integer solutions can be found in a systematic way.

Example

In the following example the algorithms of the considered integer estimators are illustrated. Consider the following two-dimensional float ambiguity solution:

$$\hat{a} \;=\; \begin{bmatrix} 2.51 \\ 2.23 \end{bmatrix}; \quad Q_{\hat{a}} \;=\; \begin{bmatrix} 0.2767 & 0.2152 \\ 0.2152 & 0.1680 \end{bmatrix} \tag{3.44}$$

For this 2D float solution the integer rounding, bootstrapping and least-squares solutions are computed.

Integer rounding

The integer rounding solution reads simply:

$$\check{a}_R \;=\; \left[\begin{array}{c} nint(2.51) \\ nint(2.23) \end{array}\right] \;=\; \left[\begin{array}{c} 3 \\ 2 \end{array}\right] \tag{3.45}$$

Note that the squared distance of this integer solution to the real solution, in the metric of $Q_{\hat{a}}$, is $\|\hat{a} - \check{a}_R\|^2_{Q_{\hat{a}}} \;=\; 592.81$.

Integer bootstrapping

There are two ways to compute the integer bootstrapping solution: Either by starting with the first ambiguity, or by starting with the second ambiguity. When the algorithm is started with the first ambiguity, the solution reads:

$$\check{a}^{(1)}_B \;=\; \left[\begin{array}{c} nint(2.51) \\ nint(2.23 - \frac{0.2152}{0.2767}(2.51 - 3)) \end{array}\right] \;=\; \left[\begin{array}{c} 3 \\ 3 \end{array}\right] \tag{3.46}$$

The squared distance of this solution to the float solution is $\|\hat{a} - \check{a}^{(1)}_B\|^2_{Q_{\hat{a}}} \;=\; 240.62$. When the second ambiguity is used as starting point, the bootstrapped solution reads:

$$\check{a}^{(2)}_B \;=\; \left[\begin{array}{c} nint(2.51 - \frac{0.2152}{0.1680}(2.23 - 2)) \\ nint(2.23) \end{array}\right] \;=\; \left[\begin{array}{c} 2 \\ 2 \end{array}\right] \tag{3.47}$$

with the following squared distance to the float solution, $\|\hat{a} - \check{a}^{(1)}_B\|^2_{Q_{\hat{a}}} \;=\; 44.96$. Note that both solutions are not equivalent, and they are also not equal to the integer rounding solution.

Integer least-squares (search)

The integer least-squares minimization problem boils in 2D down to a search over grid-points within an *ellipse* as described by:

$$(\hat{a} - a)^T Q^{-1}_{\hat{a}} (\hat{a} - a) \;=\; \chi^2 \tag{3.48}$$

In Fig. 3.1 this ambiguity search space is visualized. The factor χ^2 has been set to 296.80 to have about 10 candidates lying inside the search space.

For this 2D example, the first ambiguity is bounded as follows:

$$\begin{array}{rcll} a_1 & \geq & \hat{a}_1 - \sigma_{\hat{a}_1}\chi \;\approx\; -6.55 & \text{(lower bound)} \\ a_1 & \leq & \hat{a}_1 + \sigma_{\hat{a}_1}\chi \;\approx\; 11.57 & \text{(upper bound)} \end{array} \tag{3.49}$$

The bounding of the second ambiguity depends on the value of the conditional ambiguity $\hat{a}_{2|1}$, and this latter value depends on the value of the candidate integer for a_1. The standard deviation of the conditional ambiguity is $\sigma_{\hat{a}_{2|1}} = 0.0251$. The bounds of the a_2-ambiguity read:

$$\begin{array}{rcll} a_2 & \geq & \hat{a}_{2|1} - \sigma_{\hat{a}_{2|1}}\sqrt{\chi^2 - (\hat{a}_1 - a_1)^2 / \sigma^2_{\hat{a}_1}} & \text{(lower bound)} \\ a_2 & \leq & \hat{a}_{2|1} + \sigma_{\hat{a}_{2|1}}\sqrt{\chi^2 - (\hat{a}_1 - a_1)^2 / \sigma^2_{\hat{a}_1}} & \text{(upper bound)} \end{array} \tag{3.50}$$

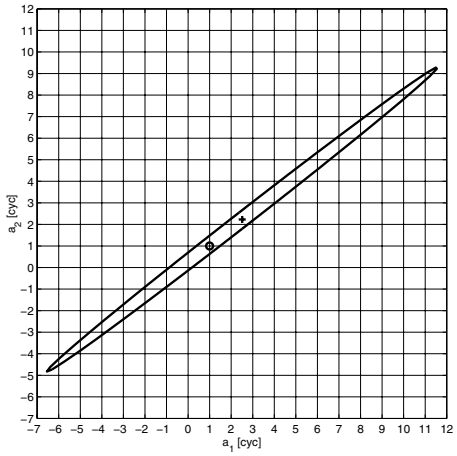

Fig. 3.1. 2D ambiguity search space, centered around float solution (marked with a cross) and integer solution (marked with a circle)

In Table 3.1 the candidate integer vectors are given. For all candidate integers for a_1 the lower and upper bounds according to Eq. (3.50) are given in the table as well. If one or more integer values for a_2 are within these bounds they are given. If there are no integers within the bounds, this is denoted with a '-'. In this way the complete ambiguity search space is searched for candidate integer vectors.

Table 3.1 shows that within the search space 13 candidate integer vectors are found. For 5 candidate integers of a_1 however no candidate integers for a_2 could be found. These are called 'dead ends', see e.g. [Teunissen and Kleusberg, 1998]. From all found candidate vectors the vector $(1,1)^T$ minimizes the criterium in Eq (3.34) and is therefore assigned as the *integer least-squares solution*:

$$\check{a}_{LSQ} = \begin{bmatrix} 1 \\ 1 \end{bmatrix} \tag{3.51}$$

Note that this solution is not equal to both integer bootstrapped solutions, nor the integer rounding solution. The squared distance of this integer solution to the float solution is $\|\hat{a} - \check{a}_{LSQ}\|^2_{Q_{\hat{a}}} = 13.14$, which is the shortest squared distance, compared to the integer rounding and bootstrapping solutions. Note that when the size of the ambiguity search space was set using the *bootstrapped solution* (starting with the most precise ambiguity), it would be set at $\chi^2 = 44.96$, and a much smaller space could have been searched, which would still contain the integer least-squares solution.

Table 3.1. Results LAMBDA search procedure: Original ambiguities

a_1	$\hat{a}_{2\|1}$	lower a_2	upper a_2	a_2	$(\hat{a}-a)^T Q_{\hat{a}}^{-1}(\hat{a}-a)$
-6	-4.39	-4.54	-4.24	-	-
-5	-3.61	-3.85	-3.37	-	-
-4	-2.83	-3.13	-2.53	-3	197.33
-3	-2.06	-2.40	-1.71	-2	114.58
-2	-1.28	-1.65	-0.90	-1	195.66
-1	-0.50	-0.90	-0.10	-	-
0	0.28	-0.14	0.69	0	145.17
1	1.06	0.63	1.48	1	13.14
2	1.83	1.40	2.27	2	44.96
3	2.61	2.18	3.04	3	240.62
4	3.39	2.96	3.82	3	247.68
5	4.17	3.75	4.58	4	66.39
6	4.94	4.55	5.34	5	48.94
7	5.72	5.35	6.10	6	195.33
8	6.50	6.16	6.84	-	-
9	7.28	6.98	7.58	7	274.30
10	8.06	7.81	8.30	8	207.59
11	8.83	8.68	8.98	-	-

3.5 Decorrelating ambiguity transformation

The problem of finding 'dead ends', as was shown in the example in the previous section, makes the search time-consuming and thus inefficient. For the simple example in the previous section only five dead ends were found, but in real GPS practice this number is usually much larger, since the ambiguity search ellipse may be tremendously elongated, which is caused by to the strong correlation between the ambiguities (mainly when data of short time spans are used).

It is obvious that when the ambiguity search space would be much less elongated (ideally: The shape of a hyper-sphere), the search can be carried out more efficiently. In the extreme case, with a completely *diagonal* ambiguity vc-matrix, $Q_{\hat{a}} = \mathrm{diag}(\sigma^2_{\hat{a}_1}, \ldots, \sigma^2_{\hat{a}_q})$, the integer least-squares algorithm boils down to a simple integer *rounding* of each of the entries of the float ambiguity solution and no search would be needed at all. So the aim is to *decorrelate* the original float ambiguity solution before the search procedure starts. A complete decorrelation (such that the ambiguity vc-matrix becomes a diagonal matrix) is however not allowed, since the integer property of the ambiguities would be lost in that case. When the decorrelated ambiguity vector is denoted as $\hat{z}$, then the following transformation can be carried out:

$$\boxed{\hat{z} \;=\; Z^T\hat{a}; \quad Q_{\hat{z}} \;=\; Z^T Q_{\hat{a}} Z} \tag{3.52}$$

This transformation should however fulfil the following criteria to be *admissible* [Teunissen, 1993]: i) The matrix Z should have integer entries, and ii) The transformation should be volume-preserving ($|Z| = \pm 1$), which implies that Z is invertible. An ambiguity transformation which satisfies these criteria is a decorrelation based on an integer approximation of the conditional least-squares transformation in Eq. (3.35). This transformation is known as the *decorrelating Z-transformation* [Teunissen, 1993]. Together with the integer least-squares search technique, the decorrelating ambiguity transformation forms the widely used *LAMBDA* (Least-squares AMBiguity Decorrelation Adjustment) method.

That an alternative search based on the decorrelated ambiguities also results in a minimization of the integer least-squares criterium, can be seen as follows:

$$\begin{aligned}(\hat{z}-z)^T Q_{\hat{z}}^{-1}(\hat{z}-z) &= (\hat{a}-a)^T Z Z^{-1} Q_{\hat{a}}^{-1} Z^{-T} Z^T (\hat{a}-a) \\ &= (\hat{a}-a)^T Q_{\hat{a}}^{-1}(\hat{a}-a)\end{aligned} \tag{3.53}$$

The solution of this minimization problem, denoted as $\check{z}$, can, if desired, be back-transformed to an integer solution in the original domain, via the inverse Z-transformation:

$$\boxed{\check{a} = Z^{-T}\check{z}} \tag{3.54}$$

The following example, which is a continuation of the previous example, illustrates the construction of this Z-matrix.

Example (continued)

The aim is to decorrelate the 2D ambiguity vc-matrix of Eq. (3.44). In 2D the procedure for constructing the Z^T-matrix consists of an alternating application of two basic transformation matrices, Z_a^T and Z_b^T, to the vc-matrix $Q_{\hat{a}}$. These basic transformation matrices read:

$$Z_a^T = \begin{bmatrix} 1 & -nint(\sigma_{\hat{a}_1\hat{a}_2}\sigma_{\hat{a}_2}^{-2}) \\ 0 & 1 \end{bmatrix}; \quad Z_b^T = \begin{bmatrix} 1 & 0 \\ -nint(\sigma_{\hat{a}_2\hat{a}_1}\sigma_{\hat{a}_1}^{-2}) & 1 \end{bmatrix} \tag{3.55}$$

The procedure ends when the matrices Z_a^T and Z_b^T simplify into identity matrices. In Table 3.2 the results of the procedure of constructing the Z^T-matrix can be found.

According to the table, the last two matrices Z_3^T and Z_4^T are equivalent to the identity matrix, such that the Z^T-matrix is only based on the matrices Z_1^T and Z_2^T. The matrix Z^T plus its inverse read:

$$Z^T = Z_2^T Z_1^T = \begin{bmatrix} 1 & -1 \\ -3 & 4 \end{bmatrix}, \quad Z^{-T} = Z_1^{-T} Z_2^{-T} = \begin{bmatrix} 4 & 1 \\ 3 & 1 \end{bmatrix} \tag{3.56}$$

Table 3.2. Stepwise construction of the Z-matrix

i	Z_i^T	$Q_{\hat{z}_i} = Z_i^T Q_{\hat{z}_{i-1}} Z_i$
0	-	$\begin{bmatrix} 0.2767 & 0.2152 \\ 0.2152 & 0.1680 \end{bmatrix}$
1	$\begin{bmatrix} 1 & -nint(\frac{0.2152}{0.2767}) \\ 0 & 1 \end{bmatrix} = \begin{bmatrix} 1 & -1 \\ 0 & 1 \end{bmatrix}$	$\begin{bmatrix} 0.0143 & 0.0472 \\ 0.0472 & 0.1680 \end{bmatrix}$
2	$\begin{bmatrix} 1 & 0 \\ -nint(\frac{0.0472}{0.0143}) & 1 \end{bmatrix} = \begin{bmatrix} 1 & 0 \\ -3 & 1 \end{bmatrix}$	$\begin{bmatrix} 0.0143 & 0.0043 \\ 0.0043 & 0.0135 \end{bmatrix}$
3	$\begin{bmatrix} 1 & -nint(\frac{0.0043}{0.0135}) \\ 0 & 1 \end{bmatrix} = \begin{bmatrix} 1 & 0 \\ 0 & 1 \end{bmatrix}$	$\begin{bmatrix} 0.0143 & 0.0043 \\ 0.0043 & 0.0135 \end{bmatrix}$
4	$\begin{bmatrix} 1 & 0 \\ -nint(\frac{0.0043}{0.0143}) & 1 \end{bmatrix} = \begin{bmatrix} 1 & 0 \\ 0 & 1 \end{bmatrix}$	$\begin{bmatrix} 0.0143 & 0.0043 \\ 0.0043 & 0.0135 \end{bmatrix}$

Application of the constructed Z^T-matrix to the original ambiguities results in the following decorrelated ambiguities:

$$\hat{z} = Z^T \hat{a} = \begin{bmatrix} 0.28 \\ 1.39 \end{bmatrix}; \quad Q_{\hat{z}} = Z^T Q_{\hat{a}} Z = \begin{bmatrix} 0.0143 & 0.0043 \\ 0.0043 & 0.0135 \end{bmatrix} \tag{3.57}$$

Although the decorrelating transformation was originally designed to be used in combination with the integer least-squares estimator in the LAMBDA method, it can also be applied to decorrelate the ambiguities to improve integer estimation based on *rounding* or *bootstrapping*. This is illustrated in the following, in which the decorrelated float solution of Eq. (3.57) serves as input for the integer rounding, bootstrapping and least-squares estimators.

Integer rounding

The integer rounding solution is simply obtained as:

$$\check{z}_R = \begin{bmatrix} nint(0.28) \\ nint(1.39) \end{bmatrix} = \begin{bmatrix} 0 \\ 1 \end{bmatrix} \tag{3.58}$$

The squared distance of this rounding solution to the decorrelated float solution reads $\|\hat{z} - \check{z}_R\|^2_{Q_{\hat{z}}} = 13.14$, which is a much shorter squared distance than the squared distance of the integer rounding solution in the original domain. Back-transforming the integer rounding solution to the original ambiguity domain, results in the following integer solution $\check{a}'_R$:

$$\check{a}'_R = \begin{bmatrix} 1 \\ 1 \end{bmatrix} \tag{3.59}$$

Note that this transformed solution does *not* correspond to the integer rounding solution obtained using the original ambiguities in Eq. (3.45): $\check{a}'_R \neq \check{a}_R$.

Integer bootstrapping

Like in the original ambiguity domain, using the integer bootstrapping estimator two solutions can be obtained, depending on with which ambiguity the process is started. They both read:

$$\begin{aligned} \check{z}_B^{(1)} &= \begin{bmatrix} nint(0.28) \\ nint(1.39 - \frac{0.0043}{0.0143}(0.28 - 0)) \end{bmatrix} = \begin{bmatrix} 0 \\ 1 \end{bmatrix} \\ \check{z}_B^{(2)} &= \begin{bmatrix} nint(0.28 - \frac{0.0043}{0.0135}(1.39 - 1)) \\ nint(1.39) \end{bmatrix} = \begin{bmatrix} 0 \\ 1 \end{bmatrix} \end{aligned} \tag{3.60}$$

with the following squared distances to the float solution: $\|\hat{z} - \check{z}_B^{(1)}\|^2_{Q_{\hat{z}}} = \|\hat{z} - \check{z}_B^{(2)}\|^2_{Q_{\hat{z}}} = 13.14$. So both bootstrapped solutions based on the decorrelated ambiguities are equivalent, in contrast to the solutions in the original domain, see Eq. (3.46) and (3.47). Transformation of both decorrelated solutions back to the original domain, results in the following integer solutions, denoted as $\check{a}_B^{(1)'}$ and $\check{a}_B^{(2)'}$:

$$\check{a}_B^{(1)'} = \check{a}_B^{(2)'} = \begin{bmatrix} 1 \\ 1 \end{bmatrix} \tag{3.61}$$

These back-transformed bootstrapped solutions are equivalent since they are obtained from equivalent decorrelated solutions. However they are *not* equal to the bootstrapped solutions obtained in the original domain, see Eqs. (3.46) and (3.47): $\check{a}_B^{(1)'} \neq \check{a}_B^{(1)}$ and $\check{a}_B^{(2)'} \neq \check{a}_B^{(2)}$.

Integer least-squares (search)

Figure 3.2 shows the *transformed* ambiguity search space (using $\chi^2 = 296.80$; the same as in the case with the original ambiguities), which is much less elongated than the original search space in Fig. 3.1.

As result of the LAMBDA-search on the transformed ambiguities, in Table 3.3 the candidate integer vectors are given. From the table one can see that for each z_1 integer candidate there are *more than one* integer candidates for z_2. Using the original ambiguities however, at most just one candidate for a_2 could be found for a certain candidate integer a_1 (see Table 3.1). Moreover, for five a_1 candidates no candidates for a_2 could be found at all (the dead ends), no dead ends arise using the transformed ambiguities. From this example we may therefore conclude that the search for the integer least-squares solution in the transformed domain is performed in a much more efficient way than in the original domain. The integer least-squares solution in the transformed domain reads:

$$\check{z}_{LSQ} = \begin{bmatrix} 0 \\ 1 \end{bmatrix} \tag{3.62}$$

Note that this solution is equal to the bootstrapped and rounding solutions in the same domain, and thus it also holds that $\|\hat{z} - \check{z}_{LSQ}\|^2_{Q_{\hat{z}}} = 13.14$. Back-transforming

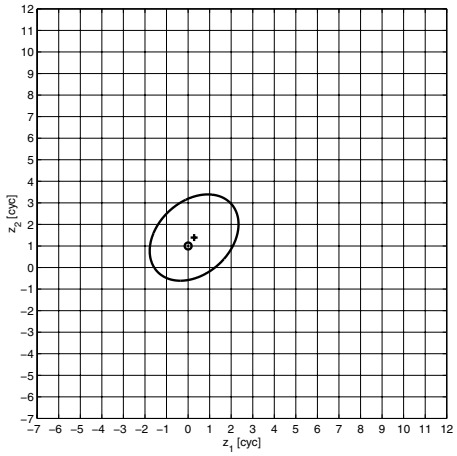

Fig. 3.2. LAMBDA-transformed 2D ambiguity search space, centered around float solution (marked by a cross) and integer solution (marked by a circle)

the solution in the transformed domain to the original DD-domain, results in the following solution:

$$\check{a}'_{LSQ} \;=\; Z^{-T}\check{z}_{LSQ} \;=\; \begin{bmatrix} 1 \\ 1 \end{bmatrix} \tag{3.63}$$

This back-transformed solution is exactly the solution as was found using the search in the original domain: $\check{a}'_{LSQ} = \check{a}_{LSQ}$.

In contrast to the integer rounding and bootstrapping estimators, the integer least-squares estimator is the only estimator for which its solution in the transformed domain is equal to the solution as obtained using the ambiguities in the original domain. This is not surprising, since in Eq. (3.53) it was shown that both minimization problems, in the original as well as the Z-transformed domain, are exactly equivalent. This equivalence does however *not* hold for the integer rounding and integer bootstrapping estimators. The cause for this phenomenon is explained in the following, by considering the *pull-in regions* of the different integer solutions.

Pull-in regions and the correct integer solution

Before discussing the pull-in regions, assume that the *correct* integer solution for our 2D example corresponds to the estimated integer least-squares solution, denoted as a in the original domain, and denoted as z in the LAMBDA-transformed domain:

$$a \;=\; \check{a}_{LSQ} \;=\; \begin{bmatrix} 1 \\ 1 \end{bmatrix}, \quad z \;=\; \check{z}_{LSQ} \;=\; \begin{bmatrix} 0 \\ 1 \end{bmatrix} \tag{3.64}$$

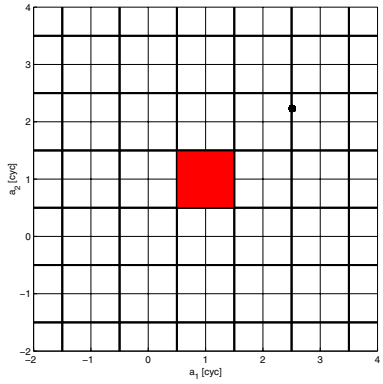

Fig. 3.3. *Integer rounding* in the original domain

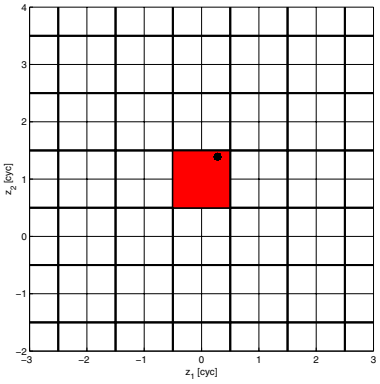

Fig. 3.4. *Integer rounding* in the decorrelated domain

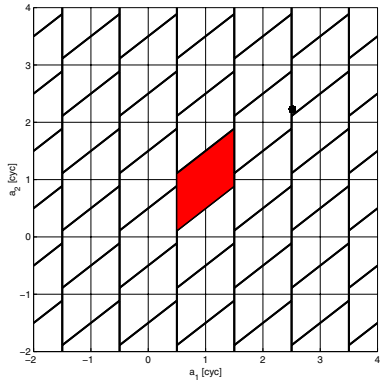

Fig. 3.5. *Integer bootstrapping* in the original domain

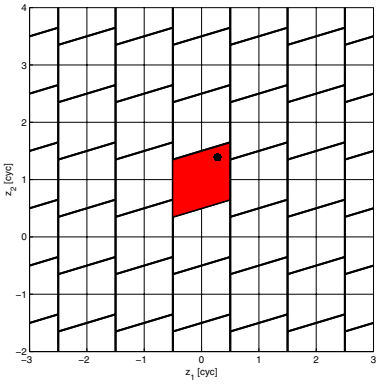

Fig. 3.6. *Integer bootstrapping* in the decorrelated domain

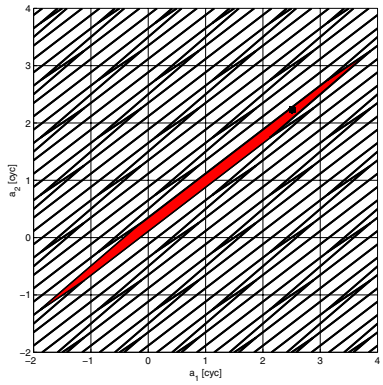

Fig. 3.7. *Integer least-squares* in the original domain

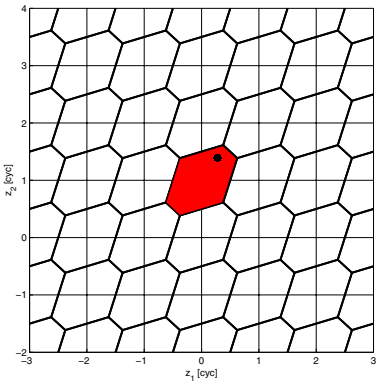

Fig. 3.8. *Integer least-squares* in the decorrelated domain

Table 3.3. Results LAMBDA search procedure: Decorrelated ambiguities

z_1	$\hat{z}_{2\|1}$	lower z_2	upper z_2	z_2	$(\hat{z}-z)^T Q_{\hat{z}}^{-1}(\hat{z}-z)$
-1	1.01	-0.49	2.50	0	197.33
				1	114.58
				2	195.66
0	1.31	-0.58	3.19	0	145.17
				1	13.14
				2	44.96
				3	240.62
1	1.61	-0.18	3.39	0	247.68
				1	66.39
				2	48.94
				3	195.33
2	1.91	0.86	2.95	1	274.30
				2	207.59

In Figs. 3.3 and 3.4 the pull-in regions of the integer *rounding* estimator are plotted, in the original as well as in the transformed domain. The figures show that in both domains the pull-in regions are simple squares, where each square is centered around a grid-point. The pull-in regions corresponding to the assumed correct integer solution are grey-shaded. Also in the figures the float solution is depicted (marked by a dot), and it can be seen that in the original domain the float vector is lying *outside* the pull-in region of the correct solution. In the Z-domain, it is however *inside* the pull-in region. So in this case it is better to decorrelate the ambiguities first, in order to obtain the correct integer solution. A similar phenomenon is visible for the integer *bootstrapping* estimator. In Figs. 3.5 and 3.6 for this estimator the pull-in regions are shown (starting with the first ambiguity). In 2D these pull-in regions are parallelograms centered around the grid points. Like for integer rounding, in the original domain the float ambiguity vector is *not* mapped to the correct integer solution, however in the Z-domain it is. Finally, Figs. 3.7 and 3.8 show the pull-in regions of the integer *least-squares* estimator. In 2D these turn out to be *hexagons* centered around the grid points. As can be seen from the figures, for this integer estimator it makes no difference whether the ambiguities are first decorrelated or not, since its integer solution was assumed as the correct one.

From the considered example the following conclusions can be drawn. Although for integer least-squares solution it makes no difference whether the ambiguities are not, the estimation based on the decorrelated ambiguities turns out to be more efficient (faster) than using the ambiguities in the original domain. Besides, with decorrelated ambiguities it is for this example also possible to obtain the correct integer solution using the much simpler rounding and bootstrapping estimators.

3.6 On the quality of the integer and real solutions

In the example of the previous section the integer least-squares solution was *assumed* to be the correct integer solution. But, since one is always able to compute an integer solution, one still does not know whether this is really the case. How to judge the quality of the integer ambiguity solution will be subject of this section. In order to do so, one needs the *probability distribution* of the integer ambiguities, which is, like the integer ambiguities themselves, of the *discrete-type*. Having derived a quality description of the integer ambiguities, one is not finished yet, since the quality of the other parameters, among others the parameters of interest, also needs to be assessed. Because of the discrete probability mass function of the integer ambiguities, this is a non-trivial task, and one has to go back to the probability distribution of the fixed real-valued parameters in order to make any inferences.

3.6.1 Probability distribution of the integer ambiguities

In order to derive the probability distribution of the integer ambiguities, we first go back to the distribution of the observables. It is assumed that the GPS observables are normally or Gaussian distributed, with mean A_1a+A_2b and dispersion Q_y (see Eq. (3.7)):

$$y \;\sim\; N(A_1a + A_2b,\; Q_y), \quad a \in Z^q \tag{3.65}$$

The probability density function (pdf) for normally distributed observables follows as (see e.g. [Teunissen, 2000c]):

$$p_y(x) \;=\; \frac{1}{\sqrt{|Q_y|}(2\pi)^{\frac{1}{2}l}} \exp\left\{-\frac{1}{2}\|y - A_1a - A_2b\|^2_{Q_y}\right\} \tag{3.66}$$

Since the float ambiguities are a linear function of the observations, they also have a normally distributed pdf:

$$p_{\hat{a}}(x) \;=\; \frac{1}{\sqrt{|Q_{\hat{a}}|}(2\pi)^{\frac{1}{2}q}} \exp\left\{-\frac{1}{2}\|x - a\|^2_{Q_{\hat{a}}}\right\} \tag{3.67}$$

where the first moment is assumed to be the true though unknown integer mean, and the dispersion the vc-matrix of the float ambiguities:

$$E\{\hat{a}\} \;=\; a, \qquad D\{\hat{a}\} \;=\; Q_{\hat{a}} \tag{3.68}$$

This normal distribution of the float ambiguities is used to derive the distribution of the integer ambiguities. Using the pull-in region concept, we know that the probability that the integer solution $\check{a}$ coincides with a certain integer vector z, is the probability that the float ambiguity solution lies within the pull-in region of z (see Eq. (3.29)). This probability is computed by taking the integral of the float ambiguity pdf over the pull-in region:

$$\boxed{P(\check{a} = z) \;=\; P(\hat{a} \in S_z) \;=\; \int_{S_z} p_{\hat{a}}(x)dx} \tag{3.69}$$

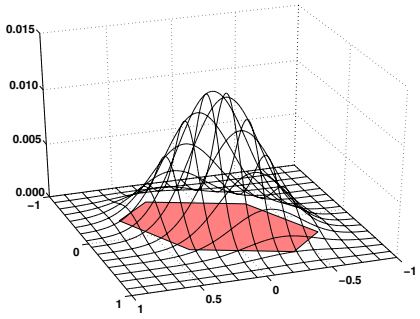

Fig. 3.9. Example of the float ambiguity pdf in 2D (taken from [Joosten, 2000])

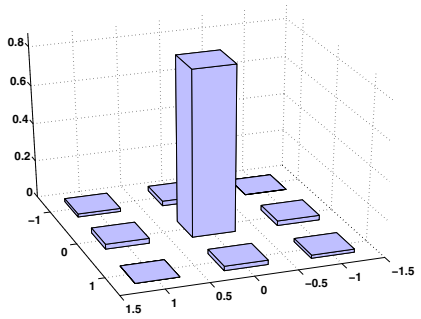

Fig. 3.10. Example of the integer ambiguity pmf in 2D (taken from [Joosten, 2000])

This equation describes the distribution of the integer ambiguities, which is a *probability mass function* (pmf), with zero masses at non-grid-points and non-zero masses at the grid-points. This pmf will be referred to as the *integer normal distribution* of the ambiguities, according to [Teunissen, 1998c].

Figs. 3.9 and 3.10 show examples of the float ambiguity pdf and the integer ambiguity pmf in 2D. In both examples it is assumed that $(0,0)^T$ is the correct integer solution.

3.6.2 Properties of the integer normal distribution

The properties of the integer normal distribution are discussed and proved in [Teunissen, 1998c]. They are summarized below:

- Assuming that a is the correct integer solution, the probability of *correct* integer estimation is largest, compared to the probability of estimating any other integer vector:

$$\max_{z \in Z^q} P(\check{a} = z) \;=\; P(\check{a} = a) \tag{3.70}$$

- The integer normal distribution is, like the normal probability density function, *symmetric* about its mean:

$$P(\check{a} = a - z) \;=\; P(\check{a} = a + z),\ \forall z \in Z^q \tag{3.71}$$

- The integer ambiguity solution is, like the float solution, *unbiased*:

$$E\{\check{a}\} \;=\; \sum_{z \in Z^q} z P(\check{a} = z) \;=\; a \tag{3.72}$$

From this unbiasedness of the integer ambiguities and the unbiasedness of the float real-valued parameters, i.e. $E\{\hat{b}\} = b$, using Eq. (3.15) it follows that the fixed real-valued parameters are unbiased too:

$$E\{\check{b}\} \;=\; b - Q_{\hat{b}\hat{a}}Q_{\hat{a}}^{-1}(a - E\{\check{a}\}) \;=\; b \tag{3.73}$$

This is very fortunate, since it proves that ambiguity resolution does not result in a biased solution of the parameters of interest.

- The dispersion or *vc-matrix* of the integer ambiguities reads:

$$D\{\check{a}\} \;=\; \sum_{z \in Z^q} (z-a)(z-a)^T P(\check{a} = z) \;=\; Q_{\check{a}} \tag{3.74}$$

From this it follows that the precision of the integer ambiguities is poor when the probabilities of wrong integer estimation may not be neglected. Only when the probability of *correct* integer estimation is sufficiently large, i.e. $P(\check{a} = a) \approx 1$, it follows that the probabilities of estimating *wrong* integer vectors are almost zero and $Q_{\check{a}} \approx 0$.

3.6.3 Probability distribution of the ambiguity-fixed parameters

When the integer ambiguities may be considered as *deterministic* quantities, the fixed real-valued parameters (a.o. the parameters of interest) have a normally distributed pdf and reads:

$$p_{\hat{b}|\hat{a}}(x|y=z) \;=\; \frac{1}{\sqrt{|Q_{\hat{b}|\hat{a}}|}(2\pi)^{\frac{1}{2}p}} \exp\left\{-\frac{1}{2}\|x - b_{|\hat{a}=z}\|^2_{Q_{\hat{b}|\hat{a}}}\right\} \tag{3.75}$$

where $\hat{a} = z$ denotes the deterministic ambiguities and p the number of real-valued parameters. This distribution is a *conditional* pdf, since the ambiguities are assumed deterministic. The conditional mean plus vc-matrix read, see also Eq. (3.15) and Eq. (3.16):

$$b_{|\hat{a}=z} \;=\; b - Q_{\hat{b}\hat{a}}Q_{\hat{a}}^{-1}(a-z), \qquad Q_{\hat{b}|\hat{a}} \;=\; Q_{\hat{b}} - Q_{\hat{b}\hat{a}}Q_{\hat{a}}^{-1}Q_{\hat{a}\hat{b}} \tag{3.76}$$

The integer ambiguities are however not deterministic but stochastic variables. For the fixed real-valued parameter solution based on stochastic integer ambiguities, i.e. $\check{b} \;=\; \hat{b} - Q_{\hat{b}\hat{a}}Q_{\hat{a}}^{-1}(\hat{a} - \check{a})$, the following pdf applies [Teunissen, 1999b]:

$$\boxed{p_{\check{b}}(x) \;=\; \sum_{z \in Z^q} p_{\hat{b}|\hat{a}}(x|y=z)P(\check{a}=z)} \tag{3.77}$$

This pdf is an infinite sum of weighted conditional baseline distributions, where the weights are given by the probability masses of the distribution of the integer ambiguities. Because of these weights, the distribution is of the so-called *multi-modal* type, and not of the normal (uni-modal) type. This multi-modality has consequences for the quality description of the fixed solution, since standard procedures such as the evaluation of the vc-matrix are based on fixed parameters which are assumed to be normally distributed.

3.6.4 On the quality of the ambiguity-fixed parameters

Instead of the vc-matrix, as a measure for the quality of the fixed solution, the probability that $\check{b}$ lies in a certain region $R \subset R^p$ can be investigated [Teunissen, 2001b]:

$$P(\check{b} \in R) \;=\; \int_R p_{\check{b}}(x)dx \tag{3.78}$$

where the (confidence) region R is centered around the true but unknown b:

$$R \;=\; \left\{ x \in R^p \mid (x-b)^T Q^{-1}_{\hat{b}|\hat{a}}(x-b) \;\leq\; \beta^2 \right\} \tag{3.79}$$

Unfortunately it is difficult to evaluate the probability in Eq. (3.78) in an exact manner. It is possible to give *lower and upper bounds* for it:

$$\boxed{P(\hat{b}_{\hat{a}=a} \in R)P(\check{a}=a) \;\leq\; P(\check{b} \in R) \;\leq\; P(\hat{b}_{\hat{a}=a} \in R)} \tag{3.80}$$

where $P(\hat{b}_{\hat{a}=a} \in R) \;=\; P(\chi^2(p,0) \leq \beta^2)$ and $\chi^2(p,0)$ the central Chi-square distribution with p degrees of freedom.

In Eq. (3.80) the probability of correct ambiguity estimation (denoted as $P(\check{a}=a)$) appears. When this probability, referred to as the *ambiguity success rate*, approaches to 1, the lower and upper bounds in Eq. (3.80) become very *tight*. In that case the probability of the ambiguity-fixed real-valued parameters, $\check{b}$, becomes very close to the probability of the *conditional* parameters, $\hat{b}_{\hat{a}=a}$. Since these conditional parameters are normally distributed, only in the case that the success rate is close to 1, one is allowed to use the vc-matrix $Q_{\hat{b}|\hat{a}}$ for the precision description of the real-valued parameters. So knowledge of the ambiguity success rate is very important for inferring the quality of the fixed parameters of interest. In the next section therefore it is described how this success rate can be evaluated in a straightforward manner.

3.7 Evaluating the ambiguity success rate

In this section closed-form formulas are reviewed, which can be used to verify whether the probability of estimating the true but unknown ambiguities a, $P(\check{a}=a)$, is close enough to 1. The starting point is the integer normal distribution, the pmf of the integer ambiguities.

3.7.1 The integer normal distribution evaluated

In general it is very difficult to evaluate the integer normal distribution as given in Eq. (3.69), because of the complicated geometry of the pull-in region. However, for two special situations, namely when the ambiguity vc-matrix is a *diagonal* matrix, or in case the *integer bootstrapping* estimator is used, it is possible to derive *closed-form expressions* for this pmf. Although the pmfs of the integer rounding

estimator and, more important, the integer least-squares estimator cannot be evaluated in a straightforward manner, they can be approximated using the pmfs in case of uncorrelated ambiguities and integer bootstrapping. Another possibility to evaluate the pmf of the integer least-squares estimator is to *simulate* the integer normal distribution.

Uncorrelated ambiguities

If the ambiguities are uncorrelated, $Q_{\hat{a}}$ is a diagonal matrix and the integer ambiguity estimates are obtained by simply rounding of the float ambiguities to their nearest integers. The pmf of the integer ambiguities is in this case a product of q individual probabilities [Teunissen, 1998b]:

$$P(\check{a}_{Q_{\hat{a}}=\text{diag}} = z) \;=\; \prod_{i=1}^{q} \left[\Phi\left(\frac{1+2c_i^T(z-a)}{2\sigma_{\hat{a}_i}} \right) + \Phi\left(\frac{1-2c_i^T(z-a)}{2\sigma_{\hat{a}_i}} \right) - 1 \right] \tag{3.81}$$

where $c_i = (0, \ldots, 1, \ldots, 0)^T$ (with the 1 at the ith position) and $\Phi(x)$ the well-known *standard normal cumulative distribution function*, evaluated at x:

$$\boxed{\Phi(x) \;=\; \int_{-\infty}^{x} \frac{1}{\sqrt{2\pi}} \exp\{-\frac{1}{2}v^2\} dv} \tag{3.82}$$

Bootstrapping

For the integer bootstrapped estimator, the pmf is very similar to the pmf in case of a diagonal ambiguity vc-matrix. The differences are that the standard deviations of the ambiguities are replaced by their *conditional* counterparts, and that the vector c_i is replaced by the vector l_i [Teunissen, 1998b]:

$$P(\check{a}_B = z) \;=\; \prod_{i=1}^{q} \left[\Phi\left(\frac{1+2l_i^T(z-a)}{2\sigma_{\hat{a}_{i|I}}} \right) + \Phi\left(\frac{1-2l_i^T(z-a)}{2\sigma_{\hat{a}_{i|I}}} \right) - 1 \right] \tag{3.83}$$

with l_i the i^{th} column of the lower triangular matrix L^{-T} (see Eq. (3.36)).

Simulating the distribution

Approximations of the probabilities $P(\check{a} = z)$ can be obtained by simulation, see [Teunissen, 1998c]. To obtain these probability masses, the distribution of the *float* ambiguities, i.e. $N(a, Q_{\hat{a}})$ is shifted over a. From the resulting distribution $N(0, Q_{\hat{a}})$ samples are drawn, which are used to obtain the corresponding integer samples by means of solving the integer least-squares problem, see Eq. (3.34). When this procedure is repeated a sufficient number of times, the required frequency table can be built up, from which the simulated ambiguity success rate follows as $P(\check{a} = 0)$. Since the integer least-squares problem needs to be carried out many times, it is better to base the simulation on the *decorrelated* ambiguities, instead of the original ambiguities. Results of this simulation are described in [Joosten, 2000].

3.7.2 Closed-form expression for the ambiguity success rate

Based on the integer normal distributions, in case of a diagonal ambiguity vc-matrix or in case of the integer bootstrapping technique is applied, closed-form expressions for the ambiguity success rate can be derived. For that purpose in Eq. (3.81), respectively Eq. (3.83), we need to set $z = a$. In case of a diagonal $Q_{\hat{a}}$-matrix, this success rate is computed as follows:

$$\boxed{P(\check{a}_{Q_{\hat{a}}=\text{diag}} = a) \;=\; \prod_{i=1}^{q} \left[2\Phi\left(\frac{1}{2\sigma_{\hat{a}_i}} \right) - 1 \right]} \tag{3.84}$$

In case of integer bootstrapping the ambiguity success rate is:

$$\boxed{P(\check{a}_B = a) \;=\; \prod_{i=1}^{q} \left[2\Phi\left(\frac{1}{2\sigma_{\hat{a}_{i|I}}} \right) - 1 \right]} \tag{3.85}$$

Note that the only difference between this expression and the previous one is that the ambiguity standard deviation is replaced by its conditional counterpart.

3.7.3 Bounding the ambiguity success rate

Lower bounds

Instead of simulating the integer least-squares success rate, the expression for the success rate of integer bootstrapping in Eq. (3.85) can be used to *lower bound* the integer least-squares success-rate. It can namely be proved that the integer least-squares success rate is always larger or at least equal to the bootstrapped success rate, see [Teunissen, 1999a]:

$$P(\check{a}_{LSQ} = a) \;\geq\; P(\check{a}_B = a) \tag{3.86}$$

So when it is guaranteed that the bootstrapped success rate is close to 1, this automatically implies that the least-squares success rate is also close to 1.

For the integer rounding success rate, a lower bound is given by the success rate in case of a diagonal vc-matrix, which is computed using Eq. (3.84), since it holds that [Teunissen, 1998b]:

$$P(\check{a}_R = a) \;\geq\; P(\check{a}_{Q_{\hat{a}}=\text{diag}} = a) \tag{3.87}$$

Integer least-squares is optimal

In [Teunissen, 1998b] it was also shown that the integer bootstrapping success rate lower bounded by the integer rounding success rate. Using this, and the lower bound in Eq. (3.86) it is possible to arrange the success rates of the three admissible integer estimators in the following order:

$$\boxed{P(\check{a}_{LSQ} = a) \;\geq\; P(\check{a}_B = a) \;\geq\; P(\check{a}_R = a)} \tag{3.88}$$

In addition to this, in [Teunissen, 1999a] it is proved that the integer least-squares estimator gives the largest probability of estimating the correct integer ambiguities of *all* (admissible) integer estimators:

$$\boxed{P(\check{a}_{LSQ} = a) \;\geq\; P(\check{a}_X = a)} \tag{3.89}$$

where X stands for an arbitrary admissible integer estimator.

Invariant upper bounds

A disadvantage of the bootstrapped success rate (see Eq. (3.86)) is that it depends on the ambiguity with which the bootstrapping process is started. Another ambiguity will influence this lower bound for the integer least-squares success rate. An invariant *upper bound* of the integer least-squares success rate can be computed using the $ADOP$ (Ambiguity Dilution Of Precision, see [Teunissen, 1997b]), and can be given as follows [Teunissen, 2000b]:

$$P(\check{a}_{LSQ} = a) \;\leq\; P\left(\chi^2_q \leq \frac{c_q}{ADOP^2}\right) \tag{3.90}$$

where $ADOP = |Q_{\hat{a}}|^{\frac{1}{2q}}$, and χ^2_q a variable which has a central Chi-square distribution with q degrees of freedom. Moreover, $c_q = \left[\frac{q}{2}\Gamma(\frac{q}{2})\right]^{2/q}/\pi$, where Γ denotes the Gamma function. The $ADOP$ is a scalar measure and like the ambiguities expressed in *cycles*. This $ADOP$-based upper bound is invariant to a change of ambiguity reparametrization, such as a change of pivot receiver or satellite, but also the LAMBDA (Z-) transformation, since the determinant of the ambiguity vc-matrix is invariant for it [Teunissen and Odijk, 1997]:

$$|Q_{\hat{z}}| \;=\; |Z^T Q_{\hat{a}} Z| \;=\; |Z^T||Q_{\hat{a}}||Z| \;=\; |Q_{\hat{a}}| \tag{3.91}$$

Because of this invariance, the $ADOP$ is a true measure of the intrinsic ambiguity precision. Based on the $ADOP$, also an invariant upper bound for the bootstrapped success rate can be given as [Teunissen, 1998b]:

$$P(\check{a}_B = a) \;\leq\; \left[2\Phi\left(\frac{1}{ADOP}\right) - 1\right]^q \tag{3.92}$$

In [Teunissen, 2000b] it is proved that this bootstrapped upper bound is smaller or at most equal to the aforementioned least-squares upper bound:

$$\left[2\Phi\left(\frac{1}{ADOP}\right) - 1\right]^q \;\leq\; P\left(\chi^2_q \leq \frac{c_q}{ADOP^2}\right) \tag{3.93}$$

Example (continued)

Table 3.4 shows for our 2D example the computed and simulated ambiguity success rates plus the discussed lower and upper bounds. This has been done for the ambiguities in the original domain, as well as for the LAMBDA (Z-) transformed ambiguities.

Table 3.4. Example ambiguity success rates

success rate	original ambiguities	decorrelated ambiguities
lower bound rounding	0.51171	0.99995
bootstrapping (1st ambiguity)	0.65816	0.99996
bootstrapping (2nd ambiguity)	0.77749	0.99997
$ADOP$ upper bound bootstrapping	0.99997	0.99997
simulated least-squares	not computed	0.99998
$ADOP$ upper bound least-squares	0.99999	0.99999

The table shows that the probability of estimating the correct ambiguities is indeed largest using the integer least-squares estimator: The simulated success-rate (based on the decorrelated ambiguities) is 0.99998. Note that the probability of 0.99999 is only an *upper bound* for the least-squares success-rate, and cannot be used when inferring the correctness of the integer solution. Although the simulated success-rate is largest, it is sharply lower bounded by both the bootstrapping success-rates and also the lower bound for rounding, however provided that the ambiguities are *decorrelated*. In Figures 3.3 – 3.6 this beneficial effect of decorrelation was already visible.

Note that for the success-rate of integer bootstrapping, which can be computed exactly, it makes sense to start the bootstrapping with the most precise ambiguity (the second ambiguity) as this yields a higher success-rate, although there is only a marginal difference in the decorrelated case.

3.7.4 The bias-affected success rate

The closed-form expressions for the success rate are based on an unbiased float ambiguity solution, $E\{\hat{a}\} = a$. In the presence of *unmodelled biases* in the GPS observations however, the performance of ambiguity resolution will be degraded, but when the ambiguity pdf is sufficiently peaked and the bias vector falls *within* the pull-in region, the success rate can still be sufficiently high.

It is possible to derive expressions for the success rate of integer bootstrapping when the float ambiguity solution is biased. For this, the float solution normally

distributed assumed, but with a mean which is biased with the vector ξ:

$$\hat{a} \;\sim\; N(a+\xi,\; Q_{\hat{a}}) \tag{3.94}$$

The closed-form expression for the *bias-affected* bootstrapped success rate is derived as [Teunissen et al., 2000], [Teunissen, 2001c]:

$$\boxed{P_\xi(\check{a}_B = a) \;=\; \prod_{i=1}^{q}\left[\Phi\left(\frac{1+2\zeta_i}{2\sigma_{\hat{a}_{i|I}}}\right) + \Phi\left(\frac{1-2\zeta_i}{2\sigma_{\hat{a}_{i|I}}}\right) - 1\right]} \tag{3.95}$$

where ζ_i the i^{th} entry of the bias vector $\zeta = L^{-1}\xi$, with L the lower triangular from the factorization $Q_{\hat{a}} = LDL^T$ (see Eq. (3.36)). Note that when the bias-affected success rate is evaluated for the decorrelated ambiguities, the conditional standard deviations $\sigma_{\hat{z}_{i|I}}$ should be used, as well as the bias vector $\zeta = L^{-1}Z^T\xi$, where L in this case follows from $Q_{\hat{z}} = LDL^T$.

Example (continued)

For the considered 2D example, bias-affected bootstrapped success rates are computed, for three different bias vectors, whose directions are plotted as vectors 1, 2 and 3 in Fig. 3.11.

1. There is bias in the direction of the a_1-axis (vector 1):

$$\xi = \begin{bmatrix} 1 \\ 0 \end{bmatrix} bias \tag{3.96}$$

2. There is bias in the direction of the a_2-axis (vector 2):

$$\xi = \begin{bmatrix} 0 \\ 1 \end{bmatrix} bias \tag{3.97}$$

3. There is bias in the direction of vector 3:

$$\xi = \frac{1}{\sqrt{1^2 + \left(1 + \frac{\sigma_{\hat{a}_1\hat{a}_2}}{\sigma^2_{\hat{a}_1}}\right)^2}} \begin{bmatrix} 1 \\ 1 + \frac{\sigma_{\hat{a}_1\hat{a}_2}}{\sigma^2_{\hat{a}_1}} \end{bmatrix} bias \;=\; \begin{bmatrix} 0.490 \\ 0.872 \end{bmatrix} bias \tag{3.98}$$

Note that in all three cases the length of the bias vector is the same and equal to the variable *bias*. In Fig. 3.11 the direction of these three biases are plotted. In Fig. 3.12 the ambiguity success rates are plotted as function of *bias*. The success rates are computed for the decorrelated ambiguities, as this gives a sharp lower bound for the integer least-squares success rates.

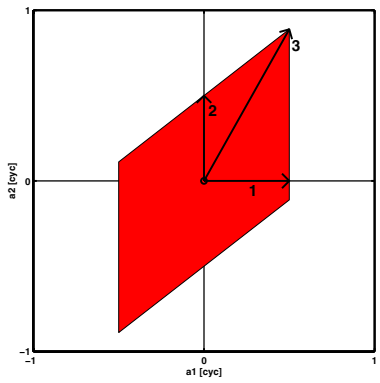

Fig. 3.11. Bias direction vectors and bootstrapped pull-in region

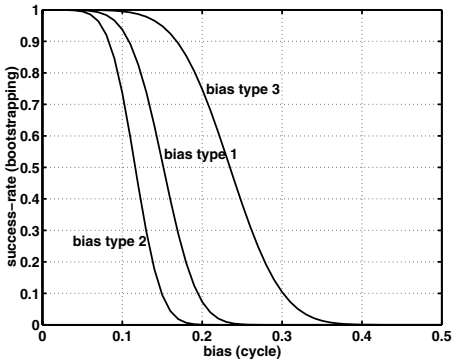

Fig. 3.12. Bootstrapped success rate in the presence of biases in the directions of vectors 1, 2 and 3.

The figure shows first of all that the third type of bias may be larger compared to the other two to obtain the same level of success rate. This can be explained from Fig. 3.11, in which it is visible that the type three bias lies in the longest direction of the pull-in region. If it is required that the success rate should be at least 0.999, then the type three bias may be about 0.07 cycle, whereas the type one bias may be 0.04 cycle and the type two bias 0.03 cycle.

3.8 Concluding remarks

In this chapter a general procedure has been described to solve the mathematical model as derived in Chap. 2 for high-precision fast GPS applications. Crucial to this procedure is that advantage is taken of the integer property of the carrier-phase ambiguities. Because of these integer ambiguities, the procedure is split into three parts: i) Float solution, ii) Ambiguity resolution and iii) Fixed solution. In the latter solution the estimated integer ambiguities are held fixed, assuming that they are the correct values. To resolve the ambiguities, different integer estimators are admissible, but the integer least-squares search, which is implemented in the LAMBDA method, yields the highest probability of estimating the correct integers, compared to all other admissible estimators. Besides, the integer least-squares estimator in the LAMBDA method is also very efficient, since the ambiguities are first decorrelated. To decide whether the estimated integers may be held fixed to compute the parameters of interest with high precision, one should assure that the ambiguity success rate is sufficiently close to 1. This success rate can be computed from the float ambiguity vc-matrix. A very easy-to-compute sharp lower bound for the integer least-squares success rate is given by the bootstrapped success rate, provided that it is based on the decorrelated ambiguities.

Chapter 4

The ionospheric error in GPS observations

4.1 Introduction

In the derivation of the GPS model in Chap. 2 the errors in the phase and code observations due to propagation through the Earth's atmosphere were assumed to be absent. To make an inclusion of these error terms in the GPS model possible, in this chapter the *physical* backgrounds of the atmospheric errors in GPS phase and code observations are reviewed.

The chapter is set up as follows. In Sect. 4.2 it is explained that for GPS applications the atmosphere is divided into an *ionospheric* and *tropospheric* part. In Sect. 4.3 the propagation of the GPS signals through these media is described by analyzing the geometric effects of atmospheric refraction. The main focus is on the ionospheric refraction effects, since it of more importance to fast precise GPS applications than the effects of tropospheric refraction (which mainly influence the height component). In Sect. 4.4 it is reviewed that the ionospheric error can be approximated as a sum of error components, referred to as first-order, higher-order and signal bending terms. To assess whether these effects are of relevance for relative positioning in Sect. 4.5 a simple single-layer representation of the ionosphere is introduced, which is used in Sect. 4.6 to approximate the higher-order and bending effects. In Sects. 4.7 and 4.8 it is tried to give a quantification of the ionospheric effects which can be expected for the relative GPS applications in this thesis. These simulations are carried out assuming worst-case ionospheric conditions and receiver-satellite configurations. In Sect. 4.9 the concluding remarks of this chapter are summarized.

4.2 Division of the Earth's atmosphere

GPS signals from a satellite at about 20,200 km altitude above the Earth's surface travel through the atmosphere to reach the receiver on Earth. The atmosphere is a relatively thin layer of gases (air) and dust surrounding the Earth. The interaction with particles in the atmosphere affects the propagation of GPS signals: *Atmospheric refraction* occurs. To describe this phenomenon the atmosphere is

divided into two parts, according to the presence of charged particles: An *ionized* part, where charged particles are present, and a *non-ionized* part where charged particles are practically absent.

4.2.1 Non-ionized part of the atmosphere

The non-ionized part or neutral atmosphere (neutrosphere) extends from 0 to about 80 km altitude above the Earth's surface. Based on the temperature, this part of the atmosphere can be divided into three layers: The *troposphere*, *stratosphere* and *mesosphere*, see Fig. 4.1. To an altitude of about 15 km (at the poles: About 9 km) extends the troposphere, which consists of a (neutral) mixture of gases. In the troposphere our daily weather takes place and the propagation of radio waves depends on the temperature, air pressure and humidity. In the troposphere the temperature decreases with increasing altitude. From 15 to 50 km altitude one speaks of the stratosphere where the temperature rises and from 50 to 80 km altitude the temperature decreases again in the mesosphere.

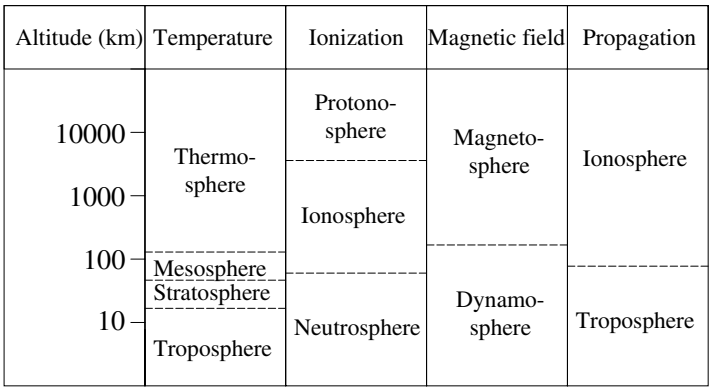

Fig. 4.1. Possible subdivisions of the Earth's atmosphere (after [Seeber, 1993])

4.2.2 Ionized part of the atmosphere

The ionized part of the atmosphere, above 80 km altitude, consists of the *ionosphere* and the *protonosphere* (above 1,000 km; also referred to as *plasmasphere*). The ionosphere consists of a mix of uncharged and charged particles. The charged particles are created by *photo-ionization* caused by incoming UV- and X-radiation from the Sun: Gas molecules are heated and electrons are liberated from them. The rate of this ionization depends on the density of gas molecules and the intensity of the radiation. In the neutral atmosphere charged particles are practically absent, since the created charged particles are recombined rapidly due to the high density of particles. In the ionosphere however the particle density is extremely

small and collisions between electrons and ions are relatively infrequent, so recombination takes place only very slowly. Not all the particles in the ionosphere are charged ions and electrons; the degree of ionization is in fact very low. In the ionosphere however only the charged particles are able to influence the propagation of radio waves. Mainly the free electrons affect the propagation, since the free ions are much heavier than the electrons. The particle density in the protonosphere is very low, but in contrast to the ionosphere in this layer almost *each* atom is ionized. Very little is known about the protonosphere.

4.2.3 The variability of the ionospheric free electron density

Because of a varying intensity in solar radiation, the ionospheric free electron density is highly variable both in space and time. Several regular and irregular variations can be recognized, see e.g. [Giraud and Petit, 1978], [Klobuchar, 1991] and [Spoelstra, 1996]. In this section the for GPS relevant effects are summarized.

Altitude

In Fig. 4.2 the global path of the electron density in the atmosphere is plotted against the height above the Earth's surface. As can be seen from the figure, the electron density increases with an increasing height, but only up to a certain height, where a maximum in the electron density is reached (h_{max}). This part of the curve is called the *bottomside* profile. This increase in electron density is caused since the absorption of the solar radiation decreases with altitude, such that more gas molecules become ionized. Above the height h_{max} the electron density decreases again (*topside* profile), which is caused by a decreasing amount of gas molecules left to be ionized.

A more accurate investigation of the change of electron density with altitude, usually leads to a stratification of the ionosphere in a number of horizontal layers, see Table 4.1. From this table, note that for GPS the *F2 layer* is the significant layer, showing the largest electron density peak in the atmosphere, with its maximum usually at a height of 350-400 km. In Fig. 4.3 this stratification is visible for a typical mid-latitude vertical electron density profile. Note that the ionospheric layers are not sharply bounded. There is a gradual change of one layer into the other.

Geomagnetic latitude

The ionized part of the atmosphere is influenced by the Earth's *magnetic field*. Hence, the ionospheric electron density shows a large dependence on the latitude in a *geomagnetic* reference frame. In Fig. 4.4 the world is dived into three types of geomagnetic regions: *Equatorial*, *mid-latitude* and *auroral* or polar regions. It is known that the size and variability of the electron density is usually the largest in the equatorial zone (about 15°-20° at both sides of the geomagnetic equator) and the auroral/polar zones (above 70° north or south latitude). At the geomagnetic mid-latitude regions the size and variability of the electron density are relatively

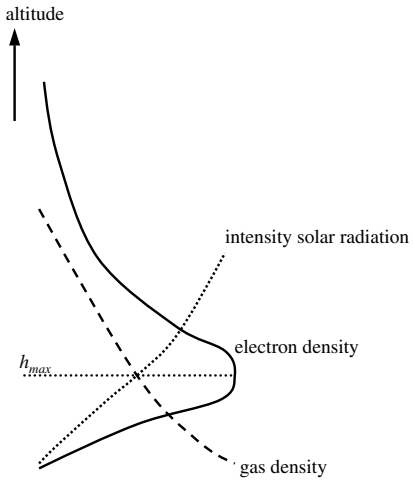

Fig. 4.2. Global profile of electron density, gas density and intensity of solar radiation with altitude

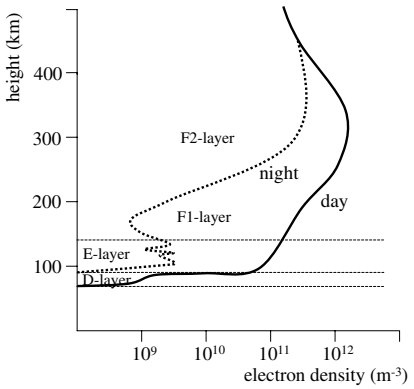

Fig. 4.3. Typical bottomside vertical electron density profile

low.

Time of day or geomagnetic longitude

The free electron density in the ionosphere also shows strong correlation with the *diurnal* period of the Earth. Around local noon the solar activity is at its daily maximum. During nighttime it is at its minimum (see Fig. 4.6). The ionization in the plasmasphere can be significant at nighttime, when the amount of free electrons may be 50% of the free electrons in the atmosphere. During daytime conditions the plasmasphere is of less importance (normally only 10% of the free electrons in the atmosphere).

Table 4.1. Horizontal layers in the ionosphere

layer	height [km]	typical electron density [m^{-3}]		remarks
D	80 - 90	- (night)	10^{10} (day)	disappears at night
E	90 - 140	$5 \cdot 10^9$ (night)	10^{11} (day)	sporadic Es at 120 km
F1	140 - 200	- (night)	$5 \cdot 10^{11}$ (day)	goes up into F2 at night
F2	200 - ∞	10^{11} (night)	10^{12} (day)	max. density at 350 km

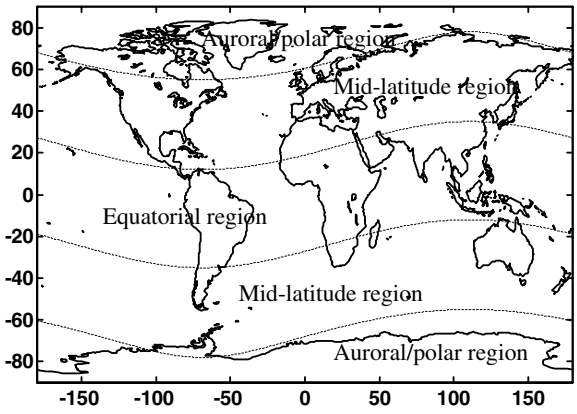

Fig. 4.4. Division of the Earth into geomagnetic regions. Plotted are the geomagnetic parallel lines $66.5°N$, $23.5°N$, $23.5°S$ and $66.5°S$ in the geodetic reference frame.

Season

Due to the inclination of the Earth's equator with respect to the ecliptic, the solar activity and therefore the electron density fluctuate with the seasons.

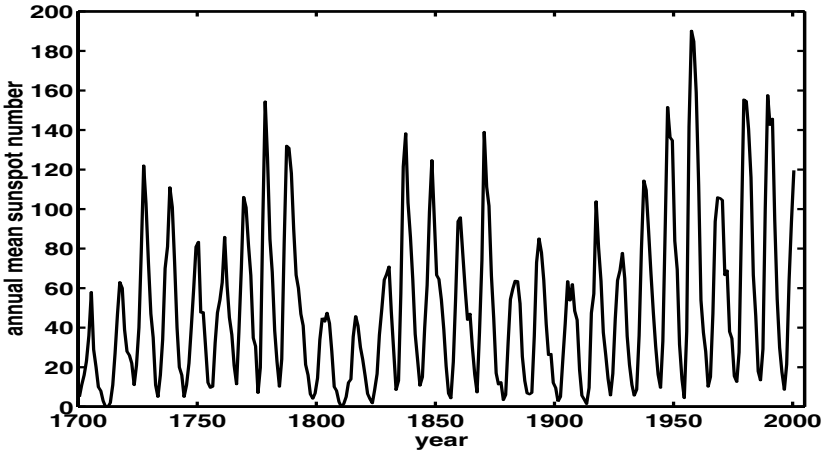

Fig. 4.5. Yearly mean sunspot numbers since 1700 (data courtesy of Solar Influences Data analysis Center (SIDC), Belgium)

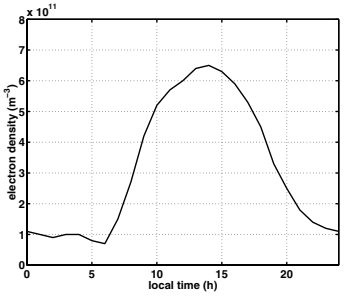

Fig. 4.6. Example of diurnal variation of ionospheric electron density

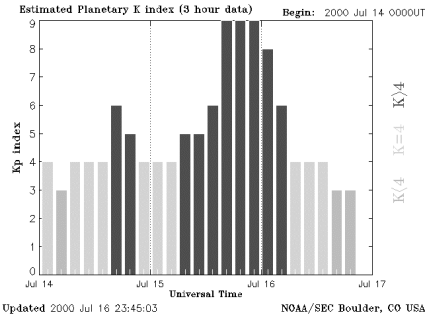

Fig. 4.7. Planetary Kp-index from July 14th to July 17th 2000 (graph courtesy of NOAA/SEC, USA)

Year-to-year (solar cycle)

The UV radiation from the Sun is influenced by the number of *sunspots* on the Sun's "surface", which shows a cycle of about 11 years (see Fig. 4.5). The last so-called *solar minimum* was in 1996, currently (2002) we are in a *solar maximum* period. In Fig. 4.8 the progression of the current solar cycle (no. 23) is visible. Measured (and smoothed) sunspot numbers are plotted until January 2002. As can be seen, the current solar maximum consists in fact of two maxima (the first, which is the largest, in June 2000 and the second in the last months of 2001). From the depicted prediction graphs it seems that the low level of solar activity as it was in 1996 is not expected before 2004.

Geomagnetic or ionospheric storms

Besides the presence charged particles due to photo-ionization, at all times the Sun ejects a stream of high-energy particles, which is known as the *solar wind*. This solar wind interacts with the geomagnetic field (this may get compressed). Sometimes this charged particle stream increases enormously, caused by explosions (*solar flares*) which occur at the Sun's "surface". Other enormous particle originate in the Sun's atmosphere, the Corona, and are referred to as *Coronal Mass Ejections*. Some of these CMEs are able to compress the Earth's magnetic field enormously, causing a so-called *geomagnetic storm* which may (but do not automatically have to) disturb the ionosphere. When it does disturb the ionosphere, the free electron density may rapidly change. Geomagnetic or ionospheric storms especially occur in the northern auroral regions, lasting for several hours [Klobuchar, 1991]. In these polar regions the charged particles flow along the geomagnetic field lines and they may interact with the neutral atmosphere causing colored displays (the well-known *aurora borealis*). Sometimes geomagnetic storms, which are generated in auroral zones, penetrate into lower (middle and equatorial)

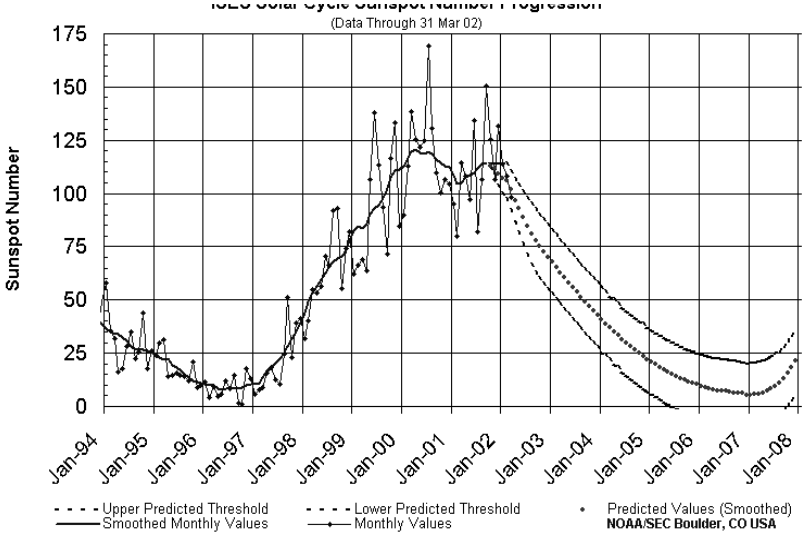

Fig. 4.8. Progression of solar cycle 23: Measured and predicted sunspot numbers (graph courtesy of NOAA Space Environment Center (SEC), USA)

latitudes and may possibly degrade the performance of GPS receivers (in the worst case scintillation effects may occur, see below).

Fortunately, very severe geomagnetic storms are very rare. Their frequency of occurrence is related to the solar cycle: During a solar maximum period there is a higher chance of having geomagnetic storm events than during solar minimum. A measure for the geomagnetic activity is the *Planetary Kp-index*, which is computed every three hours. Another often used measure is the Ap-index, which is one-to-one related with the Kp-index. Both indices are measures of the general level of geomagnetic activity over the globe for a given (UT) day. They are derived from measurements made at a number of stations world-wide of the variation of the geomagnetic field due to currents flowing in the Earth's ionosphere. In Table 4.2 geomagnetic storms are classified by means of the Kp-index. As can be seen, one speaks of a geomagnetic storm when the Kp-value is between 5 (minor) and 9 (extreme).

On July 15th 2000 an extreme geomagnetic storm occurred which was caused by CMEs. This storm was one of the 30 strongest disturbances since 1932 [Kunches, 2000]. In Fig. 4.7 for July 14 to July 17 the Kp-index is plotted and on July 15th from 15:00 UTC to 24:00 UTC the extreme levels are visible.

Table 4.2. Scale for geomagnetic storms [NOAA, 2001]

scale	Kp value	# storm events per cycle
G5 (extreme)	9	4
G4 (severe)	8	100
G3 (strong)	7	200
G2 (moderate)	6	600
G1 (minor)	5	1700

Travelling ionospheric disturbances (TIDs)

A *travelling ionospheric disturbance* or TID is a ripple or wave in the ionospheric electron density that propagates in horizontal direction. Although little is known about these structures, one usually distinguishes two types of TIDs, depending on the wavelength, period and propagation speed of these structures [Van Velthoven, 1990]:

- *Large-scale* travelling ionospheric disturbances (LSTIDs) with a wavelength larger than 1000 km, which are probably generated in the auroral regions. An LSTID can move with a speed up to 1000 m/s and usually propagates in the direction of the equator. The period of such a structure lies between 30 minutes and 3 hours.
- *Medium-scale* travelling ionospheric disturbances (MSTIDs) with wavelengths of a few 100 km and periods of 10 minutes to 1 hour. MSTIDs are believed to be generated by thunderstorm activity in the troposphere.

MSTIDs frequently occur, even at mid-latitudes, and have their largest amplitude around daily noon (10:00-16:00 local time), see [Van Velthoven, 1990], [Spoelstra, 1996] and [Wanninger, 1999]. Often a second maximum of occurrence is recognized around midnight. Moreover, during winter months (from November to March) in solar maximum years there is the highest chance of having TIDs.

Ionospheric scintillations

Small-scale ionospheric disturbances which have a few hundred meter scale size may cause phase and amplitude *scintillations* of the received GPS signal. In case of phase scintillations a sudden change in the phase occurs and in case of amplitude scintillations a degrading of the signal strength or even a loss-of-lock may occur. Scintillation effects are more severe during solar maximum years and in periods of heavy geomagnetic storms, mainly in equatorial and auroral regions. In mid-latitude regions the occurrence of ionospheric scintillation is extremely *rare*: They happen only once or twice during the 11-year solar cycle [Klobuchar and Doherty, 1998]. In equatorial regions however, scintillation can be very strong and frequent, usually just after local sunset.

4.3 Atmospheric propagation of the GPS signals

In this section the effect of atmospheric propagation of the GPS signals is reviewed. We restrict ourselves to geometric effects and for this purpose the concept of the *geometric optics* is used. In this concept it is assumed that all changes in the medium (the Earth's atmosphere in this case) are very small within one wavelength of the signal (in case of GPS this is about 20 cm). For this short wavelength signal absorption effects are not of importance and are not discussed.

4.3.1 Atmospheric refraction

When an electro-magnetic (EM) wave propagates in free space, its velocity is known to be equal to the *velocity of light*. When a wave propagates in the atmosphere, its velocity changes due to interaction with particles present in that medium. We say the signal is *refracted*. The 'amount' of refraction is described by a medium specific *refractive index*.

Refractive index

To describe the propagation velocity of an EM-wave, we distinguish between the *phase velocity*, denoted as $v_{\phi,j}$, and the *group velocity* of the signal, denoted as $v_{g,j}$ (see Chap. 2). In a refractive medium they both may be different and they may also differ for each frequency. Hence, for both phase and group of the signal a refractive index can be defined, which is defined as the ratio of the velocity of light and the phase velocity respectively group velocity:

$$\boxed{\begin{array}{rcl} n_{\phi,j} & = & c/v_{\phi,j} \\ n_{g,j} & = & c/v_{g,j} \end{array}} \tag{4.1}$$

In these formulae $n_{\phi,j}$ denotes the phase refractive index and $n_{g,j}$ the group refractive index. Note that since the refractive index is a ratio of two velocities, it is a dimensionless quantity. When the refractive index is smaller than 1 we say that the wave is *advanced* and when it is larger than 1 it is *delayed*. In free space the velocity of the wave is equal to the velocity of light and so the refractive index equals 1.

Geometric refraction effects

The effect of atmospheric refraction on the distance between transmitter (satellite) and receiver can be evaluated using *Fermat's principle*. This principle states that of all possible paths that it might take, light (and other EM-waves) takes the path which requires the *shortest* time. In free space the wave propagates along a straight geometric line, but in a refractive medium it is bent, see Fig. 4.9. Using $v_{\phi,j} = dl_{\phi,j}/dt_{\phi,j}$ and $n_{\phi,j} = c/v_{\phi,j}$, the *optical path length* between transmitter

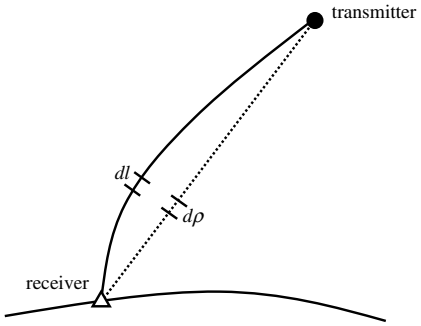

Fig. 4.9. Bending of a signal through the refractive atmosphere

and receiver of the phase of a certain signal, denoted as $\ell_{\phi,j}$, is computed as follows:

$$\begin{aligned} \ell_{\phi,j} = ct_{\phi,j} &= c\int dt_{\phi,j} = \int \tfrac{c}{v_{\phi,j}} dl_{\phi,j} = \int n_{\phi,j} dl_{\phi,j} \\ &= \rho + \underbrace{\int (n_{\phi,j}-1) d\rho}_{\vartheta_{\phi,j}} + \underbrace{(\int n_{\phi,j} dl_{\phi,j} - \int n_{\phi,j} d\rho)}_{\kappa_{\phi,j}} \end{aligned} \tag{4.2}$$

With ρ denoting the geometric distance between satellite and receiver, the excess path length due to atmospheric refraction consists of two effects: A *propagation effect*, denoted as $\vartheta_{\phi,j}$ and a *bending effect*, denoted as $\kappa_{\phi,j}$. Note that when in Eq. (4.2) the subscript ϕ is changed by g the excess path length of the *group* of the signal is obtained.

4.3.2 Separation of the atmospheric refraction

Based on the presence of charged particles, the atmospheric refraction of GPS signals is divided into two separate problems i) The *ionospheric* refraction, and ii) The *tropospheric* refraction. In fact, the term 'tropospheric refraction' is incorrect, because the troposphere is only one layer of the non-ionized part of the atmosphere, although, because of its highest density of neutral particles, the troposphere dominantly contributes to the neutral non-dispersive atmospheric refraction. Also the term 'ionospheric refraction' is wrong, since it also contains refraction due to charged particles in the protonosphere. Both terms are however common practice in satellite positioning literature and are also maintained in this thesis.

Decomposing the geometric distance as $\rho = \rho^{iono} + \rho^{tropo}$, the integral terms may be split into a part due to the ionosphere and a part due to the troposphere. For the refraction effects of phase and group of the signal we may consequently

write:

$$\begin{array}{rclcrcl} \vartheta_{\phi,j} & = & \vartheta^{iono}_{\phi,j} & + & \vartheta^{tropo}_{\phi,j}, & \qquad \kappa_{\phi,j} & = & \kappa^{iono}_{\phi,j} & + & \kappa^{tropo}_{\phi,j} \\ \vartheta_{g,j} & = & \vartheta^{iono}_{g,j} & + & \vartheta^{tropo}_{g,j}, & \qquad \kappa_{g,j} & = & \kappa^{iono}_{g,j} & + & \kappa^{tropo}_{g,j} \end{array} \tag{4.3}$$

Using this, the ionospheric and tropospheric excess path lengths, each consisting of a propagation and bending effect, read for the phase respectively group of the wave:

$$\begin{array}{rclcrcl} \imath_{\phi,j} & = & \vartheta^{iono}_{\phi,j} & + & \kappa^{iono}_{\phi,j}, & \qquad \nu_{\phi,j} & = & \vartheta^{tropo}_{\phi,j} & + & \kappa^{tropo}_{\phi,j} \\ \imath_{g,j} & = & \vartheta^{iono}_{g,j} & + & \kappa^{iono}_{g,j}, & \qquad \nu_{g,j} & = & \vartheta^{tropo}_{g,j} & + & \kappa^{tropo}_{g,j} \end{array} \tag{4.4}$$

where:

$\imath_{\phi,j}$: ionospheric phase effect [m]
$\imath_{\phi,g}$: ionospheric group effect [m]
$\nu_{\phi,j}$: tropospheric phase effect [m]
$\nu_{\phi,g}$: tropospheric group effect [m]

So the atmospheric errors for the GPS phase and code observations at frequency j, denoted as $\delta a_{,j}$ and $da_{,j}$ (see Chap. 2), may be decomposed into an ionospheric and tropospheric component:

$$\boxed{\begin{array}{rcll} \delta a_{,j} & = & \imath_{\phi,j} + \nu_{\phi,j} & \text{(atmospheric phase error)} \\ da_{,j} & = & \imath_{g,j} + \nu_{g,j} & \text{(atmospheric code error)} \end{array}} \tag{4.5}$$

4.3.3 Tropospheric refraction effects

To evaluate the geometric effects of *tropospheric refraction*, the tropospheric refractive index is needed. In contrast to the ionosphere, in the non-ionized troposphere the velocity of the phase and group of an EM-wave are exactly equal, and also independent of the frequency. Hence, using Eq. (4.1), the following applies to the tropospheric phase and group refractive index:

$$v^{tropo}_{g,j} = v^{tropo}_{\phi,j} \equiv v^{tropo} \quad \Rightarrow \quad n^{tropo}_{g,j} = n^{tropo}_{\phi,j} \equiv n^{tropo} \tag{4.6}$$

Since the tropospheric refractive index is always *larger* than 1, from now on we will refer to the excess path length of the signal as the *tropospheric delay*. This tropospheric delay is equal for both GPS phase and code observations on all frequencies:

$$\boxed{\nu_{g,j} = \nu_{\phi,j} \equiv \nu} \tag{4.7}$$

The tropospheric delay is not constant, but variable in both space and time. The size of the tropospheric delay may range up to 10 m, for signals from satellites at low elevations. More details on the tropospheric refraction effects can be found in e.g. [Kleijer, 2001].

4.4 Ionospheric refraction effects

In this section the effects of *ionospheric refraction* are described in detail. In contrast to its tropospheric counterpart, the ionospheric refractive index is *not* equal for both phase and group and also is different per frequency. Despite this, the refractive index for the ionosphere is already known for a long time and for GPS applications it may be approximated. With this approximated refractive index, rather simple expressions for the ionospheric effects can be derived.

4.4.1 The inhomogeneous, anisotropic and dispersive ionosphere

Whereas in free space the refractive index is 1 everywhere for all EM-waves, the ionospheric refractive index is unfortunately not a constant. This is because the ionosphere is an *inhomogeneous*, *anisotropic* and *dispersive* medium. In the following these three properties are explained.

Inhomogeneity

Since within the ionosphere a number of horizontal layers with a varying density of charged particles can be distinguished (see Sect. 4.2.3), the ionosphere is an *inhomogeneous* medium. As a consequence, the ionospheric refractive index varies significantly in the spatial domain.

Anisotropy

Besides the spatial variation, the refractive index also depends on the *propagation direction* of the wave. This phenomenon is called *anisotropy*. This also explains why the GPS waves are *circularly* polarized (see Chap. 2). With a *linear* polarization, the free electrons in the ionosphere would interact with the wave and cause its polarization to rotate. This phenomenon is known as *Faraday rotation*, see e.g. [Hall et al., 1996]. The intensity of this rotation depends on the electron density and since this is highly variable, this would result in a highly fluctuating signal at reception. However, the Faraday rotation does not or hardly affect the intensity of the received signal when the waves are circularly polarized.

There is also another effect. Under influence of the geomagnetic field a GPS wave is split up into *two* approximately parallel wavefronts, which each have an opposite (circular) polarization. One wave, the *ordinary* wave, has a right-handed polarization, but the other one, the *extraordinary* wave has a left-handed polarization. Both waves show a small difference in propagation velocity and consequently in refractive index. This effect is known as *double refraction* or *birefringence*. Despite this double refraction, fortunately just one wave (the ordinary wave) needs to be considered in case of GPS, since at reception within the GPS antenna the extraordinary wave is not relevant, since it contains less than 0.35% of the power (for L1) [Bassiri and Hajj, 1993].

Dispersion

Besides inhomogeneous and anisotropic, the ionosphere is a *dispersive* medium, which means that the phase velocity of a wave is a function of its frequency. Besides, the velocity of the modulation of a wave (the group velocity) is different from the phase velocity. The relation between the group velocity v_g and the phase velocity v_ϕ is given by the *Rayleigh equation*, see e.g. [Hall et al., 1996]. Using this equation, the phase and group refractive index can be connected as well:

$$v_{g,j} \;=\; v_{\phi,j} \;+\; f_j \frac{\partial v_{\phi,j}}{\partial f_j} \quad \Rightarrow \quad n_{g,j} \;=\; n_{\phi,j} \;+\; f_j \frac{\partial n_{\phi,j}}{\partial f_j} \tag{4.8}$$

4.4.2 Refractive index for the ionosphere

The Appleton-Hartree formula

The phase refractive index for the ionosphere is given by the complex *Appleton-Hartree* formula. Ignoring absorption effects due to collisions between the electrons, this formula reads, e.g. [Giraud and Petit, 1978]:

$$n^{iono}_{\phi,j,\pm} \;=\; \sqrt{1 - \frac{X_j}{1 - \frac{Y^2_{T,j}}{2(1-X_j)} \pm \sqrt{\frac{Y^4_{T,j}}{4(1-X_j)^2} + Y^2_{L,j}}}} \tag{4.9}$$

where $X_j = f_p^2/f_j^2$ and $Y_{T,j}$ and $Y_{L,j}$ the transversal respectively longitudinal components of $Y_j = f_g/f_j$. So $Y_{T,j} = Y_j|\sin\theta|$ and $Y_{L,j} = Y_j|\cos\theta|$, where θ is the angle between Y_j and $Y_{L,j}$.

The frequency f_p in the expression for X_j is known as the *electron plasma frequency*, which is the natural frequency of oscillation for a slab of neutral plasma, after the electrons have been displaced from the ions and are able to move freely. It is computed as:

$$\boxed{f_p \;=\; \sqrt{AN_e}, \qquad \text{with } A \;=\; \frac{e^2}{4\pi^2 m_e \varepsilon_0} \;\approx\; 80.6 \text{ m}^3/\text{s}^2} \tag{4.10}$$

where N_e denotes the free electron density in m^{-3}. The value for A in Eq. (4.10) is obtained using the natural constants $e = 1.60218 \cdot 10^{-19}$ Coulomb for the electron charge, $m_e = 9.10939 \cdot 10^{-31}$ kg for the electron mass, and $\varepsilon_0 = 8.85419 \cdot 10^{-12}$ Farad/meter for the *permittivity* of free space.

The frequency f_g is known as the *electron gyro frequency*, which is defined as the natural frequency at which the free electrons circle around the geomagnetic field lines. It is computed as:

$$\boxed{f_g \;=\; \frac{e}{2\pi m_e} \|B\|} \tag{4.11}$$

where $\|B\|$ denotes the length of the *geomagnetic induction* vector B (unit: Tesla = Volt second/meter^2). This induction vector is one-by-one related to the geomagnetic field vector, denoted as H (unit: Ampere/meter): $B = \mu_0 H$. Here $\mu_0 = 4\pi \cdot 10^{-7}$ Henry/meter denotes the *permeability* of free space.

Note that the inhomogeneous, anisotropic and dispersive properties of the ionosphere are all present in the Appleton-Hartree formula. The *inhomogeneity* of the ionosphere is reflected in the free electron density N_e, which is not a constant, but a function of place and time. Moreover, the *dispersive* ionosphere can be recognized in the dependence on the frequency of the wave. The *anisotropic* ionosphere is expressed in the terms depending on B. The *double-refraction* is reflected by the $\pm$ sign, which means that either a plus or minus sign can be used, depending on the polarization of the wave: A "+" corresponds to the left-handed circularly polarized wave (the extraordinary wave) and a "-" to the right-handed circularly polarized wave (the ordinary wave). Since for GPS only the ordinary wave is significant, from now on only the refractive index using the *minus sign* is considered.

Approximating the ionospheric refractive index

The electron plasma and gyro frequencies in Eq. (4.10) respectively Eq. (4.11) cannot take on any value. For *mid-latitude* regions they are namely bounded as $\|B\| < \|B\|_{\max} = 5 \cdot 10^{-5}$ Tesla and $N_e < N_{e,\max} = 10^{12}$ m^{-3}. Using these maximum values, the electron plasma and gyro frequencies are upper bounded as:

$$f_{p,\max} = 9 \text{ MHz}, \quad f_{g,\max} = 1.4 \text{ MHz} \tag{4.12}$$

Note that these maximum frequencies are both much smaller than the GPS signal frequencies f_j. Therefore, the scalars X_j and Y_j in the Appleton-Hartree formula are bounded as:

$$X_j < 3 \cdot 10^{-5}, \quad Y_j < 1 \cdot 10^{-3} \tag{4.13}$$

Using this, it is allowed to expand the ionospheric phase refractive index into the following Taylor-series of X_j and Y_j:

$$n_{\phi,j}^{iono} \doteq 1 - \frac{1}{2}X_j - \frac{1}{2}|\cos\theta|X_jY_j - \frac{1}{8}X_j^2 + R_3 \tag{4.14}$$

where R_3 denotes the remainder term. Using the bounds in Eq. (4.13) the magnitude or the terms in the Taylor-series can be assessed as $\frac{1}{2}X_j \sim 10^{-5}$, $\frac{1}{2}|\cos\theta|X_jY_j \sim 10^{-8}$, and $\frac{1}{8}X_j^2 \sim 10^{-10}$. From this, it follows that the size of the Taylor remainder R_3 lies in the order which is smaller than 10^{-10}. Since this term only contributes to the phase observations at *sub-mm* level [Brunner and Gu, 1991], while the GPS phase measurements themselves have an accuracy at mm level, it is allowed to safely neglect the Taylor-remainder term.

Using the above simplifications, the ionospheric *group* refractive index can be

computed using Eq. (4.8). Taking the frequency derivative of Eq. (4.14) and multiplying this with the frequency yields:

$$f_j \frac{\partial n^{iono}_{\phi,j}}{\partial f_j} = \frac{f_p^2}{f_j^2} + \frac{3}{2}\frac{f_p^2 f_g |\cos\theta|}{f_j^3} + \frac{4}{8}\frac{f_p^4}{f_j^4} \tag{4.15}$$

Addition of this term to the expression in Eq. (4.14) results in the expression for the group refractive index. Summarizing, both ionospheric refractive indices can be approximated as:

$$\boxed{\begin{array}{rcl} n^{iono}_{\phi,j} &=& 1 - \frac{1}{2}\frac{f_p^2}{f_j^2} - \frac{1}{2}\frac{f_p^2 f_g|\cos\theta|}{f_j^3} - \frac{1}{8}\frac{f_p^4}{f_j^4} \\ n^{iono}_{g,j} &=& 1 + \frac{1}{2}\frac{f_p^2}{f_j^2} + \frac{f_p^2 f_g|\cos\theta|}{f^3} + \frac{3}{8}\frac{f_p^4}{f_j^4} \end{array}} \tag{4.16}$$

From Eq. (4.16) it follows that the phase refractive index is always *smaller* than 1, while the group refractive index is *larger* than 1. This means that in the ionosphere the phase of the wave is *advanced*, while at the same time its group is *delayed*.

4.4.3 Ionospheric first-, higher-order and bending effects

Having derived the approximate ionospheric refractive indices in the previous subsection, they are inserted into Eq. (4.2) to evaluate the ionospheric effects for GPS observations. The phase and group *propagation* effects then read:

$$\begin{array}{rcl} \vartheta^{iono}_{\phi,j} &=& -\frac{1}{2f_j^2}\int f_p^2 d\rho - \frac{1}{2f_j^3}\int f_p^2 f_g|\cos\theta|d\rho - \frac{1}{8f_j^4}\int f_p^4 d\rho \\ \vartheta^{iono}_{g,j} &=& \frac{1}{2f_j^2}\int f_p^2 d\rho + \frac{1}{f_j^3}\int f_p^2 f_g|\cos\theta|d\rho + \frac{3}{8f_j^4}\int f_p^4 d\rho \end{array} \tag{4.17}$$

Note that the electron plasma frequency f_p and electro gyro frequency f_g are not constant along the path and therefore remain within the integrals. Eq. (4.17) shows that both the ionospheric phase advance and group delay can be expanded as a function of the *same* three effects. These three effects are better known as the ionospheric *first-*, *second-* and *third-order* delays, denoted as $\imath^{(1)}_{g,j}$, $\imath^{(2)}_{g,j}$ and $\imath^{(3)}_{g,j}$ respectively:

$$\begin{array}{rcl} \imath^{(1)}_{g,j} \doteq \frac{1}{2f_j^2}\int f_p^2 d\rho &=& \frac{A}{2f_j^2}\int N_e d\rho \\ \imath^{(2)}_{g,j} \doteq \frac{1}{f_j^3}\int f_p^2 f_g|\cos\theta|d\rho &=& \frac{eA}{f_j^3 2\pi m_e}\int \|B\||\cos\theta|N_e d\rho \\ \imath^{(3)}_{g,j} \doteq \frac{3}{8f_j^4}\int f_p^4 d\rho &=& \frac{3A^2}{8f_j^4}\int N_e^2 d\rho \end{array} \tag{4.18}$$

The second- and third-order delays are often referred to as the ionospheric *higher-order* terms. Adding the effects of signal *bending*, the ionospheric *phase advance*, denoted by $\imath_{\phi,j}$, and the ionospheric *group delay*, denoted by $\imath_{g,j}$, can be written as:

$$\boxed{\begin{array}{rcl} \imath_{\phi,j} &=& -\imath^{(1)}_{g,j} - \frac{1}{2}\imath^{(2)}_{g,j} - \frac{1}{3}\imath^{(3)}_{g,j} + \kappa^{iono}_{\phi,j} \\ \imath_{g,j} &=& \imath^{(1)}_{g,j} + \imath^{(2)}_{g,j} + \imath^{(3)}_{g,j} + \kappa^{iono}_{g,j} \end{array}} \tag{4.19}$$

From these expressions it can be seen that the first-order phase effect is equal but opposite of sign to the first-order group effect. The second- and third-order phase effects are also opposite of sign to their corresponding group counterparts, but they do not have the same magnitude: The second-order phase effect is half the second-order group effect, while the third-order phase effect is one third of the third-order group effect.

4.4.4 The first-order delay and the Total Electron Content

From Eq. (4.18) it can be seen that the first-order ionospheric delay is a function of the the integral term $\int N_e d\rho$. This term is well known as the *Total Electron Content* (TEC, unit m^{-2}) along the geometric line from receiver to satellite. TEC is often expressed in $TECU$ (TEC-unit) with $1\ TECU = 10^{16}$ electrons/m^2. Using this TEC, the first-order delay may be rewritten as:

$$\boxed{\imath_{g,j}^{(1)} = \frac{A}{2f_j^2} TEC, \qquad \text{with } A \approx 80.6\ \mathrm{m}^3/\mathrm{s}^2} \tag{4.20}$$

It should be emphasized that the Total Electron Content is not a constant, but highly variable in space as well as in time. After all, it depends on the variable electron density. Moreover, it is important to realize that TEC strongly depends on the elevation of the satellite (receiver-satellite geometry), as with a lower elevation the signal path through the ionosphere gets longer.

4.5 A single-layer ionosphere approximation

The previous section showed that the geometric effect of ionospheric refraction can be written as a sum of components. Since these components are based on integrals over the geometric distance between receiver and satellite, they may differ considerably for satellites at different positions in the sky. For example, the range to a satellite with low elevation is much longer than for a satellite in the zenith of the receiver. In order to make an (rough) assessment of the ionospheric error components, it is beneficial to split the ionospheric error in a part which is in fact due to the receiver-satellite geometry and a part which is a "real" ionospheric effect.

4.5.1 Ionospheric mapping function

For this purpose, the *slant* ionospheric error is *mapped* to a *vertical* or zenith effect. In practice the so-called *cosecant* ionospheric mapping function is usually taken, see e.g. [Georgiadou and Kleusberg, 1988]. For the mapping the ionosphere is assumed to be an *infinitesimal thin* single layer at a fixed altitude from the Earth. All free electrons in the ionosphere are assumed to be concentrated in this single layer.

By assuming this single layer the mapping of the slant to the vertical (and vice versa) is very simple: It is based on a fixed mapping point, the so-called *ionospheric*

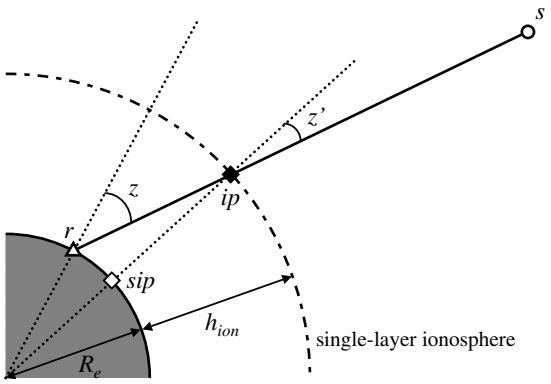

Fig. 4.10. Geometry of the single-layer ionosphere

(piercing) point, defined as the intersection of the receiver-satellite line-of-sight with the ionospheric layer (the point *ip* in Fig. 4.10). The point *sip* in the figure, which is located on the Earth's surface just below the ionospheric point, is referred to as the *sub-ionospheric* point. Mathematically, the mapping can be given as follows:

$$\boxed{\imath_{,j} \;=\; (1/\cos z')\imath_{v,j}, \qquad z' \;=\; \arcsin\left(\frac{R_e}{R_e+h_{ion}}\sin z\right)} \tag{4.21}$$

where:

$\imath_{v,j}$	:	vertical ionospheric effect above the sub-ionospheric point
$\imath_{,j}$	:	slant ionospheric effect (phase advance or group delay)
z	:	zenith angle at receiver location
z'	:	zenith angle at ionospheric point
R_e	:	radius of the Earth (often fixed at 6371 km)
h_{ion}	:	height of the ionospheric layer above the Earth's surface

Note that the geodetic coordinates of the (sub-) ionospheric point can be computed from the receiver coordinates (φ_r, λ_r) and the zenith- and azimuth angles (z, a) to the satellite as follows:

$$\begin{aligned} \varphi' &= \arcsin\left[\sin\varphi_r\cos(z-z') + \cos\varphi_r\sin(z-z')\cos a\right] \\ \lambda' &= \lambda_r + \arcsin\left[\frac{\sin(z-z')\sin a}{\cos\varphi_r}\right] \end{aligned} \tag{4.22}$$

Instead of the ionospheric delay, the *Vertical* Total Electron Content ($VTEC$) can be mapped to the (slant) TEC as:

$$TEC \;=\; (1/\cos z')VTEC \tag{4.23}$$

As example, in Fig. 4.11 the mean *global* $VTEC$ is plotted for the period January 1995 to April 2002. From more than 100 globally distributed IGS stations the Center for Orbit Determination in Europe (CODE) computed every two hours $VTEC$ values [Schaer et al., 1998]. The figure clearly shows the difference in the mean $VTEC$ for solar minimum and solar maximum years. In general, the mean $VTEC$ is bounded as follows: $5 \leq VTEC \leq 60$ TECU.

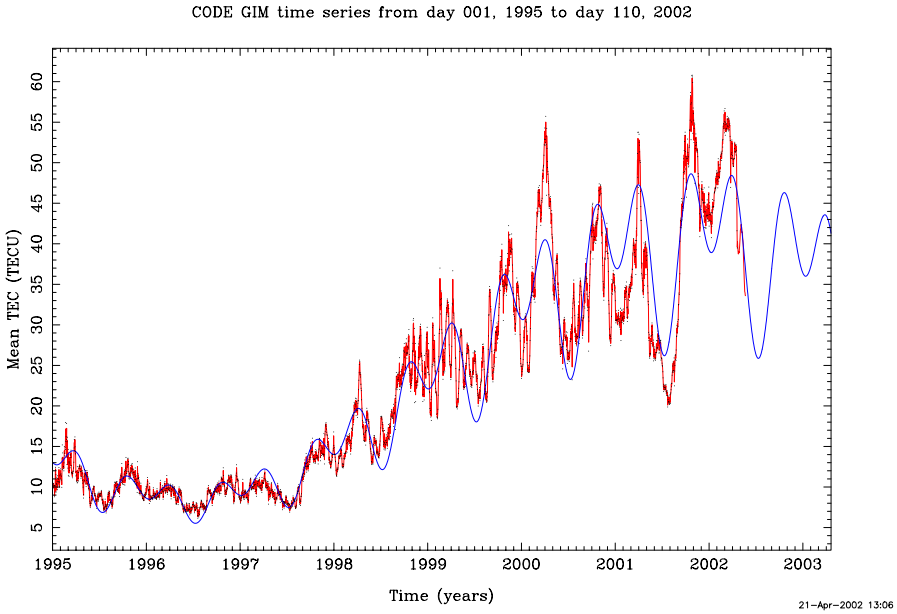

Fig. 4.11. Two-hourly estimated and predicted mean $VTEC$ values from January 1995 to April 2002 (graph courtesy of CODE, Switzerland)

4.5.2 Sensitivity to the height of the ionospheric layer

The cosecant mapping function depends on the height in which all free electrons are assumed to be concentrated, h_{ion}. Since this height is not exactly known, it is often assumed at 350 km. In Fig. 4.12 for three heights of the ionospheric layer, 350, 400 and 500 km the mapping factor $1/\cos z'$ is plotted against the zenith angle z. The figure shows that only for large zenith angles (above about 70°), the differences between the three choices become apparent in the mapping factor. From the figure note that for a satellite at the horizon, the ionospheric effect is about three times as large as for a satellite at the zenith. So when the $VTEC$ is 60 TECU, the ionospheric effect on L1 in the zenith is about 10 m, while at the horizon it is about 30 m.

In Fig. 4.13 for the three different heights of the ionospheric layer the difference in latitude of the receiver and the sub-ionospheric point is plotted against the

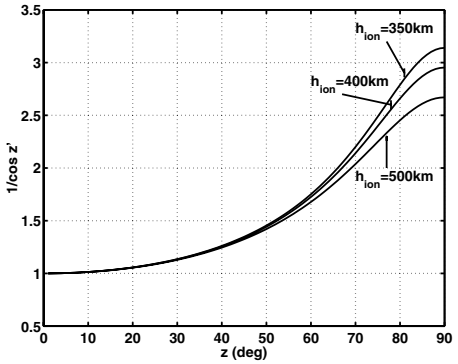

Fig. 4.12. Mapping factor as function of the zenith angle for three heights of the ionospheric layer (taken from [Van der Marel, 1993])

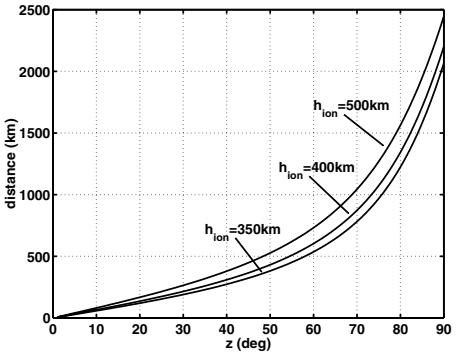

Fig. 4.13. Distance from receiver to sub-ionospheric point as function of the zenith angle for three heights of the ionospheric layer (taken from [Van der Marel, 1993])

zenith angle. In this figure it can be seen that the sub-ionospheric point can be as far away as 2500 km from the receiver. The ionospheric conditions over there can be completely different than in the zenith of the receiver.

4.6 Approximating the higher-order/bending effects

In this section the ionospheric single-layer approximation is used to approximate the expressions for the higher-order and bending effects which are given in Eq. (4.18). These approximations are based on [Bassiri and Hajj, 1993]. Next, these approximations are used to quantify the ionospheric effects for a worst-case scenario.

4.6.1 Approximating the ionospheric second-order delay

In Eq. (4.18) the second-order group delay was obtained as:

$$\imath_{g,j}^{(2)} \;=\; \frac{eA}{f_j^3 2\pi m_e} \int \|B\| |\cos\theta| N_e d\rho \tag{4.24}$$

Using the infinitesimal thin single-layer representation of the ionosphere, it may be assumed that the product $\|B\||\cos\theta|$ is *constant* along the signal path. Consequently, it is allowed to take it *outside* the integral:

$$\boxed{\imath_{g,j}^{(2)} \;\approx\; \frac{eA}{f_j^3 2\pi m_e} \|B\| |\cos\theta| \int N_e d\rho \;=\; \frac{eA}{f_j^3 2\pi m_e} \|B\| |\cos\theta| \; TEC} \tag{4.25}$$

So in the approximation, the second-order delay can, like the first-order delay, be written as a function of TEC. To assess the effect, it is also necessary to

evaluate the product $\|B\||\cos\theta|$. For this purpose, this product is recognized as the *inner product* of the vector B of geomagnetic induction and the unit vector $\jmath$ of propagation direction of the signal, at the height of the ionospheric layer (see Fig. 4.14):

$$\boxed{\|B\| \, |\cos\theta| \;=\; \|B\| \, \|\jmath\| \, |\cos\theta| \;=\; B^T \jmath} \tag{4.26}$$

Since $\jmath$ is a unit vector, it holds that $\|\jmath\| = 1$. Note that the direction of this propagation vector is exactly opposite to the unit receiver-satellite vector as introduced in Chap. 2: $\jmath = -u$.

The inner product $B^T\jmath$ can be evaluated much easier in a *geomagnetic reference frame*, rather than the usual geodetic frame. For this purpose a *dipole approximation* of the geomagnetic field is used.

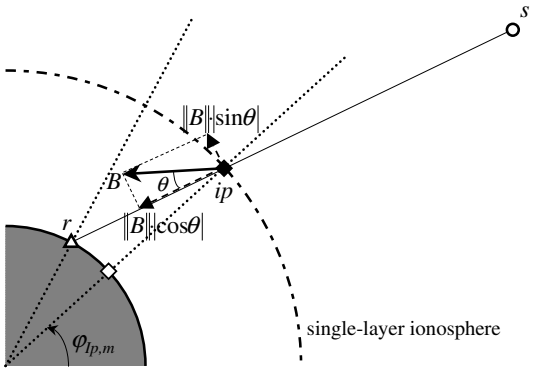

Fig. 4.14. Single-layer ionosphere and geomagnetic induction vector B

A dipole geomagnetic field approximation

A dipole approximation of the geomagnetic field coincides for about 75% with the true geomagnetic field [Bassiri and Hajj, 1993]. The dipole geomagnetic field is assumed to be Earth-centered and the z-axis of the geomagnetic reference frame intersects the Earth in the geodetic reference frame at $(\varphi_0, \lambda_0) = (78.5^{\circ}\text{ N}, 291^{\circ}\text{ E})$, the geomagnetic North-pole, and at $(78.5^{\circ}\text{ S}, 111^{\circ}\text{ E})$, the geomagnetic South-pole. See Fig. 4.15 for the orientation of the geomagnetic frame with respect to the geodetic frame. Using the geodetic coordinates of the geomagnetic North-pole, the transformation from geodetic coordinates (x, y, z) to geomagnetic coordinates

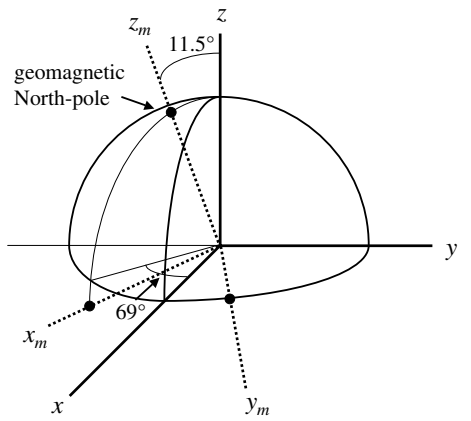

Fig. 4.15. Orientation of the geomagnetic frame with respect to the geodetic frame

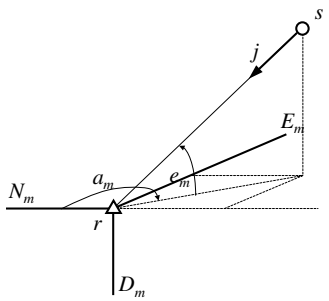

Fig. 4.16. Geomagnetic local reference frame

(x_m, y_m, z_m) then reads:

$$\begin{bmatrix} x_m \\ y_m \\ z_m \end{bmatrix} = \begin{bmatrix} \sin\varphi_0 \cos\lambda_0 & \sin\varphi_0 \sin\lambda_0 & -\cos\varphi_0 \\ -\sin\lambda_0 & \cos\lambda_0 & 0 \\ \cos\varphi_0 \cos\lambda_0 & \cos\varphi_0 \sin\lambda_0 & \sin\varphi_0 \end{bmatrix} \begin{bmatrix} x \\ y \\ z \end{bmatrix} \tag{4.27}$$

Evaluation of the inner product $B^T \jmath$

To evaluate the inner product $B^T \jmath$ it is easier to use a local *North-East-Down* system originated at the receiver (see Fig. 4.16). The components of the vector of propagation $\jmath$ in this local system read:

$$\jmath = \begin{bmatrix} -\sin z_m \cos a_m \\ -\sin z_m \sin a_m \\ \cos z_m \end{bmatrix} \tag{4.28}$$

with a_m the azimuth and z_m the zenith angle of the satellite in the geomagnetic reference frame. The components of the geomagnetic induction vector B at a height h_{ion} above the Earth's surface in this local frame can be given as [Giraud and Petit, 1978]:

$$B = \begin{bmatrix} \cos\varphi'_m \\ 0 \\ 2\sin\varphi'_m \end{bmatrix} \left(\frac{R_e}{R_e + h_{ion}} \right)^3 B_{eq} \tag{4.29}$$

where φ'_m is the geomagnetic latitude of the ionospheric point and B_{eq} the magnitude of the geomagnetic induction at the geomagnetic equator (at the surface).

Choosing the height of the ionospheric layer at $h_{ion} = 350$ km and the magnitude of the geomagnetic induction at the equator at $B_{eq} = 3.12 \cdot 10^{-5}$ T, the magnitude of the geomagnetic induction ranges from a minimum value of $2.6 \cdot 10^{-5}$ T in the ionospheric point above the geomagnetic equator to a maximum value of $5.2 \cdot 10^{-5}$ T above the geomagnetic North-pole, which is twice the value at the equator, see Fig. 4.17.

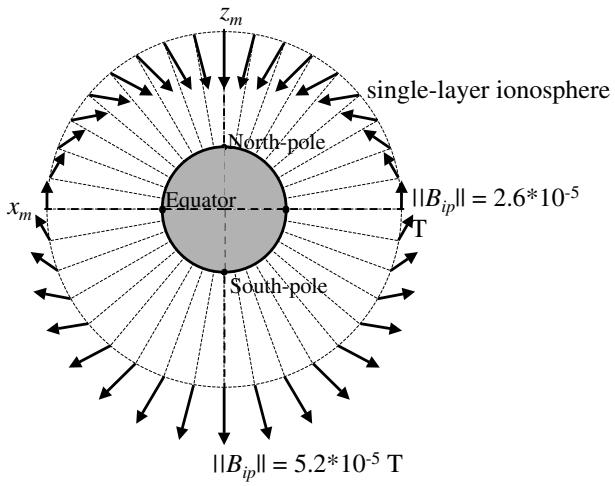

Fig. 4.17. Geomagnetic induction vectors in (x_m, z_m) plane, plotted at height of ionospheric points (Note that the height of the ionospheric layer is not to scale!)

Using the above decompositions, the inner product of the vectors in Eq. (4.29) and Eq. (4.28) can be given as a function of the receiver and satellite position (through φ'_m, a_m and z_m) and assumptions about the height of the ionospheric layer and the geomagnetic induction at the equator:

$$B^T \jmath \;=\; |\cos\varphi'_m \sin z_m \cos a_m \;-\; 2\sin\varphi'_m \cos z_m| \left(\frac{R_e}{R_e + h_{ion}}\right)^3 B_{eq} \tag{4.30}$$

4.6.2 Approximating the ionospheric third-order delay

The third-order ionospheric delay was obtained in Eq. (4.18) as:

$$\imath_{,j}^{(3)} \;=\; \frac{3A^2}{8f_j^4} \int N_e^2 d\rho \tag{4.31}$$

Because of the quadratic term, this integral is difficult to evaluate. In [Hartmann and Leitinger, 1984] an approximation for the integral is found, leading to the

following approximation of the third-order delay:

$$\boxed{\iota_{,j}^{(3)} \approx \frac{3A^2}{8f_j^4}\eta\, N_{e,\max}\int N_e d\rho = \frac{3A^2}{8f_j^4}\eta N_{e,\max} TEC, \quad \text{with } \eta = 0.66} \tag{4.32}$$

So in the approximation the third-order delay can, like the first-order and second-order delay, also be written as a function of TEC. In addition, the third-order delay is a function of the maximum electron density $N_{e,\max}$ and a certain *shape factor* η, for which the constant value of 0.66 was taken from [Hartmann and Leitinger, 1984].

4.6.3 Approximating the ionospheric bending effect

To evaluate the ionospheric bending effect, in [Hartmann and Leitinger, 1984] the following approximation is given:

$$\kappa_{\phi,j}^{iono} = \int n_{\phi,j}^{iono} dl_{\phi,j} - \int n_{\phi,j}^{iono} d\rho \approx \frac{\tan^2 z'}{8\cos z'}\frac{A^2}{f_j^4} VTEC^2 \left(\frac{\eta N_{e,\max}}{VTEC} - \frac{1}{h}\right) \tag{4.33}$$

with h the height of the satellite above the Earth's surface. The shape factor η is the same as in the approximation of the third-order delay.

Since GPS satellites are at very high altitude (about 20,200 km), the term containing the satellite height ($1/h$) only contributes at *sub-mm* level to the total bending effect and may consequently be neglected. Rewriting Eq. (4.33) using TEC instead of $VTEC$, results in the following simplified approximation for the ionospheric bending effect:

$$\boxed{\kappa_{\phi,j}^{iono} \approx \frac{A^2}{8f_j^4}(\tan z')^2 \eta N_{e,\max} TEC} \tag{4.34}$$

Also the ionospheric bending effect can be approximated as a function of TEC. Besides, it depends on the maximum electron density and the same shape factor as the third-order delay.

4.6.4 Absolute ionospheric effects for GPS: An example

In the previous section it was shown that the ionospheric first-order effect and the approximated second-, third- and bending effects could all be written as functions of TEC. Since this TEC heavily depends on the satellite zenith angle, in this section the ionospheric first-order, higher-order and bending effects are evaluated function of the zenith angle from receiver to satellite, assuming a constant, *worst-case* value for the vertical TEC ($VTEC$). These effects are not only evaluated for the two existing L1 and L2 frequencies, but also for the future L5 frequency. For these three frequencies only the *phase* effects are computed, and their magnitude is plotted. To compute these effects, it is necessary to make some assumptions, which are summarized in Table 4.3.

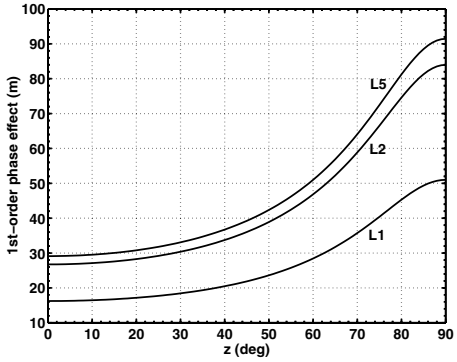

Fig. 4.18. Magnitude of the 1st-order phase effect

Figure 4.18 shows the magnitude of the *first-order* ionospheric phase effects. Using the extreme value for $VTEC$ the first-order effect on the L1 frequency ranges from 16 m in the zenith to about 50 m at the horizon. For L2 and the future L5 the effects are a factor 1.65 respectively 1.79 larger than for L1.

From Eq. (4.30) follows that the *second-order* phase effect does not only depend on the satellite's zenith angle, but also on its azimuth. Therefore in Fig. 4.19 for the location $(\varphi, \lambda) = (54°N,\ 5°E)$ in The Netherlands (mid-latitudes) the phase effect on L1 has been plotted as an *azimuth-zenith* diagram. In this diagram the contours of constant zenith angle are plotted as circles (conform a 'skyplot'). Note that to plot the figure azimuths in the *geomagnetic* reference frame are used. The figure shows that the second-order effect is *symmetric* in the North-South line. This property of symmetry is a consequence of the induction vector B, which does not have a component in the local East-West direction in the geomagnetic frame (see Eq. (4.29)). Besides, it can be seen that the second-order effect is close to zero for large zenith angles, but only when the azimuth is in the first or fourth quadrant. When the azimuth is about 180°, the second-order effect is however very large for satellites at large zenith angles.

Table 4.3. Some assumptions in the computations

value	remarks
$h_{ion} = 350$ km	Corresponds with peak electron density of F2 layer
$VTEC = 10^{18}$ m^{-2}	According to [Klobuchar and Doherty, 1998] a realistic maximum during solar max
$N_{e,\max} = 3 \cdot 10^{12}$ m^{-3}	Maximum taken from [Bassiri and Hajj, 1993]
$B_{eq} = 3.12 \cdot 10^{-5}$ T	Holds at the geomagnetic equator (at the surface)

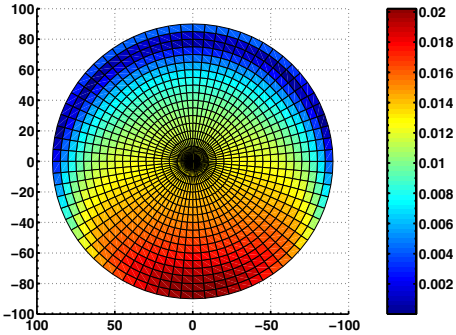

Fig. 4.19. Azimuth vs. zenith angle plot for 2nd-order phase effect on L1

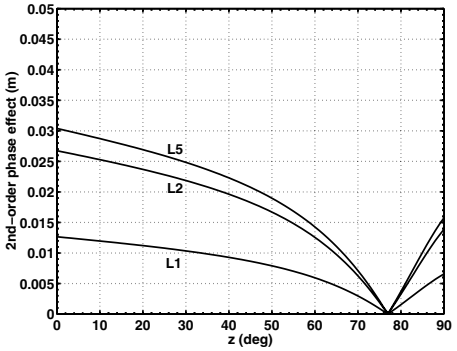

Fig. 4.20. Magnitude of the 2nd-order phase effect for $a_m = 0°$

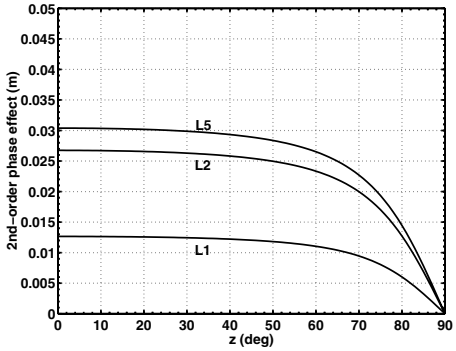

Fig. 4.21. Magnitude of the second-order phase effect for $a_m = 90°$ and $a_m = 270°$

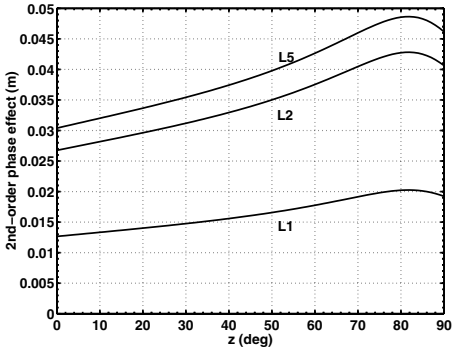

Fig. 4.22. Magnitude of the 2nd-order phase effect for $a_m = 180°$

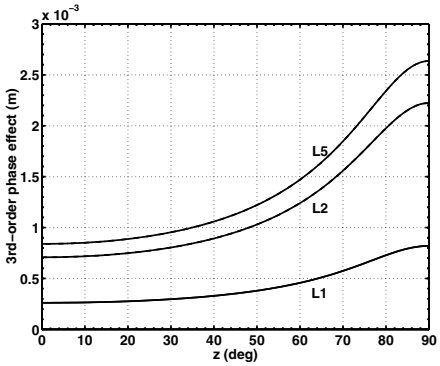

Fig. 4.23. Magnitude of the 3rd-order phase effect

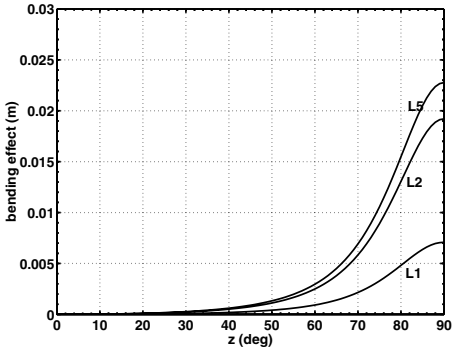

Fig. 4.24. Magnitude of the phase bending effect

This remarkable behavior of the second-order effect is shown in more detail in Figs. 4.20 – 4.22, in which for *fixed azimuths* the second-order effects are plotted as a function of the zenith angle. When the azimuth is fixed at 0°, the second-order effect slowly decreases to zero for a zenith angle of about 75°, but after that it increases again for an increasing zenith angle (see Fig. 4.20). This annihilation of the second-order effect for a zenith angle of 75° is caused by the vector of propagation, whose direction is apparently perpendicular to the vector of geomagnetic induction (at the height of the ionospheric layer), such that $\|B\| \, |\cos\theta| = 0$. When the azimuth is opposite, 180°, the second-order effect is *maximized* to about 5 cm for a satellite at a zenith of 80° (see Fig. 4.22). In that case the direction of the propagation vector is apparently *parallel* to the induction vector. For an azimuth of 90° the second-order effects are exactly the same as for an opposite azimuth of 270°, since the geomagnetic induction vector does not have a component in the East-direction (see Eq. (4.29)). In those cases the propagation vector for a satellite at the horizon (zenith is 90°) is exactly perpendicular to the induction vector (the second-order effect becomes zero). With respect to the different GPS frequencies, the second-order effect on L2 and L5 are a factor of about 2.11 respectively 2.40 larger than the effect on L1.

In Fig. 4.23 the *third-order* phase effect is plotted for the three frequencies. Like the first-order effect, this effect is monotone increasing as function of the zenith angle. The maximum third-order effect is about 3 mm for a satellite at the horizon, for the future L5 frequency. Finally, in Fig. 4.24 the phase *bending* effect is shown. This effect ranges from zero in the zenith to about 2.5 cm in the horizon for L5. For both the third-order and bending effects it holds that the effects on L2 and L5 are a factor of about 2.71 and 3.22 larger than the corresponding effects on the L1 frequency.

4.7 Relative ionospheric effects

In the previous section the ionospheric error was treated in absolute sense. In case of relative GPS applications, more important than the absolute ionospheric effects are the remaining effects after taking *double-differences* of them (see Chap. 2). In this section it is described how both ionospheric conditions and receiver-satellite geometry contribute to the relative ionospheric error. For this assessment again the *single-layer geometry* of the ionosphere (see Sect. 4.5) is used. Before discussing the double-difference ionospheric error, first the single-difference effect is treated.

4.7.1 Single-differenced ionospheric effects

Using the single-layer geometry, the absolute ionospheric effects of two GPS receivers (say 1 and 2) to the same satellite s, can be mapped to two different vertical delays at the height of the ionospheric layer. Using Eq. (4.21), the *single-differenced* (SD) ionospheric effect between these two receivers can be written as

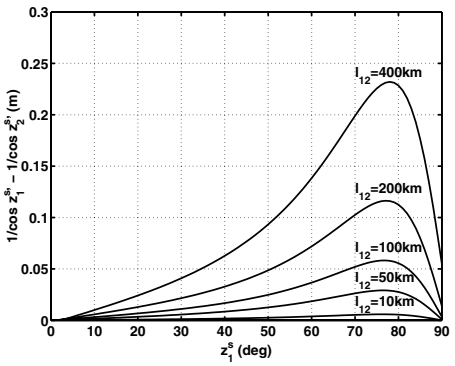

Fig. 4.25. Amplification of 1 m vertical delay into SD ionospheric effect, for different baseline lengths

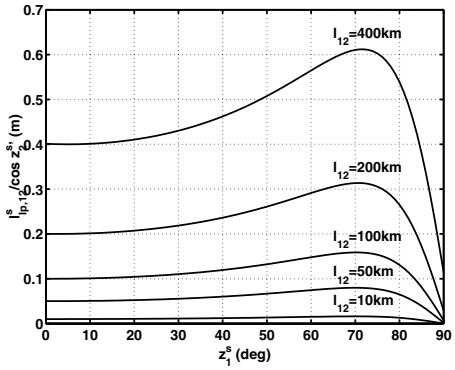

Fig. 4.26. Amplification of 1 mm/km horizontal gradient into SD ionospheric effect, for different baseline lengths

follows:

$$\boxed{\imath_{12}^s \;=\; \imath_2^s \;-\; \imath_1^s \;=\; \underbrace{-(1/\cos z_1^{s'} - 1/\cos z_2^{s'})\imath_{v,1}^s}_{\text{vertical delay effect}} \;+\; \underbrace{1/\cos z_2^{s'}\left(\imath_{v,2}^s - \imath_{v,1}^s\right)}_{\text{hor. gradient effect}}} \quad (4.35)$$

Note that in this equation we have neither used the subscript ϕ or g for phase or code, nor the subscript j for frequency, since the single-difference above can be applied for each type of ionospheric effect. Instead, we use the receiver indices 1 and 2 and the satellite index s. From Eq. (4.35) it follows that the SD ionospheric effect can be decomposed into a part that depends on the absolute vertical delay at the ionospheric layer (the *vertical delay* effect) and a part depending on the relative vertical delay between to the two receivers (the *horizontal gradient* effect). In the following both effects are analyzed separately as function of the satellite's zenith angle for different baseline lengths between the receivers.

Vertical delay effect

Figure 4.25 shows the amplification of 1 m absolute ionospheric delay into the SD delay for several lengths of the baseline (from 10 to 400 km). It can be seen that if the satellite is in the zenith, the absolute vertical delay is almost completely cancelled out in the SD delay. With a zenith angle of about 75° there is a maximal amplification into the SD effect: About 0.6 mm per km baseline length. Thus for a vertical delay of 10 m this is 6 mm/km. This effect seems to be confirmed by [Beutler et al., 1988].

Horizontal gradient effect

Since the ionosphere is a inhomogeneous medium, horizontal gradients are usually present. They may arise in north-south direction due to the high electron content

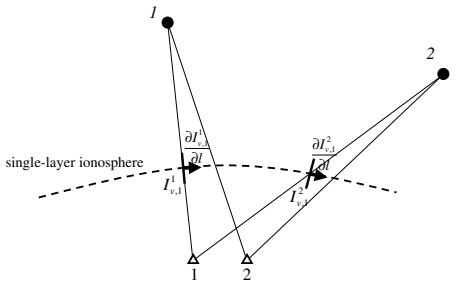

Fig. 4.27. Case A: One satellite in zenith $z_1^1 = 0°$, other at 15° elevation, $z_1^2 \approx 75°$

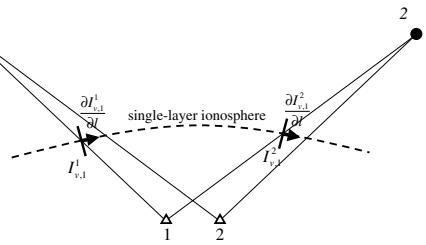

Fig. 4.28. Case B: Both satellites at 15° elevation: $z_2^1 = 75°$, $z_1^2 \approx 75°$

of the equatorial region and the lower content in the polar regions, but they can also be a result of TIDs (see Section 4.2.3). Moreover, the diurnal variation of the electron content causes horizontal gradients in east-west direction. The impact of horizontal gradients is given in Fig. 4.26. In this figure the amplification factor for a gradient of 1 mm/km into the SD delay is plotted for several baseline lengths. Use is made of the following equation [Van der Marel, 1993]:

$$\imath_{v,2}^s - \imath_{v,1}^s \;=\; 10^{-3}\;\frac{\partial \imath_{v,1}^s}{\partial l} l_{12}^s \tag{4.36}$$

where $\frac{\partial \imath_{v,1}^s}{\partial l}$ denotes the horizontal gradient [mm/km], and l_{12}^s the distance between the ionospheric points [km]. The figure shows that for a zenith angle of about 70° a gradient of 1 mm/km is maximally amplified: About 1.6 mm per km baseline length. For a gradient of 10 mm/km this is 16 mm per km baseline.

4.7.2 Double-differenced ionospheric effects

As mentioned, in relative GPS applications the double-differenced (DD) ionospheric effect is crucial, which is formed by two SD effects. The manner in which the DD ionospheric effect is influenced by vertical delay and horizontal gradients, depends on the zenith angles at which the two satellites involved in a double-difference are tracked. To get insight in this, in this subsection for two double-differences the impact of vertical delay and gradients is simulated. In Figs. 4.27 and 4.28 their respective geometries are shown. The double-difference geometry as depicted in Fig. 4.27 is referred to as Case A, and in this case the first satellite is in the zenith of receiver 1, while the second satellite is at the 75° zenith angle of this receiver. In Case B both satellites in the double-difference are at 75° zenith angle. The reason for choosing this 75° is that for this zenith angle the impact of vertical delay and gradients are maximized in the single-difference (see Figs. 4.25 and 4.26). To analyze a limited number of double-differences, it is assumed that all the vertical delays corresponding to receiver 1 in Figs. 4.27 and 4.28 are *equal*, i.e. $\imath_{v,1}^1 = \imath_{v,1}^2 \equiv \imath_v$. Besides, also the size of the horizontal gradients at the ionospheric

layer corresponding to receiver 1 are equally assumed: $\frac{\partial \imath^1_{v,1}}{\partial l} = \frac{\partial \imath^2_{v,1}}{\partial l} \equiv \frac{\partial \imath_v}{\partial l}$. Using this, for the *single-difference* effects in both figures the following expressions can be set up:

$$\begin{aligned} \imath^1_{12} &= 10^{-3}\left[a_1 \imath_v + b_1 \tfrac{\partial \imath_v}{\partial l}\right] l_{12} \\ \imath^2_{12} &= 10^{-3}\left[a_2 \imath_v + b_2 \tfrac{\partial \imath_v}{\partial l}\right] l_{12} \end{aligned} \tag{4.37}$$

where $\imath^1_{12}$ and $\imath^1_{12}$ denote the SD ionospheric effects [m], $\imath_v$ denotes the vertical delay [m], $\frac{\partial \imath_v}{\partial l}$ the horizontal gradient [mm/km], and l_{12} denotes the baseline length [km] between the two receivers. The factors a_1 and a_2 depend on how the vertical delay is amplified into the SD ionospheric effect, and can be assessed using Fig. 4.25. For example, for the single-difference of satellite 1 in Case A $a_1 = 0$ since the satellite is in the zenith, and for satellite 2 the factor is about $a_2 = 240/400 = 0.6$, since the satellite has a zenith angle of 75°. The factors b_1 and b_2 for the horizontal gradients are determined using Fig. 4.26. In Case A the factor $b_1 = 400/400 = 1$ holds for the satellite in the zenith, and $b_2 = 600/400 = 1.5$ for the satellite at 75° zenith angle. Note that the actual *sign* of the a_1 and a_2 values may differ, it can be positive or negative, depending on the geometry of the double difference.

Table 4.4. Simulated DD ionospheric effects on L1, for $\imath_v = 5$ m and $l_{12} = 10$ km

case	a_1	a_2	b_1	b_2	$\imath^{12}_{12}$ [cm] $\frac{\partial \imath_v}{\partial l}$ = 0 mm/km	$\imath^{12}_{12}$ [cm] $\frac{\partial \imath_v}{\partial l}$ = 1 mm/km	$\imath^{12}_{12}$ [cm] $\frac{\partial \imath_v}{\partial l}$ = 10 mm/km
A	0.0	-0.6	+1.0	+1.5	-3.0	-2.5	+ 2.0
			+1.0	-1.5	-3.0	-5.5	-28.0
			-1.0	-1.5	-3.0	-3.5	- 8.0
			-1.0	+1.5	-3.0	-0.5	+22.0
B	+0.6	-0.6	+1.5	+1.5	-6.0	-6.0	- 6.0
			+1.5	-1.5	-6.0	-9.0	-36.0
			-1.5	-1.5	-6.0	-6.0	- 6.0
			-1.5	+1.5	-6.0	-3.0	+24.0

The DD ionospheric effect, the difference of the two SD ionospheric effects in Eq. (4.37), now reads:

$$\imath^{12}_{12} = \imath^2_{12} - \imath^1_{12} = 10^{-3}\left[(a_2 - a_1)\imath_v + (b_2 - b_1)\frac{\partial \imath_v}{\partial l}\right] l_{12} \tag{4.38}$$

In Table 4.4 for Cases A and B the simulated DD ionospheric effects using Eq. (4.38) are given. The effects have been computed for a baseline with length $l_{12} = 10$ km, and using different pairs of values for b_1 and b_2. Per case, either A or B, the size for both parameters remains constant, but the sign may vary. Using this, the effect of gradients with a same or different direction can be investigated. For the size of the gradients, three scenarios are taken, $\frac{\partial \imath_v}{\partial l} = 0$ mm/km (no gradients at

all), 1 mm/km (a small gradient) and 10 mm/km (a large gradient). A gradient of about 1 mm/km corresponds to the 'normal' east-west gradient due to the Earth's rotation, but a large 10 mm/km may be expected at mid-latitude regions during solar maximum conditions [Wanninger and Jahn, 1991]. Note that these gradients have been assumed for the GPS L1 frequency, so the resulting DD ionospheric effects also hold for this frequency. The vertical ionospheric delay, $\imath_v$, is fixed at 5 m (L1), which is a realistic value under *average* ionospheric conditions, see Fig. 4.11.

From the table it follows that in the presence of *small* horizontal gradients, for this 10 km baseline the size of the DD ionospheric effect is below the 10 cm. With much larger gradients, the remaining DD ionospheric effect can range up to a few dm's. Although this latter effect is large, the double-differencing eliminates a large amount of the absolute ionospheric effects present. Moreover, from the example it can be concluded that the DD ionospheric effect is maximized when the gradients of the two single-differences are *opposite of sign*, and when the both satellites involved in the double-difference are tracked under *low* elevation.

4.8 Worst-case relative ionospheric effects for GPS

In the previous section it was emphasized that for the GPS applications discussed in this thesis the relative ionospheric effects are of importance. In most of the current GPS literature in relative applications only the *first-order* ionospheric effect is taken into account, while the higher-order and bending terms are simply neglected, without arguing whether this is really allowed under the circumstances. Therefore, in this section it is, by means of simulations, investigated whether or not the ionospheric higher-order and bending effects sufficiently cancel for relative GPS applications.

The ionospheric effects are simulated for GPS *phase* observations at three frequencies, i.e. L1, L2 and the future L5. The code effects are not considered, since the presence of relative higher-order and bending effects is not so critical as for the phase, because of the less precise code observations (accuracy at dm-level). The observations are assumed to be collected at (geomagnetic) *mid-latitudes*, so the results do not apply for the polar and equatorial regions. Moreover, the ionospheric effects are simulated under *worst-case* assumptions, and therefore can be considered as upper bounds for the effects which can be expected in practice.

4.8.1 Worst-case conditions

In the simulations, the following worst-case conditions are assumed:

- The observations are assumed to be collected in a *solar maximum* period, during *daytime*. This means that for the ionospheric electron content and density extremely high values are assumed, i.e. $VTEC = 10^{18}$ m^{-2} and $N_{e,\max} = 3 \cdot 10^{12}$ m^{-3}. Moreover, a *large horizontal gradient* of 10 mm/km

is assumed.

- The observations are assumed to be collected by four GPS receivers, forming two very *long baselines*. The length of one baseline is about 400 km, a distance which may be considered as a maximum baseline length in this thesis. The other baseline is half as long, about 200 km. Both baselines are perpendicularly directed to each other, the 400 km baseline in North-South direction and the 200 km baseline in East-West direction, see Fig. 4.29. The geographic coordinates of the four simulated receivers are given in Table 4.5, in both geodetic and geomagnetic reference frames.
- The two receivers of a baseline track two satellites which are under *low elevation*, of about 15°. So per baseline for each frequency a double-difference can be formed. With respect to the mentioned ionospheric gradient of the two single-differences involved in a double-difference, they are assumed to be *oppositely directed*, as to obtain maximum double-difference effects (see Sect. 4.7).

Table 4.5. Coordinates of simulated receivers

receiver	geodetic coordinates (φ, λ)	geomagnetic coordinates (φ_m, λ_m)
1	(54.0°N, 5.0°E)	(55.6°N, 90.3°E)
2	(50.5°N, 5.0°E)	(52.3°N, 88.3°E)
3	(52.5°N, 3.5°E)	(54.5°N, 87.9°E)
4	(52.5°N, 5.3°E)	(54.1°N, 89.6°E)

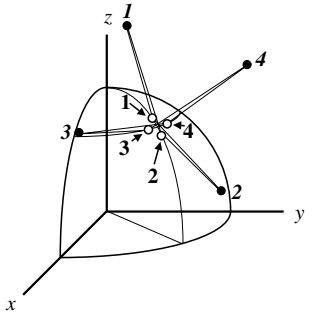

Fig. 4.29. Simulated receiver-satellite geometry in the geodetic frame: Receivers 1-2 (North-South baseline) track satellites 1-2, and receivers 3-4 (East-West baseline) track satellites 3-4

Table 4.6 shows azimuths, zenith angles (at receiver and ionospheric point), $VTEC$s and geomagnetic latitudes of the sub-ionospheric points for the four ranges involved

in a double-difference. Note that the difference between the geodetic and geomagnetic azimuths are about 30° for the involved locations. Moreover, note that the $VTEC$ for satellite 1 and receivers 1 and 2 increases, due to the positive horizontal gradient, and that the $VTEC$ of satellite 2 decreases from receiver 1 to 2, as a consequence of the negative opposite gradient. The same effects can be observed for the other baseline.

Table 4.6. Azimuths, zenith angles, $VTEC$s and geomagnetic latitude of sub-ionospheric points for the two baselines

r	s	a	a_m	z	z'	$VTEC$	φ'_m
1	1	0°	30.8°	71.1°	63.7°	$1.0000 \cdot 10^{18}$	61.7°
2	1	0°	29.5°	75.0°	66.3°	$1.1638 \cdot 10^{18}$	59.6°
1	2	180°	210.8°	75.0°	66.3°	$1.0000 \cdot 10^{18}$	47.9°
2	2	180°	209.5°	71.1°	63.7°	$0.8362 \cdot 10^{18}$	45.8°
3	3	270°	297.1°	73.1°	65.1°	$1.0000 \cdot 10^{18}$	57.4°
4	3	270°	300.7°	75.0°	66.3°	$1.0819 \cdot 10^{18}$	57.8°
3	4	90°	117.1°	75.0°	66.3°	$1.0000 \cdot 10^{18}$	49.9°
4	4	90°	120.7°	73.1°	65.1°	$0.9181 \cdot 10^{18}$	49.5°

4.8.2 Results ionospheric phase effects: Absolute and relative

Table 4.7 shows the simulated *absolute* ionospheric effects, computed using the formulas in the previous sections and the worst-case assumptions. The minus-signs appear in front of the first- and higher-order effects since the effects are computed for phase observations. The table shows that the magnitude of the first-order effects may range up to about 50 m (on L1). The magnitude of the higher-order and bending effects is at least three orders smaller than of the first-order effect.

The table also shows that the second-order effects for the ranges to satellites 2 and 4 are much higher than for the ranges to satellite 1 and 2. This is due to the geomagnetic latitudes of the ionospheric points of satellites 2 and 4, which both are about 45°, while those for satellites 1 and 2 these are about 60°. It is known that for lower geomagnetic latitudes the component of the geomagnetic induction in the directions to satellites 2 and 4 is larger than the component at the latitudes of the ionospheric points of satellites 1 and 2. The ionospheric third-order effects are all very small (max. 2 mm) and show barely differences for the two baselines. Finally, note that the ionospheric bending effects are larger than the third-order effects. For the future L5 frequency, this bending effect can range up to about 1 cm.

To judge whether these simulated higher-order and bending effects are *significant* for relative GPS positioning, in a next step single-differences are formed between receivers 1 and 2, respectively 3 and 4. In Table 4.8 the results are shown.

Table 4.7. *Absolute* ionospheric phase effects for the two baselines

	1st-order [m]			2nd-order [mm]			3rd-order [mm]			bending [mm]		
	L1	L2	L5	L1	L2	L5	L1	L2	L5	L1	L2	L5
ι_1^1	-36.710	-60.460	-65.831	-3	-7	-8	-1	-2	-2	2	6	8
ι_2^1	-47.013	-77.428	-84.307	0	-1	-1	-1	-2	-2	4	10	12
ι_1^2	-40.396	-66.530	-72.441	-18	-38	-43	-1	-2	-2	3	9	11
ι_2^2	-30.697	-50.556	-55.048	-15	-32	-36	0	-1	-2	2	5	6
ι_3^3	-38.562	-63.509	-69.152	-5	-10	-11	-1	-2	-2	3	8	9
ι_4^3	-43.705	-71.979	-78.374	-4	-8	-9	-1	-2	-2	4	10	11
ι_3^4	-40.396	-66.530	-72.441	-13	-28	-31	-1	-2	-2	3	9	11
ι_4^4	-35.404	-58.308	-63.488	-13	-27	-30	-1	-2	-2	3	7	8

From Table 4.8 the reduction of the ionospheric effects is clear. The first-order SD effects on L1 are in the order of 10 m, while all second-order effects are reduced below the cm. The third-order effects seem to be very insensitive to the ionospheric gradients, since they almost cancel out in the single-differences. The SD bending effects are at most 5 mm. Note that the ionospheric first-order and bending effects for the 200 km baseline are half as large as for their 400 km counterparts. This proportional behavior does not apply to the second-order effect, since the orientation of the two baselines is completely different.

Applying a second differencing step, i.e. taking the difference between two single-differences, results in the double-differenced ionospheric effects in Table 4.9. The table shows that only the second-order effects have been reduced as a consequence of the double-differencing. In contrast with this, the first-order and bending effects are not reduced, but their SD effects are *added*, as due to the differences in sign. The first-order DD effect is about 20 m on L1 for the 400 km baseline. Note that

Table 4.8. *Single-differenced* ionospheric phase effects for the two baselines

	1st-order [m]			2nd-order [mm]			3rd-order [mm]			bending [mm]		
	L1	L2	L5	L1	L2	L5	L1	L2	L5	L1	L2	L5
ι_{12}^1	-10.303	-16.968	-18.476	3	6	7	0	0	0	2	4	4
ι_{12}^2	9.699	15.974	17.393	3	6	7	1	1	0	-1	-4	-5
ι_{34}^3	-5.143	-8.470	-9.223	1	2	2	0	0	0	1	2	2
ι_{34}^4	4.992	8.222	8.953	0	1	1	0	0	0	0	-2	-3

Table 4.9. *Double-differenced* ionospheric phase effects for the two baselines

	1st-order [m]			2nd-order [mm]			3rd-order [mm]			bending [mm]		
	L1	L2	L5	L1	L2	L5	L1	L2	L5	L1	L2	L5
ι_{12}^{12}	20.002	32.942	35.869	0	0	0	1	1	0	-3	-8	-9
ι_{34}^{34}	10.135	16.692	18.176	-1	-1	-1	0	0	0	-1	-4	-5

this corresponds to a relative effect of 50 mm/km, which should be considered as a safe upper bound for the *first-order* ionospheric errors in DD phase observations at mid-latitudes. This effect seems to be confirmed by [Goad, 1990], who reported DD ionospheric effects up to 0.5 m for a 9-km baseline measured (at mid-latitudes) in 1988 (close to the previous solar maximum).

From Table 4.9 it also follows that the sum of the DD *higher-order* and *bending* effects, can be up to 9 mm for the future L5 frequency (for L1 it is 2 mm, and for L2 7 mm). In order to judge whether these effects are significant, the precision of the DD phase observations should be taken into account. For L5 this is not known yet, but it can be expected that it will be at the level of the precision of the L1 and L2 observations, which is about $\sigma = 2 \cdot 3 = 6$ mm (the factor 2 appears because of the double-differencing). With this standard deviation, the effect of 9 mm falls within the 2σ threshold, which is a well-known rule-of-thumb to judge the significance of parameters. This implies that for the GPS baselines considered in this thesis, it is allowed to *neglect* the ionospheric higher-order and bending effects, such that only the first-order effect remains.

4.9 Concluding remarks

The focus of this chapter was on the ionospheric refraction error in GPS observations as a consequence of the signal's propagation through the atmosphere. This ionospheric error is of more importance to fast relative GPS positioning than the tropospheric error, which mainly influences the height. Using the geometric optics approximation, the ionospheric error is split into a propagation effect, which can be approximated with a Taylor-series of the third order, and an effect due to the bending of the signal. Although the size of these higher-order plus bending terms may be up to 5 cm at mid-latitudes, it was by means of a worst-case example shown that for relative GPS applications over distances up to 400 km (the maximum GPS baseline length considered in this thesis) it is allowed to safely neglect these terms. Hence, for these applications therefore only the first-order ionospheric error remains, which is inversely proportional with the squared frequency and opposite of sign for GPS phase and code observations.

Chapter 5

The ionosphere-weighted GPS model

5.1 Introduction

In the previous chapter the physical backgrounds of the *ionospheric* error in GPS observations were explained. In the current chapter it is shown how this error can be incorporated in the mathematical models for precise GPS applications as set up in Chap. 2 in the absence of atmospheric errors. The GPS models are the positioning or geometry-based model on the one hand, and the non-positioning or geometry-free model on the other hand. Beside the ionospheric error in this chapter also the incorporation of the *tropospheric* error is discussed. Although this tropospheric error is in general smaller than its ionospheric counterpart, it may not be neglected for the GPS applications in this thesis.

Unfortunately, additional *rank deficiencies* are introduced in both geometry-based and geometry-free models due to the addition of atmospheric parameters. In Sect. 5.2 it is explained how these rank deficiencies due to the tropospheric parameters are dealt with. For the ionospheric parameters, the most general way to avoid additional rank deficiencies is to treat them as *stochastic* variables. The resulting model, in fact the central model of this thesis, is discussed in Sect. 5.3 and is referred to as the *ionosphere-weighted* model. Section 5.4 describes the functional and stochastic parts of this model and shows the links between this model and other GPS models in which ionospheric errors are accounted for.

In Sects. 5.5 – 5.7 the suitability of this ionosphere-weighted model for fast precise GPS applications is investigated. For this purpose in Sect. 5.5 *closed-form* expressions are derived for the vc-matrices of several parameters of the ionosphere-weighted model, which can be used to infer how various factors in the GPS model contribute to the (expected) precision of the unknown parameters. These vc-matrices are purely based on the functional and stochastic model assumptions. Using these closed-form expressions in Sect. 5.6 the expected quality of the position parameters is investigated, whereas the focus of Sect. 5.7 is on the *ambiguity success rate*, an important tool (introduced in Chap. 3) to infer whether ambiguity resolution with the ionosphere-weighted model can be expected successful. Sec-

tion 5.8 deals about the robustness of the model in which the ionospheric delays are neglected, against ionospheric biases. Finally, this chapter is ended with some concluding remarks.

5.2 The tropospheric error in the GPS model

Although in this thesis the focuss is on the ionospheric error, in the relative GPS model as discussed in this thesis one also needs to account for the error due to propagation through the troposphere. Recall from Chap. 4 that the tropospheric delay is *independent* of the frequency and *equal* for both phase and group of the signal. This implies that for all observable types it is sufficient to parameterize one and the same vector of *slant* tropospheric delay parameters, which is denoted as ν, and holds for n receivers, m satellites at observation epoch i:

$$\boxed{\nu(i) \;=\; \left[\left(\nu_1^1(i),\;\ldots,\;\nu_1^m(i)\right),\;\ldots,\;\left(\nu_n^1(i),\;\ldots,\nu_n^m(i)\right)\right]^T} \tag{5.1}$$

Unfortunately, including this vector to the vector of estimable parameters of the models set up in Chap. 2 would cause additional rank deficiencies in the design matrices. In this section it is explained how these rank deficiencies can be omitted for the geometry-free and geometry-based models.

5.2.1 Additional rank deficiencies

Inclusion of slant tropospheric parameters would cause a rank deficiency between the columns in the design matrix corresponding to these parameters and the *satellite clock* parameters. To see this, consider the partial design matrices of the tropospheric delays and satellite clocks (for one observation epoch):

$$\left[\begin{pmatrix} e_j \\ e_j \end{pmatrix} \otimes I_{nm},\;\; \begin{pmatrix} I_j & \\ & I_j \end{pmatrix} \otimes \mathcal{D}\right],\quad \text{with } \mathcal{D} \;=\; \underbrace{[C_n \otimes e_m,\;\; -e_n \otimes I_m]}_{nm\times(n-1+m)} \tag{5.2}$$

The rank deficiency is of size $n-1+m$ and could be removed by for example lumping the clocks of the first observable with the tropospheric delay parameters. This rank deficiency would occur for both the geometry-based and geometry-free models. For the *geometry-based* model however another rank deficiency occurs, between the partial design matrices of the tropospheric delays and the *receiver coordinates*:

$$\left[\begin{pmatrix} e_j \\ e_j \end{pmatrix} \otimes I_{nm},\;\; \begin{pmatrix} e_j \\ e_j \end{pmatrix} \otimes \mathcal{A}(i)\right],\;\text{with } \mathcal{A}(i) = \underbrace{\begin{bmatrix} 0_{m\times 3(n-1)} \\ \text{blkdiag}\,[G_2(i),\;\ldots,\;G_n(i)] \end{bmatrix}}_{nm\times 3(n-1)} \tag{5.3}$$

Elimination of this latter rank deficiency by lumping troposphere and coordinate parameters is however *not* possible, since the receiver coordinates are the parameters of interest. Instead, for the geometry-based model another approach is used,

which is based on a *reparameterization* of the tropospheric delays themselves, see Sect. 5.2.3. In this way also the first rank deficiency between the tropospheric delay and satellite clock parameters disappears. In case of the geometry-free model, where only the first rank deficiency shows up, the rank deficiency can be omitted by assuming the slant tropospheric delays as *stochastic variables*, which is further discussed in the next subsection.

5.2.2 Combined range/tropospheric pseudo-observables

Since in the geometry-free model the ranges were already modelled as stochastic variables (see Chap. 2), and the tropospheric delays have the same non-dispersive character as these ranges, a *combined* range/tropospheric variable is introduced for the geometry-free model, consisting of the *sum* of the range and tropospheric delay:

$$\boxed{\varrho_r^s(i) \;=\; \rho_r^s(i) \;+\; \nu_r^s(i), \qquad \varrho_{r,p}^s(i) \;=\; \rho_{r,p}^s(i) \;+\; \nu_{r,p}^s(i)} \tag{5.4}$$

In this way of modelling the tropospheric delays, the structure of the geometry-free model as set up in Chap. 2 does not change. The only difference is that a lumped parameter, denoted by ϱ, replaces the 'old' range parameter ρ, whereas the lumped pseudo-observable, denoted as ϱ_p, replaces the 'old' pseudo-observable ρ_p. As a consequence of this lumping, in the stochastic model the a priori variance factors of the ranges and tropospheric delays are added together, i.e. $\sigma_\varrho^2 = \sigma_\rho^2 + \sigma_\nu^2$. Note that when the receiver-satellite ranges are *known* beforehand, i.e. $\sigma_\rho = 0$, the tropospheric delays become unbiased estimable. In that case, the pseudo-observables consist solely of the tropospheric component.

5.2.3 Parameterization of zenith tropospheric delays (ZTDs)

Decomposition of the tropospheric delay

As mentioned, in case of the geometry-based model the tropospheric delay parameter is reparameterized itself: It is split into two components, a *hydrostatic or dry* component and a *wet* component. This decomposition is chosen, since the hydrostatic component consists of about 90% of the tropospheric delay, and one can reasonably well correct for it using a priori tropospheric models (e.g. the model of [Saastamoinen, 1972]). The much smaller wet component is however quite variable and more difficult to predict.

To account for these wet delays it is common practice to *map* these delays to a *zenith* delay parameter for each receiver and to estimate these zenith delays in the processing, instead of the tropospheric slant delays. Usually, when the observation time span is not too long (e.g. less than one hour), it is sufficient to estimate only one zenith delay per receiver for the entire time span. When the distance between the receivers is restricted (this thesis), the zenith delay of the pivot station in the network is not estimated, but held fixed in the adjustment, to avoid an (almost) rank deficiency between the partial design matrices of the

zenith delays and the satellite clocks. This wet zenith delay of the pivot station may possibly be fixed to *zero*, since it is known that this is usually not larger than 20-30 cm [Blewitt, 1993]. Denoting the non-temporal wet zenith delay for a receiver as ν_r, where $r = 1, \ldots, n$, the decomposition of the tropospheric delays reads:

$$\boxed{\nu_r^s(i) \;=\; \nu_r^s(i)^0 \;+\; \psi_r^s(i)\nu_r \;=\; \left[\nu_r^s(i)^0 + \psi_r^s(i)\nu_1\right] \;+\; \psi_r^s(i)\nu_{1r}} \tag{5.5}$$

In this equation $\nu_{1r} = \nu_r - \nu_1$ denotes the relative zenith tropospheric delay (abbreviated as ZTD), $\nu_r^s(i)^0$ the a priori tropospheric correction, and $\psi_r^s(i)$ the tropospheric (wet) mapping function. Several mapping functions have been developed, for an elaborate overview see e.g. [Kleijer, 2001]. Note that the simplest mapping function is $1/\cos z_r^s(i)$, with $z_r^s(i)$ the zenith angle. An accurate mapping function suitable for GPS applications is *Niell's* mapping function [Niell, 1996].

A consequence of this ZTD estimation is that the a priori tropospheric corrections and the fixing of the zenith delay of the pivot station are added to the total sum of a priori corrections for the phase and code observables, see Eq. (2.19) in Chap. 2:

$$\begin{array}{rcl} \phi_{r,j}^s(i)^c & := & \phi_{r,j}^s(i)^c \;+\; \left[\nu_r^s(i)^0 + \psi_r^s(i)\nu_1\right] \\ p_{r,j}^s(i)^c & := & p_{r,j}^s(i)^c \;+\; \left[\nu_r^s(i)^0 + \psi_r^s(i)\nu_1\right] \end{array} \tag{5.6}$$

When for the tropospheric delays is fully relied on the a priori model values and no ZTDs are estimated at all, one may speak of a *troposphere-fixed* approach. On the other hand, when ZTDs are estimated, the resulting model is in this thesis referred to as a *troposphere-float* model.

Zenith tropospheric delays as non-temporal parameters

Due to the assumed time-constancy of the zenith tropospheric delay parameters, they can be considered as additional *non-temporal* parameters in the GPS model as set up in Chap. 2. Compared to the model without atmospheric errors (see Table 2.3), the vector g, which contains relative receiver coordinate increments is extended for the ZTDs:

$$\boxed{g \;=\; \left[g_2^T,\; \ldots,\; g_n^T\right]^T, \quad \text{where } g_r = \left[\Delta r_{1r},\; \nu_{1r}\right]^T, \quad r = 2, \ldots, n} \tag{5.7}$$

As a consequence, the matrices $G_r(i)$, appearing in the geometry matrix $\mathcal{A}(i)$ (see Eq. (5.3)), are extended for the tropospheric mapping factors:

$$\boxed{G_r(i) = \underbrace{\begin{bmatrix} -u_r^1(i)^T, & \psi_r^1(i) \\ \vdots, & \vdots \\ -u_r^m(i)^T, & \psi_r^m(i) \end{bmatrix}}_{m \times 4}, \quad r = 2, \ldots, n} \tag{5.8}$$

5.3 The ionospheric error in the GPS model

In contrast to the tropospheric error, the ionospheric error is *not* equal for all observable types, since in Chap. 4 it was shown that it is different for each frequency and also for phase and code observables. When for *each* observable type different ionospheric parameters would be introduced, this leads to a large amount of additional parameters. Fortunately this is not necessary, when the conclusions from Chap. 4 are considered.

5.3.1 Neglecting ionospheric higher-order and bending effects

One conclusion of Chap. 4 is that for the distances between GPS receivers as discussed in this thesis (which may be up to 400 km), the ionospheric *higher-order* and *bending* effects may be neglected. From this it follows that it is sufficient to parameterize the ionospheric error only to the *first order*. This conclusion however holds for GPS observables in *double-differenced* (DD) mode, and this seems to be unfortunate, since the GPS model in the absence of atmospheric errors was set up for observables in the *undifferenced* mode, see Chap. 2. In that chapter it was however also shown that the solution of the undifferenced model is (under the assumptions done) equivalent to the solution of the model formulated in double-differences. For the ionospheric error this means that although the model is set up using undifferenced ionospheric parameters, only the *double-differenced* effect plays a role for the solution of the unknown parameters, such as receiver coordinates and ambiguities. Therefore, for the model based on undifferenced observables, it is allowed to only take the first-order effect into account.

5.3.2 Parameterizing the first-order ionospheric slant delays

From Chap. 4 we also know that the first-order ionospheric effect is *inversely proportional* to the squared frequency and *opposite of sign* for phase and code observations. These properties of the ionospheric error are used in parameterizing the effect in the mathematical model. For all observable types the vector of parameters is extended for the *first-order (group) delay*, which is denoted as (see Chap. 4):

$$\boxed{\imath_{g,j} \;=\; -\imath_{\phi,j} \;\equiv\; \imath^{(1)}_{g,j}} \tag{5.9}$$

Since from now on the ionospheric error is parameterized as this first-order group delay, for the notation of this ionospheric delays we will refrain from using the subscript g and the superscript (1).

Due to the dispersiveness of the ionosphere, it is sufficient to model the delay for just one frequency, which is usually the L1 frequency. The ionospheric delays on the other frequencies are related to this L1 effect via the following way of frequency scaling:

$$\boxed{\imath_{,j}(i) \;=\; \mu_j \cdot \imath_{,1}(i); \quad \mu_j \;=\; \lambda_j^2/\lambda_1^2 \;=\; f_1^2/f_j^2} \tag{5.10}$$

For observables at j frequencies, the ionospheric coefficients toegether are collected in the vector μ:

$$\boxed{\mu \;=\; [\mu_1,\; \ldots,\; \mu_j]^T} \tag{5.11}$$

For example, in case of the future triple-frequency GPS system, the ionospheric coefficient vector reads, for the L1, L2 and L5 frequencies:

$$\mu \;=\; [\mu_1, \mu_2, \mu_3]^T \;=\; \left[1, (77/60)^2, (154/115)^2\right]^T \;\approx\; [1, 1.6469, 1.7933]^T \tag{5.12}$$

From now on when speaking of the ionospheric delay, it is in fact the *first-order ionospheric (group) slant delay on L1*, expressed in meters. It is denoted as $\imath_r^s(i)$, for receiver r and satellite s at epoch i (so the frequency subscript "1" for L1 is omitted as well). This first-order ionospheric delay is one-by-one related to TEC, which is the Total Electron Content along the geometric distance (see Chap. 4):

$$TEC_r^s(i) \;=\; \frac{2f_1^2}{A}\imath_r^s(i), \qquad \text{with } A \;\approx\; 80.6 \text{ m}^3/\text{s}^2 \tag{5.13}$$

So if desired, the estimated ionospheric slant delays can be directly transformed to TEC-values.

Conform Chap. 2, the vector of ionospheric delay parameters, denoted as $\imath$, reads for n receivers, m satellites, on observation epoch i:

$$\boxed{\imath(i) \;=\; \left[\left(\imath_1^1(i),\; \ldots,\; \imath_1^m(i)\right),\; \ldots,\; \left(\imath_n^1(i),\; \ldots,\; \imath_n^m(i)\right)\right]^T} \tag{5.14}$$

5.3.3 Ionospheric pseudo-observables

When the vector of ionospheric parameters as given in Eq. (5.14) would be included in the geometry-based and geometry-free models as set up in Chap. 2, this would cause additional rank deficiencies in both models. These rank deficiencies would, like the tropospheric delays, occur between the partial design matrices of these ionospheric parameters and the clock parameters. Like the combined range/tropospheric delays in the geometry-free model, a way to circumvent these rank deficiencies is to treat the ionospheric delays as *stochastic variables*. For both the geometry-free and the geometry-based model, for each receiver-satellite combination, an *ionospheric pseudo-observable* is added to the vector of GPS observables. The following vector, denoted as $\imath_p(i)$, is added for nm receiver-satellite combinations on epoch i:

$$\boxed{\imath_p(i) \;=\; \left[\left(\imath_{p,1}^1(i) \ldots \imath_{p,1}^m(i)\right) \;\ldots\; \left(\imath_{p,n}^1(i) \ldots \imath_{p,n}^m(i)\right)\right]^T} \tag{5.15}$$

Besides the extension of the vector of observables, the vc-matrix of the observables is extended to account for the assumed precision of these ionospheric pseudo-observables. For this, it is assumed that all pseudo-observables have the same variance factor, which will be denoted as $\sigma_\imath^2$ (compare this with the factor σ_ϱ^2 for the combined range/troposphere pseudo-observables in the geometry-free model).

5.4 The ionosphere-weighted model

Since for both geometry-based and geometry-free models the presence of the ionospheric delays in the model can be weighted by tuning the size of the a priori ionospheric variance factor σ_i^2, we will refer to this model as the *ionosphere-weighted GPS model*. Note that a similar type of stochastic modelling of the ionospheric delays was already used in [Bock et al., 1986]. Other publications on this model are, among others, [Schaffrin and Bock, 1988], [Goad and Yang, 1994], [Schaer, 1994], [Teunissen et al., 1997], [Teunissen, 1998d], and, more recently, [Liu, 2001].

Note that this ionosphere-weighted method of ionospheric modelling does not require further (physical) modelling of the slant delays. Examples of physical models are the mapping of the slant delay to a vertical delay using the secant mapping function (see Chap. 4), or the parameterization of the ionospheric delay such as in the models part of the *Bernese* software, see e.g. [Rothacher and Mervart, 1996], or the model described in [Georgiadou, 1994]. It is believed that the method of ionospheric modelling as described in this thesis is more flexible than using a physical model, since for each receiver-satellite combination and for each observation epoch a new ionospheric (slant) delay parameter is estimated, regardless of the actual ionospheric conditions. In this way it should be possible to capture *small-scale* features in the ionospheric delays, such as for example due to *TIDs* (see Chap. 4). When a physical model is used one should already have insight in these ionospheric conditions, such that, depending on the 'behavior' of the ionosphere, more or less parameters for the ionospheric model are introduced in the processing.

In Table 5.1 the partial design matrices and estimable parameter vectors of the ionosphere-weighted geometry-based and geometry-free models are summarized.

The a priori variance factor of the ionospheric pseudo-observables, σ_i^2, may take on any value between the extreme 'values' *zero* and *infinity*. Note that when $\sigma_i^2 = 0$, the ionospheric delays are strictly spoken no stochastic variables, but *deterministic* quantities, implying that they are completely known beforehand. On the other hand, when $\sigma_i^2 = \infty$, the ionospheric pseudo-observations do not contribute at all to the solution of the model, they are assumed as *completely unknown* parameters. In the first case the ionosphere-weighted model reduces to the so-called *ionosphere-fixed* model, since the ionospheric delays are held fixed (known) in the adjustment, whereas in the second case the model reduces to the so-called *ionosphere-float* model, since the ionospheric delays only appear in the vector of unknown parameters. In the following subsections these two extreme versions of the ionosphere-weighted model are discussed in more detail.

5.4.1 The ionosphere-fixed model ($\sigma_i = 0$)

When the a priori ionospheric variance factor is exactly set to zero, $\sigma_i^2 = 0$, no ionospheric parameters at all are estimated in the model. In this case the structure of the (design matrices of the) geometry-based and geometry-free models becomes

Table 5.1. Ionosphere-weighted model: observables, partial design matrices and estimable parameters

	`geometry-based model`	`geometry-free model`
$y(i)$	$\left[\left(\Phi^{gb}(i)^T,\ P^{gb}(i)^T\right),\ \imath_p(i)^T\right]^T$	$\left[\left(\Phi^{gf}(i)^T,\ P^{gf}(i)^T\right),\ \left(\imath_p(i)^T,\ \varrho_p(i)^T\right)\right]^T$
$Q_{y(i)}$	$\begin{bmatrix} \begin{pmatrix} Q_\phi & \\ & Q_p \end{pmatrix} & \\ & \sigma_\imath^2 \end{bmatrix} \otimes Q(i)$	$\begin{bmatrix} \begin{pmatrix} Q_\phi & \\ & Q_p \end{pmatrix} & & \\ & \begin{pmatrix} \sigma_\imath^2 & \\ & \sigma_\varrho^2 \end{pmatrix} \end{bmatrix} \otimes Q(i)$
$A_I(i)$	$\begin{bmatrix} \begin{bmatrix} \begin{pmatrix} e_j \\ e_j \end{pmatrix} \\ 0 \end{bmatrix} \otimes \mathcal{A}(i) & \begin{bmatrix} \begin{pmatrix} \Lambda \\ 0 \end{pmatrix} \\ 0 \end{bmatrix} \otimes \mathcal{C} \end{bmatrix}$	$\begin{bmatrix} \begin{pmatrix} \Lambda \\ 0 \end{pmatrix} \\ \begin{pmatrix} 0 \\ 0 \end{pmatrix} \end{bmatrix} \otimes \mathcal{C}$
$A_{II}(i)$	$\begin{bmatrix} \begin{bmatrix} \begin{pmatrix} I_j & \\ & I_j \end{pmatrix} \\ \begin{pmatrix} 0 & 0 \end{pmatrix} \end{bmatrix} \otimes \mathcal{D} & \begin{bmatrix} \begin{pmatrix} -\mu \\ \mu \end{pmatrix} \\ 1 \end{bmatrix} \otimes I_{nm} \end{bmatrix}$	$\begin{bmatrix} \begin{bmatrix} \begin{pmatrix} I_j & \\ & I_j \end{pmatrix} \\ \begin{pmatrix} 0 & \\ & 0 \end{pmatrix} \end{bmatrix} \otimes \mathcal{D} & \begin{bmatrix} \begin{pmatrix} -\mu & e_j \\ \mu & e_j \end{pmatrix} \\ \begin{pmatrix} 1 & \\ & 1 \end{pmatrix} \end{bmatrix} \otimes I_{nm} \end{bmatrix}$
x_I	$\left[g^T,\ \left(a_1^T,\ \ldots,\ a_j^T\right)\right]^T$	$\left[a_1^T,\ \ldots,\ a_j^T\right]^T$
$x_{II}(i)$	$\left[\left(\alpha_1(i)^T,\ldots,\alpha_j(i)^T\right),\left(\beta_1(i)^T,\ldots,\beta_j(i)^T\right),\imath(i)^T\right]^T$	$\left[\left(\alpha_1(i)^T,\ \ldots,\ \alpha_j(i)^T\right),\ \left(\beta_1(i)^T,\ \ldots,\ \beta_j(i)^T\right),\ \imath(i)^T,\ \varrho(i)^T\right]^T$

g	$= \left[g_2^T,\ \ldots,\ g_n^T\right]^T$	$w(n-1)$ `coordinates/ZTDs`
a_j	$= \left[\left(M_{12,j}^{12},\ \ldots,\ M_{12,j}^{1m}\right),\ \ldots,\ \left(M_{1n,j}^{12},\ \ldots,\ M_{1n,j}^{1m}\right)\right]^T$	$j(n-1)(m-1)$ `phase ambiguities`
$\alpha_j(i)$	$= \left[\left(c\delta t_{12,j}(i),\ \ldots,\ c\delta t_{1n,j}(i)\right),\ \left(c\delta t_{1,j}^1(i),\ \ldots,\ c\delta t_{1,j}^m(i)\right)\right]^T$	$j(n-1+m)$ `phase clocks`
$\beta_j(i)$	$= \left[\left(cdt_{12,j}(i),\ \ldots,\ cdt_{1n,j}(i)\right),\ \left(cdt_{1,j}^1(i),\ \ldots,\ cdt_{1,j}^m(i)\right)\right]^T$	$j(n-1+m)$ `code clocks`
$\varrho(i)$	$= \left[\left(\varrho_1^1(i),\ \ldots,\ \varrho_1^m(i)\right),\ \ldots,\ \left(\varrho_n^1(i),\ \ldots,\ \varrho_n^m(i)\right)\right]^T$	nm `ranges/tropospheric delays`
$\imath(i)$	$= \left[\left(\imath_1^1(i),\ \ldots,\ \imath_1^m(i)\right),\ \ldots,\ \left(\imath_n^1(i),\ \ldots,\ \imath_n^m(i)\right)\right]^T$	nm `ionospheric delays`

equivalent to the structure of the model in Chap. 2 in absence of atmospheric errors. Two variants can be distinguished for this ionosphere-fixed model. The first variant is applied when *exact* a priori ionospheric information is available, and the second variant is applied when the distance between the GPS receivers are sufficiently *short*.

Exact a priori ionospheric information

The first variant of the ionosphere-fixed model is the one in which the GPS phase and code observables are corrected for exact assumed a priori ionospheric corrections. The vector of observables for the geometry-based and geometry-free models becomes as follows:

$$y(i) \;=\; \begin{cases} \begin{bmatrix} \Phi^{gb}(i) + \mu \otimes \imath_p(i) \\ P^{gb}(i) - \mu \otimes \imath_p(i) \end{bmatrix} & \text{(geometry-based model)} \\ \\ \begin{bmatrix} \Phi^{gf}(i) + \mu \otimes \imath_p(i) \\ P^{gf}(i) - \mu \otimes \imath_p(i) \\ \varrho_p(i) \end{bmatrix} & \text{(geometry-free model)} \end{cases} \tag{5.16}$$

Since the ionospheric corrections are deterministic assumed, the vc-matrix of these observables is equivalent to the vc-matrix in absence of atmospheric errors:

$$Q_{y(i)} \;=\; \begin{cases} \text{blkdiag}\left[Q_\phi,\; Q_p\right] \otimes Q(i) & \text{(geometry-based model)} \\ \\ \text{blkdiag}\left[\left(Q_\phi,\; Q_p\right),\; \sigma_\varrho^2\right] \otimes Q(i) & \text{(geometry-free model)} \end{cases} \tag{5.17}$$

Short baselines

For the second variant of the ionosphere-fixed model it is assumed that the sample values of the ionospheric pseudo-observables are exactly zero: $\imath_p(i) = 0$. Besides, it is assumed that the distances between the GPS receivers are that short such that the ionospheric delays from one satellite to all involved receivers are exactly *equal*, since due to the height of the ionosphere they all pass through approximately the same part of the ionosphere (see also Chap. 4). Mathematically, this means that the following condition is added to the model:

$$\boxed{\imath_r^s(i) \;=\; \imath_1^s(i), \quad r = 2, \ldots, n} \tag{5.18}$$

This condition is well known as the *short-baseline condition*. In practice, this distance is restricted to about 10 km or shorter, depending on the actual ionospheric conditions.

A consequence of this short-baseline condition is that the estimable *satellite clock* parameters change. The satellite clock parameters of the ionosphere-fixed model read the same as those of the ionosphere-weighted model, but corrected for the ionospheric delay of pivot station 1:

$$\begin{array}{rcl} c\delta t_{1,j}^s(i) & := & c\delta t_{1,j}^s(i) \;+\; \mu_j \imath_1^s(i) \\ cdt_{1,j}^s(i) & := & cdt_{1,j}^s(i) \;-\; \mu_j \imath_1^s(i) \end{array} \tag{5.19}$$

Note that these altered satellite clock parameters hold for both the geometry-based and geometry-free models.

5.4.2 The ionosphere-float model ($\sigma_\iota = \infty$)

Additional rank deficiency

In contrast to the situation in the previous subsection it could be that there is no a priori ionospheric information available at all. In that case the a priori ionospheric standard deviation is set to an infinite 'value': $\sigma_\iota = \infty$, implying that the ionospheric pseudo-observables virtually *disappear* from the model. This ionosphere-float model is typically applied for very long baselines. A consequence of the removal of the ionospheric pseudo-observables is that the design matrix columns of the ionospheric delays and the satellite clocks become rank-deficient (for both the geometry-based and geometry-free models). This rank deficiency can however be removed by constraining the receiver and satellite clock parameters of the first observable (usually the L1 phase) as S-basis elements, see also [De Jonge, 1998].

In Table 5.2 the resulting full-rank partial design matrices and estimable parameters for the ionosphere-float model are summarized. Note from the table the changed partial design matrices for the clock parameters, compared to their ionosphere-weighted counterparts: For the phase clock parameters the matrix I_j is replaced by the $j \times (j-1)$ matrix C_j, which is defined as:

$$C_j \;=\; \left[\begin{array}{c} 0_{1\times(j-1)} \\ I_{j-1} \end{array} \right] \tag{5.20}$$

Estimable clock parameters

The vector of estimable phase clock parameters in the ionosphere-float model does not apply to the observable type of which the clocks are constrained (the first phase observable), and to emphasize this different vector of parameters, a 'bar' symbol is used in Table 5.2. This bar symbol also appears on top of the vector of estimable code clock parameters and ionospheric parameters, which are also changed due to the elimination of the rank deficiency.

Due to the assignment of the phase clocks of the first observable as S-basis, the estimable clock parameters of the other observable types, phase as well as code, are only estimable biased with the clocks of the first observable. The estimable *phase* receiver and satellite clock parameters in the ionosphere-float model are equal to their estimable ionosphere-weighted counterparts *minus* a scaled receiver respectively satellite phase clock error on L1:

$$\begin{array}{rcl} c\bar{\delta}t_{1r,j}(i) & = & c\delta t_{1r,j}(i) - \frac{\mu_j}{\mu_1} c\delta t_{1r,1}(i) \\ c\bar{\delta}t^s_{1,j}(i) & = & c\delta t^s_{1,j}(i) - \frac{\mu_j}{\mu_1} c\delta t^s_{1,1}(i) \end{array} \tag{5.21}$$

The estimable *code* clock parameters of the ionosphere-float model are also biased

Table 5.2. Ionosphere-float model: observables, partial design matrices and estimable parameters

	`geometry-based model`	`geometry-free model`
$y(i)$	$\left[\Phi^{gb}(i)^T,\ P^{gb}(i)^T\right]^T$	$\left[\left(\Phi^{gf}(i)^T,\ P^{gf}(i)^T\right),\ \varrho_p(i)^T\right]^T$
$Q_{y(i)}$	$\begin{bmatrix} Q_\phi & \\ & Q_p \end{bmatrix} \otimes Q(i)$	$\begin{bmatrix} \begin{pmatrix} Q_\phi & \\ & Q_p \end{pmatrix} & \\ & \sigma_\varrho^2 \end{bmatrix} \otimes Q(i)$
$A_I(i)$	$\begin{bmatrix} \begin{pmatrix} e_j \\ e_j \end{pmatrix} \otimes \mathcal{A}(i) & \begin{pmatrix} \Lambda \\ 0 \end{pmatrix} \otimes \mathcal{C} \end{bmatrix}$	$\begin{bmatrix} \begin{pmatrix} \Lambda \\ 0 \\ 0 \end{pmatrix} \end{bmatrix} \otimes \mathcal{C}$
$A_{II}(i)$	$\begin{bmatrix} \begin{pmatrix} C_j & \\ & I_j \end{pmatrix} \otimes \mathcal{D} & \begin{pmatrix} -\mu \\ \mu \end{pmatrix} \otimes I_{nm} \end{bmatrix}$	$\begin{bmatrix} \begin{bmatrix} \begin{pmatrix} C_j & \\ & I_j \end{pmatrix} \\ \begin{pmatrix} 0 & 0 \end{pmatrix} \end{bmatrix} \otimes \mathcal{D} & \begin{bmatrix} \begin{pmatrix} -\mu & e_j \\ \mu & e_j \end{pmatrix} \\ \begin{pmatrix} 0 & 1 \end{pmatrix} \end{bmatrix} \otimes I_{nm} \end{bmatrix}$
x_I	$\left[g^T,\ \left(a_1^T,\ \ldots,\ a_j^T\right)\right]^T$	$\left[a_1^T,\ \ldots,\ a_j^T\right]^T$
$x_{II}(i)$	$\left[\left(\bar\alpha_2(i)^T,\ \ldots,\ \bar\alpha_j(i)^T\right),\ \left(\bar\beta_1(i)^T,\ \ldots,\ \bar\beta_j(i)^T\right),\ \bar\imath(i)^T\right]^T$	$\left[\left(\bar\alpha_2(i)^T,\ \ldots,\ \bar\alpha_j(i)^T\right),\ \left(\bar\beta_1(i)^T,\ \ldots,\ \bar\beta_j(i)^T\right),\ \bar\imath(i)^T,\ \varrho(i)^T\right]^T$

g	$= \left[g_2^T,\ \ldots,\ g_n^T\right]^T$	$w(n-1)$ `coordinates/ZTDs`
a_j	$= \left[\left(M_{12,j}^{12},\ \ldots,\ M_{12,j}^{1m}\right),\ \ldots,\ \left(M_{1n,j}^{12},\ \ldots,\ M_{1n,j}^{1m}\right)\right]^T$	$j(n-1)(m-1)$ `phase ambiguities`
$\bar\alpha_j(i)$	$= \left[\left(c\bar\delta t_{12,j}(i),\ \ldots,\ c\bar\delta t_{1n,j}(i)\right),\ \left(c\bar\delta t_{1,j}^1(i),\ \ldots,\ c\bar\delta t_{1,j}^m(i)\right)\right]^T,\quad j \geq 2$	$(j-1)(n-1+m)$ `phase clocks`
$\bar\beta_j(i)$	$= \left[\left(c\bar d t_{12,j}(i),\ \ldots,\ c\bar d t_{1n,j}(i)\right),\ \left(c\bar d t_{1,j}^1(i),\ \ldots,\ c\bar d t_{1,j}^m(i)\right)\right]^T$	$j(n-1+m)$ `code clocks`
$\varrho(i)$	$= \left[\left(\varrho_1^1(i),\ \ldots,\ \varrho_1^m(i)\right),\ \ldots,\ \left(\varrho_n^1(i),\ \ldots,\ \varrho_n^m(i)\right)\right]^T$	nm `ranges/tropospheric delays`
$\bar\imath(i)$	$= \left[\left(\bar\imath_1^1(i),\ \ldots,\ \bar\imath_1^m(i)\right),\ \ldots,\ \left(\bar\imath_n^1(i),\ \ldots,\ \bar\imath_n^m(i)\right)\right]^T$	nm `ionospheric delays`

by a scaled receiver or satellite L1 phase clock error:

$$\begin{array}{rcl} \bar{cdt}_{1r,j}(i) & = & cdt_{1r,j}(i) + \frac{\mu_j}{\mu_1} c\delta t_{1r,1}(i) \\ \bar{cdt}^s_{1,j}(i) & = & cdt^s_{1,j}(i) + \frac{\mu_j}{\mu_1} c\delta t^s_{1,1}(i) \end{array} \tag{5.22}$$

Estimable ionospheric parameters

Another consequence of the elimination of the rank deficiency is that the ionospheric parameters in the ionosphere-float model become biased by the phase clock parameters of the first observable. The estimable ionospheric parameters are formed by the undifferenced ionospheric parameters of the ionosphere-weighted model, plus the receiver and satellite clocks of the L1 phase observable:

$$\boxed{\bar{\imath}^s_r(i) \;=\; i^s_r(i) - \tfrac{1}{\mu_1}\left[c\delta t_{1r,1}(i) - c\delta t^s_{1,1}(i)\right]} \tag{5.23}$$

Note that when these biased ionospheric parameters are double-differenced, the clock biases get eliminated.

5.4.3 Relation to the ionosphere-free phase combination

In the presence of significant ionospheric delays, in GPS practice often another approach is used than to solve the ionosphere-weighted or -float models as described in the previous subsections. Instead, the so-called *ionosphere-free* linear combination of (dual-frequency) phase observations is taken to eliminate the first-order ionospheric delays. It turns out that this model of ionosphere-free phase combinations has its equivalence in the ionosphere-float model, when *only phase data* are used, thus without the inclusion of code data. As a side-path, in this subsection this equivalence is shown, but only for the geometry-based model.

Phase-only ionosphere-float model

Unfortunately, in the absence of code observations in the design matrix of the ionosphere-float model an additional rank deficiency shows up, between the columns of the ambiguities and those of the ionospheric delays. Independent of the number of frequencies the phase data are collected (at least two), the size of this rank deficiency is $(n-1)(m-1)$. This rank deficiency can be eliminated by means of an *integer reparametrization* of the ambiguities: Not the original ambiguities on each frequency are estimated, but *linear combinations* of them, between frequencies. The number of estimable integer ambiguity combinations is $(j-1)(n-1)(m-1)$, which is exactly $(n-1)(m-1)$ (the size of the rank deficiency) less than the $j(n-1)(m-1)$ estimable ambiguities when code data are included. The consequence of this integer parameterization is that the estimable ionospheric delays, which are already biased with clock terms in the ionosphere-float model even when code data are included, become *biased* by ambiguity terms.

In [Teunissen and Odijk, 2002] the estimable reparameterized integer ambiguity combinations are revealed for the current dual-frequency case, as well as for the

future triple-frequency GPS case. In the dual-frequency case the estimable integer vector, which is a combination of the L1 and L2 ambiguities, is denoted as $\bar{a}_2$. Its wavelength matrix is denoted as $\bar{\Lambda}_2$. They both read:

$$\bar{\Lambda}_2 = \begin{bmatrix} -7\lambda_1 \\ -9\lambda_2 \end{bmatrix}, \quad \bar{a}_2 = 77a_1 - 60a_2, \quad \bar{a}_2 \in Z^{(n-1)(m-1)} \tag{5.24}$$

where a_1 and a_2 denote the double-difference ambiguities for L1 respectively L2. In the triple-frequency case, the reparameterized ambiguity vector $\bar{a}_3$ plus corresponding 'wavelength' matrix $\bar{\Lambda}_3$ read:

$$\bar{\Lambda}_3 = \begin{bmatrix} 1613\lambda_1 & 180\lambda_1 \\ 2070\lambda_2 & 231\lambda_2 \\ 2160\lambda_3 & 241\lambda_3 \end{bmatrix}, \quad \bar{a}_3 = \begin{bmatrix} 77a_1 - 60a_2 \\ 24a_2 - 23a_3 \end{bmatrix}, \quad \bar{a}_3 \in Z^{2(n-1)(m-1)} \tag{5.25}$$

where a_3 denotes the future L5 ambiguity vector. So in the triple-frequency case the ambiguity combination of the dual-frequency case is extended with a second combination. Note that the 'wavelength' matrices in both cases are not diagonal anymore: One ambiguity combination does *not* correspond to one observable type.

The ionosphere-free phase combinations

Having set up the full-rank phase-only ionosphere-float model, the model ionospheric delay parameters are eliminated to obtain the model of ionosphere-free combinations. The following transformation is used for this purpose:

$$\boxed{y^{if}(i) \;=\; \Upsilon^{if} y(i), \;\; Q^{if}_{y(i)} \;=\; \Upsilon^{if} Q_{y(i)} {\Upsilon^{if}}^T, \text{ with } \Upsilon^{if} \;=\; T_j \otimes I_{nm}} \tag{5.26}$$

where T_j denotes the $(j-1) \times j$ transformation matrix. At first sight, this transformation does not seem to preserve the information content in the original phase observables, since the matrix T_j is not square: From j phase observables $j-1$ ionosphere-free combinations are formed. However, the number with which the vector of observables is reduced in the transformation corresponds exactly to the number of ionospheric delays that is eliminated. Hence, for the solution of the remaining parameters it makes no difference whether the original phase-only ionosphere-float model is solved, or this ionosphere-free model.

Considering the structure of the matrix T_j, it should fulfil the following requirements [Teunissen and Odijk, 2002]:

1. The ionospheric delays should be eliminated: $T_j \mu \;=\; 0$.
2. The transformed observables should depend in the same way on the geometry unknowns as the original observables: $T_j e_j \;=\; e_{j-1}$.
3. One ionosphere-free combination should correspond to one integer ambiguity combination, which means that: $T_j \bar{\Lambda}_j \;=\;$ diagonal matrix.

Table 5.3. Ionosphere-free phase combinations for the geometry-based model

	dual-frequency case (j=2)	(future) triple-frequency case (j=3)
T_j	$\begin{bmatrix} \frac{\mu_2}{\mu_2-\mu_1}, & \frac{-\mu_1}{\mu_2-\mu_1} \end{bmatrix} =$ $\begin{bmatrix} \frac{77^2}{77^2-60^2}, & \frac{-60^2}{77^2-60^2} \end{bmatrix}$	$\begin{bmatrix} \frac{\mu_2}{\mu_2-\mu_1} & \frac{-\mu_1}{\mu_2-\mu_1} & 0 \\ 0 & \frac{\mu_3}{\mu_3-\mu_2} & \frac{-\mu_2}{\mu_3-\mu_2} \end{bmatrix} =$ $\begin{bmatrix} \frac{77^2}{77^2-60^2} & \frac{-60^2}{77^2-60^2} & 0 \\ 0 & \frac{24^2}{24^2-23^2} & \frac{-23^2}{24^2-23^2} \end{bmatrix}$
$y^{if}(i)$	$[T_2 \otimes I_{nm}] \left[\Phi_1^{gb}(i)^T, \Phi_2^{gb}(i)^T\right]^T$	$[T_3 \otimes I_{nm}] \left[\Phi_1^{gb}(i)^T, \Phi_2^{gb}(i)^T, \Phi_3^{gb}(i)^T\right]^T$
$Q_{y(i)}^{if}$	$T_2 Q_\phi T_2^T \otimes Q(i)$	$T_3 Q_\phi T_3^T \otimes Q(i)$
$A_I^{if}(i)$	$\begin{bmatrix} \mathcal{A}(i) & [T_2\bar{\Lambda}_2]\,\mathcal{C} \end{bmatrix}$ where $[T_2\bar{\Lambda}_2] = \frac{77}{77^2-60^2}\lambda_1$	$\begin{bmatrix} e_2 \otimes \mathcal{A}(i) & T_3\bar{\Lambda}_3 \otimes \mathcal{C} \end{bmatrix}$ where $T_3\bar{\Lambda}_3 = \mathrm{diag}(\frac{77}{77^2-60^2}\lambda_1, \frac{24}{24^2-23^2}\lambda_2)$
$A_{II}^{if}(i)$	$[T_2C_2]\,\mathcal{D}$ where $[T_2C_2] = -\frac{\mu_1}{\mu_2-\mu_1}$	$T_3C_3 \otimes \mathcal{D}$ where $T_3C_3 = \left[\frac{\mu_3}{\mu_3-\mu_2}, \frac{-\mu_2}{\mu_3-\mu_2}\right]$
x_I^{if}	$\left[g^T,\ \bar{a}_2^T\right]^T$ where $\bar{a}_2 = 77a_1 - 60a_2$	$\left[g^T,\ \bar{a}_3^T\right]^T$ where $\bar{a}_3 = \begin{bmatrix} 77a_1 - 60a_2 \\ 24a_2 - 23a_3 \end{bmatrix}$
$x_{II}^{if}(i)$	$\bar{\alpha}_2(i)$	$\left[\bar{\alpha}_2(i)^T,\ \bar{\alpha}_3(i)^T\right]^T$

In Table 5.3 for the current dual-frequency and the future triple-frequency GPS the transformation matrices T_2 and T_3 and the resulting models of ionosphere-free combinations are given. Note from this table that in the triple-frequency case two ionosphere-free combinations should be processed simultaneously, i.e the current L1/L2 combination and the future L2/L5 combination. This causes additional mathematical correlation in the stochastic model, since both combinations use the L2 phase observables. The (artificial) wavelengths of the ionosphere-free combinations is for the L1/L2 combination $\frac{77}{77^2-60^2}\lambda_1 \approx 0.63$ cm, whereas for the L2/L5 combination this is much longer $\frac{24}{24^2-23^2}\lambda_2 \approx 12.47$ cm.

5.4.4 Redundancy of the ionosphere-weighted model

Similar to what was done for the GPS model in absence of atmospheric errors in Chap. 2, for the ionosphere-weighted model the *redundancy* (i.e. the number of observables minus the number of parameters) can be evaluated, as function of the number of receivers n, satellites m, frequencies j, and observation epochs k. In Table 5.4 these redundancy expressions are given. It is distinguished between the ionosphere-fixed/-weighted models on the one hand ($0 \leq \sigma_\imath < \infty$), and the ionosphere-float model ($\sigma_\imath = \infty$) on the other hand, since in the latter case additional rank deficiencies had to be eliminated, which has its impact on the redundancy. For the sake of completeness, besides the redundancy for the models

based on phase and code data, also the redundancy for the phase-only models are given.

Table 5.4. Redundancy of the ionosphere-weighted models

		phase and code	phase-only
$0 \leq \sigma_\imath < \infty$	geometry-based model	$(n-1)[(m-1)j(2k-1)-w]$	$(n-1)[(m-1)j(k-1)-w]$
	geometry-free model	$(n-1)(m-1)j(2k-1)$	$(n-1)(m-1)j(k-1)$
$\sigma_\imath = \infty$	geometry-based model	$(n-1)[(m-1)\{j(2k-1)-k\}-w]$	$(n-1)[(m-1)(j-1)(k-1)-w]$
	geometry-free model	$(n-1)(m-1)[j(2k-1)-k]$	$(n-1)(m-1)(j-1)(k-1)$

To actually have redundancy in the models, there are certain requirements that should be met. Like in the absence of atmospheric errors, a first trivial requirement is that the number of *receivers* in the network should be at least two ($n \geq 2$). Concerning the number of *satellites* that should be simultaneously tracked, in case of the geometry-free model this is two ($m \geq 2$), which was also the case in the absence of atmospheric delays. For the geometry-based model this number depends on whether ZTDs are estimated ($w = 4$), in that case at least five satellites are necessary ($m \geq 5$), or whether they are not estimated ($w = 3$). In the latter case four satellites are sufficient ($m \geq 4$). The minimum number of observation *epochs* depends on whether code data are included or not. When they are included, the models can be solved using one epoch (instantaneous) ($k \geq 1$), but phase-only models can only be solved with two epochs of data ($k \geq 2$). Considering the number of frequencies, for the ionosphere-fixed and -weighted models it is sufficient to use observations of just one *frequency* ($j \geq 1$), to solve the ionosphere-float model however, at least *two* frequencies are necessary ($j \geq 2$), since no a priori information on the ionospheric delays is used.

5.5 Closed-form vc-matrices of the parameters

As a first step of judging the suitability of the ionosphere-weighted model for precise GPS applications, in this section the precision of the estimated parameters is studied. It is possible to evaluate the (formal) vc-matrices of the parameter estimators without the use of actual GPS observations, since these vc-matrices only depend on the assumed design matrix and vc-matrix of the observations. In this section the vc-matrices for the geometry-free and geometry-based models are derived as *closed-form* expressions, which can be used to investigate the contribution of certain assumptions to the precision of the parameter estimators.

5.5.1 The reduced normal equations

Since the parameters in the ionosphere-weighted model are classified into temporal and non-temporal parameters, the model's *normal equations* are reduced for these temporal parameters. In App. C this procedure, which is also implemented in the

GPSveQ software, is explained in detail. The vc-matrices for the non-temporal parameters in the GPS model, the phase ambiguities and, in case of the geometry-based model, the coordinates and ZTDs, are derived from the following least-squares normal equations, which are *reduced* for the temporal parameters:

$$\underbrace{\left[\sum_{i=1}^{k} A_I(i)^T Q_{y(i)}^{-1} P^{\perp}_{A_{II}(i)} A_I(i)\right]}_{\mathcal{N}} \hat{x}_I \;=\; \underbrace{\sum_{i=1}^{k} A_I(i)^T Q_{y(i)}^{-1} P^{\perp}_{A_{II}(i)} y(i)}_{\mathcal{R}} \tag{5.27}$$

For the derivation of Eq. (5.27), see App. C. The matrix $P^{\perp}_{A_{II}(i)}$ is an orthogonal projector, which is defined as follows:

$$P^{\perp}_{A_{II}(i)} \;=\; I - A_{II}(i)\left[A_{II}(i)^T Q_{y(i)}^{-1} A_{II}(i)\right]^{-1} A_{II}(i)^T Q_{y(i)}^{-1} \tag{5.28}$$

For this orthogonal projector in the same appendix closed-form expressions are given. The matrix $\mathcal{N}$ is referred to as the *(reduced) normal matrix* and the matrix $\mathcal{R}$ as the *(reduced) right-hand side*. The vc-matrix of the geometry and ambiguity parameters is obtained by inverting the reduced normal matrix:

$$Q_{\hat{x}_I} \;=\; \mathcal{N}^{-1} \tag{5.29}$$

In the following subsections this reduced normal matrix is further developed for the geometry-free and geometry-based models.

Geometry-free normal matrix

In case of the *geometry-free* model, the only non-temporal parameters in the model are the ambiguities. Using Table 5.1 and App. C the reduced normal matrix $\mathcal{N}^{gf}$ for these ambiguity parameters can be derived as the following complex expression:

$$\begin{aligned}\mathcal{N}^{gf} \;=\;& \Lambda\Big[Q_\phi^{-1} - \tfrac{\omega+\sigma_\imath^{-2}}{(\omega+\sigma_\imath^{-2})(\eta+\sigma_\varrho^{-2})-\xi^2} Q_\phi^{-1}\mu\mu^T Q_\phi^{-1} + \\ & \tfrac{\xi}{(\omega+\sigma_\imath^{-2})(\eta+\sigma_\varrho^{-2})-\xi^2} Q_\phi^{-1} e_j\mu^T Q_\phi^{-1} + \\ & \tfrac{\xi}{(\omega+\sigma_\imath^{-2})(\eta+\sigma_\varrho^{-2})-\xi^2} Q_\phi^{-1}\mu e_j^T Q_\phi^{-1} - \\ & \tfrac{(\eta+\sigma_\varrho^{-2})}{(\omega+\sigma_\imath^{-2})(\eta+\sigma_\varrho^{-2})-\xi^2} Q_\phi^{-1}\mu\mu^T Q_\phi^{-1}\Big] \Lambda \otimes \Big[\textstyle\sum_{i=1}^{k} \mathcal{C}^T Q(i)^{-1} P^{\perp}_{\mathcal{D}(i)} \mathcal{C}\Big]\end{aligned} \tag{5.30}$$

In this normal matrix the orthogonal projector of the matrix $\mathcal{D}$ appears (this is the partial design matrix of the clock parameters), which is computed as:

$$P^{\perp}_{\mathcal{D}(i)} \;=\; I_{nm} \;-\; \mathcal{D}\left(\mathcal{D}^T Q(i)^{-1}\mathcal{D}\right)^{-1}\mathcal{D}^T Q(i)^{-1} \tag{5.31}$$

The scalars η, ω and ξ in the normal matrix in Eq. (5.30) are defined as follows, see App. C:

$$\begin{aligned}\eta &= \left[e_j^T\left(Q_\phi^{-1}+Q_p^{-1}\right)e_j\right] \\ \omega &= \left[\mu^T\left(Q_\phi^{-1}+Q_p^{-1}\right)\mu\right] \\ \xi &= \left[\mu^T\left(Q_\phi^{-1}-Q_p^{-1}\right)e_j\right]\end{aligned} \tag{5.32}$$

Geometry-based normal matrix

Using the expressions in Table 5.1 and in App. C, the normal matrix for the coordinate and ambiguity parameters of the *geometry-based* model, which is denoted as $\mathcal{N}^{gb}$, can be written as:

$$\mathcal{N}^{gb} = \begin{bmatrix} \mathcal{N}_g & \mathcal{N}_{ag}^T \\ \mathcal{N}_{ag} & \mathcal{N}_a \end{bmatrix} \tag{5.33}$$

The elements of this normal matrix read:

$$\boxed{\begin{array}{rcl} \mathcal{N}_g & = & \frac{(\omega+\sigma_i^{-2})\eta-\xi^2}{\omega+\sigma_i^{-2}} \left[\sum_{i=1}^k \mathcal{A}(i)^T Q(i)^{-1} P_{\mathcal{D}(i)}^{\perp} \mathcal{A}(i)\right] \\ \mathcal{N}_{ag} & = & \Lambda Q_\phi^{-1} \left[e_j - \frac{\xi}{\omega+\sigma_i^{-2}}\mu\right] \otimes \left[\sum_{i=1}^k \mathcal{C}^T Q(i)^{-1} P_{\mathcal{D}(i)}^{\perp} \mathcal{A}(i)\right] \\ \mathcal{N}_a & = & \Lambda \left[Q_\phi^{-1} - \frac{1}{\omega+\sigma_i^{-2}} Q_\phi^{-1}\mu\mu^T Q_\phi^{-1}\right] \Lambda \otimes \left[\sum_{i=1}^k \mathcal{C}^T Q(i)^{-1} P_{\mathcal{D}(i)}^{\perp} \mathcal{C}\right] \end{array}} \tag{5.34}$$

5.5.2 Simplifying the normal equations

In case of the geometry-based model, it is unfortunately extremely difficult to obtain a closed-form expression for the vc-matrix $Q_{\hat{x}_I}$. This is due to the presence of the receiver-satellite geometry vectors, which depend on the time of day, location on Earth, etc. With some simplifications however, it is possible to invert the normal matrix in an analytical way. Under the assumption that the distances between the receivers in the network is restricted (*medium-distance*), the unit vectors from all receivers to one satellite may be assumed as parallel vectors, such that the following approximation can be made:

$$G_2(i) \approx \ldots \approx G_n(i) \equiv G(i) \tag{5.35}$$

As a consequence, the partial design matrix $\mathcal{A}(i)$ can be written as a Kronecker product:

$$\mathcal{A}(i) = C_n \otimes G(i) \tag{5.36}$$

The normal equations can be further simplified, since in App. D a closed-form expression is derived for the matrix product $Q(i)^{-1}P_{\mathcal{D}(i)}^{\perp}$ which appears in Eq. (5.34), again under the assumption of a limited sized network. When it is furthermore assumed that the precision of the observations is equal for all observations of one observable type at all epochs, i.e. $Q(i) = I_{nm}$, this product reduces to:

$$Q(i)^{-1}P_{\mathcal{D}(i)}^{\perp} = P_{e_n}^{\perp} \otimes P_{e_m}^{\perp} = \left[I_n - \frac{1}{n}e_n e_n^T\right] \otimes \left[I_m - \frac{1}{m}e_m e_m^T\right] \tag{5.37}$$

Using this and $\mathcal{C} = C_n \otimes C_m$, for the receiver-dependent part of the product $\mathcal{C}^T Q(i)^{-1} P_{\mathcal{D}(i)}^{\perp} \mathcal{C}$ in Eq. (5.34) it follows that:

$$C_n^T P_{e_n}^{\perp} C_n = I_{n-1} - \frac{1}{n}e_{n-1}e_{n-1}^T = \left(D_n^T D_n\right)^{-1} \tag{5.38}$$

since $D_n^T D_n = I_{n-1} + e_{n-1}e_{n-1}^T$. A similar derivation can be made for the satellite-dependent part in the product.

Using the above approximations, the time-dependent summations in the normal matrices in Eq. (5.30) and Eq. (5.34) reduce to the following more simplified expressions:

$$\boxed{\begin{array}{lcl} \sum_{i=1}^{k} \mathcal{A}(i)^T Q(i)^{-1} P^{\perp}_{\mathcal{D}(i)} \mathcal{A}(i) & = & \left(D_n^T D_n\right)^{-1} \otimes \sum_{i=1}^{k} G(i)^T P^{\perp}_{e_m} G(i) \\ \sum_{i=1}^{k} \mathcal{C}^T Q(i)^{-1} P^{\perp}_{\mathcal{D}(i)} \mathcal{A}(i) & = & \left(D_n^T D_n\right)^{-1} \otimes k D_m^{+} \bar{G} \\ \sum_{i=1}^{k} \mathcal{C}^T Q(i)^{-1} P^{\perp}_{\mathcal{D}(i)} \mathcal{C} & = & \left(D_n^T D_n\right)^{-1} \otimes k \left(D_m^T D_m\right)^{-1} \end{array}} \tag{5.39}$$

Note that in the second equation of Eq. (5.39), $C_m^T P^{\perp}_{e_m} = \left(D_m^T D_m\right)^{-1} D_m^T \doteq D_m^{+}$ denotes the *pseudo-inverse* of D_m and matrix $\bar{G}$ denotes the *time-averaged* receiver-satellite geometry matrix over k epochs:

$$\boxed{\bar{G} \;=\; \frac{1}{k} \sum_{i=1}^{k} G(i)} \tag{5.40}$$

5.5.3 The geometry-free vc-matrices

The (float) ambiguity vc-matrix

Using the simplifications of the previous subsection, analytical inversion of the reduced normal matrix of the geometry-free model in Eq. (5.30) results in:

$$\begin{aligned} \mathcal{N}^{gf\,-1} \;=\; \Lambda^{-1} \;\Big[& Q_\phi + \tfrac{1}{\omega' + \sigma_\imath^{-2}} \mu\mu^T + \\ & \left(\tfrac{\omega' + \sigma_\imath^{-2}}{(\omega' + \sigma_\imath^{-2})(\eta' + \sigma_\varrho^{-2}) - \xi'^2} e_j - \tfrac{\xi'}{(\omega' + \sigma_\imath^{-2})(\eta' + \sigma_\varrho^{-2}) - \xi'^2} \mu \right) \\ & \left(\tfrac{\omega' + \sigma_\imath^{-2}}{(\omega' + \sigma_\imath^{-2})(\eta' + \sigma_\varrho^{-2}) - \xi'^2} e_j - \tfrac{\xi'}{(\omega' + \sigma_\imath^{-2})(\eta' + \sigma_\varrho^{-2}) - \xi'^2} \mu \right)^T \Big] \Lambda^{-1} \otimes \\ & \left[D_n^T D_n \otimes \tfrac{1}{k} D_m^T D_m \right] \end{aligned} \tag{5.41}$$

In this expression the inverse of the diagonal wavelength matrix is simply computed as $\Lambda^{-1} = \mathrm{diag}(1/\lambda_1, \;\ldots\; , 1/\lambda_j)$. Moreover, the scalars η', ω' and ξ' are defined as:

$$\begin{array}{lcl} \eta' & = & \left[e_j^T Q_p^{-1} e_j \right] \\ \omega' & = & \left[\mu^T Q_p^{-1} \mu \right] \\ \xi' & = & -\left[\mu^T Q_p^{-1} e_j \right] \end{array} \tag{5.42}$$

So these scalars only depend on the inverse of the priori *code* vc-matrix. Compare these scalars with their counterparts in Eq. (5.32), which depend on the sum of inverse of both *phase and code* vc-matrices.

The scalar elements in front of the vectors e_j and μ in Eq. (5.41) can be recognized as (co-) variances of the *double-differenced* range and ionosphere unknowns

of the (ambiguity-float) geometry-free model using a *single* observation epoch, cf. [Teunissen, 1998d]:

$$\begin{bmatrix} \frac{\eta'+\sigma_\varrho^{-2}}{(\omega'+\sigma_\imath^{-2})(\eta'+\sigma_\varrho^{-2})-\xi'^2} & \frac{\xi'}{(\omega'+\sigma_\imath^{-2})(\eta'+\sigma_\varrho^{-2})-\xi'^2} \\ \frac{\xi'}{(\omega'+\sigma_\imath^{-2})(\eta'+\sigma_\varrho^{-2})-\xi'^2} & \frac{\omega'+\sigma_\imath^{-2}}{(\omega'+\sigma_\imath^{-2})(\eta'+\sigma_\varrho^{-2})-\xi'^2} \end{bmatrix} \doteq \frac{1}{4}\begin{bmatrix} \sigma^2_{\hat{\imath}^{dd}(\imath,\varrho)} & \sigma_{\hat{\imath}\hat{\varrho}^{dd}(\imath,\varrho)} \\ \sigma_{\hat{\varrho}\hat{\imath}^{dd}(\imath,\varrho)} & \sigma^2_{\hat{\varrho}^{dd}(\imath,\varrho)} \end{bmatrix} \tag{5.43}$$

To emphasize that these variances and covariances are a function of the a priori ionosphere and range precision, they are denoted using $(\imath,\varrho)$. The factor $\frac{1}{4}$ appears in Eq. (5.43), since the variances of the estimated range and ionosphere parameters are in double-difference mode, whereas the a priori vc-matrices are all in undifferenced mode.

From Eq. (5.43) it follows that when the a priori range standard deviation is set to zero, i.e. $\sigma_\varrho = 0$, the so-called *range-fixed* ionospheric variance is obtained as:

$$\sigma^2_{\hat{\imath}^{dd}(\imath)|\varrho} = 4\frac{1}{\omega'+\sigma_\imath^{-2}} \tag{5.44}$$

which is equal to four times the scalar in front of $\mu\mu^T$ in Eq. (5.41).

Using the DD variances and covariances as given above, the *ambiguity vc-matrix* of the geometry-free model can finally be written as the following compact expression:

$$\begin{aligned} Q_{\hat{a}(\imath,\varrho)} = {} & \Lambda^{-1}\left[Q_\phi + \tfrac{1}{4}\sigma^2_{\hat{\imath}^{dd}(\imath)|\varrho}\mu\mu^T\right]\Lambda^{-1} \otimes \tfrac{1}{k}Q^{dd}(i) + \\ & \Lambda^{-1}\left[e_j - \frac{\sigma_{\hat{\varrho}\hat{\imath}^{dd}(\imath,\varrho)}}{\sigma^2_{\hat{\varrho}^{dd}(\imath,\varrho)}}\mu\right]\left[e_j - \frac{\sigma_{\hat{\varrho}\hat{\imath}^{dd}(\imath,\varrho)}}{\sigma^2_{\hat{\varrho}^{dd}(\imath,\varrho)}}\mu\right]^T\Lambda^{-1} \otimes \tfrac{1}{4}\sigma^2_{\hat{\varrho}^{dd}(\imath,\varrho)}\tfrac{1}{k}Q^{dd}(i) \end{aligned} \tag{5.45}$$

where $Q^{dd}(i) = D_n^T D_n \otimes D_m^T D_m$, see also Eq. (2.72). Note that from this closed-form expression already several interesting aspects are visible, which are relevant for ambiguity resolution, since this for a large part depends on the ambiguity vc-matrix. Trivial aspects that can be seen from the expression are that the precision of the ambiguities improves when the precision of the phase data improves and when the number of epochs is increased. More interesting is that when the precision with which the ranges and the ionospheric delays are estimated improves, this also has a beneficial effect on the precision of the ambiguities.

The fixed ionosphere and range vc-matrices

After the integer ambiguities are resolved, for the other parameters of the geometry-free model ambiguity-fixed vc-matrices can be computed. Since the ambiguities are the only non-temporal parameters in the geometry-free model, from App. C

it follows that when $Q_{\hat{x}_I} = 0$, the vc-matrix of the temporal parameters is simply obtained as:

$$\boxed{\begin{array}{lcll} Q_{\hat{x}_{II}(i)} & = & \Big[A_{II}(i)^T Q_{y(i)}^{-1} A_{II}(i)\Big]^{-1}, & i = 1, \ldots, k \\ Q_{\hat{x}_{II}(i)\hat{x}_{II}(l)} & = & 0, & i \neq l \end{array}} \tag{5.46}$$

So when the ambiguities are fixed, the temporal parameters become *uncorrelated* in time.

Using Table C.2 in App. C, the vc-matrix of the fixed *undifferenced* ionosphere and range parameters together, follows as:

$$\begin{bmatrix} Q_{\check{\imath}(\imath,\varrho)}(i) & Q_{\check{\imath}\check{\varrho}(\imath,\varrho)}(i) \\ Q_{\check{\varrho}\check{\imath}(\imath,\varrho)}(i) & Q_{\check{\varrho}(\imath,\varrho)}(i) \end{bmatrix} = \begin{bmatrix} \sigma_\imath^2 & \\ & \sigma_\varrho^2 \end{bmatrix} \otimes [I_n \otimes I_m] - \begin{bmatrix} \frac{\sigma_\imath^2\left[\omega(\eta+\sigma_\varrho^{-2})-\xi^2\right]}{(\omega+\sigma_\imath^{-2})(\eta+\sigma_\varrho^{-2})-\xi^2} & -\frac{\xi}{(\omega+\sigma_\imath^{-2})(\eta+\sigma_\varrho^{-2})-\xi^2} \\ -\frac{\xi}{(\omega+\sigma_\imath^{-2})(\eta+\sigma_\varrho^{-2})-\xi^2} & \frac{\sigma_\varrho^2\left[\eta(\omega+\sigma_\imath^{-2})-\xi^2\right]}{(\omega+\sigma_\imath^{-2})(\eta+\sigma_\varrho^{-2})-\xi^2} \end{bmatrix} \otimes \left[P_{e_n}^\perp \otimes P_{e_m}^\perp\right] \tag{5.47}$$

where η, ω and ξ are defined in Eq. (5.32). Since for relative GPS applications the double-differenced parameters play a prominent role, it is worthwhile to derive the vc-matrix of the *double-differenced* ionosphere and range parameters. This vc-matrix is obtained from the undifferenced vc-matrix in Eq. (5.47) by applying the double-difference operators D_n^T and D_m^T. Since it holds that $\left(D_n^T P_{e_n}^\perp\right) \otimes \left(D_m^T P_{e_m}^\perp\right) = D_n^T \otimes D_m^T$, the vc-matrix of the DD ionosphere and range parameters follows as:

$$\begin{bmatrix} Q_{\check{\imath}^{dd}(\imath,\varrho)}(i) & Q_{\check{\imath}\check{\varrho}^{dd}(\imath,\varrho)}(i) \\ Q_{\check{\varrho}\check{\imath}^{dd}(\imath,\varrho)}(i) & Q_{\check{\varrho}^{dd}(\imath,\varrho)}(i) \end{bmatrix} = \begin{bmatrix} \frac{\eta+\sigma_\varrho^{-2}}{(\omega+\sigma_\imath^{-2})(\eta+\sigma_\varrho^{-2})-\xi^2} & \frac{\xi}{(\omega+\sigma_\imath^{-2})(\eta+\sigma_\varrho^{-2})-\xi^2} \\ \frac{\xi}{(\omega+\sigma_\imath^{-2})(\eta+\sigma_\varrho^{-2})-\xi^2} & \frac{\omega+\sigma_\imath^{-2}}{(\omega+\sigma_\imath^{-2})(\eta+\sigma_\varrho^{-2})-\xi^2} \end{bmatrix} \otimes Q^{dd}(i) \tag{5.48}$$

Note that in this DD vc-matrix, the scalar elements in the 2×2 matrix in Eq. (5.48) can be nicely recognized as the *ambiguity-fixed* counterparts of the single-epoch DD ionosphere and range (co-) variances as given in Eq. (5.43):

$$\boxed{\begin{bmatrix} \frac{\eta+\sigma_\varrho^{-2}}{(\omega+\sigma_\imath^{-2})(\eta+\sigma_\varrho^{-2})-\xi^2} & \frac{\xi}{(\omega+\sigma_\imath^{-2})(\eta+\sigma_\varrho^{-2})-\xi^2} \\ \frac{\xi}{(\omega+\sigma_\imath^{-2})(\eta+\sigma_\varrho^{-2})-\xi^2} & \frac{\omega+\sigma_\imath^{-2}}{(\omega+\sigma_\imath^{-2})(\eta+\sigma_\varrho^{-2})-\xi^2} \end{bmatrix} \doteq \frac{1}{4}\begin{bmatrix} \sigma^2_{\check{\imath}^{dd}(\imath,\varrho)} & \sigma_{\check{\imath}\check{\varrho}^{dd}(\imath,\varrho)} \\ \sigma_{\check{\varrho}\check{\imath}^{dd}(\imath,\varrho)} & \sigma^2_{\check{\varrho}^{dd}(\imath,\varrho)} \end{bmatrix}} \tag{5.49}$$

This ambiguity-fixed precision is, as expected, governed by the *phase* precision, whereas its ambiguity-float counterpart is determined by the *code* precision.

5.5.4 The geometry-based vc-matrices

Float coordinate and ambiguity vc-matrices

For the geometry-based model, the inverse of the reduced normal matrix in Eq. (5.33) is computed using the well-known matrix lemma, see e.g. [Koch, 1999], resulting in:

$$\mathcal{N}^{gb^{-1}} = \begin{bmatrix} Q_{\hat{g}(\imath)} & -Q_{\hat{g}(\imath)}\mathcal{N}_{ag}^T\mathcal{N}_a^{-1} \\ -\mathcal{N}_a^{-1}\mathcal{N}_{ag}Q_{\hat{g}(\imath)} & \left(\mathcal{N}_a^{-1}+\mathcal{N}_a^{-1}\mathcal{N}_{ag}Q_{\hat{g}(\imath)}\mathcal{N}_{ag}^T\mathcal{N}_a^{-1}\right) \end{bmatrix} \tag{5.50}$$

where $Q_{\hat{g}(\imath)} = \left(\mathcal{N}_g - \mathcal{N}_{ag}\mathcal{N}_a^{-1}\mathcal{N}_{ag}\right)^{-1}$. In this inverse normal matrix the float vc-matrix of the geometry parameters (coordinates, ZTDs), $Q_{\hat{g}(\imath)}$, is not yet specified. It is computed as:

$$\boxed{Q_{\hat{g}(\imath)} = \tfrac{1}{2}D_n^T D_n \otimes Q_{\hat{b}(\imath)}} \tag{5.51}$$

where $Q_{\hat{b}(\imath)}$ denotes the float geometry vc-matrix of one of the receivers in the network. Note that in case of a *single-baseline*, it holds that $Q_{\hat{g}(\imath)} = Q_{\hat{b}(\imath)}$. This matrix is computed as [Teunissen, 1998d]:

$$Q_{\hat{b}(\imath)} = \sigma^2_{\hat{e}^{dd}(\imath)}\left[\frac{\sigma^2_{\hat{e}^{dd}(\imath)}}{\sigma^2_{\hat{e}^{dd}(\imath)}}2k\bar{G}^T P^{\perp}_{e_m}\bar{G} \;+\; 2\sum_{i=1}^{k}\left(G(i)-\bar{G}\right)^T P^{\perp}_{e_m}\left(G(i)-\bar{G}\right)\right]^{-1} \tag{5.52}$$

Because of the dependence on the actual receiver-satellite geometry, it is not possible to further develop the inverse term in Eq. (5.52).

The complete ambiguity-float vc-matrix of the non-temporal parameters is denoted as:

$$Q_{\hat{x}_I} = \begin{bmatrix} Q_{\hat{g}(\imath)} & Q^T_{\hat{a}\hat{g}(\imath)} \\ Q_{\hat{a}\hat{g}(\imath)} & Q_{\hat{a}(\imath)} \end{bmatrix} \tag{5.53}$$

The different parts of this vc-matrix can be computed as follows, using the simplifications in Sect. 5.5.2:

$$\boxed{\begin{aligned} Q_{\hat{a}\hat{g}(\imath)} &= \Lambda^{-1}\left[e_j - \tfrac{\sigma_{\hat{\varrho}\hat{\imath}^{dd}(\imath)}}{\sigma^2_{\hat{\varrho}^{dd}(\imath)}}\mu\right]\otimes\left[\tfrac{1}{2}D_n^T D_n \otimes D_m^T\bar{G}Q_{\hat{b}(\imath)}\right] \\ Q_{\hat{a}(\imath)} &= \Lambda^{-1}\left[Q_\phi + \tfrac{1}{4}\sigma^2_{\hat{\imath}^{dd}(\imath)|\varrho}\mu\mu^T\right]\Lambda^{-1}\otimes\tfrac{1}{k}Q^{dd}(i) + \\ &\quad \Lambda^{-1}\left[e_j - \tfrac{\sigma_{\hat{\varrho}\hat{\imath}^{dd}(\imath)}}{\sigma^2_{\hat{\varrho}^{dd}(\imath)}}\mu\right]\left[e_j - \tfrac{\sigma_{\hat{\varrho}\hat{\imath}^{dd}(\imath)}}{\sigma^2_{\hat{\varrho}^{dd}(\imath)}}\mu\right]^T\Lambda^{-1}\otimes \\ &\quad \left[\tfrac{1}{2}D_n^T D_n \otimes D_m^T\bar{G}Q_{\hat{b}(\imath)}\bar{G}^T D_m\right] \end{aligned}} \tag{5.54}$$

Note the correspondence of the geometry-based ambiguity vc-matrix with its geometry-free counterpart in Eq. (5.45). Like in the geometry-free case, in the

geometry-based expressions also the ambiguity-float single-epoch DD range and ionosphere (co-) variances appear. There is however an important difference with the geometry-free model: For the geometry-based model the standard deviation of the ranges needs to be set to *infinity*: $\sigma_\varrho = \infty$. This means that the *range-float* variances should be applied here.

For the geometry-based model, the ambiguity vc-matrix consists of two parts: A part which is *independent* of the receiver-satellite geometry (the first part of $Q_{\hat{a}(\imath)}$) and a part which depends on it (the second part, after the plus sign). When this geometry is a priori *known* (when the receiver coordinates are known), so when it is assumed that $Q_{\hat{b}(\imath)} = 0$, the geometry-based ambiguity vc-matrix becomes *equivalent* with the vc-matrix of the geometry-free model with $\sigma_\varrho = 0$ (*range-fixed*):

$$\boxed{Q_{\hat{a}(\imath)|g} \;=\; Q_{\hat{a}(\imath)|\varrho} \;=\; \Lambda^{-1}\left[Q_\phi + \tfrac{1}{4}\sigma^2_{\hat{\imath}^{dd}(\imath)|\varrho}\mu\mu^T\right]\Lambda^{-1} \otimes \tfrac{1}{k}Q^{dd}(i)} \tag{5.55}$$

From this expression it follows that in case of a priori known receiver-satellite ranges, the precision of the ambiguities only depends on the a priori precision of the phase data and the precision with which the ionospheric delays can be estimated (which depends on the a priori code precision). Although the geometry parameters are fixed, the ambiguities are *not* uncorrelated, even when Q_ϕ is a diagonal matrix. There remains correlation due to the fact that one set of ionospheric delay parameters is estimated for all frequencies and there is also correlation due to double-differencing.

Fixed coordinate and ionosphere vc-matrices

When it is allowed to fix the ambiguities as *deterministic* quantities, the geometry parameters remain as the only non-temporal parameters in the geometry-based model. The *ambiguity-fixed* vc-matrix of the geometry parameters can be computed by simply inverting $\mathcal{N}_g$. Applying the simplifications as discussed in Sect. 5.5.2 we find for the fixed geometry vc-matrix:

$$\boxed{Q_{\check{g}(\imath)} \;=\; \tfrac{1}{2}D_n^T D_n \otimes Q_{\check{b}(\imath)}} \tag{5.56}$$

with $Q_{\check{b}(\imath)}$ the fixed vc-matrix in case of a single-baseline [Teunissen, 1998d]:

$$Q_{\check{b}(\imath)} \;=\; \sigma^2_{\check{\varrho}^{dd}(\imath)}\left[2\sum_{i=1}^{k} G(i)^T P^\perp_{e_m} G(i)\right]^{-1} \tag{5.57}$$

The ambiguity-fixed vc-matrix of the *temporal* parameters (ionospheric delays) is time-correlated, because of the presence of the time-constant geometry parameters.

It can be computed using the following formulas (see App. C):

$$\boxed{\begin{array}{rcl} Q_{\hat{x}_{II}(i)} & = & \left[A_{II}(i)^T Q_{y(i)}^{-1} A_{II}(i)\right]^{-1} + \left[A_{II}(i)^T Q_{y(i)}^{-1} A_{II}(i)\right]^{-1} A_{II}(i)^T \cdot \\ & & Q_{y(i)}^{-1}\left[A_I(i) Q_{\hat{x}_I} A_I(i)^T\right] Q_{y(i)}^{-1} A_{II}(i)\left[A_{II}(i)^T Q_{y(i)}^{-1} A_{II}(i)\right]^{-1} \\ Q_{\hat{x}_{II}(i)\hat{x}_{II}(l)} & = & \left[A_{II}(i)^T Q_{y(i)}^{-1} A_{II}(i)\right]^{-1} A_{II}(i)^T Q_{y(i)}^{-1}\left[A_I(i) Q_{\hat{x}_I} A_I(l)^T\right] \cdot \\ & & Q_{y(l)}^{-1} A_{II}(l)\left[A_{II}(l)^T Q_{y(l)}^{-1} A_{II}(l)\right]^{-1}, \quad i \neq l \end{array}} \tag{5.58}$$

In this case the vc-matrix of the non-temporal parameters, $Q_{\hat{x}_I}$, equals $Q_{\check{g}(\imath)}$. For the matrix $\left[A_{II}(i)^T Q_{y(i)}^{-1} A_{II}(i)\right]^{-1}$ the part corresponding to the ionospheric delays of the geometry-free model can be taken, see Eq. (5.46). Like in the case of the geometry-free model, we compute for the geometry-based model the vc-matrix of the *double-difference* ionospheric delays, instead of the undifferenced delays:

$$\boxed{\left[A_{II}(i)^T Q_{y(i)}^{-1} A_{II}(i)\right]^{-1} \;=\; Q_{\check{\imath}^{dd}(\imath)|\varrho}(i) \;=\; \frac{1}{4}\sigma^2_{\check{\imath}^{dd}(\imath)|\varrho} Q^{dd}(i)} \tag{5.59}$$

where $\frac{1}{4}\sigma^2_{\check{\imath}^{dd}(\imath)|\varrho} = \frac{1}{\omega+\sigma_\imath^{-2}}$. Note that this is in fact the vc-matrix of the ambiguity-fixed DD ionospheric delays when all coordinates and ZTDs in the networks are fixed as well. To compute the other parts of the vc-matrix of the ionospheric delays in the geometry-based model, we find using Table C.2 in App. C:

$$\left[A_{II}(i)^T Q_{y(i)}^{-1} A_{II}(i)\right]^{-1} A_{II}(i)^T Q_{y(i)}^{-1} A_I(i) \;=\; \tfrac{-\xi}{\omega+\sigma_\imath^{-2}}\left[P^\perp_{e_n} C_n \otimes P^\perp_{e_m} G(i)\right] \tag{5.60}$$

In this expression the ratio $\frac{\sigma_{\check{\varrho}\check{\imath}^{dd}(\imath)}}{\sigma^2_{\check{\varrho}^{dd}(\imath)}} = \frac{\xi}{\omega+\sigma_\imath^{-2}}$ can be recognized. This results in:

$$\begin{aligned} &\left[A_{II}(i)^T Q_{y(i)}^{-1} A_{II}(i)\right]^{-1} A_{II}(i)^T Q_{y(i)}^{-1}\left[A_I(i) Q_{\hat{x}_I} A_I(i)^T\right] Q_{y(i)}^{-1} A_{II}(i)\left[A_{II}(i)^T Q_{y(i)}^{-1} A_{II}(i)\right]^{-1} = \\ &\qquad \left[\frac{\sigma_{\check{\varrho}\check{\imath}^{dd}(\imath)}}{\sigma^2_{\check{\varrho}^{dd}(\imath)}}\right]^2 \left[\frac{1}{2} P^\perp_{e_n} C_n D_n^T D_n C_n^T P^\perp_{e_n} \otimes P^\perp_{e_m} G(i) Q_{\check{b}(\imath)} G(i)^T P^\perp_{e_m}\right] \end{aligned} \tag{5.61}$$

To obtain the vc-matrix of the *double-difference* ionospheric delays, the difference operators D_n^T and D_m^T need to be applied to the second part of the right-hand side of Eq. (5.61):

$$\begin{aligned} &\left[D_n^T \otimes D_m^T\right]\left[\tfrac{1}{2} P^\perp_{e_n} C_n D_n^T D_n C_n^T P^\perp_{e_n} \otimes P^\perp_{e_m} G(i) Q_{\check{b}(\imath)} G(i)^T P^\perp_{e_m}\right]\left[D_n \otimes D_m\right] \\ &= \tfrac{1}{2} D_n^T P^\perp_{e_n} C_n D_n^T D_n C_n^T P^\perp_{e_n} D_n \otimes D_m^T P^\perp_{e_m} G(i) Q_{\check{b}(\imath)} G(i)^T P^\perp_{e_m} D_m \\ &= \tfrac{1}{2} D_n^T D_n \otimes D_m^T G(i) Q_{\check{b}(\imath)} G(i)^T D_m \end{aligned} \tag{5.62}$$

Note that use is made of the equalities $D_n^T P_{e_n}^{\perp} = D_n^T$ and $D_n^T C_n = I_{n-1}$. Finally, the compact expression for the vc-matrix of the ambiguity-fixed DD ionospheric delays reads as follows:

$$\begin{array}{rcl} Q_{\check{\imath}^{dd}(\imath)}(i) & = & Q_{\check{\imath}^{dd}(\imath)|\varrho}(i) \; + \; \left[\frac{\sigma_{\check{\varrho}\check{\imath}^{dd}(\imath)}}{\sigma^2_{\check{\varrho}^{dd}(\imath)}}\right]^2 \left[\tfrac{1}{2} D_n^T D_n \otimes D_m^T G(i) Q_{\check{b}(\imath)} G(i)^T D_m\right] \\ Q_{\check{\imath}^{dd}(\imath)}(i,l) & = & \left[\frac{\sigma_{\check{\varrho}\check{\imath}^{dd}(\imath)}}{\sigma^2_{\check{\varrho}^{dd}(\imath)}}\right]^2 \left[\tfrac{1}{2} D_n^T D_n \otimes D_m^T G(i) Q_{\check{b}(\imath)} G(l)^T D_m\right], \quad i \neq l \end{array} \tag{5.63}$$

Like the ambiguity vc-matrix, the vc-matrix of the fixed ionospheric delays consists of a part independent of the receiver-satellite geometry ($Q_{\check{\imath}^{dd}(\imath)|\varrho}(i)$) and a part which depends on it. Note that when the receiver coordinates are known, the vc-matrix becomes $Q_{\check{\imath}^{dd}(\imath)|\varrho}$, which is *uncorrelated* in time.

5.6 Analyzing the (formal) coordinate precision

To infer whether the ionosphere-weighted model can be applied for precise positioning applications, in this section the expected precision of the *coordinate* parameters is analyzed. Starting point of this analysis is the in the previous section derived expressions for the vc-matrix of the coordinates. For a *single-baseline* they read in the ambiguity-float respectively ambiguity-fixed case, see Eq. (5.52) and Eq. (5.57):

$$\begin{array}{rcl} Q_{\hat{b}(\imath)} & = & \sigma^2_{\check{\varrho}^{dd}(\imath)} \left[\frac{\sigma^2_{\check{\varrho}^{dd}(\imath)}}{\sigma^2_{\check{\varrho}^{dd}(\imath)}} 2k \bar{G}^T P_{e_m}^{\perp} \bar{G} \; + \; 2\sum_{i=1}^{k} \left(G(i) - \bar{G}\right)^T P_{e_m}^{\perp} \left(G(i) - \bar{G}\right)\right]^{-1} \\ Q_{\check{b}(\imath)} & = & \sigma^2_{\check{\varrho}^{dd}(\imath)} \left[2 \sum_{i=1}^{k} G(i)^T P_{e_m}^{\perp} G(i)\right]^{-1} \end{array} \tag{5.64}$$

In this section we will investigate the contributing factors to the coordinate precision: The (change of) receiver-satellite geometry, the number of frequencies and the observable noise assumptions in the stochastic model. A distinction is made between single-epoch (instantaneous) applications and multi-epoch applications.

5.6.1 Single-epoch coordinate precision

Reduced closed-form expressions

In the situation only one single-epoch of data is used, the number of epochs is set to $k = 1$ in the expression for the float geometry vc-matrix (Eq. (5.64)). This has the consequence that the summation term within the inverse disappears, since $\bar{G} = G(i)$. The expressions for the vc-matrices in Eq. (5.64) reduce to:

$$Q_{\hat{b}(\imath)}^{k=1} \; = \; \sigma^2_{\check{\varrho}^{dd}(\imath)} \left[2G(1)^T P_{e_m}^{\perp} G(1)\right]^{-1}, \qquad Q_{\check{b}(\imath)}^{k=1} \; = \; \sigma^2_{\check{\varrho}^{dd}(\imath)} \left[2G(1)^T P_{e_m}^{\perp} G(1)\right]^{-1}$$

(5.65)

So the structure of both vc-matrices become very similar in the single-epoch case. The only difference between both is the single-epoch variance in front of the inverse term: In the float case this is the variance of the *float* DD ranges, whereas in the fixed case this is its *fixed* counterpart. Both variances can be computed by setting $\sigma_\varrho = \infty$ in Eq. (5.43), respectively Eq. (5.49). This nice decomposition of the vc-matrices of the coordinate parameters implies that the benefit of *ambiguity resolution* on the single-epoch coordinate precision, is completely governed by the difference in variances $\sigma^2_{\hat{\varrho}^{dd}(\imath)}$ and $\sigma^2_{\check{\varrho}^{dd}(\imath)}$.

Analyzing the DD range and ionosphere precision

From Eq. (5.43) and Eq. (5.49) it appears that the ambiguity-float variances of the ranges (and the ionospheric delays as well) are completely determined by the a priori *code* precision, while their ambiguity-fixed counterparts are determined by both a priori *phase and code* vc-matrices. However, since the phase precision is much better than the code precision (about a factor 100), the ambiguity-fixed ionosphere and range variances are predominantly governed by the a priori *phase* precision. This can be shown as follows. Suppose that the vc-matrices of the phase and code observables may be assumed as diagonal vc-matrices with a constant variance, $Q_\phi = \sigma^2_\phi I_j$ and $Q_p = \sigma^2_p I_j$. Since the phase precision is much better than the code precision, i.e. $\sigma^2_\phi/\sigma^2_p \approx 10^{-4}$, neglecting this factor in Eq. (5.43) and Eq. (5.49) results in the following expressions for the ambiguity-float respectively ambiguity-fixed range/ionosphere precision:

$$\begin{aligned}
\begin{bmatrix} \sigma^2_{\hat{\imath}^{dd}(\imath)} & \sigma_{\hat{\imath}\hat{\varrho}^{dd}(\imath)} \\ \sigma_{\hat{\varrho}\hat{\imath}^{dd}(\imath)} & \sigma^2_{\hat{\varrho}^{dd}(\imath)} \end{bmatrix} &= \frac{4\sigma^2_p}{\left[e_j^T e_j\right]\left(\left[\mu^T\mu\right]+\frac{\sigma^2_p}{\sigma^2_\imath}\right)-\left[\mu^T e_j\right]^2} \begin{bmatrix} \left[e_j^T e_j\right] & \left[e_j^T \mu\right] \\ \left[\mu^T e_j\right] & \left[\mu^T\mu\right]+\frac{\sigma^2_p}{\sigma^2_\imath} \end{bmatrix} \\
\sigma^2_{\hat{\imath}^{dd}(\imath)|\varrho} &= \frac{4\sigma^2_p}{\left[\mu^T\mu\right]+\frac{\sigma^2_p}{\sigma^2_\imath}} \\
\\
\begin{bmatrix} \sigma^2_{\check{\imath}^{dd}(\imath)} & \sigma_{\check{\imath}\check{\varrho}^{dd}(\imath)} \\ \sigma_{\check{\varrho}\check{\imath}^{dd}(\imath)} & \sigma^2_{\check{\varrho}^{dd}(\imath)} \end{bmatrix} &\approx \frac{4\sigma^2_\phi}{\left[e_j^T e_j\right]\left(\left[\mu^T\mu\right]+\frac{\sigma^2_\phi}{\sigma^2_\imath}\right)-\left[\mu^T e_j\right]^2} \begin{bmatrix} \left[e_j^T e_j\right] & \left[e_j^T \mu\right] \\ \left[\mu^T e_j\right] & \left[\mu^T\mu\right]+\frac{\sigma^2_\phi}{\sigma^2_\imath} \end{bmatrix} \\
\sigma^2_{\check{\imath}^{dd}(\imath)|\varrho} &\approx \frac{4\sigma^2_\phi}{\left[\mu^T\mu\right]+\frac{\sigma^2_\phi}{\sigma^2_\imath}}
\end{aligned} \tag{5.66}$$

Using these simplifications, the only difference between the float and fixed precision is that on the places where the code standard deviation appears in the float expressions, in their fixed counterparts it is replaced by the phase standard deviation.

Figures 5.1 – 5.6 show graphs of the precision of the DD range and ionosphere parameters as function of the a priori ionospheric precision in the ionosphere-weighted model. The graphs are given for the *ambiguity-fixed* standard deviations, $\sigma_{\check{\varrho}^{dd}(\imath)}$, $\sigma_{\check{\imath}^{dd}(\imath)}$ and $\sigma_{\check{\imath}^{dd}(\imath)|\varrho}$. In all graphs the a priori ionospheric precision ranges

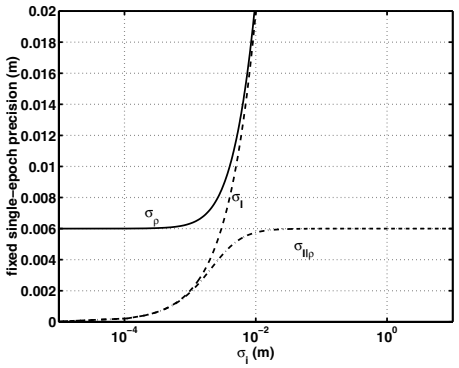

Fig. 5.1. *Single-frequency* data, $\sigma_\phi = 0.003$ m, $\sigma_p = 0.300$ m

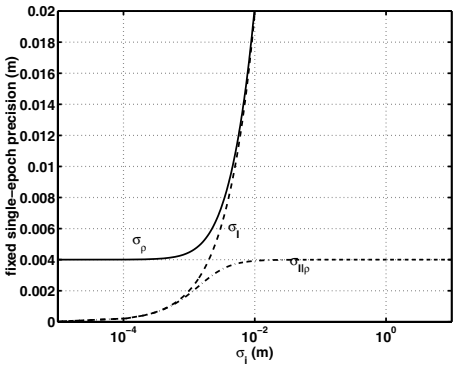

Fig. 5.2. *Single-frequency* data, $\sigma_\phi = 0.002$ m, $\sigma_p = 0.200$ m

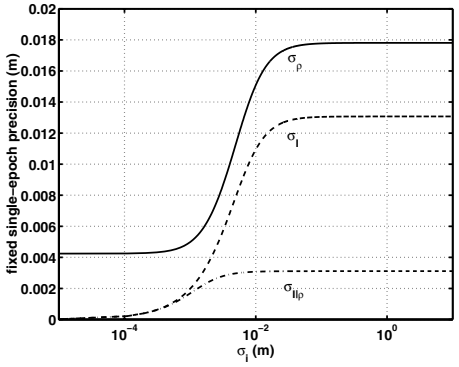

Fig. 5.3. *Dual-frequency* data, uncorrelated phase and code

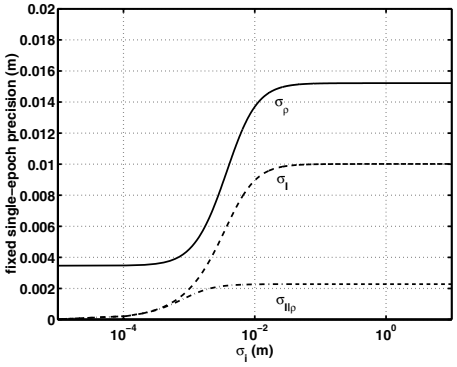

Fig. 5.4. *Triple-frequency* data, uncorrelated phase and code

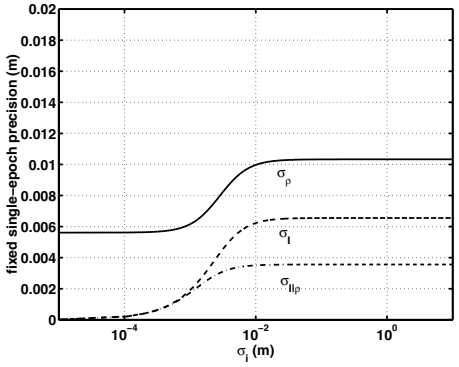

Fig. 5.5. *Dual-frequency* data, cross-correlated phase and code: $c = +0.75$

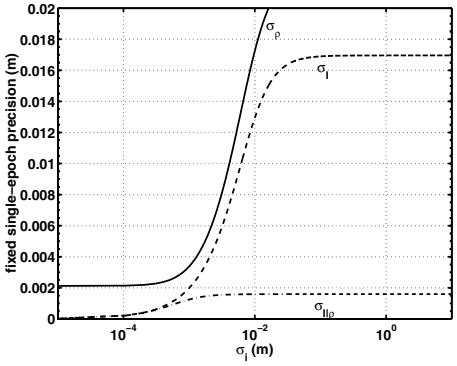

Fig. 5.6. *Dual-frequency* data, cross-correlated phase and code, $c = -0.75$

from a very small $\sigma_\imath = 10^{-5}$ m, to a very large $\sigma_\imath = 10^{1}$ m. To cover this wide range, the x-axis of the plots is logarithmic. The graphs are made for a varying number of frequencies and varying assumptions on the stochastic model of the phase and code observables.

Single-frequency precision
To start, in Figs. 5.1 and 5.2 the fixed range and ionospheric standard deviations are plotted in the case only one frequency (L1) is used. This case is included, since the ionosphere-weighted model is already solvable with just one frequency. In the single-frequency case, we need to set $j = 1$ in the expressions in Eq. (5.66), which results in the following reduced expressions for the fixed standard deviations:

$$\begin{aligned} \sigma_{\breve{\varrho}^{dd}(\imath)} &\approx 2\sigma_\phi \sqrt{\tfrac{\sigma_\imath^2}{\sigma_\phi^2}\mu_1^2 + 1} \;=\; 2\sigma_\imath \sqrt{\mu_1^2 + \tfrac{\sigma_\phi^2}{\sigma_\imath^2}} \\ \sigma_{\breve{\imath}^{dd}(\imath)} &\approx 2\sigma_\imath \\ \sigma_{\breve{\imath}^{dd}(\imath)|\varrho} &\approx 2\sigma_\imath / \sqrt{\tfrac{\sigma_\imath^2}{\sigma_\phi^2}\mu_1^2 + 1} \;=\; 2\sigma_\phi / \sqrt{\mu_1^2 + \tfrac{\sigma_\phi^2}{\sigma_\imath^2}} \end{aligned} \tag{5.67}$$

In Fig. 5.1 graphs are shown for these three standard deviations, assuming $\sigma_\phi = 3$ mm for the phase standard deviation. The behavior of the three graphs can be easily explained using the expressions in Eq. (5.67). It can be seen that for the fixed *range* precision two expressions are included, for which the first expression (immediately right of the approximation sign) is valid when the ionospheric standard deviation is significantly smaller than the phase standard deviation. In that situation $\sigma_\imath^2/\sigma_\phi^2 \approx 0$, which implies that $\sigma_{\breve{\varrho}^{dd}(\imath)}$ becomes only dependent on the *phase* standard deviation. This effect is visible in Fig. 5.1, since the range precision stays at a level of $2 \cdot 3 = 6$ mm for $\sigma_\imath < 3$ mm. When the ionospheric standard deviation is significantly larger than its phase counterpart, for the evaluation of the range precision we should use the second expression, in Eq. (5.67) immediately right after the equivalence sign. In that situation namely $\sigma_\phi^2/\sigma_\imath^2 \approx 0$, which implies that $\sigma_{\breve{\varrho}^{dd}(\imath)}$ becomes only dependent on the *ionospheric* standard deviation. And this behavior agrees with Fig. 5.1, in which the range standard deviation increases when the ionospheric standard deviation increases. Using Eq. (5.67) we see that the fixed *ionosphere* precision shows another behavior: It is a *linear* function of the a priori ionospheric standard deviation. This behavior is visible in Fig. 5.1 but as a consequence of the logarithmic x-axis the graph is not a straight line. The third fixed standard deviation finally, the ionospheric precision conditioned on the ranges, shows a typical *S-curve* behavior. This can again be explained using the expressions in Eq. (5.67): For small values of the a priori ionospheric standard deviation compared to the phase standard deviation, $\sigma_{\breve{\imath}^{dd}(\imath)|\varrho}$ is governed by this small a priori ionospheric standard deviation, while for large values of the ionospheric standard deviation $\sigma_{\breve{\imath}^{dd}(\imath)|\varrho}$ is governed by the phase standard deviation. In Fig. 5.2 all three graphs are plotted using a lowered phase standard deviation (2 mm), which has a proportional lowering effect on the three standard deviations.

Dual- vs. triple-frequency precision
In Figs. 5.3 and 5.4 similar graphs are shown as for the single-frequency case,

but for a *dual-frequency* (Fig. 5.3) and a future *triple-frequency* situation (Fig. 5.4). For both figures all phase observables and code observables are uncorrelated assumed with a constant standard deviation of 3 mm for the phase data, and 30 cm for the code data. In contrast to the single-frequency case, in the dual- and triple-frequency cases now *all* three graphs are S-curves as function of the a priori ionospheric standard deviation. This is explained from the fact that the ionosphere-weighted model becomes solvable for $\sigma_\imath = \infty$ (the ionosphere-float model) when at least two frequencies are used. From the graph of the range precision it can be seen that it starts to rise after a value of about $\sigma_\imath = 10^{-3}$ m (1 mm) and again becomes stable after a value of about $\sigma_\imath = 10^{-1.5}$ m (3 cm). From this it may be concluded that concerning the range precision, and thus the fixed (single-epoch) coordinate precision, an ionosphere-weighted approach only makes *sense* when the ionospheric standard deviation may be chosen within these bounds: 1 mm $\leq \sigma_\imath \leq$ 3 cm. Selecting a value smaller than 1 mm would equal the precision obtained with the ionosphere-*fixed* model, while a standard deviation larger than 3 cm would result in the precision of the ionosphere-*float* model. Comparing Fig. 5.3 with Fig. 5.4 leads to the conclusion that the addition of a *third* GPS frequency improves the single-epoch coordinate precision (and also the ionosphere precision) only marginally, since the graphs in the triple-frequency case are only at a slightly lower level than the precision level of their dual-frequency counterparts. Note that the precision of the coordinates when estimated with the ionosphere-float model are about a factor 4 worse than when estimated with the ionosphere-fixed model.

Influence of cross-correlation

The aforementioned results hold for a diagonal vc-matrix of the GPS observables. For current GPS receivers under Anti-Spoofing the observables on L1 and on L2 may however be *cross-correlated*. This cross-correlation depends on the type and make of the used GPS receiver (see Sect. 2.8), and therefore here we assume it to be present in the stochastic model in a rather general way. Instead of the diagonal matrices for the phase and code observables the following a priori vc-matrices are assumed, $Q_\phi = \sigma_\phi^2 R_2$ and $Q_p = \sigma_p^2 R_2$, where R denotes the matrix which takes the cross-correlation between L1 and L2 into account:

$$R_2 \;=\; \begin{bmatrix} 1 & c \\ c & 1 \end{bmatrix}, \quad \text{where } -1 \leq c \leq +1 \tag{5.68}$$

where the scalar c denotes the cross-correlation coefficient. The expressions for the three fixed standard deviations can now be evaluated using the cross-correlated stochastic model. Because the resulting expressions are rather complex, we restrict ourselves here by giving the expressions for the two extreme versions of the ionosphere-weighted model: The ionosphere-fixed model ($\sigma_\imath^2 = 0$) and the ionosphere-float model ($\sigma_\imath^2 = \infty$). The expressions for the fixed range standard deviation become for these two models, as function of the cross-correlation coefficient c:

$$\begin{array}{lcll} \sigma_\imath^2 = \infty & : & \sigma^2_{\breve{\varrho}^{dd}}(c) & \approx \;\; \frac{4\sigma_\phi^2}{(\mu_1-\mu_2)^2}(\mu_1^2 - 2c\mu_1\mu_2 + \mu_2^2) \\ \sigma_\imath^2 = 0 & : & \sigma^2_{\breve{\varrho}^{dd}|_\imath}(c) & \approx \;\; 2\sigma_\phi^2(1+c) \end{array} \tag{5.69}$$

Since the cross-correlation coefficient can be either positive or negative, from these expressions it cannot be concluded that cross-correlation has a beneficial effect on the range precision or not. From Eq. (5.69) namely the following inequalities can be set up, which show that *depending on the sign* of the cross-correlation coefficient, the range precision is better/worse than the range precision without cross-correlation:

$$\begin{array}{lcccccc} \sigma_\imath^2 = \infty & : & \sigma^2_{\breve{\varrho}^{dd}}(c<0) & > & \sigma^2_{\breve{\varrho}^{dd}}(c=0) & > & \sigma^2_{\breve{\varrho}^{dd}}(c>0) \\ \sigma_\imath^2 = 0 & : & \sigma^2_{\breve{\varrho}^{dd}|_\imath}(c<0) & < & \sigma^2_{\breve{\varrho}^{dd}|_\imath}(c=0) & < & \sigma^2_{\breve{\varrho}^{dd}|_\imath}(c>0) \end{array} \tag{5.70}$$

For the ionosphere-weighted model it then follows that when the ionospheric standard deviation is large, a *positive* correlation coefficient has a beneficial effect on the range precision, but that a *negative* coefficient has a bad effect on the range precision. When the ionospheric standard deviation is very small, these effects are opposite. See for this remarkable behavior Figs. 5.5 and 5.6. In the first figure a cross-correlation coefficient of $+0.75$ was assumed, while for the second figure a cross-correlation coefficient of -0.75 was assumed. From the figures it can be seen that the behavior of the fixed ionosphere precision is the same as of the range precision, but that the behavior of the fixed ionosphere precision conditioned on the ranges is opposite.

5.6.2 Multi-epoch coordinate precision

Approximated closed-form expressions

In the case that more than one epoch of data is used in the processing, the change of receiver-satellite geometry starts to contribute to the precision of the coordinate parameters. To see this, the ambiguity-float geometry vc-matrix in Eq. (5.52) is approximated by setting the very small variance-ratio $\sigma^2_{\breve{\varrho}^{dd}(\imath)}/\sigma^2_{\hat{\varrho}^{dd}(\imath)}$ (which is determined by the phase-code variance ratio) to zero. Hence, in the multi-epoch case the vc-matrices of the ambiguity-float respectively ambiguity-fixed coordinate parameters read:

$$\begin{array}{lcl} Q_{\hat{b}(\imath)} & \approx & \sigma^2_{\breve{\varrho}^{dd}(\imath)} \left[2 \sum_{i=1}^{k} \left(G(i) - \bar{G} \right)^T P^{\perp}_{e_m} \left(G(i) - \bar{G} \right) \right]^{-1} \\ Q_{\check{b}(\imath)} & = & \sigma^2_{\breve{\varrho}^{dd}(\imath)} \left[2 \sum_{i=1}^{k} G(i)^T P^{\perp}_{e_m} G(i) \right]^{-1} \end{array} \tag{5.71}$$

Note that since in both expressions the same variance $\sigma^2_{\breve{\varrho}^{dd}(\imath)}$ appears, the difference between the float and fixed vc-matrices stems from the differences in the inverse terms. In the following it is explained how these inverse terms contribute to the coordinate precision.

Within a *short* observation time span, the geometry matrices $G(i)$ do not differ very much from each other (as a consequence of the slowly changing receiver-satellite geometry) and they will not differ a lot from their time-averaged counterpart $\bar{G}$. Hence, the summation within the inverse term of the *ambiguity-float* vc-matrix will be quite small and as a consequence of this the coordinate precision will be

quite poor. Using data of a sufficient *long* time span (e.g. one hour or more), the receiver-satellite geometry will change significantly and the individual geometries, as captured in $G(i)$, will differ considerably from the geometry which is averaged over the entire time span (captured in $\bar{G}$). As a result, the summation within the inverse term of the ambiguity-float vc-matrix will be quite large and the resulting coordinate precision will be much better, compared to the short time span. So in the ambiguity-float case the changing receiver-satellite geometry has a very beneficial effect on the precision of the geometry parameters. Note from the expression within the inverse term in the expression of the *ambiguity-fixed* vc-matrix that in this case there is no need for a sufficient change of the receiver-satellite geometry, since the time-averaged geometry is not 'subtracted' from the individual geometries. In this situation the geometry precision will already be at a high level using data of just a short time span. Note that the gain in baseline precision due to ambiguity fixing is elaborated in [Teunissen, 1997a] using the *gain number* concept.

Example

To demonstrate the effect of a multi-epoch approach, for a representative GPS receiver-satellite geometry at mid-latitudes (in Flevoland, the Netherlands) the standard deviations of the North, East and Up coordinates of a single-baseline are plotted as function of the number of epochs, during a time span of *one hour*. The coordinate precision is computed for the ambiguity-float and ambiguity-fixed variants of the ionosphere-weighted model using dual-frequency phase and code observations. In the stochastic model diagonal observable vc-matrices have been assumed, with $\sigma_\phi = 3$ mm, $\sigma_p = 30$ cm and $\sigma_\imath = 1$ cm. This value for the ionospheric standard deviation is just an arbitrary choice, lying within the interval between 1 mm and 3 cm. Three scenarios are analyzed, in which the number of satellites, the sampling interval, and the troposphere estimation is varied.

Influence of the number of satellites
In Fig. 5.7 the float and fixed coordinate precision is plotted for a (minimum) number of 4 satellites, whereas in Fig. 5.8 a number of 8 satellites is used. In both cases no zenith tropospheric delays were estimated. The data sampling interval is 30 s and the total number of epochs is 120 for the one hour time span. Note that in each figure two sets of three curves are plotted, where the upper three refer to the ambiguity-float curves, and the lower three to their ambiguity-fixed counterparts. From both figures the significant gain of ambiguity resolution can be seen, especially when the number of epochs is low. With 8 satellites, using only one epoch ($k = 1$), the ambiguity-fixed precision is already at the cm-level, while in the ambiguity-float case this level is only reached after collecting data for about 70 epochs (more than 30 min.). Using 4 satellites these numbers are somewhat larger.

Influence of the sampling interval
In the previous figures a sampling interval of 30 s was used. Although this sampling interval is standard for many permanent GPS networks, for surveying purposes

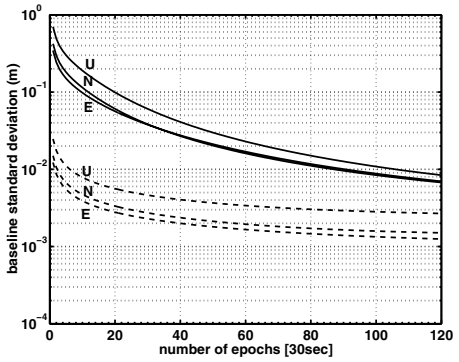

Fig. 5.7. Fixed (dashed) and float (dotted) baseline precision, 4 satellites, 30 s sampling interval

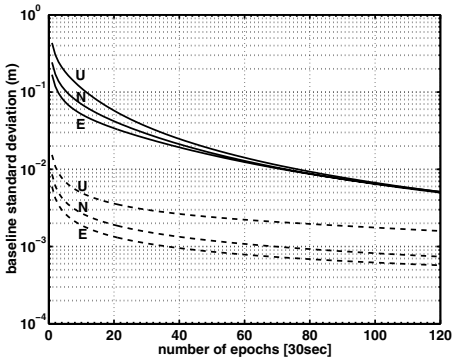

Fig. 5.8. Fixed (dashed) and float (dotted) baseline precision, 8 satellites, 30 s sampling interval

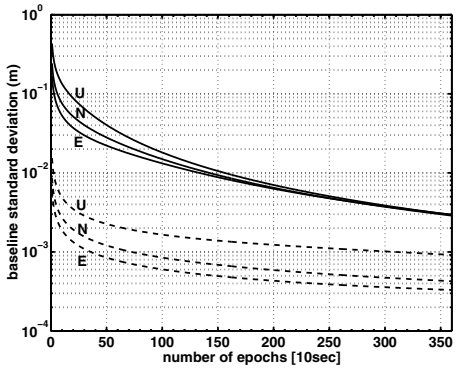

Fig. 5.9. Fixed (dashed) and float (dotted) baseline precision, 8 satellites, 10 s sampling interval

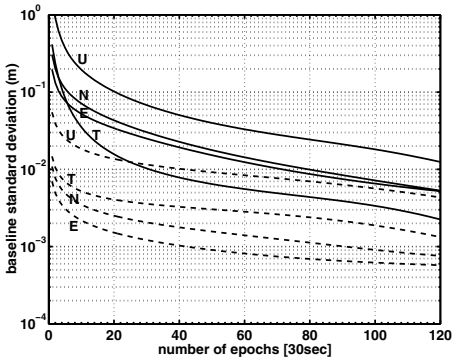

Fig. 5.10. Fixed (dashed) and float (dotted) baseline precision, 8 satellites, 30 s sampling interval, ZTD estimation

this interval might be too long, since many GPS receivers can track data with a higher sampling-rate. In Fig. 5.9 a plot of the standard deviations is shown for a number of 8 satellites, but with an increased data sampling-rate of 10 s The time span is kept the same at one hour, so in the figure the x-axis ranges to 360 epochs. The figure shows a beneficial effect of increasing the sampling-rate. For example, the ambiguity-fixed East component reaches mm-precision after about 20 min. with a 30 s sampling interval, while this time span is only 5 min. using a 10 s sampling interval. A shorter sampling interval than 10 s might introduce *time-correlation* between the observations (see also Chap. 2), which is harmful, since in many processing software (such as *GPSveQ*) it cannot be accounted for.

Influence of ZTD estimation
In the previous graphs the coordinate precision was analyzed *without* the estimation of zenith tropospheric delays (ZTDs) in the model. However, since not in all GPS applications the tropospheric delays can be accounted for without estimating ZTDs, it is of interest to analyze how the estimation of ZTDs impacts the precision of the coordinates. It is assumed that just one ZTD is valid for the entire time span of maximum one hour. In this case the non-temporal ZTD can be regarded as a *fourth* coordinate component (besides the North, East and Up components). In Fig. 5.10 for the 8 satellite case (using a 30 s sampling interval) the standard deviations of the coordinate and ZTD parameters are given. This figure can be compared to Fig. 5.8 for which the same 8 satellites were used, but no ZTDs were estimated. From the figures the well-known phenomenon can be seen that estimation of a ZTD hardly affects the precision of the horizontal coordinate components (North, East), but that the precision of the Up component is drastically reduced. This deterioration of the height component is about a factor 3, see the graphs and also [Kleijer, 2002]. Especially for fast GPS applications the resulting fixed Up precision may not be sufficient when ZTDs are estimated.

5.7 Analyzing the (formal) ambiguity success rates

In this section the suitability of the ionosphere-weighted model for fast integer ambiguity estimation is analyzed. Ambiguity resolution is the crucial issue for fast GPS applications and a tool to evaluate the probability of correct ambiguity estimation without collecting real observations, is the ambiguity *success rate*, which was discussed in general in Chap. 3. This success rate is purely based on the vc-matrix of the ambiguities $Q_{\hat{a}}$. In this section for a typical GPS example the expected success rate is analyzed for varying assumptions underlying the ionosphere-weighted GPS model.

5.7.1 Judging the ambiguity success rate

Recall from Chap. 3 that the LAMBDA method for ambiguity resolution, implemented in the *GPSveQ* software, is based on the strict integer *least-squares* search. For this integer estimator it is difficult to evaluate the *exact* ambiguity success rate. Fortunately this least-squares success rate is bounded from below by

the success rate for the integer *bootstrapping* estimator, which can be computed in an *exact* manner, see Eq. (3.85). With *decorrelated* ambiguities, in Chap. 3 it was shown that the bootstrapped success rate is a very *sharp* lower bound of the least-squares success rate. So the integer least-squares success rate is approximated by the integer bootstrapped success rate, which should be close to 1:

$$\boxed{P(\check{z}_{LSQ} = z) \;\geq\; P(\check{z}_B = z) \;=\; 1 - \varepsilon, \quad \text{with } \varepsilon \text{ small}} \tag{5.72}$$

To emphasize the decorrelated ambiguities, in Eq. (5.72) the ambiguities are denoted by a z. Ideally, it should hold that $\varepsilon = 0$ in Eq. (5.72), but this is impossible since the success rate is based on stochastic observations. It depends on the type of GPS application how large ε may actually be. In the example in the following subsection it is required that $\varepsilon = 0.001$, i.e. in 1 out of 1,000 times one is willing to accept a wrong integer solution.

5.7.2 Example success rates

For the same receiver-satellite geometry as in the example in Sect. 5.6.2, in Figs. 5.11 – 5.14 the *minimum number of epochs* necessary to obtain a bootstrapped success rate of $P(\check{z}_B = z) \geq 0.999$ with the *geometry-based* model is plotted as function of the a priori ionospheric standard deviations. This has been done for varying scenarios and unless stated otherwise, for all scenarios the data sampling interval was assumed as 10 s The stochastic model of the observables was assumed as $Q_\phi = (0.003)^2 I_j$ m^2, $Q_p = (0.300)^2 I_j$ m^2, with j the number of frequencies. Success rates were computed for the single-, dual- and triple-frequency cases. For each scenario two different numbers of satellites were maintained, i.e. $m = 5$, the minimum number when both coordinates and ZTD are estimated, and $m = 8$, a rather large number of satellites. Note that the graphs plotted are sometimes not so smooth. This is because to different values of $\sigma_\imath$ an *equal* minimum number of epochs may correspond.

Ambiguity success rates for the ionosphere-weighted model

The figures show first of all that the minimum number of epochs in general increases when the ionospheric standard deviation increases. This behavior can be explained from the fact that the ionosphere-weighted model becomes weaker the worse the precision of the ionospheric pseudo-observables. To be more precise, except for the single-frequency case the graphs are *S-curves*. This S-curve behavior was also present in the graphs of the fixed coordinate/ionosphere precision, see Sect. 5.6.1. From the success rate graphs it seems that ambiguity resolution with the ionosphere-weighted model only makes sense when the ionospheric standard deviation is within the interval 1 cm $\leq \sigma_\imath \leq$ 1 m. When $\sigma_\imath <$ 1 cm, it is easier to use the *ionosphere-fixed* model, while when $\sigma_\imath >$ 1 m, the success rates are the same as obtained with the *ionosphere- float* model.

Figure 5.12 shows that when the receiver coordinates are *not* estimated but fixed in the processing (such that only a ZTD remains as non-temporal parameter),

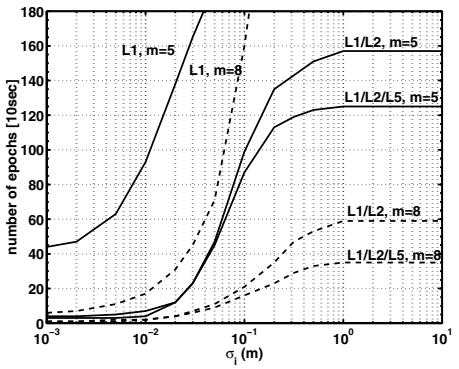

Fig. 5.11. Estimation of coordinates and ZTD, $Q_\phi = (0.003)^2 I_j$ m^2, $Q_p = (0.300)^2 I_j$ m^2

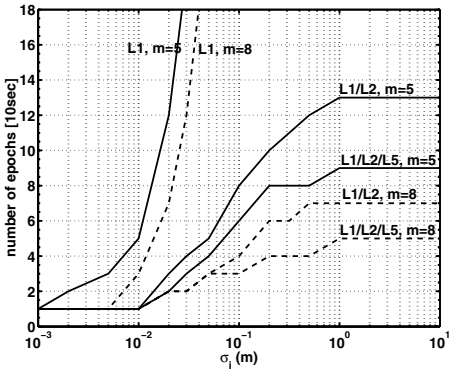

Fig. 5.12. Coordinates fixed, estimation of ZTD, $Q_\phi = (0.003)^2 I_j$ m^2, $Q_p = (0.300)^2 I_j$ m^2

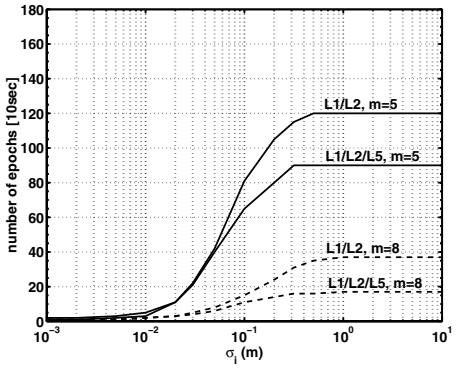

Fig. 5.13. Estimation of coordinates and ZTD, $Q_\phi = (0.002)^2 I_j$ m^2, $Q_p = (0.200)^2 I_j$ m^2

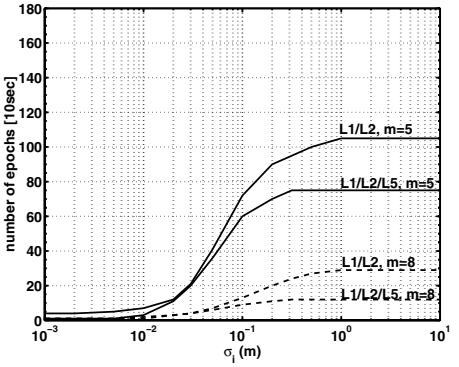

Fig. 5.14. Estimation of coordinates and ZTD, $Q_\phi = (0.003)^2 R_j$ m^2, $Q_p = (0.300)^2 R_j$ m^2

the minimum number of epochs necessary for successful ambiguity resolution is much less than when the coordinates are estimated. For example, to resolve the ambiguities of dual-frequency observations of 5 satellites when $\sigma_\iota = 10$ cm, with the coordinates fixed just 8 epochs (about 1.5 min.) are sufficient, while in the case that coordinates are estimated at least 100 epochs (about 17 min.) should be 'waited' before the success rate is high enough.

In Fig. 5.13 graphs are given for the same setup as in Fig. 5.11, but with a slightly better assumed stochastic model for the GPS observables: For the phase observables a standard deviation of 2 mm instead of 3 mm was assumed, while for the code observables the standard deviation was set to 20 cm instead of 30 cm. Note that in Fig. 5.13 the success rates are only evaluated for the dual- and triple-frequency cases, and not for the single-frequency case. Comparing Fig. 5.13 with Fig. 5.11 shows that the improved precision of the GPS observables has a beneficial effect on the success rates, especially for a large ionospheric standard deviation, although this improvement is not spectacular. For example, using the 'old' stochastic model in the dual-frequency case with 5 satellites a time span of 26 min. is needed to obtain a sufficient high success rate when $\sigma_\iota = 10$ m, with the new stochastic model this time span is reduced to about 20 min.

Finally, in Fig. 5.14 the success rates are plotted using a stochastic model in which cross-correlation is modelled between the mutual phase and the mutual code observables. Like in the analysis of the coordinate precision, for this purpose the following stochastic model is assumed: $Q_\phi = \sigma_\phi^2 R_j$ and $Q_p = \sigma_p^2 R_j$, with $\sigma_\phi = 3$ mm and $\sigma_p = 30$ cm, and where R_j denotes the matrix in which the cross-correlation is modelled. Between the different frequencies a *positive* cross-correlation coefficient of $+0.75$ was assumed. Figure 5.14 shows that this positive cross-correlation has a beneficial effect on the ambiguity success rate, and, like in the case of a better precision of the GPS observables in Fig. 5.13, this is mainly an improvement for relative large values of the ionospheric standard deviation. For example, the minimum time span using dual-frequency data of 5 satellites is for $\sigma_\iota = 10$ m reduced to about 17 min. for a success rate of 0.999.

From all figures note that an increased *number of satellites* has a very beneficial effect on the success rate. This effect is much more pronounced than the addition of a *third frequency* to the current dual-frequency system.

Short time spans and the ionospheric standard deviation

In this thesis *short observation times* are crucial, but from the figures above (those in which coordinates are estimated) it can hardly be inferred how large the a priori ionospheric standard deviation is allowed to be when short time spans are required. Therefore, in Table 5.5 admissible values for σ_ι are given to obtain a bootstrapped success rate of 0.999 in this example. These values are assessed for three short time spans: A single-epoch or *instantaneous* 'time span', a time span of *1 minute* (6 epochs for a 10 s sampling interval) and a time span of *5 minutes*.

For the single-epoch time span, three variants are given: i) Dual-frequency data with a 'standard' stochastic model $Q_\phi = (0.003)^2 I_2$ m^2, $Q_p = (0.300)^2 I_2$ m^2, ii) Dual-frequency data which are more precise assumed: $Q_\phi = (0.002)^2 I_2$ m^2, $Q_p = (0.200)^2 I_2$ m^2, and iii) Triple-frequency data with a 'standard' stochastic model $Q_\phi = (0.003)^2 I_3$ m^2, $Q_p = (0.300)^2 I_3$ m^2. For the 1 min. and 5 min. time spans only the dual-frequency cases with standard model $Q_\phi = (0.003)^2 I_2$ m^2, $Q_p = (0.300)^2 I_2$ m^2 are evaluated. For each considered time span two cases are considered with respect to the estimation of non-temporal parameters: In case A only coordinates are estimated, whereas in case B besides these three coordinates a ZTD is estimated as well. In each case the number of satellites is varied from $m = 5$ to $m = 8$.

Table 5.5. Admissible ionospheric standard deviation σ_ι [m] for $P(\check{z}_B = z) \geq 0.999$. In Case A only coordinates are estimated, in case B coordinates plus a ZTD are estimated. In all cases a diagonal vc-matrix for the GPS phase and code observables was assumed.

	m	inst. (k=1) dual-frequency σ_ϕ = 0.003 m σ_p = 0.300 m	inst. (k=1) dual-frequency σ_ϕ = 0.002 m σ_p = 0.200 m	inst. (k=1) triple-frequency σ_ϕ = 0.003 m σ_p = 0.300 m	1 min. (k=6) dual-frequency σ_ϕ = 0.003 m σ_p = 0.300 m	5 min. (k=30) dual-frequency σ_ϕ = 0.003 m σ_p = 0.300 m
A	5	-	0.004	0.005	0.018	0.050
	6	0.004	0.008	0.008	0.025	0.080
	7	0.007	0.011	0.009	0.030	0.170
	8	0.009	0.012	0.010	0.050	0.210
B	5	-	-	-	0.008	0.035
	6	-	0.003	0.005	0.018	0.050
	7	0.002	0.007	0.007	0.023	0.090
	8	0.004	0.009	0.007	0.030	0.180

From the table note that, concerning the feasibility of *instantaneous* ambiguity resolution with the ionosphere-weighted model, in the absence of a ZTD parameter the ionospheric standard deviation is restricted to a quite small value, maximum about 1 cm for 8 satellites. Note that this value is hardly improved when the accuracy of the GPS observables is improved or a third frequency is added. In the case that a ZTD is estimated as well, this value is even lower: About 5 mm in the dual-frequency case with a 'standard' stochastic model. In the latter case only with a minimum of 7 satellites a success rate of at least 0.999 could be obtained.

With a longer time span also a much larger value for the ionospheric standard deviation is allowed. Besides, already with 5 satellites success rates of at least 0.999 are feasible. Note from the table that for this example for the time span of 1 min. the allowed ionospheric standard deviation is about a factor 5-8 larger than for the single-epoch time spans. For the 5 min. time spans this factor increases to

about 20-45! For example, in the absence of a ZTD parameter, with 8 satellites an ionospheric standard deviation of more than 20 cm is allowed. This larger admissible ionospheric standard deviation is explained from the fact that for the longer time spans the changing receiver-satellite geometry starts to contribute to the resolution of the ambiguities, and that not so much has to be relied on the ionospheric pseudo-observables.

5.8 Robustness of the ionosphere-fixed model

Since ionospheric delays are parameterized, application of the ionosphere-weighted model (and also the ionosphere-float model) results in estimates of the remaining parameters that are completely *free* of ionospheric biases. With the *ionosphere-fixed* model however, the parameter solutions are not always free of ionospheric biases, since it is only *assumed* that the relative ionospheric delays may be neglected (see Sect. 5.4.1). There is a risk that (undetected) ionospheric biases will bias ambiguity resolution and coordinate estimation. Therefore in this section it is by means of an example investigated how *robust* the ionosphere-fixed geometry-based model is against unmodelled ionospheric biases.

5.8.1 Ionosphere-biased ambiguity and coordinate solutions

Recall from Chap. 2 that under certain assumptions the results of the *undifferenced* model are equivalent with those obtained with the model based on *double-differenced* (DD) observations. Then the parameter estimators of the geometry-based model may be written as function of DD observables. Assume that the DD phase and code observables are *biased* by unmodelled DD ionospheric delays, then the DD observable vector on a certain epoch i becomes biased as follows:

$$\boxed{\nabla y^{dd}(i) \;=\; \begin{bmatrix} -\mu \\ \mu \end{bmatrix} \otimes \imath^{dd}(i)} \tag{5.73}$$

where $\nabla y^{dd}(i)$ denotes the biased DD observable vector as consequence of the DD ionospheric biases in $\imath^{dd}(i)$. It can be proved that the bias in the solutions of the DD ambiguity parameters, denoted as $\nabla\hat{a}|\imath$ and the bias in the ambiguity-fixed coordinate parameters, denoted as $\nabla\check{g}|\imath$, can be written as function of $\nabla y^{dd}(i)$:

$$\begin{array}{rcl} \nabla\hat{a}|\imath & = & \sum_{i=1}^{k} X_{\hat{a}|\imath}(i)\nabla y^{dd}(i) \\ \nabla\check{g}|\imath & = & \sum_{i=1}^{k} X_{\check{g}|\imath}(i)\nabla y^{dd}(i) \end{array} \tag{5.74}$$

where:

$$\begin{array}{rcl} X_{\hat{a}|\imath}(i) & = & \left[\Lambda^{-1}\otimes\frac{1}{k}\left(I_{n-1}\otimes I_{m-1}\right),\ 0\right] \;- \\ & & \Big[\Lambda^{-1}e_j e_j^T Q_\phi^{-1}\otimes\left(I_{n-1}\otimes\tfrac{1}{2}D_m^T\bar{G}Q_{\hat{b}|\imath}\left(G(i)-\bar{G}\right)^T D_m^{+\,T}\right),\ldots \\ & & \Lambda^{-1}e_j e_j^T Q_p^{-1}\otimes\left(I_{n-1}\otimes\tfrac{1}{2}D_m^T\bar{G}Q_{\hat{b}|\imath}G(i)^T D_m^{+\,T}\right)\Big] \\ X_{\check{g}|\imath}(i) & = & \left[e_j^T Q_\phi^{-1},\ e_j^T Q_p^{-1}\right]\otimes\left[I_{n-1}\otimes\tfrac{1}{2}Q_{\check{b}|\imath}G(i)^T D_m^{+\,T}\right] \end{array}$$

(5.75)

Since these are rather complex expressions, we will simplify them based of certain assumptions. First, it is assumed that there are just two receivers (*single-baseline* setup), such that $n = 2$. Second, it is assumed that the observations are collected during a *short time span*, such that the receiver-satellite geometry changes slowly during this time span: $G(i) \approx \bar{G}$. Besides, it is assumed that the DD ionospheric delays change *smoothly* within this short time span, such that the ionospheric delays at one epoch is approximately equal to the time-averaged ionospheric delay over the entire time span: $\imath^{dd}(i) \approx \bar{\imath}^{dd}$. Finally, the vc-matrices of the phase and code observables are diagonal assumed, i.e. $Q_\phi = \sigma_\phi^2 I_j$ and $Q_p = \sigma_p^2 I_j$, where the phase precision is assumed much better than the code precision, $\sigma_\phi^2 << \sigma_p^2$, such that $\sigma_\phi^2/\sigma_p^2 \approx 0$. Using these simplifications and the expressions in Eq. (5.64), we may write for the float and fixed coordinate vc-matrices:

$$\begin{array}{rcl} Q_{\hat{b}|\imath} & \approx & \frac{2\sigma_p^2}{jk}\left[\bar{G}^T P_{e_m}^{\perp} \bar{G}\right]^{-1} \\ Q_{\check{b}|\imath} & \approx & \frac{2\sigma_\phi^2}{jk}\left[\bar{G}^T P_{e_m}^{\perp} \bar{G}\right]^{-1} \end{array} \tag{5.76}$$

This leads to the following simplified bias vectors:

$$\boxed{\begin{array}{rcl} \nabla\hat{a}|\imath & \approx & -\Lambda^{-1}\left(\mu \otimes \bar{\imath}^{dd} + e_j \otimes D_m^T \bar{G}\left[\bar{G}^T P_{e_m}^{\perp} \bar{G}\right]^{-1} \bar{G}^T D_m^{+T} \bar{\mu}\bar{\imath}^{dd}\right) \\ \nabla\check{b}|\imath & \approx & -\left[\bar{G}^T P_{e_m}^{\perp} \bar{G}\right]^{-1} \bar{G}^T {D_m^+}^T \bar{\mu}\bar{\imath}^{dd} \end{array}} \tag{5.77}$$

where $\bar{\mu}$ denotes the *frequency-averaged* ionospheric coefficient and $\bar{\imath}^{dd}$ the vector of $m-1$ *time-averaged* DD ionospheric delays:

$$\bar{\mu} = \frac{1}{j}\sum_{l=1}^{j} \mu_l, \quad \bar{\imath}^{dd} = \frac{1}{k}\sum_{i=1}^{k} \imath^{dd}(i) \tag{5.78}$$

5.8.2 Example

Mapping the ionospheric bias

The ambiguity and coordinate bias expressions in Eq. (5.77) are a function of $m-1$ time-averaged DD ionospheric delays. To evaluate the biases as function of just *one parameter*, which is easier than a number of parameters, another simplification is made: The DD ionospheric delays are mapped to just one time-constant vertical ionospheric delay, using the single-layer geometry of the ionosphere, as discussed in Sect. 4.5. According to Eq. (4.35) the *single-difference* ionospheric delay between receivers 1 and 2 to satellite s may be written as, using the ionospheric mapping:

$$\imath_2^s(i) - \imath_1^s(i) = \left[1/\cos z_2^s(i)' - 1/\cos z_1^s(i)'\right] \imath_v \tag{5.79}$$

where $z_r^s(i)'$ denotes the zenith angle at the ionospheric point and $\imath_v$ the vertical ionospheric delay. Note that in Eq. (5.79) *horizontal ionospheric gradients*, due to the difference in vertical ionospheric delays between the ionospheric points of 1 and 2, have been neglected. In real practice however, this mapping to one vertical delay may not be realistic, but since we deal in this example with quite short baselines, only for the purpose of this example this assumption is done.

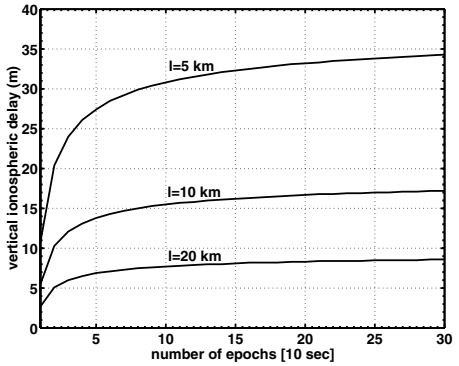

Fig. 5.15. Dual-frequency: Admissible vertical ionospheric delay for a bias-affected success rate > 0.999

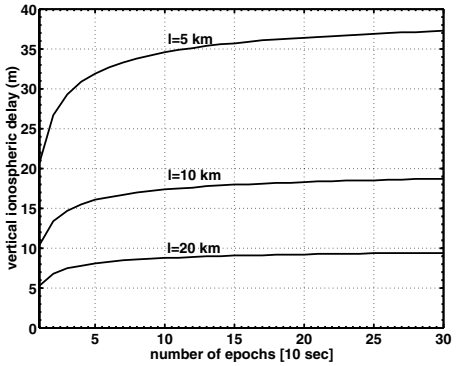

Fig. 5.16. Triple-frequency: Admissible vertical ionospheric delay for a bias-affected success rate > 0.999

Ionosphere-fixed bias-affected success rate

In Chap. 3 a closed-form expression was given to evaluate the ambiguity (bootstrapped) success rate in the presence of biases, the so-called *bias-affected* success rate, see Eq. (3.95). In this example this bias-affected success rate is evaluated for three baseline lengths, 5, 10 and 20 km, for which the coordinates of one of the receivers is fixed and for which the same receiver-satellite geometry for the second receiver is taken as used in Sects. 5.6 and 5.7. In the current example the number of satellites is fixed at 6 and the maximum evaluated time span is 10 min. (30 epochs; 10 s sampling interval). The bias-affected success rates are computed assuming phase and code data, with stochastic model $Q_\phi = (0.003)^2 I_j$ and $Q_p = (0.300)^2 I_j$. The ionosphere-fixed model was applied *without* estimation of a ZTD parameter. In Figs. 5.15 and 5.16 the admissible vertical ionospheric delay $\imath_v$ is plotted as function of the number of necessary epochs to obtain a bias-affected ambiguity success rate of 0.999. In Fig. 5.15 this is done for current dual-frequency GPS, whereas in Fig. 5.16 the graphs are given for the future triple-frequency case.

A first aspect that can be seen from Figs. 5.15 and 5.16 is that the vertical ionospheric delay, which is still admissible to resolve the ambiguities with the ionosphere-fixed model, increases when a longer time span is used. This behavior can be explained when inspecting Eq. (5.77). This equation shows that the ambiguity bias is - in the approximation - a function of the time-averaged (DD) ionospheric delay. Despite the mapping to a vertical delay, it is the *time-averaged* effect that is propagated into the ambiguity bias. This is the reason why using an increasing number of epochs more vertical delay is allowed: When this effect is averaged over time, a more or less constant effect remains.

Concerning the three baseline lengths, both figures show that the allowed ver-

tical delay is approximately *inversely proportional* to the length of the baseline. The shorter the baseline, the more vertical ionospheric delay is allowed. For example, using a single epoch of data, for the 5-km baseline the admissible vertical ionospheric delay in the dual-frequency case is about 10.6 m, for the 10-km baseline this is about 5.3 m, whereas for the 20-km baseline this effect is about 2.6 m. This behavior can simply be explained using Eq. (5.79). From Chap. 4 we know that the single-difference ionospheric mapping factor in this expression, is proportional with the baseline length. From this follows that the *double-difference* mapping factor is also proportional with the length of the baseline, which implies that for a longer baseline the admissible vertical delay $\imath_v$ is forced to be smaller to obtain a same level of (bias-affected) success rate.

In Chap. 4 it was discussed that the vertical ionospheric delay can - during extreme ionospheric conditions (solar maximum) - range up to about 16 m, for locations at mid-latitudes. When one aims at *instantaneous* ambiguity resolution during these conditions, from Fig. 5.15 it can be seen that this is probably not very likely, even for a short baseline of 5 km, since the vertical ionospheric delay is restricted to about 11 m in this example using dual-frequency data. This failing of ambiguity resolution with the ionosphere-fixed model was also shown using real GPS data of a 4-km baseline in [Odijk, 2001]. In the future triple-frequency situation, note from Fig. 5.16 that the admissible ionospheric bias increases compared to the dual-frequency case. This is especially the case for single-epoch applications, in which the admissible vertical delay may be twice as large as the delay in the dual-frequency case. Still, during conditions with a large (but realistic) vertical delay of 16 m, instantaneous ambiguity resolution for a 10-km baseline is likely to fail using the ionosphere-fixed model.

Ionosphere-fixed biased coordinate solution

Besides the impact of ionospheric biases on the ambiguity success rate, it is also important to analyze their impact on the coordinates after the ambiguities have been resolved. This impact can be evaluated using the expression for $\nabla\check{b}|\imath$ in Eq. (5.77). When computing this bias in the fixed coordinates, one needs to judge whether this is significant or not. Therefore, it is necessary to take the precision of the coordinate estimates into account. Instead of computing $\nabla\check{b}|\imath$ solely, it is better to compute a so-called *bias-to-noise ratio* (BNR) for the coordinates, as follows [Teunissen, 1997b]:

$$||\nabla\check{b}|\imath||^2_{Q_{\check{b}|\imath}} \;=\; \nabla\check{b}|\imath^T Q^{-1}_{\check{b}|\imath}\nabla\check{b}|\imath \tag{5.80}$$

Using the aforementioned simplifications, the BNR can be approximated as:

$$||\nabla\check{b}|\imath||^2_{Q_{\check{b}|\imath}} \;\approx\; \frac{j}{2\sigma^2_\phi k}\bar{\mu}\bar{\imath}^{ddT}D^+_m\bar{G}\left[\bar{G}^T P^\perp_{e_m}\bar{G}\right]^{-1}\bar{G}^T {D^+_m}^T\bar{\mu}\bar{\imath}^{dd} \tag{5.81}$$

This BNR is thus a significance measure for the (three) coordinate bias components in one. To judge the significance of these biases, an upper bound for the

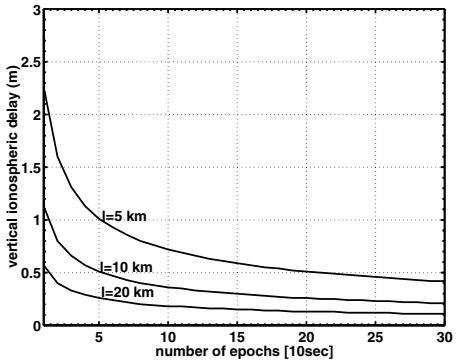

Fig. 5.17. Dual-frequency: Admissible vertical ionospheric delay for BNR ≤ 4

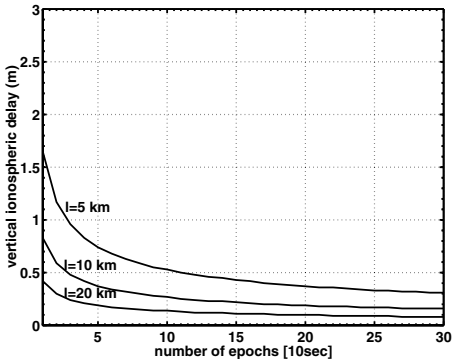

Fig. 5.18. Triple-frequency: Admissible vertical ionospheric delay for BNR ≤ 4

BNRs needs to be chosen. In this example this upper bound is 4, which is a rather conservative bound.

When the (time-averaged) DD ionospheric delay is mapped to one vertical delay (like was done for the bias-affected success rate), Figs. 5.17 and 5.18 show the admissible vertical ionospheric delay as function of the time span in the dual- and triple-frequency GPS cases to obtain a BNR which is smaller or equal to 4. For the same reason as with the bias-affected success rate, the admissible vertical delay decreases with increasing baseline length. Comparing both figures reveals that the addition of a third frequency reduces the admissible vertical delay, which is an opposite effect compared to the success rate. This behavior can simply be explained from Eq. (5.81): When j becomes larger, the entries of the time-averaged DD ionospheric bias should be smaller in order to not change the BNR value.

Concerning the admissible vertical ionospheric delay for ionosphere-fixed coordinate estimation, note that this is in general much *less* than for ionosphere-fixed ambiguity resolution. For example, in the dual-frequency case the vertical delay is allowed to be at most 2.2 m for for instantaneous fixed *coordinate estimation* for the 5-km baseline, while for instantaneous *ambiguity resolution* this delay may be about 10.6 m for the same baseline! This difference in admissible ionospheric delay becomes even larger when the time span or number of epochs increases. This example shows that the ionosphere-fixed model is *more robust* against ionospheric biases for the purpose of ambiguity resolution, than for coordinate estimation after the ambiguities have been resolved. This explains why in practice often for rather short baselines for ambiguity resolution the *ionosphere-fixed* model is used, while for (fixed) coordinate estimation the *ionosphere-float* model is used (or the ionosphere-free combination), even during solar minimum periods with low ionospheric conditions [Teunissen et al., 1997].

5.9 Concluding remarks

In this chapter the atmospheric errors in GPS observations, consisting of tropospheric and ionospheric delays, were included in the relative GPS models as set up in Chap. 2. Considering the non-dispersive tropospheric delays, in the geometry-free GPS model they become lumped with the receiver-satellite range parameters and pseudo-observables, whereas in the geometry-based model they are mapped to time-constant zenith delay parameters. Considering the dispersive ionospheric delays, for both geometry-free and geometry-based models a stochastic modelling approach is used, in which for every ionospheric parameter an ionospheric pseudo-observable is added (like the ranges in the geometry-free model). This model is referred to as the *ionosphere-weighted* model. For the processing of these ionospheric pseudo-observables it is necessary to specify sample values plus a stochastic model.

The ionosphere-weighted model is a very general model, of which the ionosphere-fixed model and the ionosphere-float model are 'extreme' versions. In the ionosphere-fixed model ($\sigma_\imath = 0$) the ionospheric delays are assumed known or zero, whereas in the ionosphere-float model ($\sigma_\imath = \infty$) the ionospheric delays only appear as unknown parameters (no pseudo-observables). Note that this ionosphere-float model is closely related to the well-known ionosphere-free phase combination. So the precision of the parameter estimates and the ambiguity success rate of the ionosphere-weighted model *interpolate* between the results of the ionosphere-fixed and -float models:

$$\boxed{\begin{array}{lcll} Q_{\hat{x}|\imath} & < & Q_{\hat{x}}(\imath) & < & Q_{\hat{x}} \\ P(\check{a}|\imath = a) & > & P(\check{a}(\imath) = a) & > & P(\check{a} = a) \end{array}} \tag{5.82}$$

The ionosphere-weighted model only differs from its extreme versions, when the a priori standard deviation of the pseudo-observables lies within a certain range. For coordinate estimation this is 1 mm $\leq \sigma_\imath \leq$ 3 cm, but for ambiguity resolution this is another range, about 1 cm $\leq \sigma_\imath \leq$ 1 m. The ionosphere-weighted model is very powerful in principle since it can be used for *fast* ambiguity resolution, although a much smaller ionospheric standard deviation is admissible than the mentioned range, e.g. for instantaneous positioning applications it may be about 1 cm at most.

With the ionosphere-weighted model both ambiguity resolution and fixed coordinate estimation are fully *robust* against ionospheric delays. It may uniform the awkward processing of rather short baselines (< 10 km), for which ambiguity resolution is usually based on the ionosphere-fixed model, while the ambiguity-fixed coordinate estimation is based on the ionosphere-float model. Besides this, also successful processing of the data of longer (medium) baselines is expected. Crucial to the successful application of the ionosphere-weighted model are however a proper selection of the ionospheric corrections, plus the corresponding ionospheric standard deviation. In Chap. 6 examples of the ionosphere-weighted approach for the processing of medium baselines are given.

Chapter 6

Fast GPS positioning using ionospheric information

6.1 Introduction

In the previous chapter it was concluded that for fast GPS positioning applications over medium distances precise *a priori ionospheric information* is absolutely necessary. This ionospheric information may originate from different sources. In this chapter the main focus is on the application of ionospheric corrections determined from the data of a *permanent GPS network* in the vicinity of a user. Since such networks collect GPS observations all the time and have been set up in many parts of the world, they are in potential an excellent source of precise ionospheric information. Besides information derived from such a network, also other ionospheric sources may be used. During the last decades a number of *physical* models of the global ionosphere have been developed. Well known is *Klobuchar's model*, which is broadcast in the GPS satellite's navigation message (hence it is also known as the *GPS broadcast model*). Despite the expectation that the ionospheric information derived from such a model is less precise than estimated from a permanent network, in this chapter the performance of Klobuchar's model is analyzed for fast GPS positioning (see Sect. 6.2). After that, the remaining part of this chapter is spent to (permanent) *network-based* GPS positioning. In Sect. 6.3 the general concept is explained. Section 6.4 focusses on the procedure for processing the GPS observations collected at the stations of the permanent network. Thereby, much attention is paid to fast (preferably instantaneous) processing of the network data, by making advantage of the *smoothness* of the ionospheric delays in time. The results of this processing, the network parameters, are input for the generation of *Virtual Reference Station* (VRS) data, described in Sect. 6.5. A crucial part of this VRS data generation procedure is the generation of the virtual atmospheric delays, which is carried out by *interpolation* of the network ionospheric and tropospheric estimates. The interpolation algorithm used for this is described in Sect. 6.6. Section 6.7 treats the processing of the data observed by the user's receiver relative to the VRS. In Sect. 6.8 this VRS-based positioning concept is demonstrated for real practice situations in some case studies. Finally, Sect. 6.9 ends

the chapter with some concluding remarks.

6.2 Fast positioning using global ionospheric models

Global ionospheric models are models in which the world-wide ionospheric delays are parameterized using a relatively few number of coefficients. Klobuchar's ionospheric model is the most famous *global* ionosphere model. In Sects. 6.2.1 and 6.2.2 the performance of Klobuchar's model fast ambiguity resolution is investigated. Another type of global ionospheric models are those based on the *Global Ionosphere Maps* (GIMs), determined and published by *CODE*, the Center for Orbit Determination in Europe. They are computed (and also predicted) for every two hours, using data from about 150 GPS sites of the International GPS Service (IGS) and other institutes [Schaer et al., 1998]. Unfortunately, the performance of these GIMs for fast GPS positioning is not investigated in this thesis (due to time restrictions).

6.2.1 Klobuchar's ionospheric model

Klobuchar's ionospheric model is the simplest model to account for the ionospheric delay. The method for the computation of the ionospheric delay at a certain location on Earth and for a certain epoch, is described in [Klobuchar, 1987]. In a first step, the slant ionospheric delay is mapped to a vertical delay using the *cosecant* mapping function (see Chap. 4). Next, the diurnal variation of this vertical ionospheric delay is modelled as a *cosine function* during daytime and as a *constant* of approximately 1.5 m during the night. The cosine may vary in amplitude and period, dependent on the user latitude and the predicted ionospheric activity, but has its daily maximum at 14.00 h local time at the *sub-ionospheric point*. The vertical ionospheric delay is computed as follows:

$$\imath^s_{v,r}(i) \;=\; \begin{cases} c\left[5\cdot 10^{-9} + \left(\sum_{l=0}^{3} \alpha_l \left[\varphi^s_{m,r}(i)'/\pi\right]^l\right) \cos x^s_r(i)\right], & |x^s_r(i)| < \frac{\pi}{2} \\ c\cdot 5\cdot 10^{-9} \;\approx\; 1.5 \text{ m}, & |x^s_r(i)| > \frac{\pi}{2} \end{cases} \tag{6.1}$$

with $x^s_r(i) \;=\; \frac{2\pi(t^s_r(i)' - 14\cdot 60^2)}{\sum_{l=0}^{3} \beta_l \left[\varphi^s_{m,r}(i)'/\pi\right]^l}$, and where:

$\imath^s_{v,r}(i)$	:	vertical ionospheric delay [m]
c	:	velocity of light [m/s]
$\varphi^s_{m,r}(i)'$	:	geomagnetic latitude of the sub-ionospheric point
$t^s_r(i)'$	:	local time at the sub-ionospheric point [s]
α_l $(l = 0, \ldots, 3)$	:	Klobuchar coefficients for amplitude
β_l $(l = 0, \ldots, 3)$	:	Klobuchar coefficients for period

Note that the local time at the sub-ionospheric point is computed from the *Uni-*

versal Time (UT) as:

$$t_r^s(i)' \;=\; t_{UT} + \frac{24 \cdot 60^2}{2\pi}\lambda_r^s(i)' \tag{6.2}$$

with t_{UT} the Universal Time in seconds and $\lambda_r^s(i)'$ the longitude of the sub-ionospheric point. The eight Klobuchar coefficients in Eq. (6.1) are transmitted in (the header of) the GPS satellite's *navigation message*. These coefficients are derived from an empirical model of the worldwide ionospheric behavior, determined in the 1970s by [Bent and Llewellyn, 1973]. Since July 2000, these coefficients are also computed and provided by *CODE*, claiming that these coefficients perform significantly better than the coefficients that are broadcast by the GPS satellites [CODE, 2002].

6.2.2 Performance of Klobuchar's model

To get insight in the performance of Klobuchar's ionospheric model for fast precise GPS applications, ionospheric corrections were computed for a 54-km baseline, measured on July 14, 2000 (at mid-latitudes), using the coefficients determined by *CODE*. Figs. 6.1 and 6.2 show the vertical ionospheric delay for this day according to Klobuchar's model for two sub-ionospheric points. From these figures it can be seen that the model represents the daytime ionospheric delay as a very *smooth* function of time.

DD ionospheric delays

To compare the ionospheric corrections from Klobuchar's model with the *real* ionospheric delays in the GPS observations, in Fig. 6.3 for *six hours* of the day (local time 10:00-16:00 h) double-differenced (DD) ionospheric delays are plotted for all satellites minus one (one is pivot satellite), as estimated from the dual-frequency phase and code observations. For this purpose the *ionosphere-float* model was used (see Chap. 5), with the DD ambiguities fixed to their correctly estimated integer values (ambiguity resolution was successful because of the long time span). Note that the DD ionospheric delays for this baseline can range up to about 50 cm. Figure 6.4 depicts the Klobuchar corrections for the same six hour time span, which are double-differenced with respect to the same pivot satellite as the real delays. From the figure one can immediately see that also in relative mode the Klobuchar corrections are very smooth in time, much more than the real delays.

In a next step the Klobuchar ionospheric delays were applied to correct the GPS observations. Figure 6.5 shows the residual ionospheric delays, i.e. the differences between the real delays (see Fig. 6.3) and the corrections (see Fig. 6.4), again obtained after ambiguity resolution. From the figure it can be seen that the corrections only slightly reduced the ionospheric delays in the data, since residual delays up to 30 cm remain. That these residuals are very large can be seen when Fig. 6.6 is taken into account, in which the DD ionospheric delays in the GPS data of a very short 4-km baseline are shown (for the same time span). These delays are much smaller: All below the 5 cm.

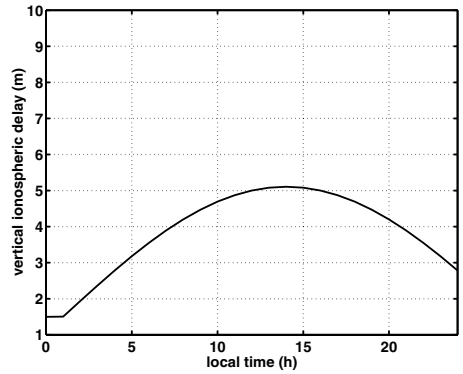

Fig. 6.1. Vertical ionospheric delay for July 14, 2000, and sub-ionospheric point $(\varphi'_m, \lambda'_m) = (53.7°, 89.1°)$

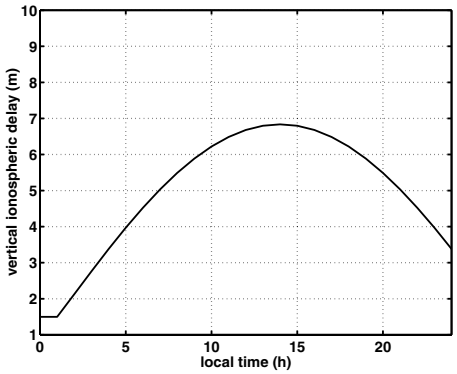

Fig. 6.2. Vertical ionospheric delay for July 14, 2000, and sub-ionospheric point $(\varphi'_m, \lambda'_m) = (36.9°, 73.5°)$

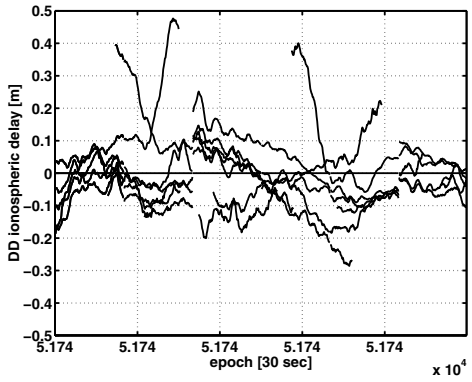

Fig. 6.3. DD ionospheric delays present in observations (ambiguity-fixed)

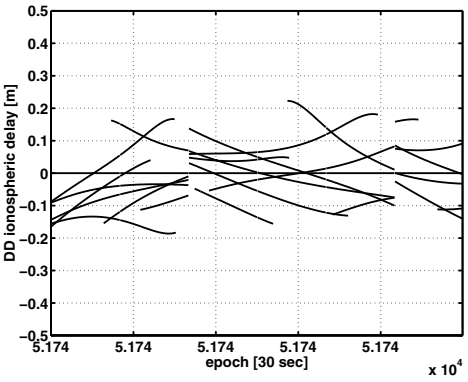

Fig. 6.4. DD ionospheric corrections determined with Klobuchar's model

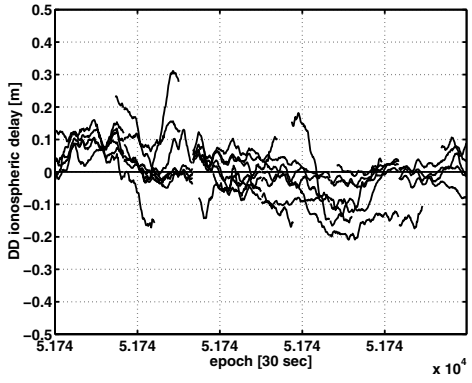

Fig. 6.5. Residual DD ionospheric delays (difference real - model delays)

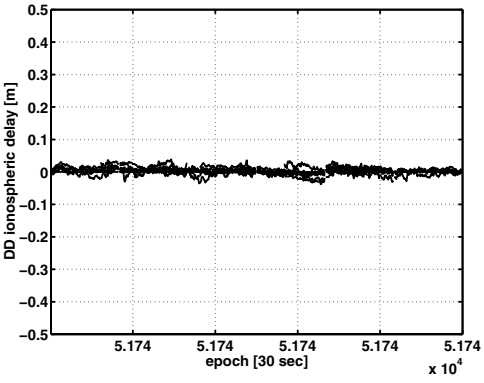

Fig. 6.6. To compare: DD ionospheric delays for a 4-km baseline

Ambiguity resolution

Due to the large residual delays in the data of the 54-km baseline, fast ambiguity resolution is not expected successful. This is confirmed by Table 6.1, which summarizes the empirical ambiguity success rates for the six-hour time span, divided into smaller windows (from instantaneous to 60 minutes). For each window it was tried to resolve the integer ambiguities *without* using information from previous windows. As can be seen from the table, the results of the ionosphere-*fixed* ($\sigma_\imath = 0$) processing with deterministic Klobuchar corrections were very disappointing. Even for windows of one hour long, the empirical ambiguity success rate was only a low 0.33. For the sake of comparison, also for the short 4-km baseline (for which the ionospheric delays are depicted in Fig. 6.6) ambiguity resolution was carried out using the ionosphere-fixed model for the same window lengths (but for this baseline without Klobuchar corrections). For the 4-km baseline ambiguity resolution was successful for *all* windows, even instantaneously, and this is what we would expect a priori. Table 6.1 also shows ambiguity success rates for the processing of the data of the 54-km baseline using the *ionosphere-float* model ($\sigma_\imath = \infty$). In this processing the ionospheric delays are completely estimated from the GPS data and a priori ionospheric corrections are not used at all. The table shows that although the empirical success rates are zero for the very short windows, for a longer time span the ionosphere-float success rates start to become higher than their ionosphere-fixed counterparts based on the Klobuchar corrections! For example, for the one hour windows, using the ionosphere-float model the ambiguities could be resolved for all windows of the six-hour time span, while using the ionosphere-fixed model this was only possible for 33% of the windows.

Table 6.1. Empirical ambiguity success rates

time span [min]	Ionosphere-fixed Klobuchar - 54km	Ionosphere-float no corr. - 54km	Ionosphere-fixed no corr. - 4km
inst.	0.00	0.00	1.00
5	0.00	0.00	1.00
10	0.00	0.11	1.00
30	0.08	0.92	1.00
60	0.33	1.00	1.00

This example shows that for fast relative GPS positioning it is better *not* to rely on ionospheric corrections determined with Klobuchar's model, since there is a risk of *overcorrecting* the ionospheric delays present in the data. This conclusion is however not so surprising, since one should keep in mind that Klobuchar's model was originally designed to correct *single-frequency code data* for *absolute* positioning and not for the relative application based on phase and code data as described in this example.

6.3 Fast network-based GPS positioning

The problem with using ionospheric corrections derived from global ionosphere models is that the world-wide network which has determined the model coefficients is usually too sparse. Hence, *small-scale* ionospheric features cannot be captured by such networks, while these may be important for medium-scale GPS applications.

Ionospheric corrections may also be generated from regional *permanent GPS networks* in the vicinity of the user's receiver. At regional scale, in many parts of the world permanent GPS networks have been set up in the last decade, to function as backbone of the (national) geometric infrastructure [De Jong, 1997]. For a user such a permanent network improves the *reliability* of his measurement setup, since there is more than one reference station for a user to relate his observations (*network-based* positioning). However, since the distance between the permanent stations may be quite long (up to 200 km), for a user operating far away from all permanent stations, still quite a long observation time span is necessary to account for significant ionospheric delays. The availability of a permanent network however offers *more* than just extra reference stations: From the network data it is possible to estimate the *atmospheric delays* between the network stations, and this information can be used to *predict* the ionospheric (and tropospheric) delays at the location of the user. This prediction is then based on the spatial coherence of the atmospheric delays. When these predictions are sufficiently precise, a user may correct his measurements to a sufficient degree such that fast ambiguity resolution becomes feasible.

Different methods of network-based positioning and spatial prediction of atmospheric delays have been developed in recent years. In this research the approach based on *Virtual Reference Stations* (VRS) is chosen as method for network-based positioning. In this section this choice is motivated. A *three-step procedure* to obtain precise positions at the user's location from the permanent network data (which includes this VRS approach), is explained in the last part of this section.

6.3.1 Single-baseline vs. network-based approach

Within GPS-based surveying a variety of measurement setups can be distinguished. They can be divided into *single-baseline* (two receiver) and multiple-baseline or *network* setups. Figures 6.7 – 6.12 show some of these measurement setups.

Single-baseline vs. network setup

Figure 6.7 depicts the traditional *single-baseline* approach: Within a network of reference stations, together with his own data a user only processes data from the *closest* reference station to minimize the atmospheric (mainly ionospheric) delays in his relative observations. In the figure the two other reference stations in the area are not used at all. In contrast to Fig. 6.7 in the measurement setup of Fig. 6.8 *all* available reference stations are used. The user collects the data of the

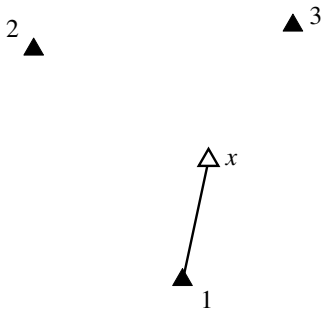

Fig. 6.7. Single-baseline approach (shortest distance)

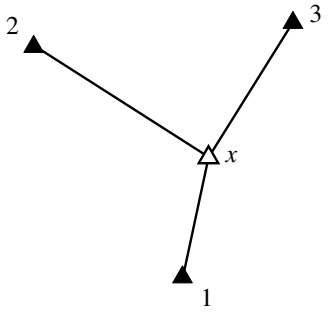

Fig. 6.8. Network approach (1): More than 1 reference station is used

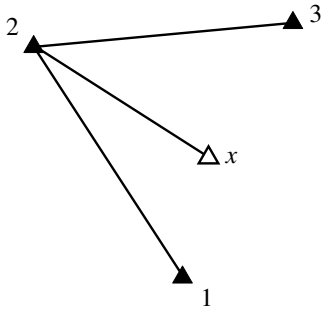

Fig. 6.9. Network approach (2), user solution equivalent to (1)

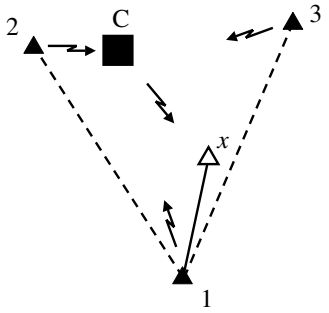

Fig. 6.10. Single-baseline approach within permanent network

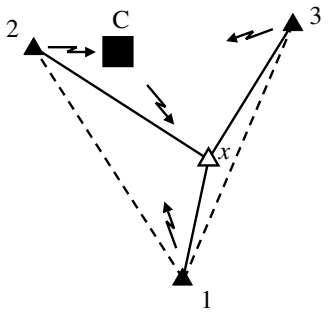

Fig. 6.11. Network approach within permanent network

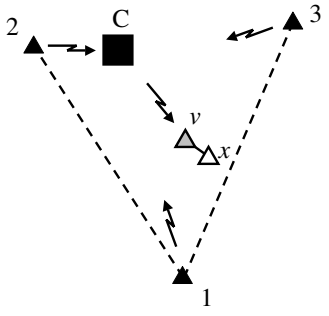

Fig. 6.12. Virtual reference station (VRS) approach

three surrounding reference stations and these observations are, together with his own observations, processed in one integral adjustment. This is the *network* approach. In this approach the choice of the baselines is *arbitrary*, but the following two conditions should be taken into account: i) The $n-1$ baselines are processed simultaneously (when n receivers are involved), and ii) The mathematical correlation between the baselines should be properly taken into account. Instead of the network in Fig. 6.8, one could therefore also process a network as shown in Fig. 6.9, which results in exactly the same coordinate solution as the solution of the network in Fig. 6.8. Note that although different sets of ambiguities are estimable in both networks, the ambiguity success rates will be exactly equal. Comparing the networks in Figs. 6.8 or 6.9 with the single-baseline in Fig. 6.7, the network ambiguity success rate will be hardly better than the single-baseline success rate. Despite that more reference stations are used in the network setups, the problem of ionospheric delays in the data remains. Although the ambiguities of the baselines between 'known' receiver locations (these are the baselines between stations 1 and 2, and 2 and 3 in Fig. 6.9) can be determined in a shorter time span than the ambiguities of the baseline to a station with unknown position (between 2 and x in Fig. 6.9), the *overall* success rate of the network ambiguities will be quite low (at least when the time span is short).

Use of a permanent GPS network

Significant improvements are possible when the processing is split into two parts: i) A processing of the data of the stations with known positions on the one hand, and ii) A processing of the data of the station(s) for which the position needs to be determined on the other hand. This is possible when a (regional) *permanent GPS network* is available in the vicinity of a user. The data collected by the permanent stations, 1, 2 and 3 in Fig. 6.10, are transmitted to a computing center (C in the figure). At this computing center a network processing is carried out based on data of all permanent stations. Note that with three permanent stations, as shown in the figure, just two network 'baselines' are independent. In Fig. 6.10 these two baselines are the *dotted* lines. Permanent station 1 in the figure is also referred to as *master reference station*. When the network ambiguities are resolved, and when these are consequently held fixed, very precise network estimates, a.o. for the network ionospheric delays, can be determined. Using these network parameters, it is possible to *spatially predict* the ionospheric delays for the user baseline, which is 1-x in the Fig. 6.9. This is possible, because the ionospheric (and also tropospheric) delays are known to be spatially correlated (up to a few hundreds of km). Consequently, these predictions are provided to the user in the form of ionospheric corrections. In the ideal situation, when the prediction is very accurate, the ionospheric delays will cancel for the user baseline, making very short observation time spans feasible, since in that case the ionosphere-fixed model can be used. In Fig. 6.10 the user only computes a shortest baseline using the corrected data, but one could also solve the three baselines from the user station to the three permanent stations simultaneously, in a network adjustment, see Fig. 6.11. The difference of this figure with Fig. 6.8 is, that in Fig. 6.11 the

relative observations are corrected for atmospheric delays, whereas in the network adjustment in Fig. 6.8 the uncorrected data are used.

Use of virtual reference stations (VRS)

Instead of the previous discussed direct application of the atmospheric corrections to the user's observations, an alternative approach is that he processes his observations together with observations of a *virtual reference station* (VRS) of the permanent network. A VRS is a non-existent GPS reference station at the approximate user's location. The observations of such a virtual station are computed from the data of the (real) permanent stations and resemble as much as possible the observations a *real* GPS receiver would have produced at the approximate user's location [Van der Marel, 1998]. The purpose of a VRS is that the user does not have to use data of the individual reference stations and does not have to apply corrections for the atmospheric delays. Like in the setup of Fig. 6.11, a spatial prediction of the atmospheric delays is carried out, but this is part of the VRS data generation procedure, and thus 'hidden' for a user of VRS data. The relative ionospheric delays between the virtual and user data should be reasonably small (ideally zero), since the virtual station location is chosen at the (approximate) position of the user receiver. In Fig. 6.12 the measurement setup using a virtual reference station is shown. Note that in this figure the distance between VRS v and user station x is exaggerated: In reality this is only a few m, since the VRS coordinates are equal to the approximate user coordinates. In case of post-processing applications, the VRS observations should be provided to the user in the usual RINEX format, allowing the user to easily use them as if they were real observations. These RINEX data should be placed on the World Wide Web, such that the user can download the VRS data himself. In case of real-time applications the VRS data should be directly transmitted to the user. Although important for real-time applications, in this chapter the focus will be barely on *data communication* aspects for real-time applications. For actual issues on this, the reader is referred to, among others, [Euler et al., 2001].

6.3.2 Geometric vs. physical approach for spatial prediction

For the spatial prediction of the atmospheric delays to the user's location several methods are described in the literature. Considering the ionospheric delays, in many publications the slant delay for a certain receiver-satellite combination is first mapped to vertical ionospheric delay, which is modelled over the entire area of interest as a function of latitude and longitude (or hour angle of the Sun). The unknown coefficients of such polynomial functions are then estimated in the network processing. Examples of such *physical* models of the ionospheric delays can be found in e.g. [Webster and Kleusberg, 1992], [Georgiadou, 1994], [Rothacher and Mervart, 1996], and [Stewart, 1997]. The estimated coefficients can consequently be provided to users in the coverage of the network from which they may compute their ionospheric corrections. Drawback of this approach is that often no physical knowledge about the ionosphere is available, i.e. it is not known

a priori how many coefficients need to be estimated to cover the ionospheric delays. Besides, one may question whether the used mapping function to obtain vertical delays (usually the cosecant mapping function, see Chap. 4), is sufficiently precise. Another type of physical model, i.e. a so-called two-layer *tomographic* model, was used in [Colombo et al., 1999].

In the approach described in this thesis however *no* mapping of the ionospheric delays is carried out, and no a priori specified function is assumed. Instead, the approach is a pure *geometric* one: Using a collocation-type of prediction the (slant) ionospheric delays are *interpolated* at the user's location. This method is described in detail in Sect. 6.6. Since no physical assumptions are involved, our approach is expected to function under conditions of small-scale ionospheric features.

6.3.3 VRS-based vs. area correction-based approach

In this thesis the VRS-based approach is chosen, since it has some advantageous properties over an approach in which the corrections for, among others, the atmospheric delays are *explicitly* distributed to users, who can consequently correct their GPS observations. This latter approach is referred to as the *area correction* approach, or sometimes as FKP approach, where FKP is German for *Flächen Korrektur Parameter*, see [Wübbena and Willgalis, 2001]. These area correction parameters are usually the coefficients from a certain assumed physical model of the error components, see the previous subsection. Publications describing approaches on these area correction parameters are, among others, [Wanninger, 1995], [Gao et al., 1997], [Raquet, 1998], [Rizos et al., 1998], [Varner, 2000], and [Dai et al., 2001a]. VRS-based approaches are reported in, among others, [Van der Marel, 1998], [Wanninger, 1999], [Odijk et al., 2000], [Vollath et al., 2000], [Jaeggi et al., 2001], and [Namie et al., 2001]. For a systematic overview and comparison of both types of approaches, we refer to [Dai et al., 2001b] and [Fotopoulos and Cannon, 2001].

The *advantages* of a VRS-based approach over a correction-based approach can be summarized as follows:

- The user does not have to correct his observations for atmospheric delays (except maybe for an a priori troposphere model). Since the VRS data can be provided in *RINEX* format, the user can apply his normal GPS processing software, and no additional software tools need to be used to account for explicit corrections (which requires extra effort, administration, etc.).
- The user only has to deal with *one (virtual) reference station* and does not have to download data from more than one reference station.
- Because of one reference station, the user can suffice with *single-baseline* software and does not need to use more complex network software.
- Because of the VRS data which are *undifferenced*, the user does not have to know about any reference station or reference satellite dependency, which is

however important when explicit differential corrections are used.

Some *disadvantages* of a VRS-based approach are:

- Since the user cannot distinguish between the different components that together form the VRS observables, he has no complete self control over the processing.
- When not made public, the user has no insight in the generation procedure of the virtual data.
- In case of real-time applications, a *two-way* data-link is necessary: A user has to broadcast its approximate position to the network's computing center, whereas the computing center has to broadcast the VRS data.
- In case of a VRS approach, the number of users is *restricted*, since a VRS provider (the permanent network) has to generate VRS data, which are different for different users. In case of FKP this is just one set valid for all users.

6.3.4 Three-step procedure

The general procedure to estimate precise positions based on the VRS approach is schematically depicted in Fig. 6.13. This procedure consists of three separate procedures: i) Network processing, ii) VRS data generation, and iii) User's processing. These three steps are described in full detail in Sect. 6.4 – 6.7. First, in Sect. 6.4 the network processing is explained, in which network parameters are estimated from GPS data collected at the permanent reference stations. Some of these network estimates form the input of the generation of the VRS observations, and this procedure is described in Sect. 6.5. An important aspect of this procedure is the interpolation of the network atmospheric delays, which is described in a separate section (Sect. 6.6). Finally, the procedure in which the desired positions are estimated using the VRS and the user's data, is described in Sect. 6.7.

6.4 Network processing

The purpose of the network processing is to resolve the integer ambiguities and to estimate ambiguity-fixed network parameters, such as ionospheric and tropospheric delays and satellite clock parameters. Traditionally, the processing of reference network data is based on a quite *long observation time span*, e.g. a safe one hour or more, in order to resolve the network ambiguities with the *ionosphere-float* model, using dual-frequency phase and code data. For the purpose of *fast* positioning however, this network processing should be based on a strategy requiring only a few observation epochs. Ideally, the network processing should be carried out using data of just one single epoch, such that the parameters can be estimated *instantaneously* and provided in *real-time* to users operating within the coverage of the network.

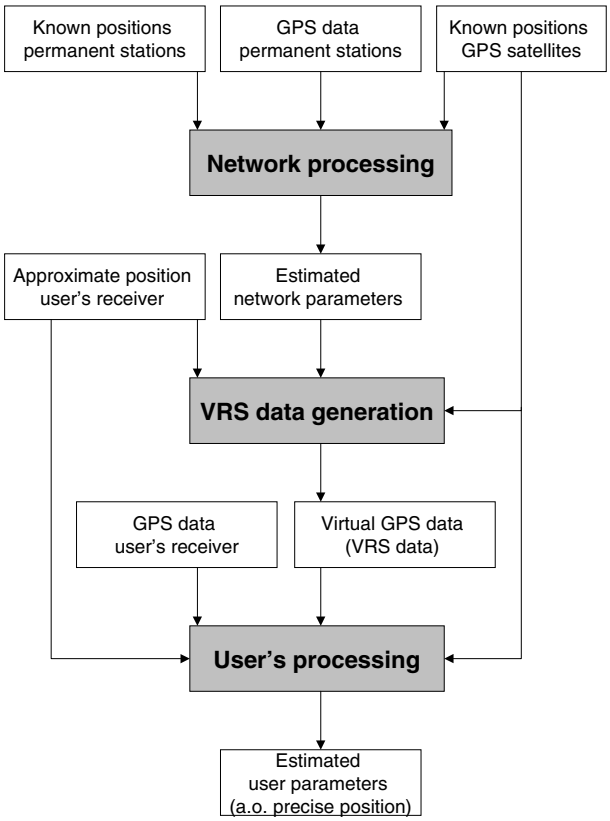

Fig. 6.13. Three-step procedure for positioning within a permanent GPS network

Many recent publications deal with fast network processing, e.g. [Dai et al., 2001a], [Chen, 2000], [Chen et al., 2000], [Gao et al., 1997], and [Schaer et al., 1999]. In this section another mathematical model is described which is suitable for fast, possibly instantaneous processing of network observations. An important difference of this model with the models as described in the literature, is the *temporal prediction* of the ionospheric delays. Another difference is that it is tried to resolve the *complete* ambiguity vector all the time, instead of forming subsets such as wide lanes, narrow lanes, etc. Linear combinations of ambiguities are only determined by the *decorrelating transformation* of the LAMBDA method. In case of instantaneous processing, for each epoch the ambiguities are resolved again. In this section

this method is described in detail. The section ends with two subsections in which examples are given of the network processing.

6.4.1 Parameters in the network model

The network model can be either based on the ionosphere-float model, or the ionosphere-weighted model. The first is only suitable for post-processing applications, while the second should be used for fast possibly real-time applications. In both models however certain parameters are treated in a similar way, though in a different way compared to the general ionosphere-weighted and ionosphere-float models as described in Chap. 5. In this subsection these parameters are described.

Receiver positions

A major difference with the models introduced in Chap. 5 is that in the network model it is *not* necessary to parameterize receiver positions. In case of permanent networks they are namely precisely known, at mm-cm level (especially when the network exists for a long time). Hence, in the processing they are held fixed to their *a priori known values*.

Satellite positions

Besides the receiver positions, in the network model also the satellite positions are fixed. For this purpose use is made of the precise orbit products of the IGS. For post-processing applications the final IGS orbits can be taken, but for real-time applications the satellite positions should be computed using the new, *ultra-rapid* IGS orbits [Springer and Hugentobler, 2001]. Data of satellites for which the ultra-rapid coordinates are of low quality (indicator in header is larger than 10) or even not included (because of bad quality), should thereby be removed from the processing.

Tropospheric delays

Because the receiver and satellite positions are both fixed, the receiver-satellite ranges are precisely known. In this situation the *geometry-free* version of the ionosphere-weighted model (see Chap. 2 and Chap. 5) becomes exceptionally suited to function as mathematical model for the network processing. With known ranges, the *tropospheric delays* can be estimated unbiased as slant delay parameters, and with the addition of tropospheric pseudo-observations they can be estimated for each receiver-satellite combinations as well (like the ionospheric delays in the ionosphere-weighted model). Although in theory these are good criteria, in this thesis the geometry-free model is *not* used for the network processing, since it is not yet implemented in the *GPSveQ* software (due to time restrictions). Instead, the geometry-based model is used in which *zenith tropospheric delays* (ZTDs) are estimated. In this model with ZTDs also a priori tropospheric corrections are used, for example using Saastamoinen's model.

6.4.2 Three-step network processing

For the network processing, time is divided into discrete, consecutive *windows*, consisting of an equal number of k epochs. For each window, a network processing procedure is carried out, as schematically depicted in Fig. 6.14. When $k = 1$, the smallest window length possible, we speak of instantaneous network processing.

For each window the well-known three-step procedure, i.e. *float solution - ambiguity resolution - fixed solution* (as explained in Chap. 3), is carried out. For the float and fixed solution standard least-squares adjustments are performed, while for ambiguity resolution the integer least-squares technique (as implemented in the LAMBDA method) is used. So the complete vector of network ambiguities is resolved each time again for each window. For these ambiguities it is known that they remain time-constant as long as no cycle slips or loss-of-locks occur. However, this natural ambiguity property is only used to resolve the ambiguities *within* a window and not *between* consecutive windows when the same ambiguities apply for different windows. Although the ambiguity link between consecutive windows strengthens the model, it is in our case not really necessary, since precise ionospheric information already links between windows (see Sect. 6.4.4). Another advantage of removing the ambiguity link between windows is that in case of instantaneous processing the procedure is insensitive to possible *cycle slips*, and it is therefore not necessary to test on them.

Cycle-slip tests plus other tests (see Chap. 3) should however be carried out *within* each separate window, when the window length is longer than one epoch. To resolve the ambiguities in each of these windows, use is made of the time-constancy of the ambiguities and cycle slips could harm the estimation, when undetected.

6.4.3 Example: Network ionospheric delays

In this subsection a typical example is given of the size and variability of the ionospheric delays estimated from a medium GPS network (at mid-latitudes). The data is taken from the AGRS.NL network, the *Active GPS Reference System in the Netherlands*, which is the Dutch governmental permanent GPS network. This network consists of five stations at an average distance of about 150 km, see Fig. 6.15. All the reference stations are equipped with Trimble 4700 GPS receivers. The network is maintained by the Dutch *Cadastre* and the *Survey Department of Rijkswaterstaat*. A central computing center has been set up in Apeldoorn (APEL) where the data are stored and network computations are carried out.

For three time spans in the period from September 30th to October 6th 2001 ionospheric delays were estimated from dual-frequency phase and code observations after the integer ambiguities had been resolved. The satellite cut-off elevation was fixed at 15° and the data sampling interval was 30 s. The three selected time spans are: i) 2 October 2001, 00:06 – 03:50 UTC, ii) 3 October 2001, 12:06 – 03:50 UTC, and iii) 5 October 2001, 00:06 – 03:50 UTC. Note that the first and

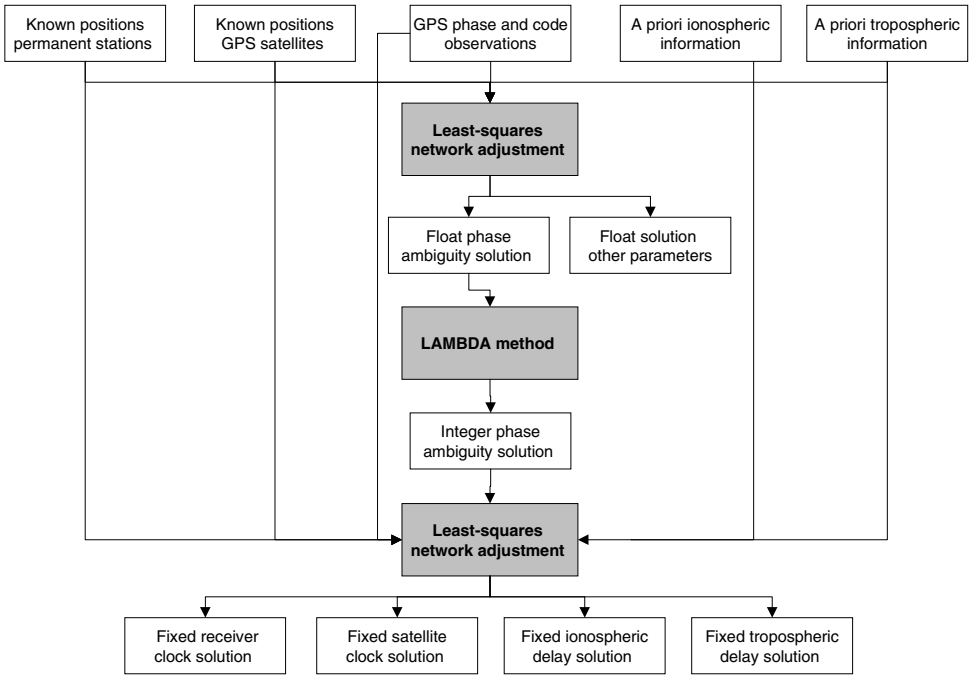

Fig. 6.14. Schematic overview of the network processing for each time window

the third time spans are both *nighttime* periods, while the second one is during *daytime*. The reason for selecting these time spans is to demonstrate the impact of different geomagnetic conditions on the ionospheric delays: During the first two periods the geomagnetic conditions were disturbed (Kp $>$ 4), while during the third time span these conditions were much more quiet (Kp $<$ 2), see Fig. 6.16.

Since the purpose of this example is only to illustrate network ionospheric delays, the *ionosphere-float* model is used (in post-processing mode based on a long time span). Although the estimable ionospheric delays with this model are biased by clock terms (see Chap. 5), double-differencing of this ionospheric estimates eliminates these terms. When estimating the ambiguity-fixed DD ionospheric delays, station DELF was chosen as master reference station. Using this, four network baselines were formed, i.e. DELF-TERS (163 km), DELF-WSRA (183 km), DELF-APEL (111 km) and DELF-EIJS (164 km), for which the DD ionospheric delays are plotted in Figs. 6.17 – 6.28. In these figures the first of the three 'columns' presents the results for the first time span, whereas the second column shows the results of the second time span and the third column the results of the third time span.

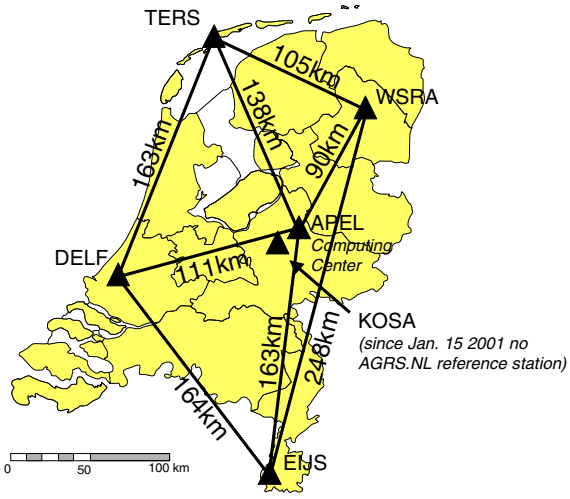

Fig. 6.15. The AGRS.NL network. Station KOSA (Kootwijk) was until the operation of station APEL on January 15 2001 part of the network.

Comparison of the *first* with the *third* 'column' reveals that the size and variability of the ionospheric delays is closely related to the geomagnetic activity. Both columns concern a nighttime period and since the same time span from 00:06 – 03:50 UTC is used, the receiver-satellite geometry for the two periods is about the same (because of the daily repeating satellite configuration). Since also the same pivot satellite is used for both time spans, the differences between corresponding figures in the two columns stem from a difference in ionospheric conditions. Since the DD ionospheric delays in the first column are in general larger and more fluctuating, it is probably due to the increased geomagnetic activity within that period.

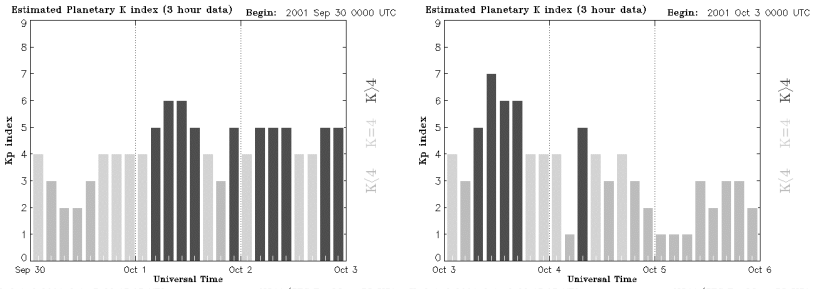

Fig. 6.16. Planetary Kp-index from September 30 to October 6, 2001

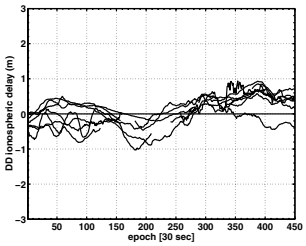

Fig. 6.17. DELF-TERS, 02-10-01, 00:06-3:50 UTC

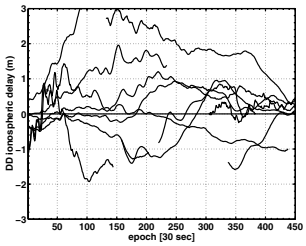

Fig. 6.18. DELF-TERS, 03-10-01, 12:06-15:50 UTC

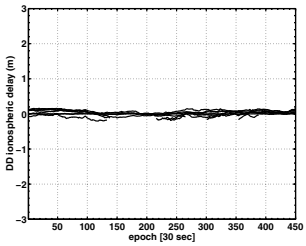

Fig. 6.19. DELF-TERS, 05-10-01, 00:06-03:50 UTC

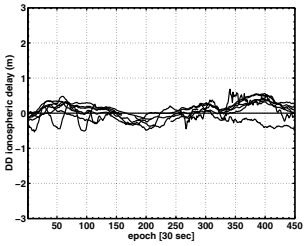

Fig. 6.20. DELF-WSRA, 02-10-01, 00:06-03:50 UTC

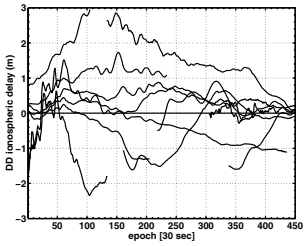

Fig. 6.21. DELF-WSRA, 03-10-01, 12:06-15:50 UTC

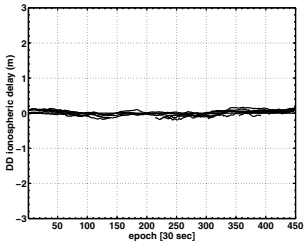

Fig. 6.22. DELF-WSRA, 05-10-01, 00:06-03:50 UTC

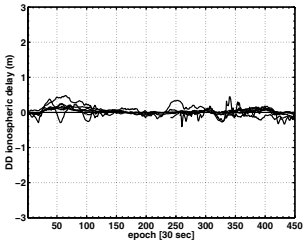

Fig. 6.23. DELF-APEL, 02-10-01, 00:06-03:50 UTC

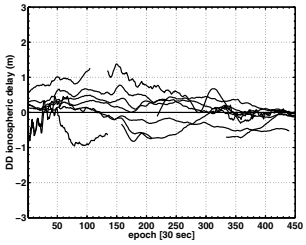

Fig. 6.24. DELF-APEL, 03-10-01, 12:06-15:50 UTC

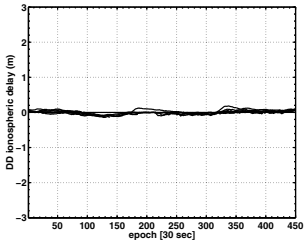

Fig. 6.25. DELF-APEL, 05-10-01, 00:06-03:50 UTC

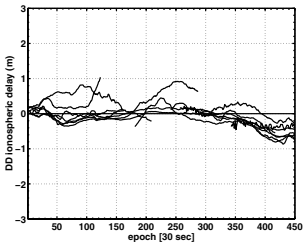

Fig. 6.26. DELF-EIJS, 02-10-01, 00:06-03:50 UTC

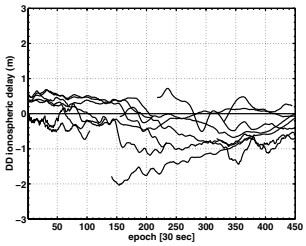

Fig. 6.27. DELF-EIJS, 03-10-01, 12:06-15:50 UTC

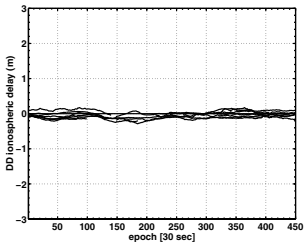

Fig. 6.28. DELF-EIJS, 05-10-01, 00:06-03:50 UTC

The DD ionospheric delays depicted in the figures in the *second* column are much larger than those in the first and third columns. This time span concerns a daytime period (12:06 – 15:50 UTC), for which the ionospheric delays are normally higher than during nighttime. Besides this, the geomagnetic activity during this daytime period was also higher than during the two nighttime periods (see Fig. 6.16). Note that during this daytime period the DD ionospheric delays may range up to 3 m, while during the nighttime period with low geomagnetic activity the DD ionospheric delays are at most about 20 cm.

Despite the large differences in size and variability of the ionospheric delays, the DD ionospheric delay time series for different network baselines during the same time span, show much resemblance in smoothness. This indicates *spatial correlation* between the network ionospheric delays.

6.4.4 Ionospheric prediction in the network processing

The use of the *ionosphere-weighted* model in the network processing requires sample values for the ionospheric pseudo-observables. A first idea is to use *zero* values as samples, but because of the medium distance between the network stations, in this case zero samples require a relatively *large* a priori ionospheric standard deviation. Such imprecise a priori ionospheric information however hampers fast network ambiguity resolution (see Chap. 5). In this section a method is described to derive *precise* ionospheric information for the network processing.

In the case of processing the data of a permanent GPS network, precise ionospheric information is in principle available. Note from the example in the previous subsection, that the temporal variation of the delays is reasonably *smooth* between consecutive epochs. This property can be used to predict the ionospheric delays for a future observation epoch, see also [Delikaraoglou, 1989]. In this section two methods are described to generate the ionospheric pseudo-observables from previous epoch(s). The first method uses a prediction based on just the *previous epoch*, while in the second method the *two previous epochs* are used.

Prediction using the previous epoch

When the temporal variation of the ionospheric delays may be considered as a *random-walk* stochastic process, the *velocity* of the ionospheric delay is assumed to be a white-noise process. In App. E it is shown that in that case the difference between the ionospheric delays on two consecutive epochs may be considered as *uncorrelated* quantities in time, with a constant variance for each epoch:

$$z_r^s(i) \;=\; \imath_r^s(i) - \imath_r^s(i-1); \quad \sigma^2_{z_r^s(i)} \;=\; q_i \Delta t \tag{6.3}$$

where Δt denotes the data sampling interval [s] and q_i the *spectral density* of the velocity of the ionospheric delays [m^2/s].

Equation (6.3) can be used for *instantaneous* network processing as follows. Con-

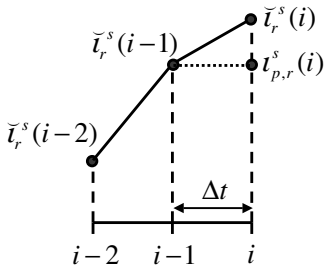

Fig. 6.29. Prediction of ionospheric delay using the previous epoch

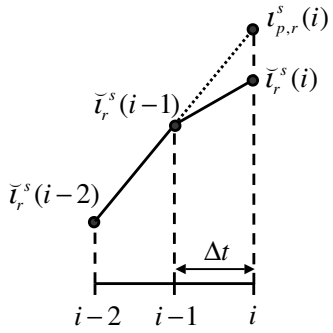

Fig. 6.30. Prediction of ionospheric delay using the previous two epochs

sider $\imath_r^s(i)$ as the sample value to be taken for the ionospheric pseudo-observable on epoch i. Then, for the sample value of $\imath_r^s(i-1)$ the precise ambiguity-fixed ionospheric solution from the previous epoch is taken. When the sample value of $z(i)$ is taken zero, the sample value plus variance for the ionospheric pseudo-observable become as follows:

$$\boxed{\imath_{p,r}^s(i) \;=\; \breve{\imath}_r^s(i-1); \qquad \sigma^2_{\imath_{p,r}^s(i)} \;=\; \sigma^2_{\breve{\imath}_r^s(i-1)} \;+\; q_\imath \Delta t} \tag{6.4}$$

where it is assumed that the ambiguity-fixed ionospheric estimates on previous epochs do not correlate with each other and also do not correlate with $z_r^s(i)$. Figure 6.29 illustrates this way of ionospheric prediction: The ionospheric pseudo-observation on epoch i is exactly equal to the ionospheric estimate from the previous epoch.

Prediction using the previous two epochs

Prediction using not only the previous epoch, but also the epoch preceding that epoch, is possible when instead of the velocity, the *acceleration* of the time-varying ionospheric delays is considered as a white-noise process. In App. E for this case it is shown that the *difference* of two differences of the ionospheric delays is the following stationary stochastic process:

$$z_r^s(i) \;=\; [\imath_r^s(i) - \imath_r^s(i-1)] \;-\; [\imath_r^s(i-1) - \imath_r^s(i-2)]\,; \quad \sigma^2_{z_r^s(i)} \;=\; \frac{2}{3} q_\imath \Delta t^3 \tag{6.5}$$

In case of *instantaneous* network processing, the sample value of the ionospheric pseudo-observable is computed from the ambiguity-fixed ionospheric estimates on the previous two epochs. Like in the previous case, the sample value of $z_r^s(i)$ is taken exactly zero, but its variance is taken into account:

$$\boxed{\imath_{p,r}^s(i) \;=\; 2\breve{\imath}_r^s(i-1) - \breve{\imath}_r^s(i-2); \qquad \sigma^2_{\imath_{p,r}^s(i)} \;=\; 4\sigma^2_{\breve{\imath}_r^s(i-1)} + \sigma^2_{\breve{\imath}_r^s(i-2)} + \frac{2}{3} q_\imath \Delta t^3}$$

(6.6)

For the variance of the pseudo-observable it is again assumed that the fixed ionospheric estimates on previous epochs do not correlate with each other and also do not correlate with $z_r^s(i)$. Fig. 6.30 shows that the predicted value is in fact a *linear extrapolation* from the ionospheric estimates on the two previous epochs.

From the literature it seems that this second method, thus in which the 'ionospheric acceleration' is assumed as white-noise, is more common for predicting the temporal variation of the ionospheric delay, than the first one (see e.g. [Loomis et al., 1989] and [Jin, 1996]). Therefore, in the network processing we will restrict ourselves to the *second* method of prediction. In [Jin, 1996] a typical value for the spectral density of the ionospheric acceleration is found, i.e. $q_{\ddot{\imath}} = 10^{-8}$ m^2/s^3, which holds under moderate ionospheric conditions. This value can be used in Eq. (6.6), to infer whether the standard deviation of the ionospheric pseudo-observables is sufficiently small for the network processing. Assuming that both ionospheric estimates on the two previous epochs have a precision of say 4 mm (note that they are ambiguity-fixed), then with a network data sampling interval of $\Delta t = 10$ s, the ionospheric standard deviation is computed as $\sigma_{\imath_{p,r}^s(i)} = \sqrt{5 \cdot 0.004^2 + \frac{2}{3}10^{-8} \cdot 10^3}$ ≈ 1 cm. Note that this value is just small enough to expect successful *instantaneous* resolution of the integer network ambiguities (see Chap. 5).

In the processing for all windows a *constant* ionospheric standard deviation is used for all pseudo-observables, which is denoted as $\sigma_{\imath,net}$. Figure 6.31 shows a sequence of three network processing windows. From this figure, note that the only link between the different windows are the ionospheric pseudo-observations, formed by the estimates of previous windows (in the figure these links are emphasized by the bold arrows).

Initializing the ionospheric prediction

A problem with the discussed ionospheric prediction algorithm is that there are certain situations in which ionospheric estimates from previous epochs are *not* available. When however just for a *short time span* observations are missing, then the linear ionospheric prediction of Eq. (6.6) might still be used, since under average ionospheric conditions the delays change smoothly. In general, when for $l-1$ epochs in between the ionospheric estimates are missing, the prediction can be based on the two epochs *before* the missing epochs:

$$\imath_{p,r}^s(i) \;=\; (l+1)\check{\imath}_r^s(i-l) - l\check{\imath}_r^s(i-l-1), \qquad l \geq 1 \tag{6.7}$$

Note that with a sampling interval of 30 s this should only be used in case when a few epochs are missing, say $l < 5$. If the sampling is higher, then more epochs may be missing.

In case of *longer data gaps* (e.g. several minutes) the prediction might fail and the ionospheric pseudo-observations need to be (re-)initialized. This initialization is

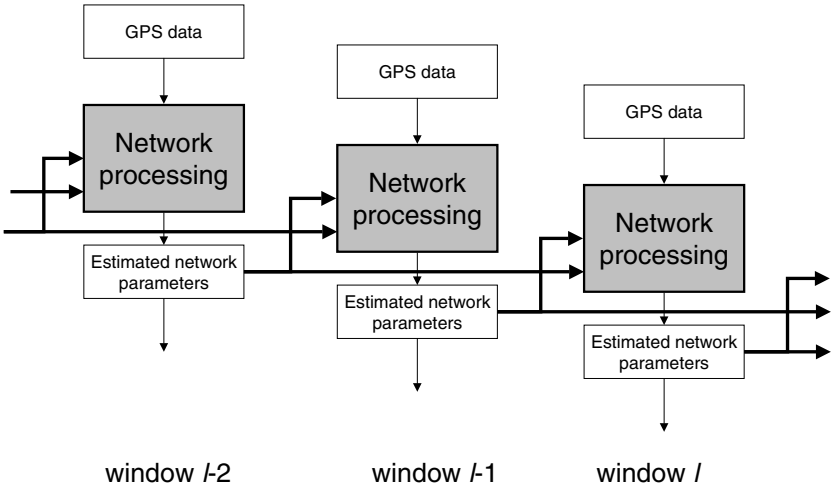

Fig. 6.31. Sequence of three network processing windows

also necessary at the *very first beginning* of operation of the permanent network and when *a new satellite* rises above the cut-off elevation. In the initialization process precise ionospheric estimates are derived using data of a sufficient long time span, which are processed using the the ionosphere-weighted model. In contrast to the *main* network processing, for this initialization it is allowed to use *zero samples* for the ionospheric pseudo-observables, since the a priori ionospheric standard deviation may be taken as a rather large value (for example: 30 cm). Using zero samples and a ionospheric standard deviation of a few dm's ambiguity resolution is feasible within a few minutes, depending on the data sampling interval and the time-constancy of the ambiguities (see [Odijk, 1999] and also Fig. 5.12 in Chap. 5). This 'initialization processing' lasts until the ambiguities are resolved. In case of a long data gap or at the first beginning of operation of the network during this period warnings should be issued that a network solution cannot be obtained. In the case that a *new satellite* rises, it is fortunately not necessary to stop the main processing to re-initialize *all* the ambiguities. Instead, a so-called *side-processing* should be started, in which the ambiguities and ionospheric delays are estimated for the data of the newly risen satellite. This side-processing should run parallel to the main processing, and the ionospheric estimates for the new satellite should not be included in the ionospheric prediction until the correct ambiguities are resolved. Figure 6.32 shows in a schematic way this side-processing running parallel to the main processing, which is an instantaneous processing in the figure. Having 'initialized' the ambiguities, the estimated ambiguity-fixed ionospheric delays at the two last epochs of this initialization form the input for the ionospheric prediction sequence.

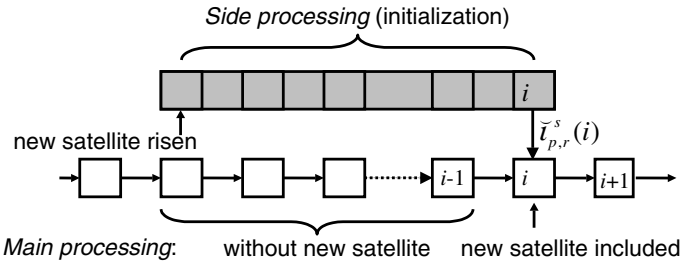

Fig. 6.32. Schematic situation of processing in case a new satellite rises

Ending the ionospheric prediction

When for a certain receiver-satellite combination the predicted value deviates too much from the real ionospheric delay, this combination is *removed* from the processing, since otherwise there is a high chance of estimating the wrong integer ambiguities. This deviation normally happens when a satellite is about to *set*, since in that case the ionospheric delays for this satellite may increase rapidly, because of the longer path of the GPS signals through the ionosphere.

To test the deviation of the predicted value with the estimated value, the ambiguity-fixed *outlier w-test* for the ionospheric pseudo-observations is used, since this is computed on each epoch, for every receiver-satellite combination. The test statistic reads (see Table C.1 in App. C):

$$w^o_{y(i)} = \frac{c_y^T Q^{-1}_{y(i)} \check{\epsilon}(i)}{\sqrt{c_y^T Q^{-1}_{y(i)} Q_{\check{\epsilon}(i)} Q^{-1}_{y(i)} c_y}}, \quad \text{where } c_y = \left[(0,\ 0,\ 0,\ 0,\ 1)^T \otimes (c_n \otimes c_m)\right] \tag{6.8}$$

Since $Q_{y(i)}$ is a diagonal matrix, and assuming $Q(i) = I_{nm}$, this w-test statistic reduces to the following simplified expression:

$$w_{\iota^s_{p,r}(i)} = \frac{\check{\epsilon}^s_{\iota_p,r}(i)}{\sigma_{\check{\epsilon}^s_{\iota_p,r}(i)}} = \frac{\iota^s_{p,r}(i) - \check{\iota}^s_r(i)}{\sqrt{\sigma^2_{\iota,net} - \sigma^2_{\check{\iota}^s_r(i)}}} \tag{6.9}$$

where $\sigma_{\iota,net}$ denotes the a priori ionospheric standard deviation in the network processing. The test now reads to remove a certain receiver-satellite combination from the processing, when $w^2_{\iota^s_{p,r}(i)} > F_\alpha(1,\infty)$, with $F_\alpha(1,\infty)$ a critical value based on the F-distribution with one degree of freedom and for a significant level α.

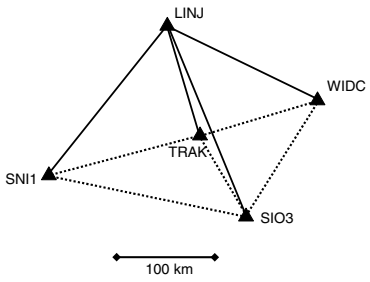

Fig. 6.33. Simulated permanent GPS network for this example

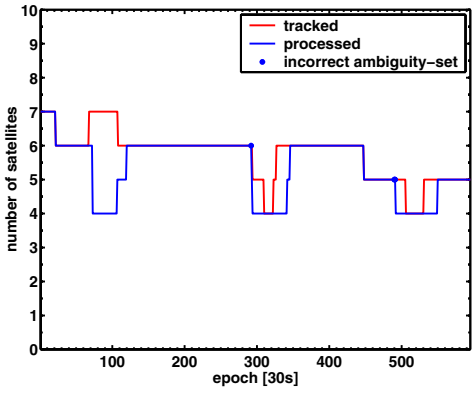

Fig. 6.34. Number of satellites tracked vs. number of satellites processed

6.4.5 Example: Instantaneous network processing

In this subsection the performance of the in the previous subsection described method of ionospheric prediction in the network processing is illustrated. For this purpose, some stations of the *Southern California Integrated GPS Network* (SCIGN) in the USA are assigned as fictitious permanent network consisting of five stations. Note that the data of this very dense GPS network, which is mainly used for crustal deformation monitoring in the seismic active Californian area (see [Bock et al., 1997]), are made freely available to the scientific community through the internet (*www.scign.org*). This free data availability plus the density of the stations makes this network an excellent source of data for testing purposes.

The configuration of the selected five stations is depicted in Fig. 6.33. The average distance between the stations is more than 100 km. Since there are five stations, *four* 'network baselines' are independent. All stations are equipped with Ashtech Z-XII GPS receivers and track dual-frequency phase and code observations each 30 s (cut-off elevation: 10°).

The GPS data are taken for July 14th 2000, from 19:00 UTC to 24:00 UTC. For this five-hour time span it is known that the ionospheric activity was reasonably high, see Fig. 4.7 in Chap. 4, in which the Planetary Kp-index is shown for, among others, this day. In the instantaneous network processing the satellite positions are computed using the predicted IGS orbits. Because of the low quality of the coordinates of PRN 15 and PRN 23 during the five-hour time span (according to the SP3-header), they were not included. In the processing of all the 600 epochs the a priori ionospheric standard deviations was assumed at $\sigma_{\iota,net} = 2$ cm. The results with this standard deviation were very good: For 597 of the 600 epochs the ambiguities were resolved to their correct values, resulting in a success rate of

$597/600 = 99.5\%$. For only three epochs the wrong ambiguities were estimated for some receiver-satellite combinations. At all these three epochs it concerned wrong ambiguities for satellites which were about to *set*. Unfortunately the outlier w-tests for ionospheric pseudo-observations (see Eq. 6.9) were wrongly accepted for these receiver-satellites combinations. Figure 6.34 shows the difference between the number of satellites tracked by the receivers and the number of satellites which were really used in the processing, for the five-hour time span. The differences occur during the periods satellites set and rise. Table 6.2 gives a summary of the epochs at which satellites are removed or included in the instantaneous processing. Note that 'amb. init.' gives information of the so-called 'side-processing', i.e. the processing based on the ionosphere-weighted model using zero samples, which is necessary to resolve the ambiguities of a newly risen satellite.

Table 6.2. Summary instantaneous network processing (overall success rate: 99.5%)

epoch	satellites included	satellites removed	remarks
19:00:30	PRN 03, 06, 17, 21, 22, 26, 29		start processing
19:11:00		PRN 22	
19:36:30		PRN 06-26	
19:53:30	PRN 09		amb. init. 19:34:00-19:53:30
20:00:30	PRN 31		amb. init. 19:51:00-20:00:30
21:27:00			PRN 09 wrong ambiguities
21:27:30		PRN 09	
21:28:00		PRN 17	
21:52:00	PRN 25		amb. init. 21:42:30-21:52:00
21:54:00	PRN 11		amb. init. 21:44:30-21:54:00
22:45:30		PRN 03	
23:07:00			PRN 31 wrong ambiguities
23:07:30			PRN 31 wrong ambiguities
23:08:00		PRN 31	
23:37:00	PRN 20		amb. init. 23:27:30-23:37:00

6.5 Generation of virtual reference station data

The second step in the procedure for network-based positioning is the generation of virtual reference station (VRS) data. A VRS observable (in units of distance) consists basically of a *geometric range* from the virtual station location to the position of the satellite. This *virtual range* is computed from the known satellite positions and the *approximated position* of the virtual station. This approximate virtual station position is taken equal to the approximate position of the user re-

ceiver.

To imitate a real GPS reference station at the virtual location, besides this receiver-satellite range, additional error terms need to be accounted for. These additional error terms are generated from the estimated *network parameters*. Since the network processing can be performed using either the *ionosphere-weighted* or the *ionosphere-float* model, the network estimates will differ due to a difference in *rank deficiencies* of both models (see Chap. 5). The ionosphere-weighted model should be applied for fast (real-time) applications, while the ionosphere-float model can be used in case of post-processing applications. Independent of this, a VRS observable is basically generated from the following three types of network estimates: i) The network *satellite clock* estimates, ii) The network *ionospheric* estimates, and iii) The network *tropospheric* estimates. Note that it is not necessary to use estimates of the network *receiver clock* and network *phase ambiguities*, since the network satellite clock estimates and also the network ionospheric estimates (in case of the ionosphere-float model) are biased by these terms. This will be explained in more detail in Sect. 6.5.1. It will be clear that the network estimates used for the VRS data generation should be the estimates obtained with fixed *integer ambiguities*, since they have the best possible precision.

For the generation of VRS observations the program *Virint* has been written, which reads in the undifferenced *GPSveQ* network estimates and outputs VRS observations in RINEX format.

6.5.1 Generating the VRS observations

From the geometric range and the network estimates the VRS observables for phase and code can be constructed as follows:

$$
\begin{aligned}
\lambda_j \varphi^s_{v,j}(i) \;=\; & \rho^s_v(i) \;+\; \phi^s_{v,j}(i)^o \;+\; \psi^s_v(i)\tilde{\nu}_{1v} \;+ \\
& \begin{cases} -c\check{\delta}t^s_{1,j}(i) \;-\; \mu_j \tilde{\imath}^s_{v,1}(i), & \text{for} \quad 0 < \sigma_{\imath,net} < \infty \\ -c\check{\bar{\delta}}t^s_{1,j}(i) \;-\; \mu_j \tilde{\bar{\imath}}^s_{v,1}(i), & \text{for} \quad \sigma_{\imath,net} = \infty \end{cases} \\
\vartheta^s_{v,j}(i) \;=\; & \rho^s_v(i) \;+\; p^s_{v,j}(i)^o \;+\; \psi^s_v(i)\tilde{\nu}_{1v} \;+ \\
& \begin{cases} -c\check{d}t^s_{1,j}(i) \;+\; \mu_j \tilde{\imath}^s_{v,1}(i), & \text{for} \quad 0 < \sigma_{\imath,net} < \infty \\ -c\check{\bar{d}}t^s_{1,j}(i) \;+\; \mu_j \tilde{\bar{\imath}}^s_{v,1}(i), & \text{for} \quad \sigma_{\imath,net} = \infty \end{cases}
\end{aligned}
\tag{6.10}
$$

where the estimates of the satellite clock and ionospheric delay parameters are different, depending on the network processing model. An *ionosphere-weighted* network processing is emphasized with $0 < \sigma_{\imath,net} < \infty$ and an *ionosphere-float* network processing with $\sigma_{\imath,net} = \infty$. Note also that ionosphere-float quantities have a 'bar' on top. Concerning the other symbols on top, the 'check' emphasizes the ambiguity-*fixed* estimates, whereas the 'tilde' is used for *interpolated* quantities.

The variables in Eq. (6.10) have the following meaning:

$\varphi^s_{v,j}(i)$	:	generated virtual phase observation [cyc]
$\phi^s_{v,j}(i)^0$	:	sum of virtual phase corrections [m]
$\vartheta^s_{v,j}(i)$	:	generated virtual code observation [m]
$p^s_{v,j}(i)^0$	:	sum of virtual code corrections [m]
$\rho^s_v(i)$	:	range virtual station - satellite [m]
$\psi^s_v(i)$	:	tropospheric mapping factor for virtual station [-]
$\tilde{\nu}_{1v}$	:	interpolated network zenith tropospheric delay (w.r.t. pivot 1) [m]
$c\check{\delta}t^s_{1,j}(i)$	:	network phase satellite clock estimate ($0 < \sigma_{\iota,net} < \infty$) [m]
$c\check{d}t^s_{1,j}(i)$	:	network code satellite clock estimate ($0 < \sigma_{\iota,net} < \infty$) [m]
$c\check{\bar{\delta}}t^s_{1,j}(i)$	:	network phase satellite clock estimate ($\sigma_{\iota,net} = \infty$) [m]
$c\check{\bar{d}}t^s_{1,j}(i)$	:	network code satellite clock estimate ($\sigma_{\iota,net} = \infty$) [m]
$\tilde{\iota}^s_{v,1}(i)$	:	interpolated network ionospheric delay ($0 < \sigma_{\iota,net} < \infty$) [m]
$\tilde{\bar{\iota}}^s_{v,1}(i)$	:	interpolated network ionospheric delay ($\sigma_{\iota,net} = \infty$) [m]

Below the different components of the VRS observables are explained in more detail. Figure 6.35 schematically depicts the VRS data generation from the network parameters.

Network satellite clock estimates

The estimates of the satellite clock error are different for an ionosphere-float or an ionosphere-weighted network processing. In case of an *ionosphere-weighted* processing, the satellite clock estimates for phase and code are (see Chap. 5):

$$0 < \sigma_{\iota,net} < \infty \begin{cases} c\check{\delta}t^s_{1,j}(i) = c\check{\delta}t^s_{,j}(i) - c\check{\delta}t_{1,j}(i) - \lambda_j \check{M}^s_{1,j} & \text{(phase satellite clock)} \\ c\check{d}t^s_{1,j}(i) = c\check{d}t^s_{,j}(i) - c\check{d}t_{1,j}(i) & \text{(code satellite clock)} \end{cases} \tag{6.11}$$

So the estimated satellite clock consists of the unbiased satellite clock error, the receiver clock error of pivot station 1, the (non-integer) ambiguity of pivot station 1 and the zenith tropospheric delay of pivot station 1 multiplied with its mapping factor. In case of an *ionosphere-float* network processing, the satellite clock estimates are even more biased, by the satellite clocks of the first observable (phase on L1) as a consequence of removing the rank deficiency of the ionosphere-float model (see also Chap. 5):

$$\sigma_{\iota,net} = \infty \begin{cases} c\check{\bar{\delta}}t^s_{1,j}(i) = c\check{\delta}t^s_{1,j}(i) - \frac{\mu_j}{\mu_1} c\check{\delta}t^s_{1,1}(i) & \text{(phase satellite clock)} \\ c\check{\bar{d}}t^s_{1,j}(i) = c\check{d}t^s_{1,j}(i) + \frac{\mu_j}{\mu_1} c\check{\delta}t^s_{1,1}(i) & \text{(code satellite clock)} \end{cases} \tag{6.12}$$

Interpolation of the network ionospheric delays

To obtain a value for the ionospheric delay in the VRS observable the estimated network ionospheric delays are *interpolated* at the virtual location. This interpolation should highly approximate the real ionospheric delays at the virtual location,

and is carried out *per satellite*, since the ionospheric delays from one satellite to all receivers in the network seem to be spatially correlated (see for example Figs. 6.42, 6.44 and 6.46 in the previous section).

In case of an *ionosphere-weighted* network processing, the interpolated ionospheric delay is obtained from the estimated network ionospheric delays as follows:

$$0 < \sigma_{\imath,net} < \infty : \quad \tilde{\imath}^s_{v,1}(i) \;=\; h_v^T \begin{bmatrix} \check{\imath}^s_{1,1}(i) \\ \check{\imath}^s_{2,1}(i) \\ \vdots \\ \check{\imath}^s_{n,1}(i) \end{bmatrix} \quad \text{(interpolated ionospheric delay)} \tag{6.13}$$

In this equation h_v denotes the $n \times 1$ *interpolation vector*. In Sect. 6.6 the attention is focussed on the choice of this interpolation vector. When the network processing is performed based on the *ionosphere-float* model, the estimated network delays are biased by network receiver- and satellite clock terms (see Chap. 5). Hence, the interpolated ionospheric delay at the virtual station is *biased* as well:

$$\sigma_{\imath,net} = \infty : \;\; \tilde{\check{\imath}}^s_{v,1}(i) \;\;=\;\; h_v^T \begin{bmatrix} \check{\imath}^s_{1,1}(i) - \frac{1}{\mu_1}\left(c\check{\delta}t_{11,1}(i) - c\check{\delta}t^s_{1,1}(i)\right) \\ \check{\imath}^s_{2,1}(i) - \frac{1}{\mu_1}\left(c\check{\delta}t_{12,1}(i) - c\check{\delta}t^s_{1,1}(i)\right) \\ \vdots \\ \check{\imath}^s_{n,1}(i) - \frac{1}{\mu_1}\left(c\check{\delta}t_{1n,1}(i) - c\check{\delta}t^s_{1,1}(i)\right) \end{bmatrix} \tag{6.14}$$

One of the biases here is the L1 satellite clock estimate, $c\check{\delta}t^s_{1,1}(i)$. This bias also appeared in the expression for the biased satellite clock estimate of the ionosphere-float model, Eq. (6.12). To eliminate this bias in the virtual observables, the interpolation vector should be chosen in that way, that it fulfils the following condition:

$$\boxed{h_v^T e_n \;=\; 1} \tag{6.15}$$

With this condition namely the biased interpolated delay can be written as:

$$\sigma_{\imath,net} = \infty : \quad \tilde{\check{\imath}}^s_{v,1}(i) \;\;=\;\; \tilde{\imath}^s_{v,1}(i) \;-\; \tfrac{1}{\mu_1}\left[c\tilde{\check{\delta}}t_{1v,1}(i) \;-\; c\check{\delta}t^s_{1,1}(i)\right] \tag{6.16}$$

where the interpolated relative receiver clock error of the virtual station is computed as:

$$c\tilde{\check{\delta}}t_{1v,1}(i) \;=\; h_v^T \begin{bmatrix} c\check{\delta}t_{11,1}(i) \\ c\check{\delta}t_{12,1}(i) \\ \vdots \\ c\check{\delta}t_{1n,1}(i) \end{bmatrix} \quad \text{(interpolated relative receiver clock error)} \tag{6.17}$$

In this equation the first network receiver clock estimate is by definition zero: $c\check{\delta}t_{11,1}(i) = 0$. The biased interpolated ionospheric delay can then be written as a sum of an *unbiased* interpolated ionospheric delay, denoted as $\tilde{\imath}^s_{v,1}(i)$ (which equals the interpolated delay using the ionosphere-weighted model, see Eq. (6.13)), a (scaled) *interpolated network receiver clock* error with respect to pivot station 1, denoted as $c\tilde{\delta}t_{1v,1}(i)$, plus a (scaled) satellite clock error, $c\check{\delta}t^s_{1,1}(i)$. Note that both clock errors are on the L1 frequency. Moreover, note the correspondence of Eq. (6.16) with Eq. (5.23) in Chap 5.

Interpolation of the network tropospheric delays

The network tropospheric delay parameters estimated with the geometry-based model are zenith tropospheric delays (ZTDs) and the ZTD at the virtual station location is, like the ionospheric delays, *interpolated* from the network ZTD estimates. Since these network zenith delays are all *relative* to the pivot station of the network (1), the interpolated value is also relative to this reference station 1 (see Eq. (5.7) in Chap. 5):

$$\tilde{\nu}_{1v} = h_v^T \begin{bmatrix} \check{\nu}_{11} \\ \check{\nu}_{12} \\ \vdots \\ \check{\nu}_{1n} \end{bmatrix} = h_v^T \begin{bmatrix} \check{\nu}_1 \\ \check{\nu}_2 \\ \vdots \\ \check{\nu}_n \end{bmatrix} - \nu_1 = \tilde{\nu}_v - \nu_1, \quad \text{(interpolated relative ZTD)} \tag{6.18}$$

where $\tilde{\nu}_v$ denotes the interpolated absolute ZTD and ν_1 the fixed ZTD of pivot station 1. Again, use is made of $h_v^T e_n = 1$. Note that the zenith tropospheric delay estimate for the pivot station is included, though is zero by definition: $\check{\nu}_{11} = 0$.

Other network corrections

Finally, the same (a priori) corrections should be added to the virtual observations, as were applied to the network observations:

$$\begin{array}{rcl} \phi^s_{v,j}(i)^o & = & \phi^s_{v,j}(i)^c + \left[\nu^s_v(i)^0 + \psi^s_v(i)\nu_1\right] \quad \text{(phase corrections)} \\ p^s_{v,j}(i)^o & = & p^s_{v,j}(i)^c + \left[\nu^s_v(i)^0 + \psi^s_r(i)\nu_1\right] \quad \text{(code corrections)} \end{array} \tag{6.19}$$

These correction terms concern, among others, antenna phase center variations (PCVs), denoted as $\phi^s_{v,j}(i)^c$ for phase and denoted as $p^s_{v,j}(i)^c$ for code, and the a priori tropospheric values in the network processing, see also Eq. (5.5). The a priori troposphere model value is denoted as $\nu^s_v(i)^0$, and for this the *same* model as used in the network processing should be used (e.g. the Saastamoinen model). The tropospheric mapping function for the ZTDs, denoted as $\psi^s_v(i)$ should also be the same mapping function as applied in the network processing (e.g. Niell's mapping function).

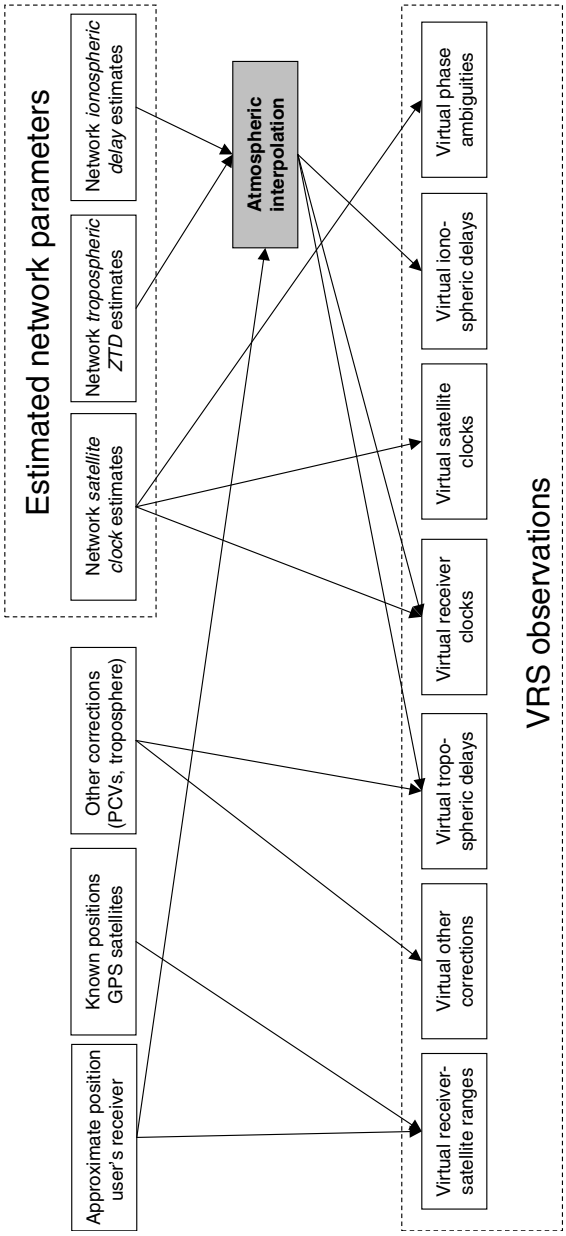

Fig. 6.35. VRS data generation scheme

6.5.2 VRS phase and code observation equations

In the previous subsection it was explained which network estimates are needed to generate the VRS observables. In this subsection it is described how these network estimates together form the error components of the virtual observables. In an analogue manner to the real GPS observables (see Chap. 2), the *observation equations* for VRS data can be written as follows, for phase and code data:

$$\begin{array}{rcl} \phi^s_{v,j}(i) & = & \rho^s_v(i) + \nu^s_v(i) + c\delta t_{v,j}(i) - c\delta t^s_{,j}(i) - \mu_j i^s_{v,1}(i) + \lambda_j M^s_{v,j} + \epsilon_{\phi^s_{v,j}}(i) \\ p^s_{v,j}(i) & = & \rho^s_v(i) + \nu^s_v(i) + cdt_{v,j}(i) - cdt^s_{,j}(i) + \mu_j i^s_{v,1}(i) + \epsilon_{p^s_{v,j}}(i) \end{array} \tag{6.20}$$

Below we will focuss on the different components of the VRS observation equations.

Virtual observables

The virtual phase and code observables are both expressed in meter and read:

$$\begin{array}{rcl} \phi^s_{v,j}(i) & = & \lambda_j \varphi^s_{v,j}(i) \; - \; \phi^s_{v,j}(i)^c \\ p^s_{v,j}(i) & = & \vartheta^s_{v,j}(i) \; - \; p^s_{v,j}(i)^c \end{array} \tag{6.21}$$

Like with the observation equations for real GPS observables (see Chap. 2), the a priori corrections are subtracted from the formed observations.

Virtual receiver-satellite range

As mentioned, the virtual receiver-satellite range, denoted by ρ^s_v, reads as follows:

$$\rho^s_v(i) \; = \; \|r^s(i) - r_v(i)\| \tag{6.22}$$

where $r^s(i)$ denotes the satellite coordinates and $r_v(i)$ the virtual station coordinates.

Virtual tropospheric delay

The virtual tropospheric delay is equal for both phase and code and consists of the a priori term, plus the interpolated network ZTD multiplied with its mapping factor:

$$\nu^s_v(i) \; = \; \nu^s_v(i)^0 + \psi^s_v(i)\tilde{\nu}_v \tag{6.23}$$

Virtual receiver clock error

The virtual receiver clock errors, $c\delta t_{v,j}(i)$ for phase and $cdt_{v,j}(i)$ for code, follow from the (biased) network satellite clock estimates and, in case of an ionosphere-float network processing, from the (biased) ionospheric delay estimates. It can be shown that in case of an *ionosphere-weighted* network processing the virtual receiver clocks are in fact equivalent with the receiver clock estimates of network

pivot station 1:

$$0 < \sigma_{\iota,net} < \infty : \left\{ \begin{array}{lcll} c\delta t_{v,j}(i) & = & c\check{\delta} t_{1,j}(i) & \text{(virtual phase receiver clock)} \\ cdt_{v,j}(i) & = & c\check{dt}_{1,j}(i) & \text{(virtual code receiver clock)} \end{array} \right. \tag{6.24}$$

In case of an *ionosphere-float* network processing, the virtual receiver clock errors contain, besides the receiver clock estimates of pivot station 1, the (scaled) interpolated network relative receiver clock error, see Eq. (6.17):

$$\sigma_{\iota,net} = \infty \left\{ \begin{array}{lcll} c\delta t_{v,j}(i) & = & c\check{\delta} t_{1,j}(i) + \frac{\mu_j}{\mu_1} c\tilde{\delta} t_{1v,1}(i) & \text{(virtual phase receiver clock)} \\ cdt_{v,j}(i) & = & c\check{dt}_{1,j}(i) - \frac{\mu_j}{\mu_1} c\tilde{\delta} t_{1v,1}(i) & \text{(virtual code receiver clock)} \end{array} \right. \tag{6.25}$$

Virtual satellite clock error

Due to the condition $h_v^T e_n = 1$ the clock term $\frac{\mu_j}{\mu_1} c\check{\delta} t^s_{1,1}(i)$ is eliminated in the virtual observables in case of an ionosphere-float network processing. The consequence is that the *satellite clock errors* of the virtual observable in both the ionosphere-weighted and ionosphere-float models are equivalent and read:

$$\begin{array}{rcll} c\delta t^s_{,j}(i) & = & c\check{\delta} t^s_{,j}(i) & \text{(virtual phase satellite clock)} \\ cdt^s_{,j}(i) & = & c\check{dt}^s_{,j}(i) & \text{(virtual code satellite clock)} \end{array} \tag{6.26}$$

Note that this virtual satellite clock error is *unbiased* and equal to the network satellite clock. This is fortunate, since in the user's processing use is made of this property of the satellite clocks (they should have the same coefficients in the design matrix in an undifferenced processing; possibility of elimination in a double-difference set up).

Virtual ionospheric delay

The virtual ionospheric delay is the interpolated value of the network delays:

$$\iota^s_{v,1}(i) \; = \; \tilde{\iota}^s_{v,1}(i) \tag{6.27}$$

Virtual non-integer ambiguity

For the virtual phase observable a *virtual (non-integer) ambiguity* appears, $\check{M}^s_{1,j}$, which is equivalent with the ambiguity of the pivot station in the network:

$$M^s_{v,j} \; = \; \check{M}^s_{1,j} \tag{6.28}$$

The consequence of this is that when the *double-difference* ambiguities of the phase observations of a user receiver relative to the observations of the virtual station are resolved, exactly the *same* integer values should be obtained as when the integer ambiguities of the user receiver with respect to the *network pivot station* would be resolved. Note also that when the ambiguities of the virtual station relative to this network pivot station are resolved, this will yield *zero* estimates for the integer ambiguities.

Virtual noise

The last terms in the virtual observation equations are *virtual noise* terms for phase and code. These are stochastic variables, of which in the generation of the VRS observables the sample values are *zero*:

$$\begin{aligned} \epsilon_{\phi^s_{v,j}}(i) &= 0 \\ \epsilon_{p^s_{v,j}}(i) &= 0 \end{aligned} \tag{6.29}$$

It is necessary to include these terms in the virtual observation equations, since their dispersion should be reflected in the stochastic model of the VRS observables, see the next subsection.

6.5.3 Stochastic model of the VRS observables

Important to the user's processing relative to a VRS is the stochastic model of the VRS phase and code observables. In principle, the precision of the VRS observables should follow from *propagating* the uncertainty of the different components, which together form the VRS phase and code observables (as explained in the previous subsection). This is however a difficult task, which requires research that has not been conducted for this thesis. Intuitively, especially the VRS *phase* observations will be of lower quality than their corresponding *real* counterparts collected in the user receiver, which is mainly due to errors in the interpolation of ionospheric and tropospheric delays. Therefore, the precision of the VRS phase observables should be assumed at cm-level, while the VRS code observables may have a comparable precision as their real counterparts (dm-level).

6.6 Atmospheric interpolation method

In the previous section it was discussed that for the generation of VRS observations both the estimated network ionospheric delays and (zenith) tropospheric delays need to be interpolated in the spatial domain. This section focusses on the choice of a useful interpolation method. Note that in this section no distinction is made between ionospheric and tropospheric interpolation, and an equal interpolation method is used for both delays. Hence, in this section we speak of *atmospheric* interpolation, which may be either ionospheric or tropospheric interpolation. The atmospheric interpolated value at location v can mathematically be given as:

$$\boxed{\tilde{\alpha}_v \;=\; h_v^T \check{\alpha}, \quad \text{where } h_v^T e_n = 1} \tag{6.30}$$

In the equation above $\tilde{\alpha}_v$ denotes the interpolated value, h_v the interpolation (weights) vector and $\check{\alpha} = (\check{\alpha}_1, \ldots, \check{\alpha}_n)^T$ the estimated network atmospheric delays (for n network stations). So these atmospheric delays could be either the undifferenced ionospheric delay estimates, or the relative zenith tropospheric delay estimates, see the previous section. Note that for each observation epoch for the ionospheric delays for each individual satellite an interpolation needs to be carried out, whereas for the zenith tropospheric delays just one interpolation is performed. The condition $h_v^T e_n = 1$ follows from the previous section (see Eq. 6.15).

6.6.1 Least-squares collocation

A method which fully takes the spatial correlation between given points into account to predict the value for a point in between, is *least-squares collocation*. According to this method, the interpolation vector reads as follows [Moritz, 1976]:

$$h_v^T \;=\; c_v^T C_{pp}^{-1}, \quad \text{where:} \begin{cases} c_v \;=\; [c_{v1}\; c_{v2}\; \ldots\; c_{vn}]^T \\ C_{pp} \;=\; \begin{bmatrix} c_{11} & c_{12} & \cdots & c_{1n} \\ c_{21} & c_{22} & \cdots & c_{2n} \\ \vdots & \vdots & \ddots & \vdots \\ c_{n1} & c_{n2} & \cdots & c_{nn} \end{bmatrix} \end{cases} \tag{6.31}$$

where the scalar $c_{r_1 r_2}$ denotes the *covariance function* between locations r_1 and r_2, and needs to be specified to perform the interpolation. Note that Eq. (6.31) is also known as the *Wiener-Kolmogorov* prediction formula. Regardless of the choice of this covariance function (we will focuss on this function later on), from the collocation formula Eq. (6.31) it can immediately be seen that in general it does not fulfil the condition in Eq. (6.30), since:

$$h_v^T e_n \;=\; \left[c_v^T C_{pp}^{-1} e_n\right] \;\neq\; 1 \tag{6.32}$$

Therefore, in the following subsection the interpolation vector based on collocation is extended, such that it fulfils the condition above.

6.6.2 Kriging

The condition $h_v^T e_n = 1$ can be accounted for by extending the unconditioned 'system' of equations corresponding to Eq. (6.31), i.e. $C_{pp} h_v = c_v$, to the following system:

$$\begin{bmatrix} C_{pp} & e_n \\ e_n^T & 0 \end{bmatrix} \begin{bmatrix} h_v \\ \lambda_v \end{bmatrix} \;=\; \begin{bmatrix} c_v \\ 1 \end{bmatrix} \tag{6.33}$$

In this system λ_v is known as the *Lagrange multiplier* [Teunissen, 2000a]. The equations in Eq. (6.33) are also known as the *kriging* equations, see e.g. [Christensen, 1991]. To determine the vector h_v from this system, the following inverse matrix is computed analytically:

$$\begin{bmatrix} C_{pp} & e_n \\ e_n^T & 0 \end{bmatrix}^{-1} \;=\; \begin{bmatrix} C_{pp}^{-1} - \frac{1}{\left[e_n^T C_{pp}^{-1} e_n\right]} C_{pp}^{-1} e_n e_n^T C_{pp}^{-1} & \frac{1}{\left[e_n^T C_{pp}^{-1} e_n\right]} C_{pp}^{-1} e_n \\ \frac{1}{\left[e_n^T C_{pp}^{-1} e_n\right]} e_n^T C_{pp}^{-1} & \frac{-1}{\left[e_n^T C_{pp}^{-1} e_n\right]} \end{bmatrix} \tag{6.34}$$

Using this, the solution for the interpolation vector h_v follows as:

$$\boxed{h_v^T \;=\; c_v^T C_{pp}^{-1} - \lambda_v e_n^T C_{pp}^{-1}, \quad \text{with } \lambda_v \;=\; \frac{\left[c_v^T C_{pp}^{-1} e_n\right] - 1}{\left[e_n^T C_{pp}^{-1} e_n\right]}} \tag{6.35}$$

From this equation it can be easily verified that the interpolation vector now fulfils the condition $h_v^T e_n = 1$, regardless of the choice of the spatial covariance function.

In fact, using the interpolation vector above, the interpolation becomes equivalent with *ordinary kriging*. Note that the interpolation vector in Eq. (6.35) exactly corresponds to the vector used in [Jarlemark and Emardson, 1998] for the spatial interpolation of (wet) ZTDs from a network.

6.6.3 Choice of the covariance function

In order to really perform the interpolation using the interpolation vector in Eq. (6.35), it is necessary to specify a suitable spatial covariance function. Throughout this thesis, for both the ionospheric and tropospheric interpolations, this covariance function is chosen as a simple *linear* function of the distance:

$$\boxed{c_{r_1 r_2} \;=\; \gamma(l_{max} - l_{r_1 r_2})} \tag{6.36}$$

where $l_{r_1 r_2}$ [km] denotes the distance between locations r_1 and r_2, l_{max} a certain maximum distance [km] and γ (in [km]) a factor to convert the distances to *squared* distances, since matrix C_{pp} in Eq. (6.31) can be regarded as a vc-matrix. Here we choose $\gamma = 1$ km. Note that the interpolation vector h_v is *insensitive* to the choice of this factor γ, since it is eliminated in Eq. (6.35). The Lagrange multiplier however depends on the choice of γ. With respect to the choice of l_{max}, in order to guarantee that the matrix C_{pp} is *positive-definite*, it should be larger than the longest distance between the permanent stations:

$$l_{max} \;>\; \max l_{r_1 r_2} \tag{6.37}$$

6.6.4 Properties of the interpolation method

The kriging interpolator has some advantageous properties which are described in this subsection. These properties are: i) The interpolator is *optimal* (BLUP) when the covariance function is correct, ii) The interpolator is *independent* of the choice of l_{max}, iii) The interpolator is *exact*, and iv) The interpolator is invariant against *differencing*. Below these properties are explained in more detail.

The interpolator is optimal (BLUP)

The kriging interpolation is optimal in the sense that when the covariance function is correct, it is a *best linear unbiased predictor* (BLUP) [Goldberger, 1962]. It is also referred to as the *least-squares interpolator*. Below the properties of a BLUP are explained.

- *Linearity*
  From Eq. (6.30) it immediately follows that the general interpolation function is a linear function:

  $$\tilde{\alpha}_v \;=\; h_v^T \breve{\alpha} \tag{6.38}$$

- *Unbiasedness*
  When it is assumed that the expectation of the interpolator at the given data

points (reference station locations) is equal to the expectation at a location v in between, i.e. $E\{\check{\alpha}\} = e_n\alpha_v$, then, using the property $h_v^T e_n = 1$, the expectation of the interpolator at location v follows as:

$$E\{\tilde{\alpha}_v\} = h_v^T E\{\check{\alpha}\} = h_v^T e_n \alpha_v = \alpha_v \tag{6.39}$$

which shows that the interpolator is an unbiased predictor.

- *Best*
  The interpolator is a best predictor, if the variance of the *interpolation error* is minimal. This interpolation error is the difference between the interpolated value and the real unknown value at location v:

$$\tilde{\alpha}_v - \alpha_v = \left[h_v^T, -1\right] \begin{bmatrix} \check{\alpha} \\ \alpha_v \end{bmatrix} \tag{6.40}$$

  Its variance is obtained by applying the propagation law of variances:

$$\begin{aligned} \sigma^2_{\tilde{\alpha}_v - \alpha_v} &= \left[h_v^T, -1\right] \begin{bmatrix} C_{pp} & c_v \\ c_v^T & al_{max} \end{bmatrix} \begin{bmatrix} h_v \\ -1 \end{bmatrix} \\ &= h_v^T C_{pp} h_v - 2h_v^T c_v + \gamma l_{max} \\ &= h_v^T C_{pp} h_v - 2h_v^T c_v + \gamma l_{max} + 2\lambda_v \left(h_v^T e_n - 1\right) \end{aligned} \tag{6.41}$$

  For the variance to be minimal, the first derivative of (6.41) with respect to h_v^T needs to be zero:

$$2C_{pp}h_v - 2c_v + 2\lambda_v e_n = 0 \tag{6.42}$$

  Since Eq. (6.42) is nothing else than the upper equation of the *kriging* equations, see Eq. (6.33), the first derivative is indeed equal to zero. To have a minimal variance, the second derivative of Eq. (6.41) should be larger than zero. This second derivative equals $2C_{pp}$. Since C_{pp} is positive-definite also this holds true and hence the interpolator is the best predictor.

The interpolator is independent of l_{max}

Although in the covariance function in Eq. (6.36) a distance-independent factor l_{max} appears, the kriging interpolator is independent of the choice of this factor. To proof this, the vector c_v and matrix C_{pp} are rewritten as:

$$c_v = \gamma(l_{max}e_n - l_v), \qquad C_{pp} = -\gamma\left[L - l_{max}e_n e_n^T\right] \tag{6.43}$$

where l_v denotes the vector with distances from location v to the network stations, and L the symmetric matrix with mutual distances between the network stations:

$$l_v = \left[l_{v1}, \ldots, l_{vn}\right]^T, \qquad L = \begin{bmatrix} l_{11} & \ldots & l_{1n} \\ \vdots & \ddots & \vdots \\ l_{n1} & \ldots & l_{nn} \end{bmatrix} \tag{6.44}$$

Note that the diagonal elements of L are all zero, since $l_{11} = \ldots = l_{nn} = 0$. The inverse of C_{pp} can be given as a closed-form expression using the well-known matrix lemma, see e.g. [Koch, 1999] p. 34, which reads:

$$\left(A - BD^{-1}C\right)^{-1} = A^{-1} + A^{-1}B\left(D - CA^{-1}B\right)^{-1}CA^{-1} \tag{6.45}$$

Using this lemma, the inverse of C_{pp} follows as:

$$C_{pp}^{-1} = \tfrac{1}{\gamma}\left(-L^{-1} - \left[\tfrac{l_{max}}{1-l_{max}[e_n^T L^{-1} e_n]}\right] L^{-1} e_n e_n^T L^{-1}\right) \tag{6.46}$$

Using this expression, the different elements in the kriging equations can be rewritten as follows:

$$\begin{aligned}
C_{pp}^{-1}e_n &= \tfrac{1}{\gamma}\tfrac{-1}{1-l_{max}[e_n^T L^{-1} e_n]} L^{-1}e_n \\
C_{pp}^{-1}c_v &= L^{-1}l_v + \tfrac{l_{max}\left([l_v^T L^{-1} e_n]-1\right)}{1-l_{max}[e_n^T L^{-1} e_n]} L^{-1}e_n \\
\left[e_n^T C_{pp}^{-1} e_n\right] &= \tfrac{1}{\gamma}\tfrac{-\left[e_n^T L^{-1} e_n\right]}{1-l_{max}\left[e_n^T L^{-1} e_n\right]} \\
\left[c_v^T C_{pp}^{-1} e_n\right] &= \tfrac{\left[l_v^T L^{-1} e_n\right]-l_{max}\left[e_n^T L^{-1} e_n\right]}{1-l_{max}[e_n^T L^{-1} e_n]}
\end{aligned} \tag{6.47}$$

From this it follows that both the Lagrange multiplier λ_v and interpolation vector h_v are *independent* of l_{max}:

$$\begin{aligned}
\lambda_v &= \gamma\tfrac{\left[c_v^T C_{pp}^{-1} e_n\right]-1}{\left[e_n^T C_{pp}^{-1} e_n\right]} = \tfrac{\left[l_v^T L^{-1} e_n\right]-1}{-[e_n^T L^{-1} e_n]} \\
h_v &= C_{pp}^{-1}c_v - \lambda_v C_{pp}^{-1} e_n \\
&= L^{-1}l_v + \left\{\tfrac{l_{max}\left([l_v^T L^{-1} e_n]-1\right)}{1-l_{max}[e_n^T L^{-1} e_n]} + \tfrac{\left[l_v^T L^{-1} e_n\right]-1}{[e_n^T L^{-1} e_n]}\tfrac{-1}{1-l_{max}[e_n^T L^{-1} e_n]}\right\} L^{-1}e_n \\
&= L^{-1}l_v - \tfrac{\left([l_v^T L^{-1} e_n]-1\right)\left(1-l_{max}\left[e_n^T L^{-1} e_n\right]\right)}{[e_n^T L^{-1} e_n](1-l_{max}[e_n^T L^{-1} e_n])} L^{-1}e_n \\
&= L^{-1}l_v - \tfrac{\left[l_v^T L^{-1} e_n\right]-1}{[e_n^T L^{-1} e_n]} L^{-1}e_n
\end{aligned} \tag{6.48}$$

Besides, the variance of the interpolation error can be shown to be independent of l_{max}. Using Eq. (6.41) we namely obtain:

$$\begin{aligned}
\sigma^2_{\hat{\alpha}_v - \alpha_v} &= h_v^T C_{pp} h_v - 2h_v^T c_v + \gamma l_{max} \\
&= h_v^T C_{pp} C_{pp}^{-1}\left[c_v - \lambda_v e_n\right] - 2h_v^T c_v + \gamma l_{max} \\
&= \gamma l_{max} - h_v^T c_v - \lambda_v \\
&= \gamma h_v^T l_v - \lambda_v \\
&= \gamma\left(\left[l_v^T L^{-1} l_v\right] + \tfrac{\left([l_v^T L^{-1} e_n]-1\right)\left([l_v^T L^{-1} e_n]+1\right)}{[e_n^T L^{-1} e_n]}\right)
\end{aligned} \tag{6.49}$$

The interpolator is exact

When the interpolation is performed at a given network station location, the resulting interpolated values is exactly the same as the (input) estimate of this network

station. This can be proved as follows. When the interpolation is performed at the location of network station 1, then the vector l_v^T becomes in this case:

$$l_1^T \;=\; [0,\; l_{12},\; ,\ldots,\; l_{1n}]^T \tag{6.50}$$

From this follows that the Lagrange multiplier reduces to zero in this case (using Eq. (6.48)):

$$l_1^T L^{-1} \;=\; [1,\; 0,\; \ldots,\; 0] \;\Rightarrow\; \left[l_1^T L^{-1} e_n\right] \;=\; 1 \;\Rightarrow\; \lambda_1 = 0 \tag{6.51}$$

The interpolation vector at the location of network station 1, becomes as follows:

$$h_1^T \;=\; l_1^T L^{-1} \;=\; [1,\; 0,\; \ldots,\; 0] \tag{6.52}$$

Because of the 1 at the first position of vector h_1, the interpolation is exactly equal to the real value of station 1. This exactness also follows when considering the variance of the interpolation error, which is exactly zero in this case:

$$\sigma^2_{\tilde{\alpha}_1 - \alpha_1} \;=\; \gamma \left[l_1^T L^{-1} l_1\right] \;=\; 0 \tag{6.53}$$

For the other network stations, $(2, \ldots, n)$, similar derivations can be made.

The interpolator is invariant against differencing

Despite the fact that in the VRS data generation procedure *undifferenced* network estimates are used, the interpolation could also be applied to *double-differenced* (DD) network estimates (for the ionospheric delays). In that case the interpolated value will also be a DD value, with respect to the *same* pivot station and satellite as the network double-differences. In the following it is proved that this DD interpolated value could also be obtained from combining four *undifferenced* interpolated values.

Denote the $n \times 1$ vector undifferenced network estimates for a certain satellite s as $\check{\alpha}^s = (\check{\alpha}_1^s, \ldots, \check{\alpha}_n^s)^T$ and the $n \times 1$ vector of their double-differenced counterparts relative to network pivot station 1 and pivot satellite 1 as $\check{\alpha}_1^{1s} = \left(\check{\alpha}_{11}^{1s},\; \check{\alpha}_{12}^{1s},\; \ldots,\; \check{\alpha}_{1n}^{1s}\right)^T$, where $\check{\alpha}_{11}^{1s}$ is by definition zero. The DD interpolated value can be computed as follows:

$$\begin{aligned} \tilde{\alpha}_{1v}^{1s} &= h_v^T \check{\alpha}_1^{1s} \\ &= h_v^T \left[(\check{\alpha}^s - e_n \check{\alpha}_1^s) \;-\; \left(\check{\alpha}^1 - e_n \check{\alpha}_1^1\right)\right] \\ &= (h_v^T \check{\alpha}^s - h_v^T e_n \check{\alpha}_1^s) \;-\; (h_v^T \check{\alpha}^1 - h_v^T e_n \check{\alpha}_1^1) \\ &= (\tilde{\alpha}_v^s - \check{\alpha}_1^s) - \left(\tilde{\alpha}_v^1 - \check{\alpha}_1^1\right) \end{aligned} \tag{6.54}$$

Note that use is made of the property $h_v^T e_n = 1$. So, instead of interpolating the network estimates in DD mode, the DD interpolation can also be obtained by combining two undifferenced interpolations and two real delays.

Change of pivot station
In the double-differences above network station 1 was used as pivot station. Also the interpolated value was relative to this pivot station. If one wants to use another *pivot station*, say network station 2, then it is not necessary to perform the interpolation again, since the interpolated delays relative to station 2 are related to those relative to 1 via the *real* DD ionospheric delays between stations 1 and 2:

$$\tilde{\alpha}_{2v}^{1s} \;=\; \tilde{\alpha}_{1v}^{1s} - \check{\alpha}_{12}^{1s} \tag{6.55}$$

This is proved as follows, again using $h_v^T e_n = 1$:

$$\tilde{\alpha}_{2v}^{1s} \;=\; h_v^T \check{\alpha}_2^{1s} \;=\; h_v^T \left(\check{\alpha}_1^{1s} - e_n \check{\alpha}_{12}^{1s}\right) \;=\; h_v^T \check{\alpha}_1^{1s} - \check{\alpha}_{12}^{1s} \tag{6.56}$$

Change of pivot satellite
The same holds true when one wants another *pivot satellite*. The DD interpolated value relative to another network pivot satellite can be directly computed from the DD interpolated delay relative to the original pivot satellite, by subtracting the real (estimated) DD delays between both satellites (so a new interpolation is not necessary):

$$\tilde{\alpha}_{1v}^{2s} \;=\; \tilde{\alpha}_{1v}^{1s} - \tilde{\alpha}_{1v}^{12} \tag{6.57}$$

This can be proved as follows:

$$\tilde{\alpha}_{1v}^{2s} \;=\; h_v^T \check{\alpha}_1^{2s} \;=\; h_v^T \left(\check{\alpha}_1^{1s} - \check{\alpha}_1^{12}\right) \;=\; h_v^T \check{\alpha}_1^{1s} - h_v^T \check{\alpha}_1^{12} \tag{6.58}$$

Example

Consider two fictitious permanent networks, as shown by the black triangles in Figs. 6.36 and 6.37. In the first figure the permanent network consists of three stations at equal distance l of each other (such that we have an *equilateral* triangle, whereas in the second figure the triangular network is extended with a fourth station, such that two equilateral triangles are formed. The distance matrices for both networks read:

$$L_1 \;=\; l \begin{bmatrix} 0 & 1 & 1 \\ 1 & 0 & 1 \\ 1 & 1 & 0 \end{bmatrix}, \quad L_2 \;=\; l \begin{bmatrix} 0 & 1 & 1 & 1 \\ 1 & 0 & 1 & \sqrt{3} \\ 1 & 1 & 0 & 1 \\ 1 & \sqrt{3} & 1 & 0 \end{bmatrix} \tag{6.59}$$

Now for seven fictitious user receivers, the white triangles in both figures, the interpolation vectors h_v^T are evaluated, for both permanent networks, using the expression in Eq. (6.48). Note that the location of the first receiver is exactly equal to the location of the first network station. The results are given in Table 6.3. Besides the interpolation vector, the precision of the interpolation error, computed using Eq. (6.49), is also given for each user location. Note that this

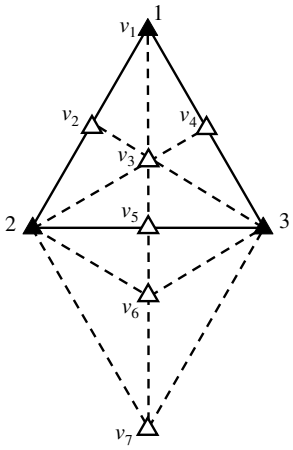

Fig. 6.36. Network 1 stations (black triangles) and user receivers within (white triangles)

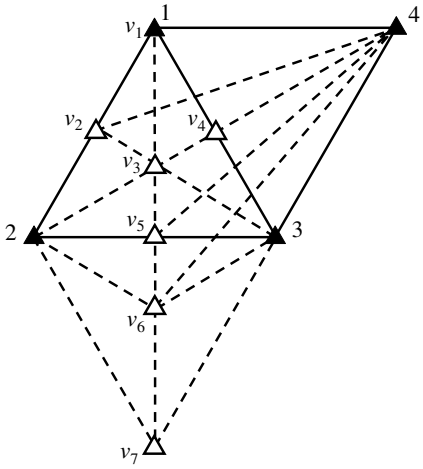

Fig. 6.37. Network 2 stations (black triangles) and user receivers within (white triangles)

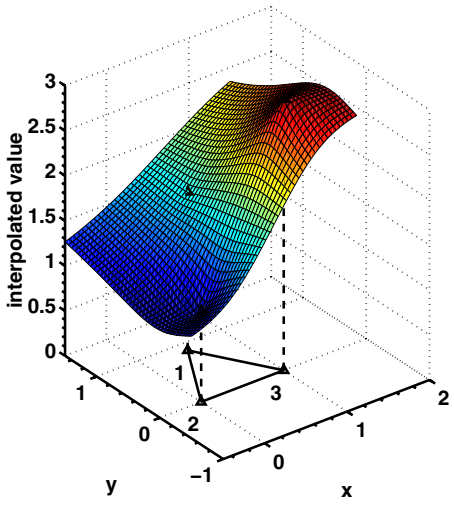

Fig. 6.38. Interpolation surface for the network consisting of 3 permanent stations

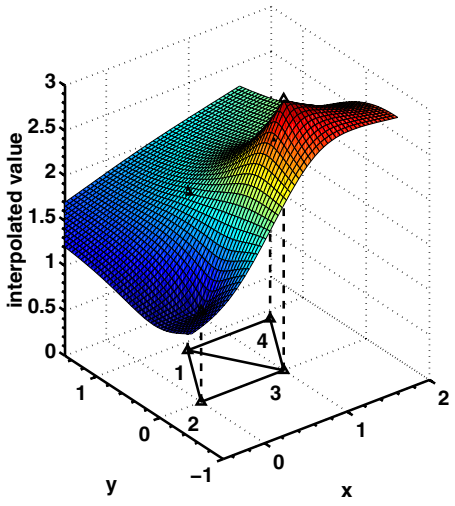

Fig. 6.39. Interpolation surface for the network consisting of 4 permanent stations

Table 6.3. Interpolation vectors for network 1 and network 2

	h_v^T network 1	$\sigma/\sqrt{l}$	h_v^T network 2	$\sigma/\sqrt{l}$
v_1	(1.000, 0.000, 0.000)	0.000	(1.000, 0.000, 0.000, 0.000)	0.000
v_2	(0.455, 0.455, 0.089)	0.636	(0.469, 0.452, 0.103,-0.023)	0.654
v_3	(0.333, 0.333, 0.333)	0.577	(0.333, 0.333, 0.333, 0.000)	0.572
v_4	(0.455, 0.089, 0.455)	0.636	(0.394, 0.106, 0.394, 0.106)	0.534
v_5	(0.089, 0.455, 0.455)	0.636	(0.103, 0.452, 0.469,-0.023)	0.654
v_6	(-0.052, 0.526, 0.526)	0.943	(-0.036, 0.522, 0.541,-0.027)	0.958
v_7	(-0.155, 0.577, 0.577)	1.902	(-0.155, 0.577, 0.577, 0.000)	1.834

standard deviation in the table is divided by $\sqrt{l}$. For example, when $l = 100$ km, and in the table the standard deviation is given as 0.636, then the precision of the interpolation error is $0.636 \cdot \sqrt{100} = 6.36$ km.

From the table the following conclusions may be drawn:

- When a user receiver is located at one of the network stations, the interpolated value is exactly the same as the (input) value of the concerning network station. The interpolation error is consequently zero. This is a consequence of the *exactness* property of the interpolator, as discussed before.
- The contribution of network station 4 in Fig. 6.37 to the interpolation vectors for the considered user locations is marginal, except maybe for user location v_4, which is lying on the line between network station 1 and 3. This means that the interpolation is very *local*: The influence of a further network station decreases rapidly. In practice this means that it might be sufficient to only use the three surrounding reference stations, instead of the complete network for the interpolation.
- For user receivers located at the edges of the triangular-shaped network, i.e. receivers v_2 and v_5, plus for receivers located really outside the network, i.e. v_6 and v_7 an undesired effect appears: The coefficients in the interpolation vector for network stations which are at a remote distance, become *negative*. For the user locations at the edges these negative coefficients are quite small, but for the two locations lying outside, these are already quite large. This means that the interpolation (or better: Extrapolation) performs quite poor. This could also be inferred from the computed standard deviations of the interpolation error, which grow rapidly the further away from the network area. Therefore, as a rule-of-thumb, the user receivers should always be *inside* the area spanned by the permanent network stations.

Finally, as an illustration, Figs. 6.38 and 6.39 show the interpolation surfaces for both networks, when the network station have the following fictitious (input)

values $\check{\alpha} = (1.75,\ 1.00,\ 3.00,\ 2.00)^T$.

6.7 User's processing

In a last step of the three-step procedure, the generated VRS observations at the approximate user's location are processed together with the user's observations to obtain precise positioning results. This user's processing can be carried out using different strategies, depending on the size of the *atmospheric residuals*, the differences between the real and interpolated atmospheric (both ionospheric and tropospheric) delays. Ideally, when the errors due to the atmospheric interpolation may be neglected, the atmospheric errors in the virtual data should be very similar to those in the real user data, such that the *ionosphere-fixed* and *troposphere-fixed* processing strategies may be applied (see Chap. 5). Unfortunately the atmospheric residuals are not known but may be significantly present depending on the actual atmospheric conditions. In this section it is explained which processing strategy a user should apply under these circumstances.

6.7.1 Accounting for ionospheric residuals

To take possible residual ionospheric errors into account, a user should apply the *ionosphere-weighted* model for his processing. When the ionospheric conditions are not too disturbed, in this user's processing the sample values of the ionospheric pseudo-observables can be taken exactly *zero*. In contrast to the *network* processing model, it may now be expected that the expected ionospheric delays are zero on average. For the corresponding *standard deviation* of these ionospheric pseudo-observables a realistic value should be chosen. Note that this a priori ionospheric standard deviation represents the *spatial* correlation of the ionospheric delays, and should hence be chosen as a *distance-dependent* function. This in contrast to the network processing, in which the choice of the ionospheric standard deviation depends on the *temporal* correlation of the ionospheric delays. In case of processing relative to a VRS, the ionospheric standard deviation should be based on the distance from the user receiver to the *closest* permanent network station, since it is expected that the closer to a network station, the smaller the residual ionospheric delays are in the virtual baseline.

In [Schaffrin and Bock, 1988] a procedure is sketched how the ionospheric standard deviation for the user's processing, denoted as $\sigma_{\iota,user}$, can be chosen as the following *linear* function of the distance l_{xr} (km) between the user receiver x and the closest network station r:

$$\sigma_{\iota,user} = \beta\, l_{xr}, \quad \text{where } 0.3 \text{ mm/km} \leq \beta \leq 3 \text{ mm/km} \tag{6.60}$$

The choice of β should depend on the actual ionospheric activity: A small value should be chosen during solar minimum periods, a large value during solar maximum years. One may question this choice of the factor β, since during solar maximum periods the size of the residual ionospheric delays between the user and virtual station may differ even from day to day, depending on irregular ionospheric

effects such as geomagnetic storms and TIDs (see [Odijk, 2001]). A better alternative than arbitrarily choosing a value for β, is to assess it *empirically* from the the ionospheric delays which are estimated in the permanent network processing, like is done in [Odijk, 2000b]. Next, this estimated factor can be made available to users. In case of real-time applications, the network data of say one hour before the actual observation epoch should be used to assess the ionospheric standard deviation.

6.7.2 Accounting for tropospheric residuals

To account for *residual tropospheric delays* in the user's observations relative to the virtual observations, in the user's processing a tropospheric delay (ZTD) should be estimated for the user receiver relative to the virtual receiver. This approach is referred to as the *troposphere-float* approach (see Chap. 5). Especially for instantaneous applications this is a drastic choice, since the estimation of a ZTD each epoch will significantly worsen the precision of the height component of the receiver position. Since no better alternative is available yet, this strategy is used in this thesis.

6.7.3 Number of frequencies

Because of this ZTD estimation plus the application of the ionosphere-weighted model in the user's processing, it is not expected that *fast* ambiguity resolution based on *single-frequency* data of the user will be successful (especially when a low number of satellites is tracked). See also Fig. 5.11 in Chap. 5 in which the expected single-frequency ambiguity success rate is plotted as function of the a priori ionospheric standard deviation. Hence, for a user of VRS-based positioning should collect data with dual-frequency receivers.

6.8 Fast VRS-based positioning results

In this section the performance of fast positioning using VRS data is demonstrated for some test cases. Here we restrict ourselves to *instantaneous* positioning, the fastest application possible.

In the first subsection a permanent network plus user station are simulated using some stations of the Californian *SCIGN* network, and in the two subsections following in a similar manner the Dutch *AGRS.NL* network is used. Although both networks are not designed for very fast user's applications, the data of the networks provide an excellent source to investigate to what extent a simulated user operating within the coverage of such a network can benefit from it. Note that the user receivers in the AGRS.NL tests were the same as used in [Van der Marel, 2000], in which the baselines with respect to the virtual stations were processed with *commercial* GPS software. In the current tests all computations were carried out with the *GPSveQ* and *Virint* software.

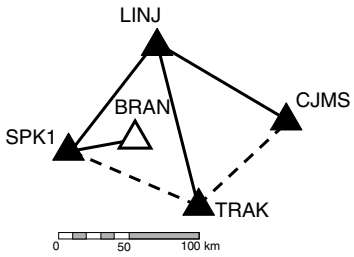

Fig. 6.40. Assigned user station BRAN (34°N, −118°E) in permanent network

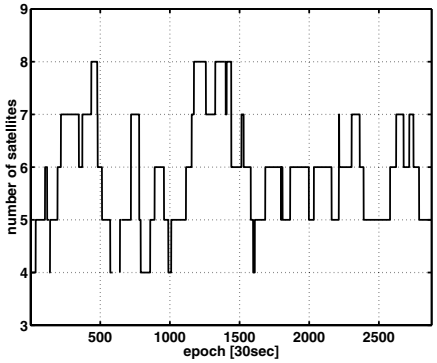

Fig. 6.41. Number of satellites

Concerning the stochastic model of the GPS observations, in all computations a 'standard' stochastic model for both phase and code data was used, with a standard deviation of 3 mm for the undifferenced phase data, and a standard deviation of 30 cm for the undifferenced code data.

6.8.1 Simulations using SCIGN data

In the first test, four SCIGN stations are assumed to simulate the permanent GPS network, whereas SCIGN station *BRAN* is for this example simulated as user station. In Fig. 6.40 the configuration of the stations is depicted. Note that the assigned permanent stations are other stations than those used in the example in Sect 6.4.5. The distance between the permanent stations in this example is at most about 100 km. The shortest distance of assigned user station BRAN to one of the network stations is 37 km (to station SPK1).

Dual-frequency GPS phase and data were downloaded for April 11, 2001, from 00:00 h UTC to 24:00 h UTC. Note that the corresponding local time in California was from 17:00 h on April 10, to 17:00 h on April 11. As to simulate a processing suitable for *real-time* applications, the satellite positions were computed using the predicted IGS (ultra-rapid) orbits. The number of satellites in the processing varied between 4 and 8 (cut-off elevation: 10°), see Fig. 6.41.

Network processing

Based on the sampling interval, 30 s, for a total of $24 \cdot 120 = 2880$ epochs an instantaneous network processing was carried out, using the procedure described in Sect. 6.4. Figure 6.41 shows the number of satellites in this network processing. The network ambiguity resolution, using a $\sigma_{\iota,net} = 2$ cm, was successful for 98% of the epochs: For a small number of epochs, around epoch 600 (05:00 UTC), the wrong ambiguities were estimated. Note that in Fig. 6.41 for this period (about 2% of the 2880 epochs in total) no satellites are 'visible'.

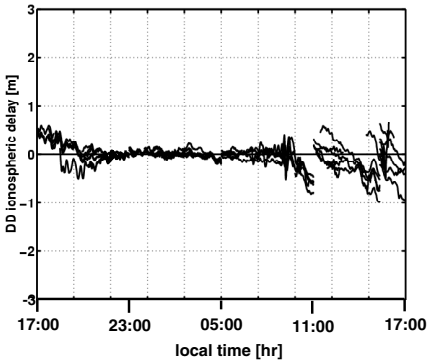

Fig. 6.42. DD ionospheric delays for network baseline LINJ-CJMS (72 km)

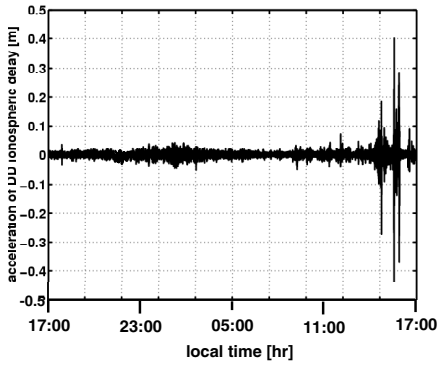

Fig. 6.43. 'Acceleration' of ionospheric delays for network baseline LINJ-CJMS

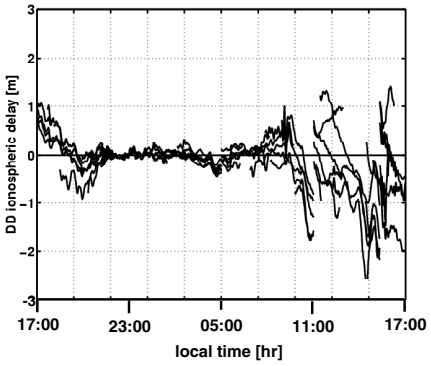

Fig. 6.44. DD ionospheric delays for network baseline LINJ-TRAK (120 km)

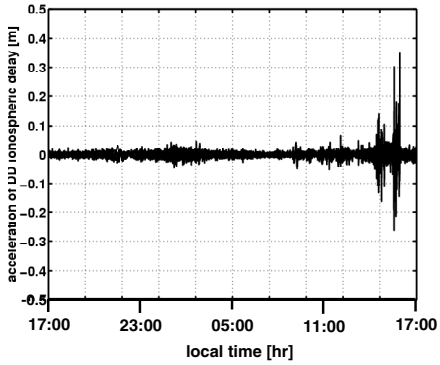

Fig. 6.45. 'Acceleration' of ionospheric delays for network baseline LINJ-TRAK

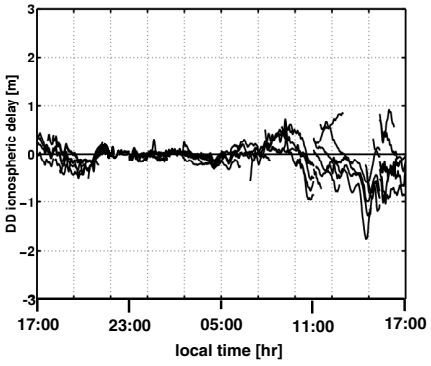

Fig. 6.46. DD ionospheric delays for network baseline LINJ-SPK1 (82 km)

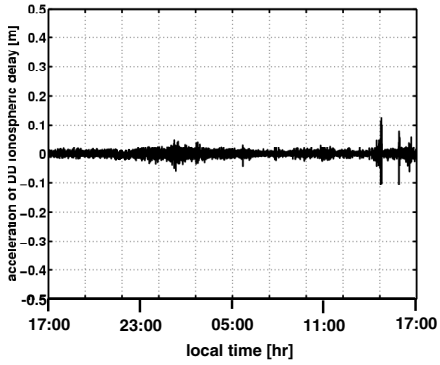

Fig. 6.47. 'Acceleration' of ionospheric delays for network baseline LINJ-SPK1

With the ambiguities fixed, precise ionospheric delays can be estimated for the three 'network baselines'. In Figs. 6.42 – 6.46 for these baselines the *double-differenced* ionospheric delays are shown. To facilitate the drawing of these graphs, not the instantaneous ionosphere-weighted ionospheric estimates were used, but their counterparts obtained from the *ionosphere-float* model, estimated in one time over the complete time span of 2880 epochs, with the ambiguities fixed. Note that this 'post-processing' with the ionosphere-float model is only carried out for drawing these plots and *not* for the VRS data generation (for that purpose the original instantaneous ionosphere-weighted results are taken). This ionosphere-float model also explains why in the three plots for the mentioned short time span for which the wrong network ambiguities were estimated instantaneously, it is possible to plot the DD ionospheric delays.

The few abrupt changes visible in Figs. 6.42 – 6.46 stem from a change of pivot satellite (when the 'old' pivot satellite sets), for example at about 11.00 h local time. When the three figures of the DD ionospheric delay time series are compared, one can immediately see the *spatial correlation* of the DD ionospheric delays: In general, the DD ionospheric delays of the longest network baseline, LINJ-TRAK (120 km), show the largest magnitude, while the DD ionospheric delays of the shortest baseline, LINJ-CMS1 (72 km) are the smallest. From the figures one may also notice that the magnitude of the DD ionospheric delays is approximately a *linear* function of the distance.

The figures also show the *diurnal variability* of the ionosphere: At nighttime (from about 23:00 h to 7:00 h local time) the DD ionospheric delays are very small, only a few dm, while at daytime they may be as large as about 3 m (for baseline LINJ-TRAK). During daytime the ionospheric delays also seem to be highly variable in time. These very large and variable ionospheric delays from about 7:00 h local time could also be related to the occurrence of a *geomagnetic* storm on April 11, 2001. Figure 6.48 shows the planetary Kp-index, which is an indicator or geomagnetic activity (see Chap. 5), and it can be seen that from 15:00 h UTC (8:00 h local time) the Kp-index increases to a level of 8, corresponding to a severe geomagnetic storm. The relation between the occurrence of geomagnetic storms and the disturbance of the smoothness of the ionospheric delays was also demonstrated in, among others, [Odijk, 2001] and [Liu, 2001].

During these ionosphere-disturbed hours, the *acceleration* of the ionospheric delays, as explained in Sect. 6.4.4, may deviate significantly from zero, see Figs. 6.43, 6.45, and 6.47, where these acceleration per epoch are plotted for the three network baselines. For most of the epochs these accelerations are only a few cm, but after about 14:00 h local time they may be as large as about 0.5 m, which is probably due to the geomagnetic storm.

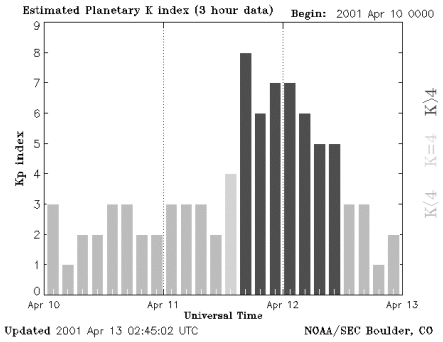

Fig. 6.48. Planetary Kp-index from April 10th to April 13th 2001

User's processing: Reduction of ionospheric delays

At the approximate position of station BRAN virtual dual-frequency phase and code observations were generated for April 11, 2001, from 00:00 – 24:00 UTC (also for 30 s sampling interval and cut-off elevation 10°), using the ambiguity-fixed network processing parameters. This virtual station is referred to as *BRAV*.

To show the reduction in ionospheric delays due to the interpolation in the permanent network (as part of the VRS data generation procedure), in Fig. 6.49 time series of DD ionospheric delays are shown for the 37-km *real* baseline SPK1-BRAN. These DD ionospheric delays are estimated using the ionosphere-float model, with the time-constant ambiguities resolved. Again note that this way of 'post-processing' using the ionosphere-float model is only used here for the purpose of visualizing the effect of the ionospheric interpolation. Figure 6.49 is closely related to Figs. 6.42–6.46, in which the DD ionospheric delays for network stations CJMS, TRAK and SPK1 were plotted relative to network station LINJ, but for the same time span on April 10-11, 2001. Note from the figure the low ionospheric delays during the night, and the large fluctuations during the daytime hours of April 11. These large and variable ionospheric delays during the day corresponds to the occurrence of a geomagnetic storm on this day (after 15.00 h, see Fig. 6.48).

Figure 6.49 also shows that the size of the DD ionospheric delays in the baseline SPK1-BRAN can range to values of about 0.5 m. To show the effect of the ionospheric interpolation, Fig. 6.49 should be compared to Fig. 6.50, in which the DD ionospheric delays are plotted for the *virtual* baseline BRAV-BRAN, which are in fact the residual delays after the interpolation. Although these residuals are not zero, at first sight one can see from the figure that the ionospheric interpolation has performed reasonably well, since the size of the DD ionospheric delays of the virtual baseline is over the entire day below the 10 cm, except for some epochs around 10:00 h local time. Also during nighttime the use of ionospheric corrections in (through the VRS observations) makes sense, although the reduction of

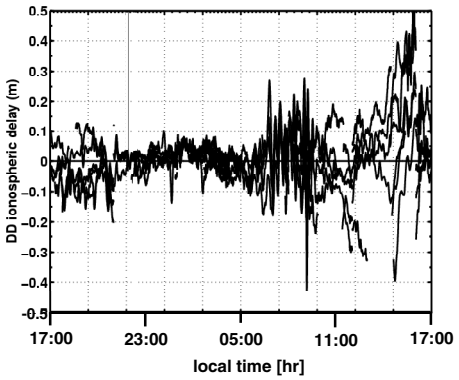

Fig. 6.49. Real DD ionospheric delays for baseline SPK1-BRAN (37 km)

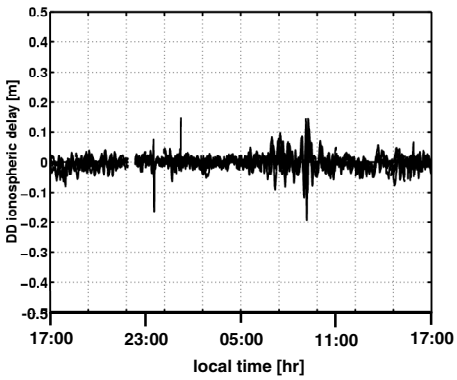

Fig. 6.50. Residual DD ionospheric delays for virtual baseline BRAV-BRAN

the ionospheric delays is much smaller than during daytime.

Instantaneous user processing: Ionosphere-fixed, troposphere-fixed

In a next step, fast positioning is simulated for the virtual baseline BRAV-BRAN by trying to resolve the integer ambiguities instantaneously. So for all 2880 epochs during the day it was tried to resolve the ambiguities for each epoch again, without using information from previous epoch(s). Although it was shown that the (residual) DD ionospheric delays for this virtual baseline can be up to 10 cm (see Fig. 6.50), it was first tried to resolve the ambiguities using the *ionosphere-fixed* model, in which the ionospheric delays are completely neglected. Also no tropospheric delays were estimated (*troposphere-fixed* approach). The empirical ambiguity success rate using this model was however quite low: For just 63% of the 2880 epochs the correct ambiguities were estimated. For these 'successful' epochs in a next step the ambiguities were held fixed and coordinate parameters (North, East, Up) were estimated. Figures 6.51, 6.53 and 6.55 show the estimated corrections on the a priori coordinates, which are the approximate values of BRAN. Note that for these approximate values the *precisely known* coordinates of BRAN were taken (since it is in reality a SCIGN permanent station). For the epochs for which wrong ambiguities were estimated no coordinates are plotted in the three figures. Note that these epochs with wrong ambiguities are particularly clustered between epochs 1700 and 2000, which corresponds to 7:00 - 10:00 h local time. From Fig. 6.50 it can be seen that during this time interval the *residual ionospheric delays* in the virtual baseline data are largest and can range up to a large 20 cm.

The *empirical* standard deviations of the three fixed coordinate time series were assessed at 4 cm for North, 8 cm for East and 25 cm for the Up component. These values are quite large, which may indicate residual *unmodelled* biases in the data.

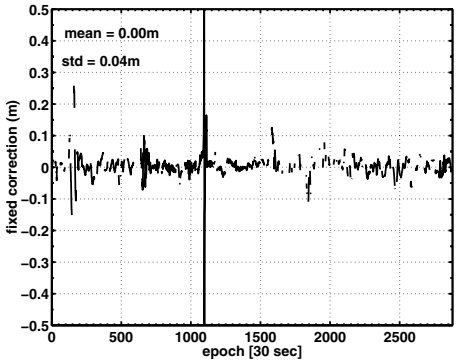

Fig. 6.51. North corr. (ion-fix, trop-fix)

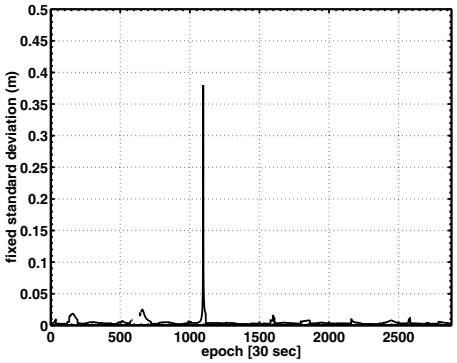

Fig. 6.52. North std. (ion-fix, trop-fix)

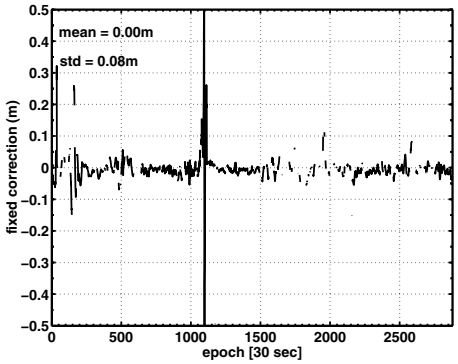

Fig. 6.53. East corr. (ion-fix, trop-fix)

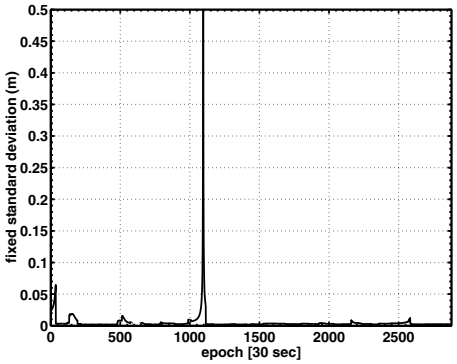

Fig. 6.54. East std. (ion-fix, trop-fix)

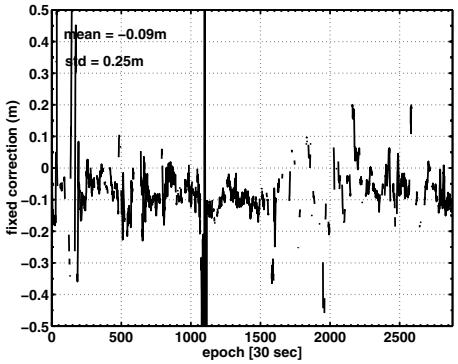

Fig. 6.55. Up corr. (ion-fix, trop-fix)

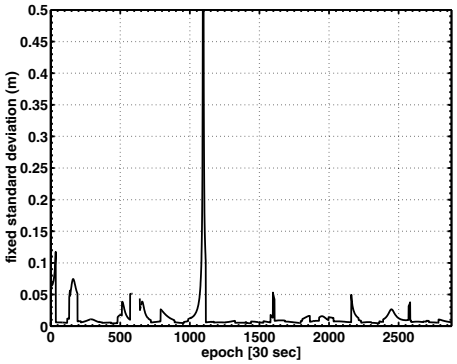

Fig. 6.56. Up std. (ion-fix, trop-fix)

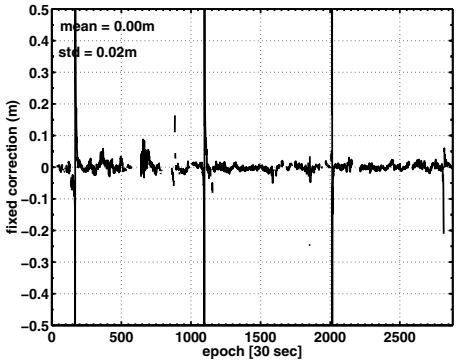

Fig. 6.57. North corr. (ion-wei, trop-flo)

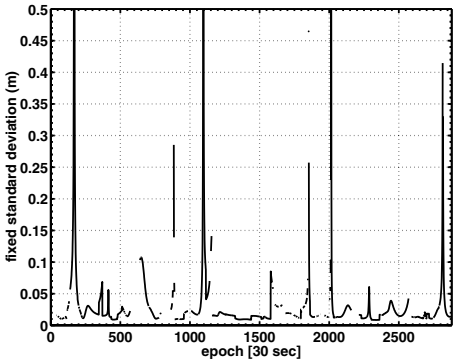

Fig. 6.58. North std. (ion-wei, trop-flo)

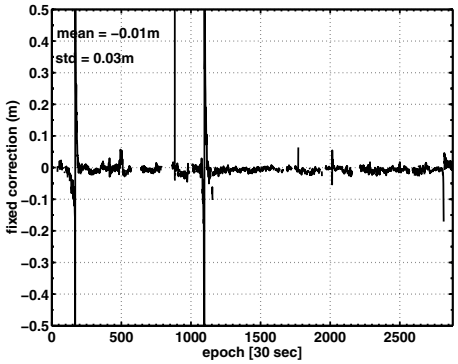

Fig. 6.59. East corr. (ion-wei, trop-flo)

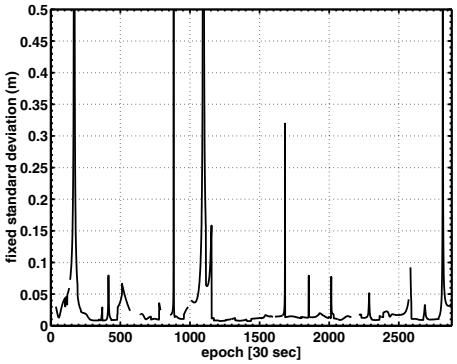

Fig. 6.60. East std. (ion-wei, trop-flo)

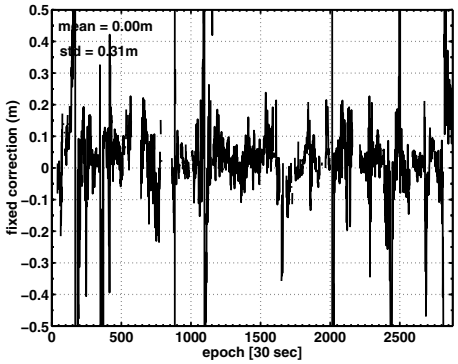

Fig. 6.61. Up corr. (ion-wei, trop-flo)

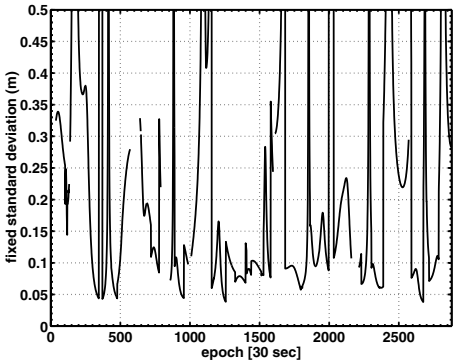

Fig. 6.62. Up std. (ion-wei, trop-flo)

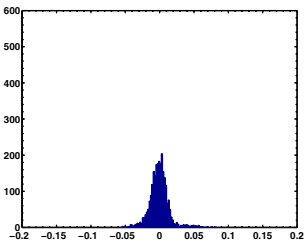

Fig. 6.63. *North* BRAN (ion-weighted, trop-fixed)

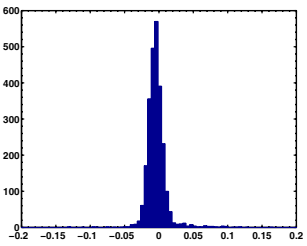

Fig. 6.64. *East* BRAN (ion-weighted, trop-fixed)

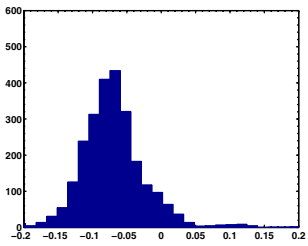

Fig. 6.65. *Up* BRAN (ion-weighted, trop-fixed)

This suspicion is confirmed when the formal instantaneous fixed standard deviations are plotted for the three coordinate components during the time interval, see Figs. 6.52, 6.54 and 6.56. These three figures show that the formal standard deviations are generally much *lower* than their empirical counterparts (despite a peak after epoch 1000 which is caused by a bad geometry at that time): For North and East at most about 1 cm, and for Up about 5 cm. Since all three coordinate components are affected, it is suspected that this is caused by significant residual *ionospheric* delays.

Instantaneous user processing: Ionosphere-weighted, troposphere-fixed

To account for the suspected ionospheric residuals, in another processing it was tried to resolve the ambiguities again for all epochs, but now using the *ionosphere-weighted* model. The sample values of the ionospheric pseudo-observables were all taken zero, and the a priori ionospheric standard deviation was for each epoch fixed at $\sigma_{\iota,user} = 2$ cm. The *troposphere-fixed* approach was still maintained. The resulting ambiguity success rate using this ionosphere-weighted strategy was much better than the success rate of the previous strategy: It increased to 89%. This large improvement of almost 30% can thus simply be reached by a stochastic modelling of the ionospheric residuals. Instead of time series, Figures 6.63, 6.64 and 6.65 show *histograms* of three fixed coordinate components. The from these histograms assessed standard deviations are 2 cm for North, 3 cm for East and 11 cm for the Up component. These standard deviations are smaller than using the ionosphere-fixed approach. Despite this, from Fig. 6.65 it can be seen that the *mean* of the Up component clearly shows a bias, which is about −7 cm. Since the means of the histograms for both horizontal components does not seem to be biased, this bias in the height is probably caused by significant residual *tropospheric* delays.

Instantaneous user processing: Ionosphere-weighted, troposphere-float

To account for the residual tropospheric delays, another ionosphere-weighted processing was carried out (again with $\sigma_{\iota,user} = 2$ cm), in which for every instantaneous epoch an additional tropospheric wet zenith delay (ZTD) parameter was

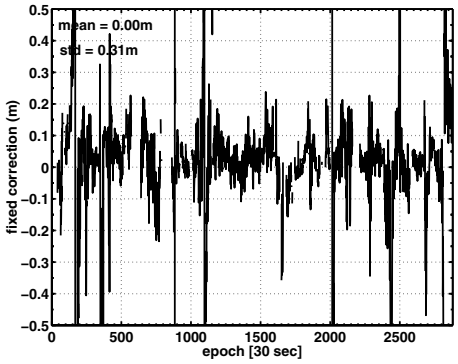

Fig. 6.66. Up corrections for BRAN (ion-weighted, trop-float)

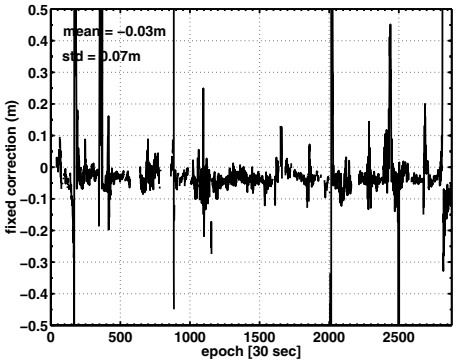

Fig. 6.67. Residual ZTDs for BRAN, (ion-weighted, trop-float)

estimated. For this purpose Niell's mapping function was used. Besides an estimation of a ZTD parameter, the observations were a priori corrected for the troposphere using Saastamoinen's model. This *troposphere-float* approach yielded an empirical ambiguity success rate of 90%, which is comparable with the success rate using the troposphere-fixed strategy (89%). The resulting fixed coordinate components are given in Figs. 6.57, 6.59 and 6.61. It should be stressed that, due to the ZTD estimation, fixed coordinates could only be estimated for epochs with at least five satellites (note that ambiguity resolution is however feasible using only four satellites, despite the additional ZTD parameter). From Fig. 6.41 it follows that for about 10% of the 2880 epochs less than five satellites are available.

The empirical standard deviations of the horizontal components (North and East) are about 2-3 cm and this seems to be in good agreement with their formal counterparts (graphs in Figs. 6.58 and 6.60). Due to the ZTD estimation per epoch, the empirical precision of the Up component is a large 30 cm (see Fig. 6.61), but its mean is now about zero. This bad empirical precision is however in agreement with the graph of the formal Up standard deviations in Fig. 6.62, which shows a very fluctuating standard deviation (at many epochs more than 0.5 m) as function of time.

That there are really residual tropospheric delays present in the virtual data is also shown by Fig. 6.67, in which the instantaneous estimates for the ZTD parameters are plotted for the day. The mean of these estimated ZTDs is not zero, but about -3 cm, with a standard deviation of about 7 cm. When this figure is compared to the figure of the fixed Up components (in Fig. 6.66 these Up corrections are plotted once again), one can see that when at a certain time the graph for Up is going up, at the same time the graph for ZTD is going down. These figures illustrate the well-known large correlation between the tropospheric delay and the height component.

6.8.2 AGRS.NL network: Case Cabauw

In this subsection an example of fast VRS-based positioning is described within the coverage of the AGRS.NL network, the Dutch permanent network earlier discussed in Sect. 6.4.3. On September 20, 2000, GPS observations were collected from 12:00 – 14:00 h UTC (30 s sampling interval) with a Trimble 4000 SSI receiver at a location in Cabauw (near Utrecht). In this case study this receiver station is assigned as user station (see Fig. 6.68 where it is referred to as CABA). The distance from CABA to the closest AGRS.NL station, station DELF, is about 37 km. Note that at the time these measurements were conducted, station KOSA was still part of the AGRS.NL (instead of APEL). Using the approximate position of the user's receiver, for the two-hour time span VRS observations were generated at the location of CABA from the ambiguity-fixed AGRS.NL network estimates (where all five stations were used). AGRS.NL station DELF was selected as master reference station. The virtual reference station is referred to as CABV. Figure 6.69 depicts the number of satellites in the processing.

As in the previous subsection, the performance of the interpolation of the network ionospheric delays to the user's location is shown by comparing the ambiguity-fixed DD ionospheric delays in the virtual baseline CABV-CABA with their counterparts in the (real) baseline DELF-CABA. Figures 6.70 and 6.71 show the DD ionospheric delay time series over the two hours. From the figures it is apparent that the interpolation has performed reasonably well: Whereas for the 37-km *real* baseline the DD ionospheric delays could be up to about 20 cm, for the *virtual* baseline these are at most about 8 cm. However, like in the previous subsection, the *ionosphere-weighted* model should be used to deal with these residual ionospheric delays. For the a priori ionospheric standard deviation a value of $\sigma_{\imath,user}$ = 1 cm was assumed. Considering the tropospheric delays, like in the previous subsection two strategies were evaluated, the *troposphere-fixed* approach, and, to account for possible residual tropospheric delays, the *troposphere-float* approach.

In the processing of 240 epochs it was tried to resolve the integer ambiguities instantaneously. The empirical success rates are as follows. For the troposphere-fixed approach it is 90%, whereas for the troposphere-float approach it is somewhat lower, using this strategy for 81% of the epochs the correct ambiguities could be resolved. To compare: Ambiguity resolution based on the *ionosphere-fixed* and troposphere-fixed strategy succeeded in only 21% of the 240 epochs. Figures 6.74 – 6.79 show the ambiguity-fixed instantaneous *coordinate* estimates using both ionosphere-weighted approaches. Like in the previous subsection, from the figures it can be seen that for the horizontal components (North, East) there are only marginal differences when using either the troposphere-fixed approach or the troposphere-float approach. A difference is that in the troposphere-float case *no* coordinates are plotted around epoch 150, since for these epochs the wrong ambiguities were estimated (which is possibly due to the low number of satellites at that time). For the troposphere-fixed Up component an average bias of about −18 cm is visible in Fig. 6.78, which is caused by residual tropospheric biases, since

the Up corrections in the *troposphere-float* case are zero on average (see Fig. 6.79).

6.8.3 AGRS.NL network: Case Damwoude

In this subsection another example of fast VRS-based positioning within the Dutch AGRS.NL network is described. This time the user station is located somewhat outside the 'triangles' which span the permanent network. This station is located in *Damwoude* (Friesland), see Fig. 6.80, where it is referred to as NG07. AGRS.NL station TERS is at closest distance from NG07 (51 km). At station NG07 on June 21 2000, an Ashtech Z-XII GPS receiver collected data at 30 s interval, for the complete 24 hours of the day. Figure 6.81 shows the number of satellites during the day, which were used in the instantaneous network processing (for which the satellite cut-off elevation was maintained at 15°). From the ambiguity-fixed network estimates virtual observations were created for the approximate location at NG07. The virtual station is referred to as NG0V.

In Fig. 6.82 the ambiguity-fixed DD ionospheric delays for the 51-km baseline TERS-NG07 are plotted for the entire day (from June 21, 02:00 local time, to June 22, 02:00 local time). Figure 6.83 shows for the same period the fixed DD ionospheric delays for the virtual baseline NG0V-NG07.

From Fig. 6.81 it follows that at many epochs the number of satellites is lower than 5, and therefore in this example of the user's processing only the *troposphere-fixed* approach is considered, despite possible residual tropospheric biases in the data. Considering the ionospheric delays, first an *ionosphere-fixed* processing was performed, but instantaneous ambiguity resolution was only successful for 57% of the 2880 epochs. Applying the *ionosphere-weighted* model to account for residual ionospheric delays, with an assumed ionospheric standard deviation of $\sigma_{\iota,user} =$ 2 cm, resulted in an empirical instantaneous ambiguity success rate of 80%. The reason that still for 20% of the epochs wrong ambiguities were obtained could be due to significant extrapolation errors of the ionospheric delays in relation to the relatively long distances between the permanent stations.

For the epochs with correct estimated integer ambiguities, the ambiguity-fixed coordinate corrections with respect to the a priori coordinates of BRAN are plotted in Figs. 6.87, 6.89 and 6.91. Their formal standard deviations are shown in Figs. 6.88, 6.90 and 6.92. Note that the time series of all three coordinate components follow their corresponding standard deviation graph, which means that fluctuations of the time series can be explained from a fluctuating geometry. For example, all three coordinate correction graphs show between epochs 1000 and 1500 a fluctuating behavior (especially the Up component). Inspection of the standard deviation graphs during this time interval reveals that similar fluctuations are also visible in the standard deviations, caused by the receiver-satellite geometry at those epochs (also the *PDOP* values are high during this time interval). Considering the empirical mean of the coordinate time series, those for the North- and Up components deviate significantly from zero (2 cm for North and

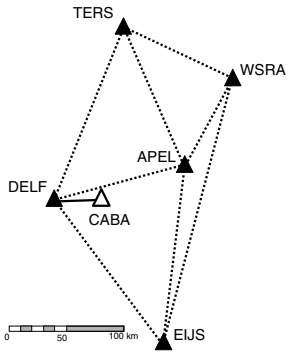

Fig. 6.68. 'User' station CABA (52°N, 5°E) in AGRS.NL network

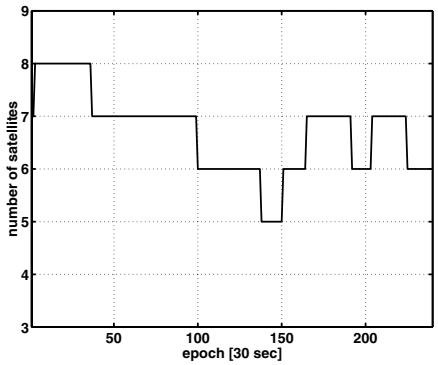

Fig. 6.69. Number of satellites for virtual baseline CABV-CABA

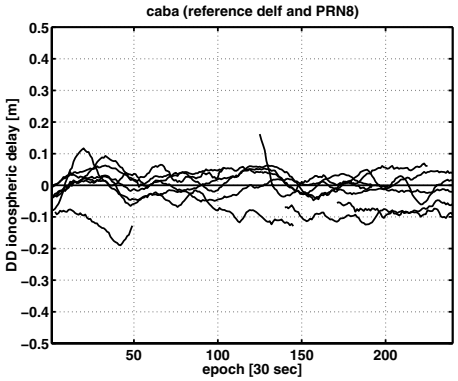

Fig. 6.70. DD ionospheric delays in real baseline DELF-CABA (37 km)

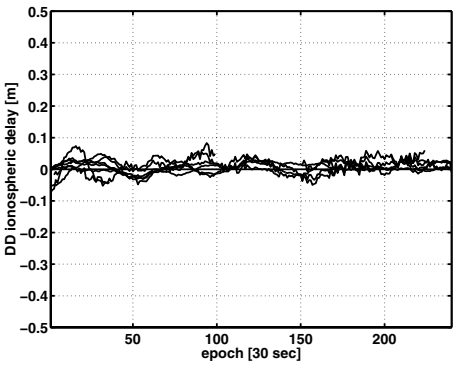

Fig. 6.71. DD ionospheric delays in virtual baseline CABV-CABA

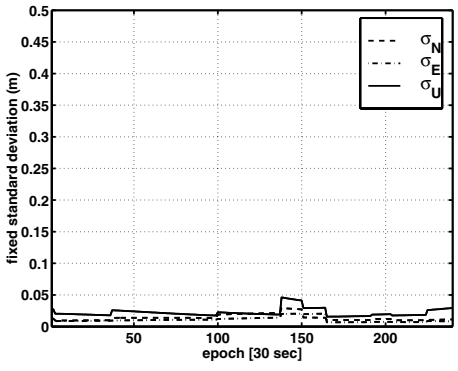

Fig. 6.72. Coordinate precision (formal) for CABA, troposphere-fixed strategy

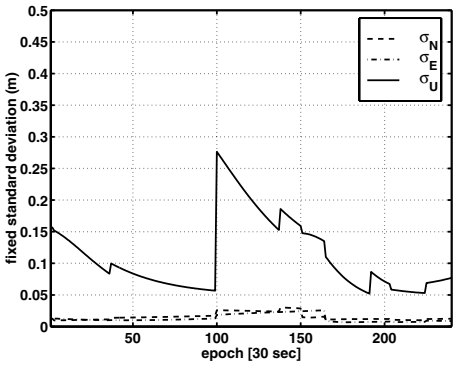

Fig. 6.73. Coordinate precision (formal) for CABA, troposphere-float strategy

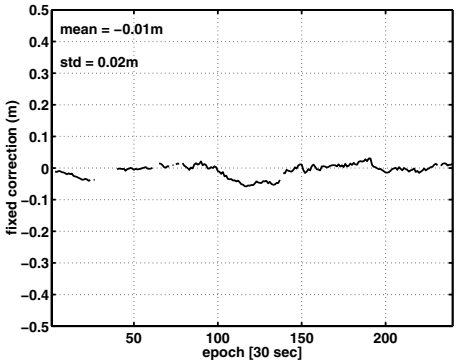

Fig. 6.74. Fixed *North* corrections for CABA, troposphere-fixed

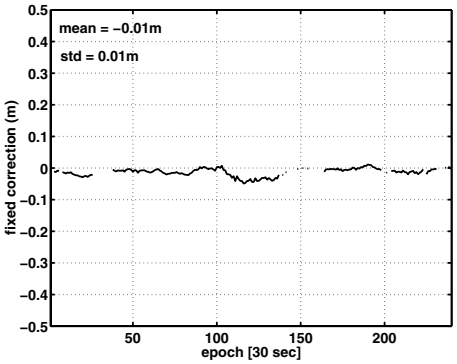

Fig. 6.75. Fixed *North* corrections for CABA, troposphere-float

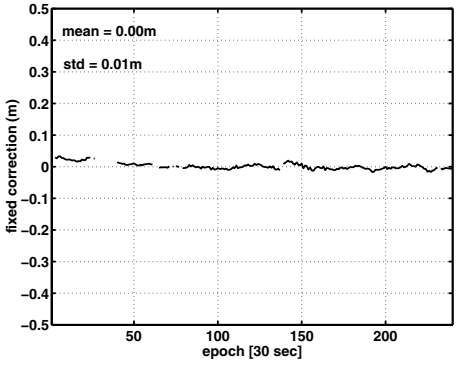

Fig. 6.76. Fixed *East* corrections for CABA, troposphere-fixed

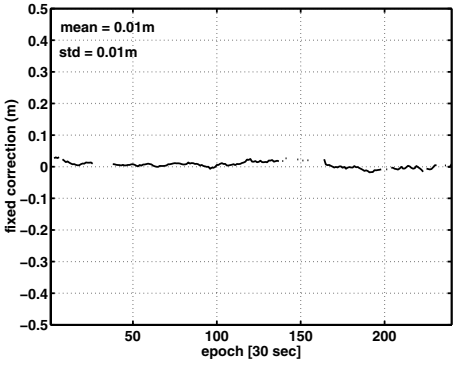

Fig. 6.77. Fixed *East* corrections for CABA, troposphere-float

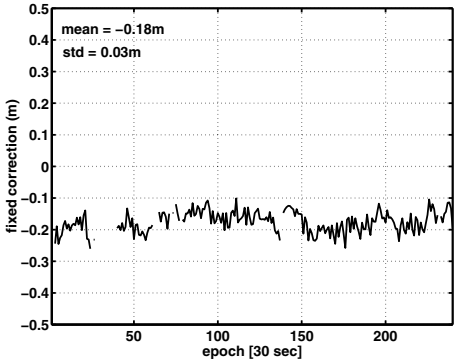

Fig. 6.78. Fixed *Up* corrections for CABA, troposphere-fixed

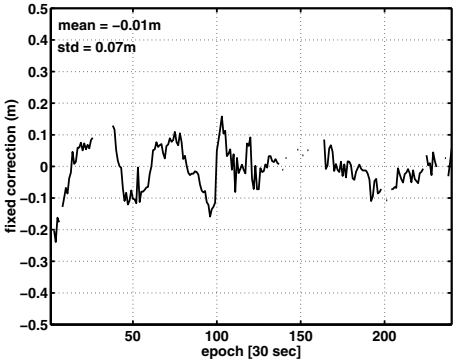

Fig. 6.79. Fixed *Up* corrections for CABA, troposphere-float

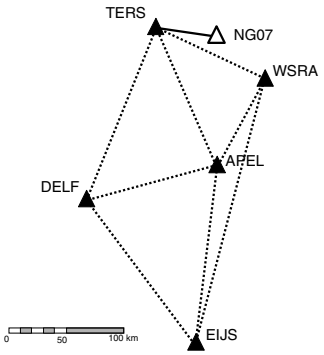

Fig. 6.80. 'User' station NG07 (53°N, 5°E) in AGRS.NL network

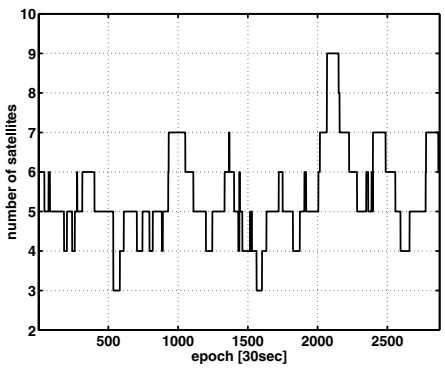

Fig. 6.81. Number of satellites for virtual baseline NG0V-NG07

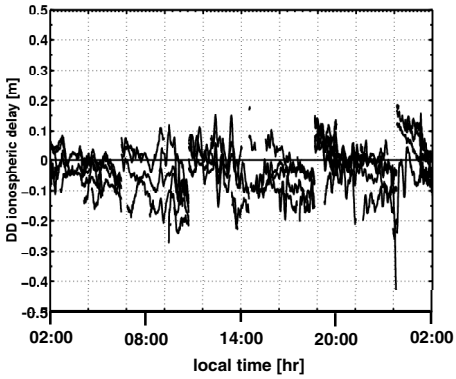

Fig. 6.82. DD ionospheric delays for real baseline TERS-NG07 (51 km)

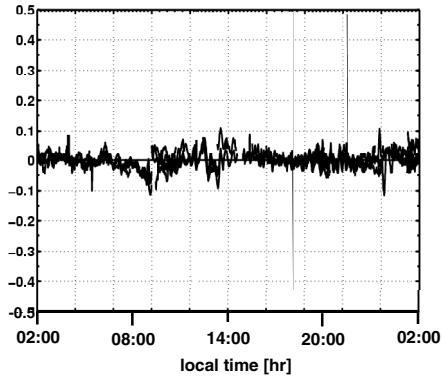

Fig. 6.83. DD ionospheric delays for virtual baseline NG0V-NG07

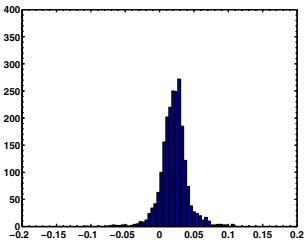

Fig. 6.84. Histogram *North* NG07

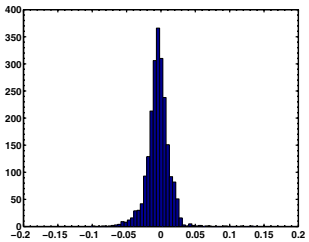

Fig. 6.85. Histogram *East* NG07

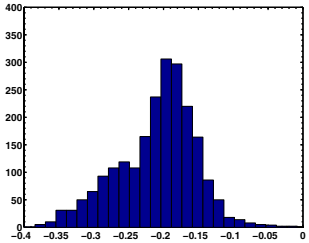

Fig. 6.86. Histogram *Up* NG07

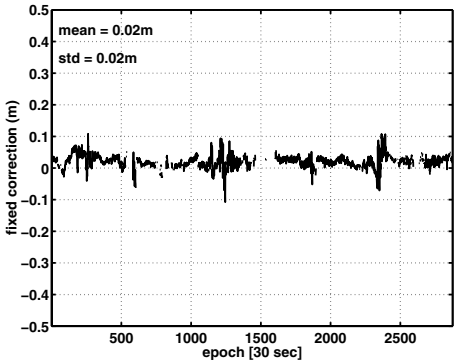

Fig. 6.87. Fixed *North* corrections for NG07, troposphere-fixed

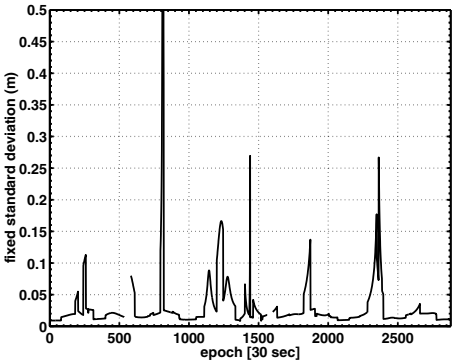

Fig. 6.88. Fixed *North* precision for NG07, troposphere-fixed

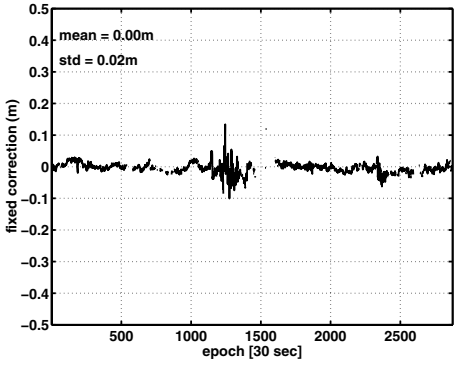

Fig. 6.89. Fixed *East* corrections for NG07, troposphere-fixed

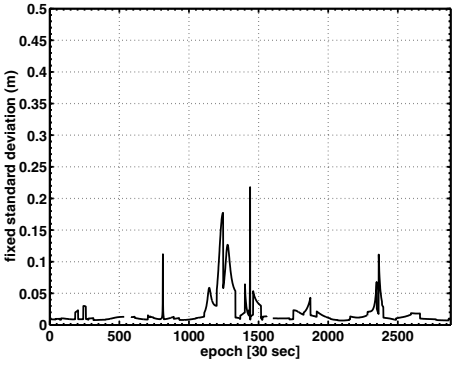

Fig. 6.90. Fixed *East* precision for NG07, troposphere-fixed

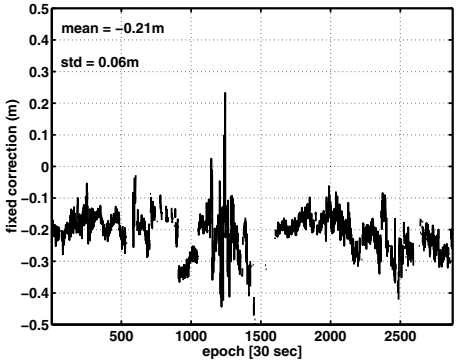

Fig. 6.91. Fixed *Up* corrections for NG07, troposphere-fixed

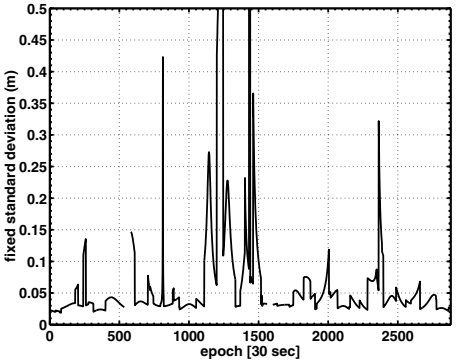

Fig. 6.92. Fixed *Up* precision for NG07, troposphere-fixed

−21 cm for Up). The deviation of the Up mean is caused by residual tropospheric biases (since the troposphere-fixed approach) was used, but the cause of the 2 cm mean for the North component is not clear, perhaps it is due to the location of NG07, which is outside the network triangles. The empirical standard deviations for this component (2 cm) seems to be realistic however. Finally, Figs. 6.84, 6.85, 6.86 show the fixed coordinate corrections of NG07 as *histograms*. The two histograms of the horizontal components show a reasonable Gaussian curve, but the Up component is certainly *not* normally distributed, which is caused by the residual tropospheric biases that are still present in the data.

6.9 Concluding remarks

Table 6.4. Summary instantaneous ambiguity success rates user processing

Virtual baseline	Ionosphere-fixed Troposphere-fixed	Ionosphere-weighted Troposphere-fixed	Ionosphere-weighted Troposphere-float
BRAV-BRAN	0.63	0.89	0.90
CABV-CABA	0.21	0.90	0.81
NGOV-NG07	0.57	0.80	not computed

In the main part of this chapter a procedure was described to be used for fast GPS positioning within the coverage of a permanent GPS network. This procedure for the processing of GPS observations collected at the GPS reference stations and the user stations in order to obtain precise geodetic user positions, consists of three steps: Network processing, correction generation and distribution, and the user's processing. In both network processing and user processing the ionosphere-weighted model plays a crucial role to incorporate ionospheric information. Very fast, instantaneous network processing is in principle feasible when ionospheric information is determined from ionospheric estimates of the two previous epochs. For the second step of the procedure, correction generation and distribution, in this thesis the VRS approach is used. A user within the area of the permanent network then processes VRS data together with his own collected GPS data. Ideally, the atmospheric delays in the virtual baseline should be zero, allowing to use the ionosphere-fixed model fast and precise positioning. Due to interpolation errors however, residual atmospheric delays are usually present for the virtual baseline. This problem can be largely overcome by using the ionosphere-weighted model in the user's processing, resulting in much higher success rates than with the ionosphere-fixed model (see Table 6.4). Using this, the resulting precision of the horizontal components of the user receiver is at the cm-level. The precision of the height component is much worse, due to residual tropospheric delays which are estimated as ZTDs in the user's processing.

Chapter 7

Conclusions and recommendations

7.1 Conclusions

The research objective of this thesis is the development of a procedure for the processing of GPS observations for medium-distance baselines (at mid-latitudes), such that precise and fast positioning is feasible, despite significant ionospheric errors in the data. This objective is elaborated as follows. The research described in this thesis can roughly be divided into three parts (not exactly corresponding to the chapter order). In the first part the significant ionospheric errors were quantified for relative GPS positioning. In the second part a suitable mathematical model was outlined, which forms the basis of the processing. This processing should be carried out following a three-step processing procedure, which is the third part of the research. In the following the conclusions of these three research parts are summarized.

Significant ionospheric errors

To determine what 'significant' means in this context, the ionospheric error in GPS observations was analyzed from a geometric point of view, using the theory of atmospheric refraction (see Chap. 4). According to this theory, the ionospheric error can be decomposed into a *first-order* term, a *higher-order* term plus a term due to ray *bending*. Since the GPS applications in this thesis are all relative, not so much the absolute, but the relative (double-difference; DD) ionospheric delays are of importance. In this thesis it was shown that under simulated *worst-case* ionospheric conditions (solar maximum, daytime) the DD first-order effect may range up to 50 mm/km (for L1), and the DD higher-order plus bending terms from 0.005 mm/km (for L1) to 0.02 mm/km (for the future L5). These figures should be considered as safe upper bounds for GPS observations collected at mid-latitudes. Fortunately, not all these effects should be taken into account in a processing, since for medium-distance baselines (max. a few hundred km length) the higher-order and bending effects fall within the 2σ precision level of the GPS (phase) observations, allowing them to neglect in the processing. So only the first-order ionospheric errors are significant.

Basis of the processing: Undifferenced ionosphere-weighted model

In this thesis the *ionosphere-weighted* model was set up for the processing of GPS observations. This model is based on *undifferenced* observables, because of the advantages of it compared to a model based on differenced observables (see Chap. 2). This undifferenced model allows estimation of coordinates, integer ambiguities, satellite and receiver clocks, first-order ionospheric delays and tropospheric (zenith) delays. The satellite positions are held fixed using IGS orbits. An important feature of this model is that the ionospheric delays are stochastically modelled by adding an ionospheric pseudo-observable for each receiver-satellite combination to the GPS phase and code observables. Although the ionospheric delays are modelled as undifferenced and thus absolute variables, it was shown that only the double-difference of four undifferenced delays determines the coordinate/ambiguity solution (see Chap. 5).

Concerning the weights of the ionospheric pseudo-observables two extreme values can be distinguished. With *infinitely large* weights namely, the model reduces to the *ionosphere-fixed* model, in which the ionospheric delays are assumed as known or deterministic variables. With *zero* weights however the *ionosphere-float* model is obtained, in which the ionospheric delays are completely unknown parameters. The ionosphere-fixed model is usually applied for short-distance baselines, in which the relative ionospheric delays are assumed to be absent since the GPS signals pass through the same part of the ionosphere. For the ionosphere-float model the baseline distance and the size of the ionospheric delays is no restriction. This model is closely related to the in GPS practice often used ionosphere-free combination.

This ionosphere-weighted model is solved in three steps to obtain precise coordinates: *Float solution - ambiguity resolution - fixed solution* (see Chap. 3). In the second step the complete vector of (dual-frequency) ambiguities is resolved using the optimal integer least-squares estimator (as part of the LAMBDA method). In Chap. 5 it was by means of planning computations shown that the ionosphere-weighted model only 'makes sense' for fast positioning when the standard deviation of the ionospheric pseudo-observation is very small. For example, an instantaneous ambiguity success rate of 99.9% requires a ionospheric standard deviation of a few mm when both coordinates and tropospheric zenith delays are estimated. When no tropospheric delays are estimated the allowed ionospheric standard deviation is somewhat larger, but still smaller than 1 cm. So a successful application of the ionosphere-weighted model for fast positioning requires very *precise a priori ionospheric information*.

Three-step procedure for fast network-based positioning

Very precise information can be extracted from data of a *permanent GPS network*, which is available in the area a user operates. This ionospheric extraction is part of a three-step procedure for network-based positioning, as proposed in this thesis (see Chap. 6):

- Network processing
- Virtual reference station data generation
- User's processing

In the first step, the *network processing*, the ionosphere-weighted model is employed to process the data of all station simultaneously. Since the station coordinates for permanent networks are precisely known they are fixed in the processing. This fixing of the receiver positions implies that the admissible ionospheric standard deviation in the model may be *larger* than when the coordinates are unknown parameters (a few cm in case of instantaneous processing). The *sample values* of the ionospheric pseudo-observations are generated by prediction from ionospheric estimates at previous windows. In this research this window length is restricted to a single epoch, aiming at *instantaneous* positioning, the fastest version of network-based positioning. These ionospheric predictions are very precise in principle, since they are based on ambiguity-fixed ionospheric estimates and because of their smoothness, ionospheric delays can be predicted very well in time. An important restriction is that no (severe) geomagnetic storms occur. Simulations using data of some stations at a distance of more than 100 km of each other, collected in a solar maximum period, demonstrated that using an ionospheric standard deviation of 2 cm and a prediction based on the previous two epochs an instantaneous network ambiguity success rate of 99% can be obtained.

In the second step, *VRS observations* are generated from the ambiguity-fixed network atmospheric (ionospheric and tropospheric) and satellite clock estimates. A virtual reference station is a non-existing reference receiver at the approximate position of the user's receiver. When the error sources in the virtual observations would be similar to those in the user's observations, the 'baseline' between virtual and user receiver could be processed using the ionosphere-fixed model, guaranteeing fast ambiguity resolution and consequently precise positioning. It was shown how the virtual satellite clock, receiver clock and ambiguity parameters follow from the network estimates. The virtual atmospheric delays must be *spatially predicted* at the user's location. For this purpose a *kriging* interpolation is used, based on the spatial coherence of the network atmospheric delays. This interpolation is the weakest part of the VRS data generation procedure, since local atmospheric effects may disturb the interpolation performance. Test computations showed that although the ambiguity-fixed DD ionospheric delays for a user's receiver relative to a VRS were not zero, but at most about 10 cm, these residual ionospheric delays are much smaller compared to the DD ionospheric delays relative to the *closest* (real) permanent station (at 37 km), which could extend to about 50 cm.

In the third and final step, the *user's processing*, the VRS observations are processed simultaneously with the observations the user's receiver collected. Also for this processing the ionosphere-weighted model is very suitable, to account of possible residual ionospheric delays. The traditional short-baseline ionosphere-fixed approach is likely to fail, since for this model the DD ionospheric bias may not

extend a few cm. *Sample values* of the ionospheric pseudo-observations are - in contrast to the network processing - taken zero, whereas the ionospheric standard deviation is chosen as function of the distance to the closest network station. Test computations showed that using a ionospheric standard deviation of 2 cm an instantaneous (empirical) ambiguity success rate of about 90% could be obtained. A drastic increase compared to the instantaneous success rate using the *ionosphere-fixed* model for the processing of the same virtual baseline, which would be at a level of 60% at most. In this context it should be emphasized that when this network-based approach would *not* be offered to the user, instantaneous ambiguity resolution and consequently fast positioning would be impossible (success rate of 0%), since in that situation the only way to account for the significant ionospheric delays would be using the weak *ionosphere-float* model for the processing of a baseline to the closest permanent station (requiring long observation time spans).

7.2 Recommendations

To improve the described procedure, a number of recommendations for research can be given, which are summarized below.

Improvements in the network-based positioning procedure

The following items may benefit the three-step procedure:

- Use of a sufficiently dense network of permanent stations
- Estimating the quality of the network ionospheric delays
- Improvements of the atmospheric interpolation
- More satellites in view

In this research it was demonstrated that the instantaneous ambiguity resolution was at most about 90%, for a user's processing within a permanent network with a typical inter-station distance of about 100 km. This success rate is expected to improve when a denser network is used. It is possible that a success rate of close to 100% can be achieved when the network station has a spacing which is half as large, e.g. at most 50 km. Using such a dense permanent network it is also believed that the a priori ionospheric standard deviation a user applies in his ionosphere-weighted processing is allowed to be lower than the value of 1-2 cm typically used, since the residual ionospheric delays between the virtual and user stations will probably be smaller. In this context one should realize that the coming years the general ionospheric activity is expected to decrease (solar minimum, excepted in 2007), which has a favorable effect on the performance of ambiguity resolution.

The performance of the user's processing might also improve when the ionospheric standard deviation (which a user needs to apply the ionosphere-weighted model)

is assessed in an empirical way by the control center of the permanent network and distributed to the users. In this way it may account for the actual ionospheric conditions. In case of real-time applications this assessment should be done from data of a sufficient long time span before the actual time of the measurements (e.g. one hour).

Another improvement may stem from the atmospheric interpolation algorithm. In this research for both the ionospheric and tropospheric interpolation the same interpolation function was used. This could probably be improved because of the different characteristics of the ionospheric and tropospheric delays.

At last, a future Galileo system might benefit the procedure. With an integration of GPS with Galileo, much more satellites can be tracked, which has a very beneficial effect on ambiguity resolution. This effect will be much more pronounced than the contribution of a third GPS frequency.

Improvements in mathematical modelling

Improvements may also be expected from a more refined mathematical model:

- Research to a better stochastic model, not only for the *real* GPS observables, but also for the *virtual* observables
- Improved modelling of tropospheric delays

In this research for the GPS phase and code observations still a very simple diagonal *stochastic model* was used. Although it seems to perform reasonably well in the computations, it is expected that, among others, ambiguity resolution may benefit from a more refined model. Although research has been initiated, more investigations to the stochastic properties of the GPS observables are necessary. More research is also necessary to the stochastic model of the virtual (VRS) phase and code observations. Like the real observables, in this research a simple diagonal vc-matrix is used, which seems to work satisfactorily. However, since the observables are artificial, as they are generated from stochastic network estimates, it is not yet clear how this propagates into the stochastic properties of the VRS observations.

To improve the precision of the *height* component of the desired receiver position, a better treatment of the *tropospheric delays* is required. In Chap. 6 it was discussed that when the geometry-free model is used for the network processing (with the receiver-satellite ranges fixed, since these are known a priori), the tropospheric delays are treated in a similar manner as the ionospheric delays in the ionosphere-weighted model. In that case, it is relatively easy to incorporate temporal predictions for the slant tropospheric delays in the network processing, which may improve the network ambiguity resolution. Also in the user's processing a stochastic treatment of the tropospheric (zenith) delays may be more beneficial to account for residual delays than the current approach of considering them as completely unknown parameters.

Bibliography

[Baarda, 1968] Baarda, W. (1968). *A testing procedure for use in geodetic networks.* Netherlands Geodetic Commission, Publications on Geodesy, New Series, 2(5).

[Baarda, 1973] Baarda, W. (1973). *S-transformations and criterion matrices.* Netherlands Geodetic Commission, Publications on Geodesy, New Series, 5(1).

[Barnes, 2000] Barnes, J.B. (2000). *Real time kinematic GPS and multipath: Characterisation and improved least squares modelling.* PhD dissertation, University of Newcastle upon Tyne.

[Bassiri and Hajj, 1993] Bassiri, S. and G.A. Hajj (1993). Higher-order ionospheric effects on the Global Positioning System observables and means of modelling them. *Manuscripta Geodaetica 18*, 280-289.

[Bent and Llewellyn, 1973] Bent, R.B. and S.K. Llewellyn (1973). *Documentation and description of the Bent Ionospheric Model.* Space & Missiles Organization, Los Angeles, USA.

[Beutler et al., 1988] Beutler, G., I. Bauersima, W. Gurtner, M. Rothacher, T. Schildknecht and A. Geiger (1988). *Atmospheric refraction and other important biases in GPS carrier phase observations*, GPS-papers presented by the Astronomical Institute of the University of Berne in the year 1987.

[Blewitt, 1993] Blewitt, G. (1993). Advances in Global Positioning System technology for geodynamics investigations: 1978-1992. *Contributions of Space Geodesy to Geodynamics Technology*, AGU Geodynamics Series, vol. 25, 195-213.

[Bock et al., 1986] Bock, Y., S.A. Gourevitch, C.C. Counselman III, R.W. King, and R.I. Abbot (1986). Interferometric analysis of GPS phase observations. *Manuscripta Geodaetica 11*, 282-288.

[Bock et al., 1997] Bock, Y., S. Wdowinski, P. Fang, J. Zhang, S. Williams, H. Johnson, J. Behr, J. Genrich, J. Dean, M. van Domselaar, D. Agnew, F. Wyatt, K. Stark, B. Oral, K. Hudnut, R. King, T. Herring, S. Dinardo, W.

Young, D. Jackson, and W. Gurtner (1997). Southern California Permanent GPS Geodetic Array: Continuous measurements of crustal deformation between the 1992 Landers and 1994 Northridge earthquakes. *Journal of Geophysical Research 102*, 18013-18033.

[Bock et al., 2000] Bock, Y., R.M. Nikolaidis, P.J. de Jonge, and M. Bevis (2000). Instantaneous geodetic positioning at medium distances with the Global Positioning System. *Journal of Geophysical Research 105 (B12)*, 28223-28253.

[Bona, 2000a] Bona, P. (2000). Accuracy of GPS phase and code observations in practice. *Acta Geod. Geoph. Hung. 35(4)*, 433-451.

[Bona, 2000b] Bona, P. (2000). Precision, cross correlation, and time correlation of GPS phase and code observations. *GPS Solutions 4(2)*, 3-13.

[Borre and Tiberius, 2000] Borre, K. and C.C.J.M. Tiberius (2000). Time series analysis of GPS observables. *Proceedings of the 13th International Technical Meeting of the Satellite Division of the Institute of Navigation, ION GPS-2000*, Salt Lake City, USA, September 19-22, 1885-1894.

[Brunner and Gu, 1991] Brunner, F.K. and M. Gu (1991). An improved model for the dual frequency ionospheric correction of GPS observations. *Manuscripta Geodaetica 16*, 205-214.

[Chen, 2000] Chen, H.-Y. (2000). An instantaneous ambiguity resolution procedure suitable for medium-scale GPS reference station networks. *Proceedings of the 13th International Technical Meeting of the Satellite Division of the Institute of Navigation, ION GPS-2000*, Salt Lake City, USA, September 19-22, 1061-1070.

[Chen et al., 2000] Chen, X., S. Han, C. Rizos, and P.C. Goh (2000). Improving real-time positioning efficiency using the Singapore Integrated Multiple Reference Station Network (SIMRSN). *Proceedings of the 13th International Technical Meeting of the Satellite Division of the Institute of Navigation, ION GPS-2000*, Salt Lake City, USA, September 19-22, 1061-1070.

[Christensen, 1991] Christensen, R. (1991). *Linear models for multivariate, time series, and spatial data.* Springer-Verlag.

[CODE, 2002] Center for Orbit Determination in Europe (CODE) (2002). *http://www.aiub.unibe.ch/ionosphere.html*

[Colombo et al., 1999] Colombo, O.L., M. Hernández-Pajares, J.M. Juan, J. Sanz, and J. Talaya (1999). Resolving carrier-phase ambiguities on the fly, at more than 100 km from the nearest reference site, with the help of ionospheric tomography. *Proceedings of the 12th International Technical Meeting of the Satellite Division of the Institute of Navigation, ION GPS-1999*, Nashville, USA, September 14-17, 1635-1642.

[Dai et al., 2001a] Dai, L., J. Wang, C. Rizos, and S. Han (2001). Real-time carrier phase ambiguity resolution for GPS/GLONASS reference station networks. *Proceedings Int. Symp. on Kinematic Systems in Geodesy, Geomatics and Navigation (KIS2001)*, Banff, Canada, June 5-8, 475-481.

[Dai et al., 2001b] Dai, L., S. Han, J. Wang, and C. Rizos. A study of GPS/GLONASS multiple reference station techniques for precise real-time carrier phase-based positioning. *Proceedings of the 14th International Technical Meeting of the Satellite Division of the Institute of Navigation, ION GPS-2001*, Salt Lake City, USA, September 11-14, 392-403.

[De Jong, 1997] Jong, C.D. de (1997). *Principles and applications of permanent GPS arrays*, PhD dissertation, Delft University Press.

[De Jong, 1998] Jong, C.D. de (1998). A unified approach to real-time integrity monitoring of single- and dual-frequency GPS and GLONASS observations. *Acta Geod. Geoph. Hung. 33*, 247-257.

[De Jonge, 1998] Jonge, P.J. de (1998). *A processing strategy for the application of the GPS in networks.* PhD dissertation, Netherlands Geodetic Commission, Publications on Geodesy, 46, 225 p.

[De Jonge and Tiberius, 1996] Jonge, P.J. de, and C.C.J.M. Tiberius (1996). *The LAMBDA method for integer ambiguity estimation: implementation aspects.* LGR-series, no. 12, Delft Geodetic Computing Centre.

[Delikaraoglou, 1989] Delikaraoglou, D. (1989). On the stochastic modelling of GPS ionospheric delays. *Manuscripta Geodaetica 14*, 100-109.

[Eissfeller et al., 2001] Eissfeller, B., C. Tiberius, T. Pany, R. Biberger, T. Schueler, and G. Heinrichs (2001). Real-time kinematic in the light of GPS modernization and Galileo. *Proceedings of the 14th International Technical Meeting of the Satellite Division of the Institute of Navigation, ION GPS-2001*, Salt Lake City, USA, September 11-14, 650-682.

[Euler and Goad, 1991] Euler, H.-J., and C.C. Goad (1991). On optimal filtering of GPS dual-frequency observations without using orbit information. *Bulletin Géodésique 65*, 130-143.

[Euler et al., 2001] Euler, H.-J., C.R. Keenan, B.E. Zebhauser, and G. Wübbena (2001). Study of a simplified approach in utilizing information from permanent reference station arrays. *Proceedings of the 14th International Technical Meeting of the Satellite Division of the Institute of Navigation, ION GPS-2001*, Salt Lake City, USA, September 11-14, 379-391.

[Fotopoulos and Cannon, 2001] Fotopoulos, G., and M.E. Cannon (2001). An overview of multi-reference station methods for cm-level positioning. *GPS Solutions 4(3)*, 1-10.

[Gao et al., 1997] Gao, Y., Z. Li and J.F. McLellan (1997). Carrier phase based regional area differential GPS for decimeter-level positioning and navigation, *Proceedings of the 10th International Technical Meeting of the Satellite Division of the Institute of Navigation, ION GPS-1997*, Kansas City, USA, September 16-19, 1305-1313.

[Georgiadou and Kleusberg, 1988] Georgiadou, Y. and A. Kleusberg (1988). On the effect of ionospheric delay on geodetic relative positioning. *Manuscripta Geodaetica 13*, 1-8.

[Georgiadou, 1994] Georgiadou, Y. (1994). *Modelling the ionosphere for an active control network of GPS stations*. LGR-series, no. 7, Delft Geodetic Computing Centre.

[Gerdan, 1995] Gerdan, G.P. (1995). A comparison of weighting double-difference pseudorange measurements. *Trans. Tasman Surveyor 1(1)*, 60-66.

[Giraud and Petit, 1978] Giraud, A. and M. Petit (1978). *Ionospheric techniques and phenomena*, Geophysics and astrophysics monographs, D. Reidel Publishing Company.

[Goad, 1990] Goad, C.C. (1990). Optimal filtering of pseudoranges and phases from single-frequency GPS receivers. *Navigation, Journal of the Institute of Navigation 37(3)*, 249-262.

[Goad and Yang, 1994] Goad, C.C., and M. Yang (1994). On automatic precision airborne GPS positioning. *Proceedings of the International Symposium on Kimematic Systems in Geodesy, Geomatics and Navigation, KIS94*, Banff, Canada, August 30 - September 2, 131-138.

[Goldberger, 1962] Goldberger, A.S. (1962). Best linear unbiased prediction in the generalized linear regression model. *Journal of the American Statistical Association 57*, 369-375.

[Hall et al., 1996] Hall, M.P.M., L.W. Barclay, and M.T. Hewitt (1996). *Propagation of radio waves*, The Institute of Electrical Engineers, London.

[Hartmann and Leitinger, 1984] Hartmann, G.K., and R. Leitinger (1984). Range errors due to ionospheric and tropospheric effects for signal frequencies above 100 MHz. *Bulletin Géodésique 58*, 109-136.

[Herring et al., 1990] Herring, T.A., J.L. Davis, and I.I. Shapiro (1990). Geodesy by radio interferometry: The application of Kalman filtering to the analysis of Very Long Baseline Interferometry data. *Journal of Geophysical Research 95 (B8)*, 12561-12581.

[Hofmann-Wellenhof et al., 2001] Hofmann-Wellenhof, B., H. Lichtenegger, and J. Collins (2001). *Global Positioning System: Theory and practice*, 5th revised edition, Springer-Verlag.

[Jaeggi et al., 2001] Jaeggi, A., G. Beutler, and U. Hugentobler (2001). Using double difference information from network solutions to generate observations for a virtual GPS reference receiver. *Proceeding of the IAG Scientific Assembly: Vistas for Geodesy in the New Millennium*, Budapest, Hungary, September 2-7, CDROM.

[Jarlemark and Emardson, 1998] Jarlemark, P.O.J. and T.R. Emardson (1998). Strategies for spatial and temporal extrapolation and interpolation of wet delay. *Journal of Geodesy 72*, 350-355.

[Jin, 1996] Jin, X.X. (1996). *Theory of carrier adjusted DGPS positioning approach and some experimental results*, Delft University Press, 163 pp.

[Jonkman, 1998a] Jonkman, N.F. (1998). Integer GPS ambiguity estimation without the receiver-satellite geometry. Publications of the Delft Geodetic Computing Centre, *LGR Series 18*.

[Jonkman, 1998b] Jonkman, N.F. (1998). The geometry-free approach to integer GPS ambiguity estimation, *Proceedings of the 11th International Technical Meeting of the Satellite Division of the Institute of Navigation, ION GPS-1998*, Nashville, USA, September 15-18, 369-379.

[Joosten, 2000] Joosten, P. (2000). Simulating the distribution of the GPS ambiguities. *Phys. Chem. Earth (A), 25(9-11)*, 687-692.

[Kleijer, 2001] Kleijer, F. (2001). *Troposphere delay modeling for space geodetic measurements.* Report to Rijkswaterstaat, 47 pp.

[Kleijer, 2002] Kleijer, F. (2002). *Parameterization of the tropospheric delay in GPS observation models.* Report to Rijkswaterstaat, 44 pp.

[Klobuchar, 1987] Klobuchar, J.A. (1987). Ionospheric time-delay algorithm for single-frequency GPS users, *IEEE Transactions on Aerospace and Electric Systems, AES-23(3)*, 325-331.

[Klobuchar, 1991] Klobuchar, J.A. (1991). Ionospheric effects on GPS, *GPS World, 4*, 48-51.

[Klobuchar and Doherty, 1998] Klobuchar, J.A. and P.H. Doherty (1998). A look ahead: Expected ionospheric effects on GPS in 2000. *GPS Solutions 2(1)*, 42-48.

[Koch, 1999] Koch, K.-R. (1999). *Parameter estimation and hypothesis testing in linear models.* 2nd edition, Springer-Verlag.

[Kunches, 2000] Kunches, J.M. (2000). In the teeth of cycle 23. *Proceedings of the 13th International Technical Meeting of the Satellite Division of the Institute of Navigation, ION GPS-2000*, Salt Lake City, USA, September 19-22, 626-633.

[Langley, 1998] Langley, R.B. (1998). Propagation of the GPS signals. Chapter 3 of *GPS for geodesy*, P.J.G. Teunissen and A. Kleusberg (eds.), 2nd edition, Springer-Verlag, Berlin Heidelberg.

[Liu, 2001] Liu, G.C. (2001). *Ionosphere-weighted Global Positioning System carrier phase ambiguity resolution*. MSc. thesis, Department of Geomatics Engineering, University of Calgary.

[Loomis et al., 1989] Loomis, P., G. Kremer, and J. Reynolds (1989). Correction algorithms for differential GPS reference stations. *Navigation, Journal of the Institute of Navigation 36(2)*, 179-193.

[Misra and Enge, 2001] Misra, P., and P. Enge (2001). *Global Positioning System. Signals, measurements and performance*. Ganga-Jamuna Press, Lincoln.

[Moritz, 1976] Moritz, H. (1976). Least squares collocation. *Manuscripta Geodaetica, 1*, pp. 1-40.

[Namie et al., 2001] Namie, H., N. Hagiwara, H. Kim, N. Nitta, Y. Shibahara, T. Imakiire, A. Yasuda (2001). RTK-GPS positioning in Japan by virtual reference station (VRS) system with GPS-based control stations, *Proceedings of the 14th International Technical Meeting of the Satellite Division of the Institute of Navigation, ION GPS-2001*, Salt Lake City, USA, September 11-14, 353-361.

[Neilan et al., 2000] Neilan, R.E., A. Moore, T. Springer, J. Kouba, J. Ray and C. Reigber (2000). International GPS Service 2000: Life without SA. *Proceedings of the 13th International Technical Meeting of the Satellite Division of the Institute of Navigation, ION GPS-2000*, Salt Lake City, USA, September 19-22, 438-446.

[Niell, 1996] Niell, A.E. (1996). Global mapping functions for the atmosphere delay at radio wavelengths. *Journal of Geophysical Research 101 (B)*, pp. 3227-3246.

[NOAA, 2001] National Oceanic and Atmospheric Administration, Space Environment Center (2001). *www.sec.noaa.gov*.

[Odijk, 1999] Odijk, D. (1999). Stochastic modelling of the ionosphere for fast GPS ambiguity resolution. *Geodesy beyond 2000. The challenges of the first decade, IAG General Assembly, Vol. 121*, Birmingham, UK, July 19-30, 387-392.

[Odijk, 2000a] Odijk, D. (2000). Improving ambiguity resolution by applying ionosphere corrections from a permanent GPS array. *Earth Planets Space, 52(10)*, 675-680.

[Odijk, 2000b] Odijk, D. (2000). Weighting ionospheric corrections to improve fast GPS positioning over medium distances. *Proceedings of the 13th International Technical Meeting of the Satellite Division of the Institute of Navigation, ION GPS-2000*, Salt Lake City, USA, September 19-22, 1113-1123.

[Odijk et al., 2000] Odijk, D., H. van der Marel, and I. Song (2000). Precise GPS positioning by applying ionospheric corrections from an active control network. *GPS Solutions, 3(3)*, 49-57.

[Odijk, 2001] Odijk, D. (2001). Instantaneous GPS positioning under geomagnetic storm conditions. *GPS Solutions 5(2)*, 29-42.

[Raquet, 1998] Raquet, J. (1998). *Development of a method for kinematic GPS carrier phase ambiguity resolution using multiple reference stations.* Ph.D. thesis, University of Calgary.

[Rao, 1973] Rao, C.R. (1973). *Linear statistical inference and its applications,* 2nd edition, Wiley.

[Rizos et al., 1998] Rizos, C., S. Han, and H.-Y. Chen (1998). Carrier phase-based, medium-range, GPS rapid static positioning in support of geodetic applications: Algorithms and experimental results. *Proceedings Spatial Information Science and Technology (SIST'98)*, Wuhan, P.R. China, December 13-16, 7-16.

[Rothacher and Mervart, 1996] Rothacher, M., and L. Mervart (eds.) (1996). *Bernese GPS Software, Version 4.0.* Astronomical Institute, University of Berne.

[Saastamoinen, 1972] Saastamoinen, J. (1972). Atmospheric correction for the troposphere and stratosphere in radio ranging of satellites. *The use of artificial satellites for geodesy, Geophys. Monogr. Ser., 15*, 247-251.

[Schaer, 1994] Schaer, S. (1994). *Stochastische Ionosphärenmodellierung beim 'Rapid Static Positioning' mit GPS.* Astronomical Institute, University of Berne.

[Schaer et al., 1998] Schaer, S., G. Beutler, and M. Rothacher (1998). Mapping and predicting the ionosphere. *Proceedings IGS AC Workshop*, Darmstadt, Germany, February 9-11.

[Schaer et al., 1999] Schaer, S., G. Beutler, M. Rothacher, E. Brockmann, A. Wiget, and U. Wild (1999). The impact of the atmosphere and other systematic errors on permanent GPS networks. *Geodesy beyond 2000. The challenges of the first decade, IAG General Assembly, Vol. 121*, Birmingham, UK, July 19-30, 373-380.

[Schaffrin and Bock, 1988] Schaffrin, B., and Y. Bock (1988). A unified scheme for processing GPS dual-band phase observations. *Bulletin Géodésique 62*, 142-160.

[Seeber, 1993] Seeber, G. (1993). *Satellite Geodesy: Foundations, methods and applications*, Walter de Gruyter.

[Shaw et al., 2000] Shaw, M., K. Sandhoo, and D. Turner (2000). Modernization of the Global Positioning System. *GPS World*, Sept. 2000, 36-44.

[Spoelstra, 1996] Spoelstra, T.A.Th. (1996). A climatology of quiet/disturbed ionospheric conditions derived from 22 years of Westerbork interferometer observations. *Journal of Atmospheric and Terrestrial Physics 58(11)*, 1229-1258.

[Springer and Hugentobler, 2001] Springer, T.A., and U. Hugentobler (2001). IGS ultra rapid products for (near-) real-time applications. *Physics and Chemistry of the Earth 26(6-8)*, 623-628.

[Stewart, 1997] Stewart, P. (1997). *The reduction of differential ionospheric delay for GPS carrier phase ambiguity resolution.* Technical Report No. 185, Department of Geodesy and Geomatics Engineering, University of New Brunswick.

[Teunissen, 1984] Teunissen, P.J.G. (1984). *Generalized inverses, adjustment, the datum problem and S-transformations.* Lecture notes International School of Geodesy. Erice, Italy, April 25 - May 10.

[Teunissen, 1993] Teunissen, P.J.G. (1993). *Least-squares estimation of the integer GPS ambiguities.* Invited lecture, Sect. IV Theory and Methodology, IAG General Meeting, Beijing, August.

[Teunissen, 1996] Teunissen, P.J.G. (1996). An analytical study of ambiguity decorrelation using dual-frequency code and carrier phase. *Journal of Geodesy 70*, 515-528.

[Teunissen, 1997a] Teunissen, P.J.G. (1997). A canonical theory for short GPS baselines. Part I: The baseline precision. *Journal of Geodesy 71*, 320-336.

[Teunissen, 1997b] Teunissen, P.J.G. (1997). A canonical theory for short GPS baselines. Part IV: Precision versus reliability. *Journal of Geodesy 71*, 513-525.

[Teunissen, 1997c] Teunissen, P.J.G. (1997). Some remarks on GPS ambiguity resolution. *Artificial Satellites 32(3)*, 119-130.

[Teunissen, 1997d] Teunissen, P.J.G. (1997). The geometry-free GPS ambiguity search space with a weighted ionosphere. *Journal of Geodesy 71*, 370-383.

[Teunissen and Odijk, 1997] Teunissen, P.J.G., and D. Odijk (1997). Ambiguity Dilution Of Precision: Definition, properties and application. *Proceedings of the 10th International Technical Meeting of the Satellite Division of the Institute of Navigation, ION GPS-1997*, Kansas City, USA, September 16-19, 891-899.

[Teunissen et al., 1997] Teunissen, P.J.G., P.J. de Jonge, D. Odijk, and C.C.J.M. Tiberius (1997). Fast ambiguity resolution in network mode. *Proceedings IAG Scientific Assembly*, Rio de Janeiro, Brazil, September 3-9, 313-318.

[Teunissen, 1998a] Teunissen, P.J.G. (1998). A class of unbiased integer GPS ambiguity estimators. *Artificial Satellites 33(1)*, 4-10.

[Teunissen, 1998b] Teunissen, P.J.G. (1998). Success probability of integer GPS ambiguity rounding and bootstrapping. *Journal of Geodesy 72*, 606-612.

[Teunissen, 1998c] Teunissen, P.J.G. (1998). On the integer normal distribution of the GPS ambiguities. *Artificial Satellites 33(2)*, 49-64.

[Teunissen, 1998d] Teunissen, P.J.G. (1998). The ionosphere-weighted GPS baseline precision in canonical form. *Journal of Geodesy 72*, 107-117.

[Teunissen and Kleusberg, 1998] Teunissen, P.J.G. and A.Kleusberg (eds.) (1998). *GPS for geodesy*, 2nd edition, Springer-Verlag.

[Teunissen, 1999a] Teunissen, P.J.G. (1999). An optimality property of the integer least-squares estimator. *Journal of Geodesy 73*, 587-593.

[Teunissen, 1999b] Teunissen, P.J.G. (1999). The probability distribution of the GPS baseline for a class of integer ambiguity estimators. *Journal of Geodesy 73*, 275-284.

[Teunissen, 2000a] Teunissen, P.J.G. (2000). *Adjustment theory; an introduction.* Delft University Press.

[Teunissen, 2000b] Teunissen, P.J.G. (2000). ADOP based upperbounds for the bootstrapped and the least-squares ambiguity success rates. *Artificial Satellites 35(4)*, 171-179.

[Teunissen, 2000c] Teunissen, P.J.G. (2000). *Testing theory; an introduction.* Delft University Press.

[Teunissen et al., 2000] Teunissen, P.J.G., P. Joosten and C.C.J.M. Tiberius (2000). Bias robustness of GPS ambiguity resolution. *Proceedings of the 13th International Technical Meeting of the Satellite Division of the Institute of Navigation, ION GPS-2000*, Salt Lake City, USA, September 19-22, 104-112.

[Teunissen, 2001a] Teunissen, P.J.G. (2001). GNSS ambiguity bootstrapping: Theory and applications. *Proceedings Int. Symp. on Kinematic Systems in Geodesy, Geomatics and Navigation (KIS2001)*, Banff, Canada, June 5-8, 246-254.

[Teunissen, 2001b] Teunissen, P.J.G. (2001). Statistical GNSS carrier phase ambiguity resolution: A review. *Proceedings of the 2001 IEEE Workshop on Statistical Signal Processing*, Singapore, August 6-8, 4-12.

[Teunissen, 2001c] Teunissen, P.J.G. (2001). Integer estimation in the presence of biases. *Journal of Geodesy 75*, 399-407.

[Teunissen, 2001d] Teunissen, P.J.G. (2001). *Dynamic data processing; recursive least-squares.* Delft University Press.

[Teunissen, 2002] Teunissen, P.J.G. (2002). The parameter distributions of the integer GPS model. *Journal of Geodesy 76*, 41-48.

[Teunissen and Odijk, 2002] Teunissen, P.J.G. and D. Odijk (2002). Rank defect integer estimation and phase-only modernized GPS ambiguity resolution. Accepted for publication in *Journal of Geodesy*.

[Tiberius, 1998] Tiberius, C.C.J.M. (1998). *Recursive data processing for kinematic GPS surveying.* PhD dissertation, Netherlands Geodetic Commission, Publications on Geodesy, 45, 248 p.

[Tiberius, 1999] Tiberius, C.C.J.M. (1999). The GPS data weight matrix: What are the issues? *Proceedings of the National Technical Meeting and the 19th Biennal Guidance Test Symposium*, San Diego, USA, January 25-27, 219-227.

[Tiberius and Borre, 1999] Tiberius, C.C.J.M., and K. Borre (1999). Probability distribution of GPS code and phase data. *Zeitschrift für Vermessungswesen 124(8)*, 264-273.

[Van der Marel, 1993] Marel, H. van der (1993). *Modelling of GPS ionospheric delays for geodetic applications*. URSI commissie G meeting, Eindhoven, March 12, 1993.

[Van der Marel, 1998] Marel, H. van der (1998). Virtual GPS reference stations in the Netherlands, *Proceedings of the 11th International Technical Meeting of the Satellite Division of the Institute of Navigation, ION GPS-1998*, Nashville, USA, September 15-18, 49-58.

[Van der Marel, 2000] Marel, H. van der (2000). *Virtual Reference Station software, Test report October 2000*. Internal report, Delft University of Technology.

[Van Velthoven, 1990] Velthoven, P.F.J. van (1990). *Medium scale irregularities in the ionospheric electron content*, PhD thesis, Technische Universiteit Eindhoven.

[Varner, 2000] Varner, C.C. (2000). *DGPS carrier phase networks and partial derivative algorithms.* Ph.D. thesis, University of Calgary.

[Vollath et al., 2000] Vollath, U., A. Buecherl, H. Landau, C. Pagels, and B. Wagner (2000). Multi-base RTK positioning using virtual reference stations. *Proceedings of the 13th International Technical Meeting of the Satellite Division of the Institute of Navigation, ION GPS-2000*, Salt Lake City, USA, September 19-22, 123-131.

[Wanninger and Jahn, 1991] Wanninger, L. and C.H. Jahn (1991). Effects of severe ionospheric conditions on GPS data processing. Poster paper presented at IAG Symposium G-2, *IUGG XX General Assembly*, August 16, 1991.

[Wanninger, 1995] Wanninger, L. (1995). Improved ambiguity resolution by regional differential modelling of the ionosphere. *Proceedings of the 8th International Technical Meeting of the Satellite Division of the Institute of Navigation, ION GPS-1995*, Palm Springs, USA, September 12-15, 55-62.

[Wanninger, 1999] Wanninger, L. (1999). Performance of virtual reference stations in active geodetic GPS networks under solar maximum conditions. *Proceedings of the 12th International Technical Meeting of the Satellite Division of the Institute of Navigation, ION GPS-1999*, Nashville, USA, September 14-17, 1419-1427.

[Webster and Kleusberg, 1992] Webster, I., and A. Kleusberg (1992). Regional modelling of the ionosphere for single frequency users of the Global Positioning System. *Proceedings 6th International Geodetic Symposium on Satellite Positioning*, Ohio, USA.

[Wübbena and Willgalis, 2001] Wübbena, G., and S. Willgalis (2001). State-space approach for precise real-time positioning in GPS reference networks. *Proceedings Int. Symp. on Kinematic Systems in Geodesy, Geomatics and Navigation (KIS2001)*, Banff, Canada, June 5-8, 72-79.

[Zumberge et al., 1997] Zumberge, J.F., M.B. Heflin, D.C. Jefferson, M.M. Watkins, and F.H. Webb (1997). Precise point positioning for the efficient and robust analysis of GPS data from large networks. *Journal of Geophysical Research 102*, 5005-5017.

Appendix A

The Kronecker product

If A is an $m \times n$ matrix and B is a $p \times q$ matrix, then their *Kronecker product* $A \otimes B$ is defined as the following $mp \times nq$ matrix, see [Rao, 1973]:

$$A \otimes B = \begin{bmatrix} a_{11}B & \dots & a_{1n}B \\ \vdots & \ddots & \vdots \\ a_{m1}B & \dots & a_{mn}B \end{bmatrix} \tag{A.1}$$

Some of its properties are (assuming that all matrices involved have appropriate dimensions):

$$\begin{array}{lcl} (A+C) \otimes B & = & A \otimes B + C \otimes B \\ A \otimes (B \otimes C) & = & (A \otimes B) \otimes C \\ (A \otimes B)(C \otimes D) & = & (AC) \otimes (BD) \\ (A \otimes B)^T & = & A^T \otimes B^T \\ \det\{A \otimes B\} & = & (\det\{A\})^m (\det\{B\})^n \\ (A \otimes B)^{-1} & = & A^{-1} \otimes B^{-1} \end{array} \tag{A.2}$$

In the last but one equation A and B are square $m \times m$ and $n \times n$ matrices respectively. In the last equation both A and B are assumed invertible.

Appendix B

Undifferenced - double-differenced models

In this appendix the *equivalence* of the undifferened, single-differenced and double-differenced models is shown, by means of volume-preserving transformations. The proofs are given here for just the *geometry-based model*; for the *geometry-free model* the proofs can be given along similar lines. Starting point is the model of *undifferenced* observation equations. Table B.1 summarizes the elements of the model, in which it is assumed that all observations are simultaneously tracked from m satellites, at n receivers, on j frequencies, during k observation epochs.

Table B.1. Undifferenced model

variable	elements
$y^{gb}(i)$	$\begin{bmatrix} \Phi^{gb}(i) \\ P^{gb}(i) \end{bmatrix} = \begin{bmatrix} \left[\Phi_1^{gb}(i)^T \ \dots \ \Phi_j^{gb}(i)^T\right]^T \\ \left[P_1^{gb}(i)^T \ \dots \ P_j^{gb}(i)^T\right]^T \end{bmatrix}$, where $\begin{cases} \Phi_j^{gb}(i) = \left[\left(\Delta\phi_{1,j}^1(i) \dots \Delta\phi_{1,j}^m(i)\right) \ \dots \ \left(\Delta\phi_{n,j}^1(i) \dots \Delta\phi_{n,j}^m(i)\right)\right]^T \\ P_j^{gb}(i) = \left[\left(\Delta p_{1,j}^1(i) \dots \Delta p_{1,j}^m(i)\right) \ \dots \ \left(\Delta p_{n,j}^1(i) \dots \Delta p_{n,j}^m(i)\right)\right]^T \end{cases}$
$Q_{y(i)}^{gb}$	$\begin{bmatrix} Q_\phi & \\ & Q_p \end{bmatrix} \otimes Q(i)$, where $Q(i) = \text{blkdiag}\left[Q_1(i), \ \dots, \ Q_n(i)\right]$
$A_I^{gb}(i)$	$\begin{bmatrix} \begin{pmatrix} e_j \\ e_j \end{pmatrix} \otimes \mathcal{A}(i) & \begin{pmatrix} \Lambda \\ 0 \end{pmatrix} \otimes \mathcal{C} \end{bmatrix}$ where $\mathcal{A}(i) = \begin{bmatrix} 0_{m \times 3(n-1)} \\ \text{blkdiag}\left[G_2(i), \ \dots, \ G_n(i)\right] \end{bmatrix}$, $\mathcal{C} = \left[C_n \otimes C_m\right]$, $C_l = \begin{bmatrix} 0_{1 \times (l-1)} \\ I_{l-1} \end{bmatrix}$
$A_{II}^{gb}(i)$	$\left[\begin{pmatrix} I_j & \\ & I_j \end{pmatrix} \otimes \mathcal{D}\right]$, where $\mathcal{D} = \left[C_n \otimes e_m, \ -e_n \otimes I_m\right]$
x_I^{gb}	$\left[g^T \ \left(a_1^T \ \dots \ a_j^T\right)\right]^T$, where $\begin{cases} g = \left[\Delta r_{12}^T \ \dots \ \Delta r_{1n}^T\right]^T \\ a_j = \left[\left(M_{12,j}^{12} \ \dots \ M_{12,j}^{1m}\right) \ \dots \ \left(M_{1n,j}^{12} \ \dots \ M_{1n,j}^{1m}\right)\right]^T \end{cases}$
$x_{II}^{gb}(i)$	$\left[\left(\alpha_1^T(i) \ \dots \ \alpha_j^T(i)\right) \ \left(\beta_1^T(i) \ \dots \ \beta_j^T(i)\right)\right]^T$, where $\begin{cases} \alpha_j(i) = \left[(c\delta t_{12,j}(i) \ \dots \ c\delta t_{1n,j}(i)) \ \left(c\delta t_{1,j}^1(i) \ \dots \ c\delta t_{1,j}^m(i)\right)\right]^T \\ \beta_j(i) = \left[(cdt_{12,j}(i) \ \dots \ cdt_{1n,j}(i)) \ \left(cdt_{1,j}^1(i) \ \dots \ cdt_{1,j}^m(i)\right)\right]^T \end{cases}$

To obtain single-differenced observables between receivers, the model of undifferenced observables is transformed using the following full-rank transformation matrix:

$$\Upsilon_1^{gb} = \begin{bmatrix} I_j & \\ & I_j \end{bmatrix} \otimes \left[E_n^T \otimes I_m\right], \text{ where } E_n^T = \underbrace{\begin{bmatrix} c_n^T \\ D_n^T \end{bmatrix}}_{n \times n}$$

The $(n-1) \times n$ matrix $D_n^T = [-e_{n-1},\ I_{n-1}]$ is known as the *difference operator for receivers*, and the $n \times 1$ vector $c_n = (1,\ 0,\ \ldots,\ 0)^T$. The transformed model elements are given in Table B.2.

Table B.2. Transformed undifferenced model

variable	elements
$\tilde{y}^{gb}(i)$	$\Upsilon_1^{gb} y^{gb}(i) = \begin{bmatrix} \left[\tilde{\Phi}_1^{gb}(i)^T \ \ldots\ \tilde{\Phi}_j^{gb}(i)^T\right]^T \\ \left[\tilde{P}_1^{gb}(i)^T \ \ldots\ \tilde{P}_j^{gb}(i)^T\right]^T \end{bmatrix}$, where $\tilde{\Phi}_j^{gb}(i) = \begin{bmatrix} \left(\Delta\phi_{1,j}^1(i) \ldots \Delta\phi_{1,j}^m(i)\right)^T \\ \left(D_n^T \otimes I_m\right) \Phi_j^{gb}(i) \end{bmatrix}$, $\tilde{P}_j^{gb}(i) = \begin{bmatrix} \left(\Delta p_{1,j}^1(i) \ldots \Delta p_{1,j}^m(i)\right)^T \\ \left(D_n^T \otimes I_m\right) P_j^{gb}(i) \end{bmatrix}$
$Q_{\tilde{y}(i)}^{gb}$	$\Upsilon_1^{gb} Q_{y(i)}^{gb} \Upsilon_1^{gbT} = \begin{bmatrix} Q_\phi & \\ & Q_p \end{bmatrix} \otimes \tilde{Q}(i)$, where $\tilde{Q}(i) = \begin{bmatrix} Q_1(i) & \left(-e_{n-1}^T \otimes I_m\right) Q_1(i) \\ \left(-e_{n-1} \otimes I_m\right) Q_1(i) & \left(D_n^T \otimes I_m\right) Q(i) \left(D_n \otimes I_m\right) \end{bmatrix}$
$\tilde{A}_I^{gb}(i)$	$\Upsilon_1^{gb} A_I^{gb}(i) = \left[\begin{pmatrix} e_j \\ e_j \end{pmatrix} \otimes \mathcal{A}(i) \quad \begin{pmatrix} \Lambda \\ 0 \end{pmatrix} \otimes \mathcal{C} \right]$, since $\left[E_n^T \otimes I_m\right] \mathcal{A}(i) = \mathcal{A}(i)$, $\left[E_n^T \otimes I_m\right] \mathcal{C} = \left[E_n^T C_n \otimes C_m\right] = \mathcal{C}$
$\tilde{A}_{II}^{gb}(i)$	$\Upsilon_1^{gb} A_{II}^{gb}(i) = \left[\begin{pmatrix} I_j & \\ & I_j \end{pmatrix} \otimes \tilde{\mathcal{D}} \right]$, where $\tilde{\mathcal{D}} = [C_n \otimes e_m,\ -c_n \otimes I_m]$, since $E_n^T C_n = C_n$ and $E_n^T e_n = c_n$
x_I^{gb}	$\left[g^T \left(a_1^T \ \ldots\ a_j^T\right)\right]^T$
$x_{II}^{gb}(i)$	$\left[\left(\alpha_1^T(i) \ \ldots\ \alpha_j^T(i)\right) \left(\beta_1^T(i) \ \ldots\ \beta_j^T(i)\right)\right]^T$

Due to this transformation, the m satellite clocks per observable type only appear as unknown parameters for the m remaining undifferenced observables per type after the transformation, e.g. $(\Delta\phi_{1,j}^1(i), \ldots, \Delta\phi_{1,j}^m(i))$. This means that these undifferenced observables are *free y^R-variates* in the transformed model. For the adjustment free y^R-variates do not contribute to the solution of the remaining parameters and may therefore be omitted from the model, see [Teunissen, 2000a]. The resulting model can be recognized as the traditional *single-differenced* model of observation equations, and this model is summarized in Table B.3. Note that in this model the clock parameters are the between-receiver clock unknowns.

Table B.3. Between-receiver single-differenced model

variable	elements
$y^{gb,sd}(i)$	$\begin{bmatrix} \left[\Phi_1^{gb,sd}(i)^T \ \ldots \ \Phi_j^{gb,sd}(i)^T\right]^T \\ \left[P_1^{gb,sd}(i)^T \ \ldots \ P_j^{gb,sd}(i)^T\right]^T \end{bmatrix}$, where $\Phi_j^{gb,sd}(i) = \left(D_n^T \otimes I_m\right) \Phi_j^{gb}(i), \quad P_j^{gb,sd}(i) = \left(D_n^T \otimes I_m\right) P_j^{gb}(i)$
$Q_{y(i)}^{gb,sd}$	$\begin{bmatrix} Q_\phi & \\ & Q_p \end{bmatrix} \otimes Q^{sd}(i)$, where $Q^{sd}(i) = \left(D_n^T \otimes I_m\right) Q(i) \left(D_n \otimes I_m\right)$
$A_I^{gb,sd}(i)$	$\begin{bmatrix} \begin{pmatrix} e_j \\ e_j \end{pmatrix} \otimes \mathcal{A}^{sd}(i) & \begin{pmatrix} \Lambda \\ 0 \end{pmatrix} \otimes \mathcal{C}^{sd} \end{bmatrix}$ where $\mathcal{A}^{sd}(i) = \text{blkdiag}\left[G_2(i), \ \ldots, \ G_n(i)\right], \quad \mathcal{C}^{sd} = I_{n-1} \otimes C_m$
$A_{II}^{gb,sd}(i)$	$\begin{bmatrix} \begin{pmatrix} I_j & \\ & I_j \end{pmatrix} \otimes \mathcal{D}^{sd} \end{bmatrix}$, where $\mathcal{D}^{sd} = I_{n-1} \otimes e_m$
$x_I^{gb,sd}$	$\left[g^T \ \left(a_1^T \ \ldots \ a_j^T\right)\right]^T$
$x_{II}^{gb,sd}(i)$	$\left[\left(\alpha_1^{sd}(i)^T \ \ldots \ \alpha_j^{sd}(i)^T\right) \ \left(\beta_1^{sd}(i)^T \ \ldots \ \beta_j^{sd}(i)^T\right)\right]^T$ where $\begin{cases} \alpha_j^{sd}(i) = [c\delta t_{12,j}(i) \ \ldots \ c\delta t_{1n,j}(i)]^T \\ \beta_j^{sd}(i) = [cdt_{12,j}(i) \ \ldots \ cdt_{1n,j}(i)]^T \end{cases}$

In a next step, the previous model of single-differenced observables can be transformed using the following full-rank transformation matrix:

$$\Upsilon_2^{gb} = \begin{bmatrix} I_j & \\ & I_j \end{bmatrix} \otimes \left[I_{n-1} \otimes E_m^T\right], \quad \text{where } E_m^T = \underbrace{\begin{bmatrix} c_m^T \\ D_m^T \end{bmatrix}}_{m \times m}$$

The $(m-1) \times m$ matrix $D_m^T = [-e_{m-1}, \ I_{m-1}]$ is known as the *difference operator for satellites*, and the $m \times 1$ vector $c_m = (1, \ 0, \ \ldots, \ 0)^T$. The transformed model elements are given in Table B.4.

Note that in the transformed single-difference model it holds that $E_m^T G_r(i) = \begin{bmatrix} -u_r^1(i)^T \\ D_m^T G_r(i) \end{bmatrix}$. When the receiver clock parameters in the model are lumped to the geometry vector to pivot satellite 1, we obtain the following reparameterized receiver clock parameters:

$$\begin{aligned} \tilde{\alpha}_j^{sd}(i) &= \left[\left(c\delta t_{12,j}(i) - u_2^1(i)^T \Delta r_{12}\right) \ \ldots \ \left(c\delta t_{1n,j}(i) - u_n^1(i)^T \Delta r_{1n}\right)\right]^T \\ \tilde{\beta}_j^{sd}(i) &= \left[\left(cdt_{12,j}(i) - u_2^1(i)^T \Delta r_{12}\right) \ \ldots \ \left(cdt_{1n,j}(i) - u_n^1(i)^T \Delta r_{1n}\right)\right]^T \end{aligned}$$

As a consequence, the $n-1$ SD observables per observable type can be recognized as free y^R-variates, which only have the above $n-1$ reparameterized clock errors per observable type as unknown parameters. Omitting these free y^R-variates results finally in the traditional model of double-differenced observation equations, see Table B.5. In this double-differenced model all clock parameters are eliminated.

Table B.4. Transformed single-differenced model

variable	elements
$\tilde{y}^{gb,sd}(i)$	$\Upsilon_2^{gb} y^{gb,sd}(i) = \begin{bmatrix} \left[\tilde{\Phi}_1^{gb,sd}(i)^T \ \dots \ \tilde{\Phi}_j^{gb,sd}(i)^T\right]^T \\ \left[\tilde{P}_1^{gb,sd}(i)^T \ \dots \ \tilde{P}_j^{gb,sd}(i)^T\right]^T \end{bmatrix}$ where $\begin{cases} \tilde{\Phi}_j^{gb,sd}(i) = \left[\Delta\phi_{12,j}^1(i) \ \left(\Delta\phi_{12,j}^{12}(i) \dots \Delta\phi_{12,j}^{1m}(i)\right), \dots \right. \\ \qquad\qquad \left. \dots \ \Delta\phi_{1n,j}^1(i) \ \left(\Delta\phi_{1n,j}^{12}(i) \dots \Delta\phi_{1n,j}^{1m}(i)\right)\right]^T \\ \tilde{P}_j^{gb,sd}(i) = \left[\Delta p_{12,j}^1(i) \ \left(\Delta p_{12,j}^{12}(i) \dots \Delta p_{12,j}^{1m}(i)\right), \dots \right. \\ \qquad\qquad \left. \dots \ \Delta p_{1n,j}^1(i) \ \left(\Delta p_{1n,j}^{12}(i) \dots \Delta p_{1n,j}^{1m}(i)\right)\right]^T \end{cases}$
$Q_{\tilde{y}(i)}^{gb,sd}$	$\Upsilon_2^{gb} Q_{y(i)}^{gb,sd} \Upsilon_2^{gbT} = \begin{bmatrix} Q_\phi & \\ & Q_p \end{bmatrix} \otimes \tilde{Q}^{sd}(i)$ where $\tilde{Q}^{sd}(i) = \begin{bmatrix} E_m^T\left[Q_1(i)+Q_2(i)\right]E_m & \dots & E_m^T Q_1(i) E_m \\ \vdots & \ddots & \vdots \\ E_m^T Q_1(i) E_m & \dots & E_m^T\left[Q_1(i)+Q_n(i)\right]E_m \end{bmatrix}$
$\tilde{A}_I^{gb,sd}(i)$	$\Upsilon_2^{gb} A_I^{gb,sd}(i) = \begin{bmatrix} \begin{pmatrix} e_j \\ e_j \end{pmatrix} \otimes \tilde{\mathcal{A}}^{sd}(i) & \begin{pmatrix} \Lambda \\ 0 \end{pmatrix} \otimes \mathcal{C}^{sd} \end{bmatrix}$ where $\tilde{\mathcal{A}}^{sd}(i) = \text{blkdiag}\left[E_m^T G_2(i), \ \dots, \ E_m^T G_n(i)\right], \quad \mathcal{C}^{sd} = I_{n-1} \otimes C_m$
$\tilde{A}_{II}^{gb,sd}(i)$	$\Upsilon_2^{gb} A_{II}^{gb,sd}(i) = \begin{bmatrix} \begin{pmatrix} I_j & \\ & I_j \end{pmatrix} \otimes \tilde{\mathcal{D}}^{sd} \end{bmatrix}$ where $\tilde{\mathcal{D}}^{sd} = I_{n-1} \otimes c_m$ since $E_m^T C_m = C_m$ and $E_m^T e_m = c_m$
$x_I^{gb,sd}$	$\left[g^T \ \left(a_1^T \ \dots \ a_j^T\right)\right]^T$
$x_{II}^{gb,sd}(i)$	$\left[\left(\alpha_1^{sd}(i)^T \ \dots \ \alpha_j^{sd}(i)^T\right) \ \left(\beta_1^{sd}(i)^T \ \dots \ \beta_j^{sd}(i)^T\right)\right]^T$

Table B.5. Double-differenced model

variable	elements
$y^{gb,dd}(i)$	$\begin{bmatrix} \left[\Phi_1^{gb,dd}(i)^T \ \dots \ \Phi_j^{gb,dd}(i)^T\right]^T \\ \left[P_1^{gb,dd}(i)^T \ \dots \ P_j^{gb,dd}(i)^T\right]^T \end{bmatrix}$ where $\Phi_j^{gb,dd}(i) = \left(D_n^T \otimes D_m^T\right)\Phi_j^{gb}(i), \quad P_j^{gb,dd}(i) = \left(D_n^T \otimes D_m^T\right) P_j^{gb}(i)$
$Q_{y(i)}^{gb,dd}$	$\begin{bmatrix} Q_\phi & \\ & Q_p \end{bmatrix} \otimes Q^{dd}(i)$, where $Q^{dd}(i) = \left(D_n^T \otimes D_m^T\right) Q(i) \left(D_n \otimes D_m\right)$
$A_I^{gb,dd}(i)$	$\begin{bmatrix} \begin{pmatrix} e_j \\ e_j \end{pmatrix} \otimes \mathcal{A}^{dd}(i) & \begin{pmatrix} \Lambda \\ 0 \end{pmatrix} \otimes \mathcal{C}^{dd} \end{bmatrix}$ where $\mathcal{A}^{dd}(i) = \text{blkdiag}\left[D_m^T G_2(i), \ \dots, \ D_m^T G_n(i)\right], \quad \mathcal{C}^{dd} = I_{n-1} \otimes I_{m-1}$
$A_{II}^{gb,dd}(i)$	0
$x_I^{gb,dd}$	$\left[g^T \ \left(a_1^T \ \dots \ a_j^T\right)\right]^T$
$x_{II}^{gb,dd}(i)$	-

Appendix C

Adjustment and testing procedure in *GPSveQ*

In this appendix the general algorithms are described for the adjustment and testing of GPS observations in the *GPSveQ* software. This software was originally developed by P.J. de Jonge, see [De Jonge, 1998].

C.1 Reduction of the normal equations

In the mathematical model, which is the basis of *GPSveQ*, the vector of parameters is partitioned in a part for the non-temporal parameters (x_I) and a part for the temporal parameters (x_{II}):

$$\boxed{E\{y\} \;=\; [A_I \; A_{II}] \begin{bmatrix} x_I \\ x_{II} \end{bmatrix}; \quad D\{y\} = Q_y} \tag{C.1}$$

To solve these parameters in a least-squares adjustment, the following system of normal equations is set up:

$$\begin{bmatrix} A_I^T Q_y^{-1} A_I & A_I^T Q_y^{-1} A_{II} \\ A_{II}^T Q_y^{-1} A_I & A_{II}^T Q_y^{-1} A_{II} \end{bmatrix} \begin{bmatrix} \hat{x}_I \\ \hat{x}_{II} \end{bmatrix} \;=\; \begin{bmatrix} A_I^T Q_y^{-1} y \\ A_{II}^T Q_y^{-1} y \end{bmatrix} \tag{C.2}$$

Since the number of non-temporal parameters is relatively small compared to the number of temporal parameters, it is advantageous to *reduce* the normal equations for the temporal parameters in the model. In this way the model can be solved in a more efficient way. The temporal parameters $\hat{x}_{II}$ are eliminated by pre-multiplying the normal equations with the following square and full-rank matrix [Teunissen, 2000a]:

$$\begin{bmatrix} I & -A_I^T Q_y^{-1} A_{II} \left(A_{II}^T Q_y^{-1} A_{II}\right)^{-1} \\ 0 & I \end{bmatrix} \tag{C.3}$$

This results in the following system of reduced normal equations:

$$\begin{bmatrix} A_I^T Q_y^{-1} \left[I - A_{II} \left(A_{II}^T Q_y^{-1} A_{II} \right)^{-1} A_{II}^T Q_y^{-1} \right] A_I & 0 \\ A_{II}^T Q_y^{-1} A_I & A_{II}^T Q_y^{-1} A_{II} \end{bmatrix} \begin{bmatrix} \hat{x}_I \\ \hat{x}_{II} \end{bmatrix} = \begin{bmatrix} A_I^T Q_y^{-1} \left[I - A_{II} \left(A_{II}^T Q_y^{-1} A_{II} \right)^{-1} A_{II}^T Q_y^{-1} \right] y \\ A_{II}^T Q_y^{-1} y \end{bmatrix} \tag{C.4}$$

Recognizing the orthogonal projector

$$P_{A_{II}}^{\perp} = I - A_{II} \left(A_{II}^T Q_y^{-1} A_{II} \right)^{-1} A_{II}^T Q_y^{-1} \tag{C.5}$$

and using the following properties

$$Q_y^{-1} P_{A_{II}}^{\perp} = P_{A_{II}}^{\perp T} Q_y^{-1} = P_{A_{II}}^{\perp T} Q_y^{-1} P_{A_{II}}^{\perp} \tag{C.6}$$

and defining $\bar{A}_I = P_{A_{II}}^{\perp} A_I$, leads to the following reduced normal equations:

$$\boxed{\begin{bmatrix} \bar{A}_I^T Q_y^{-1} \bar{A}_I & 0 \\ A_{II}^T Q_y^{-1} A_I & A_{II}^T Q_y^{-1} A_{II} \end{bmatrix} \begin{bmatrix} \hat{x}_I \\ \hat{x}_{II} \end{bmatrix} = \begin{bmatrix} \bar{A}_I^T Q_y^{-1} y \\ A_{II}^T Q_y^{-1} y \end{bmatrix}} \tag{C.7}$$

The solution for the non-temporal parameters follows from these normal equations as:

$$\hat{x}_I = \left(\bar{A}_I^T Q_y^{-1} \bar{A}_I \right)^{-1} \bar{A}_I^T Q_y^{-1} y, \qquad Q_{\hat{x}_I} = \left(\bar{A}_I^T Q_y^{-1} \bar{A}_I \right)^{-1} \tag{C.8}$$

One $\hat{x}_I$ is known, the solution of the temporal parameters follows as:

$$\begin{aligned} \hat{x}_{II} &= \left(A_{II}^T Q_y^{-1} A_{II} \right)^{-1} A_{II}^T Q_y^{-1} \left(y - A_I \hat{x}_I \right), \\ Q_{\hat{x}_{II}} &= \left(A_{II}^T Q_y^{-1} A_{II} \right)^{-1} + \\ &\quad \left(A_{II}^T Q_y^{-1} A_{II} \right)^{-1} A_{II}^T Q_y^{-1} \left(A_I Q_{\hat{x}_I} A_I^T \right) Q_y^{-1} A_{II} \left(A_{II}^T Q_y^{-1} A_{II} \right)^{-1} \end{aligned} \tag{C.9}$$

To compute the different test statistics in the software (see Chap. 3), the vector of least-squares residuals is needed, which is computed as follows:

$$\hat{\epsilon} = y - \hat{y} = y - A_I \hat{x}_I - A_{II} \hat{x}_{II} \tag{C.10}$$

From this vector its norm can be computed, $\|\hat{\epsilon}\|_{Q_y}^2$, which forms the basis of the *overall model tests* in the software.

To compute the one-dimensional *outlier* and *cycle-slip* test statistics, besides the vector of least-squares residuals, its vc-matrix is needed. This is computed *without* first computing the vc-matrix of the temporal parameters $Q_{\hat{x}_{II}}$, since this latter

matrix can be very large. In [De Jonge, 1998] it is proved that the vc-matrix of the residuals can be computed as follows:

$$Q_{\hat{e}} \;=\; P^{\perp}_{A_{II}} Q_y - P^{\perp}_{A_{II}} \left(A_I Q_{\hat{x}_1} A_I^T \right) P^{\perp^T}_{A_{II}} \tag{C.11}$$

Using this, the w-test statistic for an *outlier* in one observation follows as:

$$w_y^o \;=\; \frac{c_o^T Q_y^{-1} \hat{e}}{\sqrt{c_o^T Q_y^{-1} Q_{\hat{e}} Q_y^{-1} c_o}}, \quad \text{where } c_o \;=\; c_k^o \otimes [c_f \otimes (c_n \otimes c_m)] \tag{C.12}$$

The dimension of vector c^o is $kfnm \times 1$, where k is the number of epochs, f the number of observable types, n the number of receivers and m the number of satellites involved in the processing. In each c-vector just one 1 appears, depending on which observation is being tested (data-snooping). For example, the vector $c_i = (0,\; \ldots,\; 1,\; \ldots,\; 0)^T$ has a 1 at its ith entry.

The w-test statistic for a *cycle slip* in a phase observation which is supposed to have occurred at epoch l $(1 \leq l \leq k)$ is computed as:

$$w_y^s \;=\; \frac{c_s^T Q_y^{-1} \hat{e}}{\sqrt{c_s^T Q_y^{-1} Q_{\hat{e}} Q_y^{-1} c_s}}, \quad \text{where } c_s \;=\; c_k^s \otimes [c_f \otimes (c_n \otimes c_m)] \tag{C.13}$$

This test statistic differs from its outlier counterpart through the $k \times 1$ c_k^s vector, which reads as follows:

$$c_k^s \;=\; (0,\; \ldots,\; 0,\; 1,\; 1,\; \ldots,\; 1)^T \tag{C.14}$$

where first 1 starts at the lth entry of the vector and continues to the last entry.

C.2 Uncorrelated observations in time

In the *GPSveQ* software it is assumed that the observations are *uncorrelated* in time. Using this assumption, the mentioned variables in the adjustment and testing procedures can be evaluated in a very efficient way. In Table C.1 for all the variables the expressions are given, assuming uncorrelated observations in time.

Note from Table C.1 that many variables used for the adjustment and testing depend on the partial design matrix $A_{II}(i)$ for the temporal matrix. Due to the many temporal parameters for undifferenced observables, for each epoch this matrix can be very large. Since this matrix never depends on the actual receiver-satellite geometry, the processing can be made much more efficient (faster) when the variables depending on this $A_{II}(i)$ are not explicitly computed in the software, but directly set up using *closed-form expressions* for them. In Tables C.2 – C.5 for the following matrices closed-form expressions are given:

- $A_{II}(i)^T Q_{y(i)}^{-1}$

- $A_{II}(i)^T Q_{y(i)}^{-1} A_{II}(i)$
- $\left[A_{II}(i)^T Q_{y(i)}^{-1} A_{II}(i)\right]^{-1}$
- $\left[A_{II}(i)^T Q_{y(i)}^{-1} A_{II}(i)\right]^{-1} A_{II}(i)^T Q_{y(i)}^{-1}$
- $P_{A_{II}(i)}^{\perp} = I - A_{II}(i)\left[A_{II}(i)^T Q_{y(i)}^{-1} A_{II}(i)\right]^{-1} A_{II}(i)^T Q_{y(i)}^{-1}$
- $Q_{y(i)}^{-1} P_{A_{II}(i)}^{\perp}$

Although these closed-form expressions are in this appendix are only derived for the *geometry-free* model (see Chap. 2), they can be applied to the *geometry-based* model. For the latter model, the a priori range variance factor should be set to zero ($\sigma_\varrho^2 = 0$) and the columns in $A_{II}(i)$ for the range parameters need to be removed, since in the geometry-based model no receiver-satellite ranges are solved.

The first two tables, Tables C.2 and C.3, apply to the *ionosphere-weighted* model, but the expressions can also be applied to the *ionosphere-fixed* model, by setting the a priori ionospheric variance factor to zero ($\sigma_\iota^2 = 0$) and removing the columns in $A_{II}(i)$ corresponding to the ionospheric delays. For the *ionosphere-float* model however, two separate tables, Tables C.4 and C.5, are included in this appendix, since when the ionospheric delays are assumed as completely unknown parameters, additional rank deficiencies occur, between the columns in $A_{II}(i)$ of the ionospheric delays and the clock parameters (see Chap. 5). In this thesis these rank deficiencies are solved by constraining the clocks of the *first* observable, which is usually the phase on L1. Note that this choice of constraining does *not* influence the variables $P_{A_{II}(i)}^{\perp}$ and $Q_{y(i)}^{-1} P_{A_{II}(i)}^{\perp}$. Note that in the tables the following *scalars* appear, which are defined as:

$$\begin{array}{rcl} \omega & = & \left[\mu^T \left(Q_\phi^{-1} + Q_p^{-1}\right)\mu\right] \\ \eta & = & \left[e_j^T \left(Q_\phi^{-1} + Q_p^{-1}\right)e_j\right] \\ \xi & = & \left[\mu^T \left(Q_\phi^{-1} - Q_p^{-1}\right)e_j\right] \end{array} \tag{C.15}$$

Moreover, in the tables of the ionosphere-float model (Tables C.4 and C.5) also the following scalars appear:

$$\begin{array}{rcl} \bar{\omega} & = & \left[\mu^T \left(Q_\phi^{-1} - R_\phi\right)\mu\right] \\ \bar{\eta} & = & \left[e_j^T \left(Q_\phi^{-1} - R_\phi\right)e_j\right] \\ \bar{\xi} & = & \left[\mu^T \left(Q_\phi^{-1} - R_\phi\right)e_j\right] \end{array} \tag{C.16}$$

Compared to the first three scalar expressions, in these latter three expressions the $j \times j$ code cofactor matrix Q_p is replaced by the $j \times j$ matrix R_ϕ, which is defined as:

$$R_\phi = F_\phi^T C_j^T Q_\phi^{-1}, \quad \text{where } F_\phi = \left[C_j^T Q_\phi^{-1} C_j\right]^{-1} C_j^T Q_\phi^{-1} \tag{C.17}$$

Note that F_ϕ is a $(j-1) \times j$ matrix. In the ionosphere-float tables the vector $\bar{\mu}$ appears, which is defined as: $\bar{\mu} = [\mu_2 \ \ldots \ \mu_j]^T$.

Table C.1. *GPSveQ* adjustment and testing variables

var.	*GPSveQ*
y	$[y(1),\ \ldots,\ y(k)]^T$
Q_y	$\text{blkdiag}\left[Q_{y(1)},\ \ldots,\ Q_{y(k)}\right]$
A_I	$\left[A_I(1)^T,\ \ldots,\ A_I(k)^T\right]^T$
x_I	x_I
A_{II}	$\text{blkdiag}\left[A_{II}(1),\ \ldots,\ A_{II}(k)\right]$
x_{II}	$[x_{II}(1),\ \ldots,\ x_{II}(k)]^T$
$P^{\perp}_{A_{II}}$	$\text{blkdiag}\left[P^{\perp}_{A_{II}(1)},\ \ldots,\ P^{\perp}_{A_{II}(k)}\right]$
$\mathcal{N}$	$\bar{A}_I^T Q_y^{-1} \bar{A}_I \ = \ \sum_{i=1}^{k} A_I(i)^T Q_{y(i)}^{-1} P^{\perp}_{A_{II}(i)} A_I(i)$
$\mathcal{R}$	$\bar{A}_I^T Q_y^{-1} y \ = \ \sum_{i=1}^{k} A_I(i)^T Q_{y(i)}^{-1} P^{\perp}_{A_{II}(i)} y(i)$
$\hat{x}_I$	$\mathcal{N}^{-1}\mathcal{R}$
$Q_{\hat{x}_I}$	$\mathcal{N}^{-1}$
$\hat{x}_{II}$	$[\hat{x}_{II}(1),\ \ldots,\ \hat{x}_{II}(k)]^T$, where
	$\hat{x}_{II}(i) \ = \ \left[A_{II}(i)^T Q_{y(i)}^{-1} A_{II}(i)\right]^{-1} A_{II}(i)^T Q_{y(i)}^{-1} \left[y(i) - A_I(i)\hat{x}_I\right]$
$Q_{\hat{x}_{II}}$	$\begin{bmatrix} Q_{\hat{x}_{II}(1)} & \cdots & Q_{\hat{x}_{II}(1)\hat{x}_{II}(k)} \\ \vdots & \ddots & \vdots \\ Q_{\hat{x}_{II}(k)\hat{x}_{II}(1)} & \cdots & Q_{\hat{x}_{II}(k)} \end{bmatrix}$, where
	$Q_{\hat{x}_{II}(i)} \ = \ \left[A_{II}(i)^T Q_{y(i)}^{-1} A_{II}(i)\right]^{-1} + \left[A_{II}(i)^T Q_{y(i)}^{-1} A_{II}(i)\right]^{-1} A_{II}(i)^T \cdot$
	$Q_{y(i)}^{-1} \left[A_I(i) Q_{\hat{x}_I} A_I(i)^T\right] Q_{y(i)}^{-1} A_{II}(i) \left[A_{II}(i)^T Q_{y(i)}^{-1} A_{II}(i)\right]^{-1}$
	$Q_{\hat{x}_{II}(i)\hat{x}_{II}(l)} \ = \ \left[A_{II}(i)^T Q_{y(i)}^{-1} A_{II}(i)\right]^{-1} A_{II}(i)^T \cdot$
	$Q_{y(i)}^{-1} \left[A_I(i) Q_{\hat{x}_I} A_I(l)^T\right] Q_{y(l)}^{-1} A_{II}(l) \left[A_{II}(l)^T Q_{y(l)}^{-1} A_{II}(l)\right]^{-1}$
$\hat{\epsilon}$	$[\hat{\epsilon}(1),\ \ldots,\ \hat{\epsilon}(k)]^T$, where $\hat{\epsilon}(i) \ = \ y(i) - A_I(i)\hat{x}_I - A_{II}(i)\hat{x}_{II}(i)$
$Q_{\hat{\epsilon}}$	$\begin{bmatrix} Q_{\hat{\epsilon}(1)} & \cdots & Q_{\hat{\epsilon}(1)\hat{\epsilon}(k)} \\ \vdots & \ddots & \vdots \\ Q_{\hat{\epsilon}(k)\hat{\epsilon}(1)} & \cdots & Q_{\hat{x}_{II}(k)} \end{bmatrix}$, where
	$Q_{\hat{\epsilon}(i)} \ = \ P^{\perp}_{A_{II}(i)} Q_{y(i)} - P^{\perp}_{A_{II}(i)} \left[A_I(i) Q_{\hat{x}_I} A_I(i)^T\right] P^{\perp^T}_{A_{II}(i)}$
	$Q_{\hat{\epsilon}(i)\hat{\epsilon}(l)} \ = \ -P^{\perp}_{A_{II}(i)} \left[A_I(i) Q_{\hat{x}_I} A_I(l)^T\right] P^{\perp^T}_{A_{II}(l)}$
$\|\hat{\epsilon}\|^2_{Q_y}$	$\sum_{i=1}^{k} \hat{\epsilon}(i)^T Q_{y(i)}^{-1} \hat{\epsilon}(i)$
$w^o_{y(i)}$	$\frac{c_y^T Q_{y(i)}^{-1} \hat{\epsilon}(i)}{\sqrt{c_y^T Q_{y(i)}^{-1} Q_{\hat{\epsilon}(i)} Q_{y(i)}^{-1} c_y}}$, where $c_y \ = \ [c_f \otimes (c_n \otimes c_m)]^T$
$w^s_{y(l)}$	$\frac{-\sum_{i=1}^{l-1} c_y^T Q_{y(i)}^{-1} \hat{\epsilon}(i)}{\sqrt{c_y^T \left[W_{1,l-1} \ - \ W_{2,l-1} W_{3,l-1}\right] c_y}}$, where $c_y \ = \ [c_f \otimes (c_n \otimes c_m)]^T$, and:
	$W_{1,l-1} \ = \ \sum_{i=1}^{l-1} Q_{y(i)}^{-1} P^{\perp}_{A_{II}(i)}$
	$W_{2,l-1} \ = \ \sum_{i=1}^{l-1} Q_{y(i)}^{-1} P^{\perp}_{A_{II}(i)} A_I(i)$
	$W_{3,l-1} \ = \ \sum_{i=1}^{l-1} Q_{\hat{x}_I} A_I(i)^T P^{\perp^T}_{A_{II}(i)} Q_{y(i)}^{-1}$

Table C.2. Closed-form expressions for matrices in the geometry-free *ionosphere-weighted* model (part 1).

$A_{II}(i)$	$\left[\begin{array}{c} \left[\begin{array}{c} \left(\begin{array}{cc} I_j & \\ & I_j \end{array}\right) \\ \left(\begin{array}{cc} 0 & \\ & 0 \end{array}\right) \end{array}\right] \otimes \mathcal{D} \quad \left[\begin{array}{c} \left(\begin{array}{cc} -\mu & e_j \\ \mu & e_j \end{array}\right) \\ \left(\begin{array}{cc} 1 & \\ & 1 \end{array}\right) \end{array}\right] \otimes I_{nm} \end{array}\right]$
$Q_{y(i)}$	$\text{blkdiag}\left[\left(Q_\phi,\ Q_p\right),\ \left(\sigma_i^2,\ \sigma_\varrho^2\right)\right] \otimes Q(i)$
$A_{II}(i)^T Q_{y(i)}^{-1}$	$\left[\begin{array}{cc} \left[\left(\begin{array}{cc} Q_\phi^{-1} & \\ & Q_p^{-1} \end{array}\right) \left(\begin{array}{cc} 0 & \\ & 0 \end{array}\right)\right] \otimes \mathcal{D}^T Q(i)^{-1} & \\ \left[\left(\begin{array}{cc} -\mu_j^T Q_\phi^{-1} & \mu^T Q_p^{-1} \\ e_j^T Q_\phi^{-1} & e_j^T Q_p^{-1} \end{array}\right) \left(\begin{array}{cc} \sigma_i^{-2} & \\ & \sigma_\varrho^{-2} \end{array}\right)\right] \otimes Q(i)^{-1} & \end{array}\right]$
$A_{II}(i)^T Q_{y(i)}^{-1} A_{II}(i)$	$\left[\begin{array}{cc} \left(\begin{array}{cc} Q_\phi^{-1} & \\ & Q_p^{-1} \end{array}\right) \otimes \mathcal{D}^T Q(i)^{-1}\mathcal{D} & \left(\begin{array}{cc} -Q_\phi^{-1}\mu & Q_\phi^{-1} e_j \\ Q_p^{-1}\mu & Q_p^{-1} e_j \end{array}\right) \otimes \mathcal{D}^T Q(i)^{-1} \\ \text{symm.} & \left(\begin{array}{cc} \omega+\sigma_i^{-2} & -\xi \\ -\xi & \eta+\sigma_\varrho^{-2} \end{array}\right) \otimes Q(i)^{-1} \end{array}\right]$
$\left[A_{II}(i)^T Q_{y(i)}^{-1} A_{II}(i)\right]^{-1}$	$= \left[\begin{array}{cc} D_{11} & D_{12} \\ D_{12}^T & D_{22} \end{array}\right]$, with:
D_{11}	$= \left[\left(\begin{array}{cc} Q_\phi & \\ & Q_p \end{array}\right) + \sigma_i^2 \left(\begin{array}{cc} \mu\mu^T & -\mu\mu^T \\ -\mu\mu^T & \mu\mu^T \end{array}\right) + \sigma_\varrho^2 \left(\begin{array}{cc} e_j e_j^T & e_j e_j^T \\ e_j e_j^T & e_j e_j^T \end{array}\right)\right] \otimes \left(\mathcal{D}^T Q(i)^{-1}\mathcal{D}\right)^{-1}$
D_{12}	$= \left[-\sigma_i^2 \left(\begin{array}{c} -\mu \\ \mu \end{array}\right) \quad -\sigma_\varrho^2 \left(\begin{array}{c} e_j \\ e_j \end{array}\right)\right] \otimes \left(\mathcal{D}^T Q(i)^{-1}\mathcal{D}\right)^{-1} \mathcal{D}^T$
D_{22}	$= \left(\begin{array}{cc} \sigma_i^2 & \\ & \sigma_\varrho^2 \end{array}\right) \otimes Q(i) - \left(\begin{array}{cc} \frac{\sigma_i^2\left[\omega(\eta+\sigma_\varrho^{-2})-\xi^2\right]}{(\omega+\sigma_i^{-2})(\eta+\sigma_\varrho^{-2})-\xi^2} & -\frac{\xi}{(\omega+\sigma_i^{-2})(\eta+\sigma_\varrho^{-2})-\xi^2} \\ -\frac{\xi}{(\omega+\sigma_i^{-2})(\eta+\sigma_\varrho^{-2})-\xi^2} & \frac{\sigma_\varrho^2\left[\eta(\omega+\sigma_i^{-2})-\xi^2\right]}{(\omega+\sigma_i^{-2})(\eta+\sigma_\varrho^{-2})-\xi^2} \end{array}\right) \otimes P_{\mathcal{D}(i)}^\perp Q(i)$
$\left[A_{II}(i)^T Q_{y(i)}^{-1} A_{II}(i)\right]^{-1} A_{II}(i)^T Q_{y(i)}^{-1}$	$= \left[\begin{array}{c} K_1 \\ K_2 \end{array}\right]$, with:
K_1	$= \left[\left(\begin{array}{cc} I_j & \\ & I_j \end{array}\right), \ -\left(\begin{array}{cc} -\mu & e_j \\ \mu & e_j \end{array}\right)\right] \otimes \left(\mathcal{D}^T Q(i)^{-1}\mathcal{D}\right)^{-1} \mathcal{D}^T Q(i)^{-1}$
K_2	$= \left[\left(\begin{array}{cc} \frac{(\eta+\sigma_\varrho^{-2})}{(\omega+\sigma_i^{-2})(\eta+\sigma_\varrho^{-2})-\xi^2} & \frac{\xi}{(\omega+\sigma_i^{-2})(\eta+\sigma_\varrho^{-2})-\xi^2} \\ \frac{\xi}{(\omega+\sigma_i^{-2})(\eta+\sigma_\varrho^{-2})-\xi^2} & \frac{(\omega+\sigma_i^{-2})}{(\omega+\sigma_i^{-2})(\eta+\sigma_\varrho^{-2})-\xi^2} \end{array}\right) \left(\begin{array}{cc} -\mu^T Q_\phi^{-1} & \mu^T Q_p^{-1} \\ e_j^T Q_\phi^{-1} & e_j^T Q_p^{-1} \end{array}\right) \otimes P_{\mathcal{D}(i)}^\perp, \ \cdots$
	$\left(\begin{array}{cc} 1 & \\ & 1 \end{array}\right) \otimes I_{nm} - \left(\begin{array}{cc} \frac{\omega(\eta+\sigma_\varrho^{-2})-\xi^2}{(\omega+\sigma_i^{-2})(\eta+\sigma_\varrho^{-2})-\xi^2} & -\frac{\sigma_\varrho^{-2}\xi}{(\omega+\sigma_i^{-2})(\eta+\sigma_\varrho^{-2})-\xi^2} \\ -\frac{\sigma_i^{-2}\xi}{(\omega+\sigma_i^{-2})(\eta+\sigma_\varrho^{-2})-\xi^2} & \frac{\eta(\omega+\sigma_i^{-2})-\xi^2}{(\omega+\sigma_i^{-2})(\eta+\sigma_\varrho^{-2})-\xi^2} \end{array}\right) \otimes P_{\mathcal{D}(i)}^\perp\right]$

Table C.3. Closed-form expressions for matrices in the geometry-free *ionosphere-weighted* model (part 2).

$$\boxed{P^{\perp}_{A_{II}(i)} = \begin{bmatrix} P_{11} & P_{12} \\ P_{21} & P_{22} \end{bmatrix} \otimes P^{\perp}_{\mathcal{D}(i)}} \text{ with:}$$

$$\begin{aligned}
P_{11} &= \begin{pmatrix} I_j & \\ & I_j \end{pmatrix} - \frac{\omega+\sigma_i^{-2}}{(\omega+\sigma_i^{-2})(\eta+\sigma_\varrho^{-2})-\xi^2} \begin{pmatrix} e_j e_j^T Q_\phi^{-1} & e_j e_j^T Q_p^{-1} \\ e_j e_j^T Q_\phi^{-1} & e_j e_j^T Q_p^{-1} \end{pmatrix} - \frac{\xi}{(\omega+\sigma_i^{-2})(\eta+\sigma_\varrho^{-2})-\xi^2} \begin{pmatrix} -e_j \mu^T Q_\phi^{-1} & e_j \mu^T Q_p^{-1} \\ -e_j \mu^T Q_\phi^{-1} & e_j \mu^T Q_p^{-1} \end{pmatrix} \\
&\quad - \frac{\xi}{(\omega+\sigma_i^{-2})(\eta+\sigma_\varrho^{-2})-\xi^2} \begin{pmatrix} -\mu e_j^T Q_\phi^{-1} & -\mu e_j^T Q_p^{-1} \\ \mu e_j^T Q_\phi^{-1} & \mu e_j^T Q_p^{-1} \end{pmatrix} - \frac{\eta+\sigma_\varrho^{-2}}{(\omega+\sigma_i^{-2})(\eta+\sigma_\varrho^{-2})-\xi^2} \begin{pmatrix} \mu\mu^T Q_\phi^{-1} & -\mu\mu^T Q_p^{-1} \\ -\mu\mu^T Q_\phi^{-1} & \mu\mu^T Q_p^{-1} \end{pmatrix} \\
P_{12} &= -\begin{pmatrix} -\mu & e_j \\ \mu & e_j \end{pmatrix} \begin{pmatrix} \frac{\sigma_i^{-2}(\eta+\sigma_\varrho^{-2})}{(\omega+\sigma_i^{-2})(\eta+\sigma_\varrho^{-2})-\xi^2} & \frac{\sigma_\varrho^{-2}\xi}{(\omega+\sigma_i^{-2})(\eta+\sigma_\varrho^{-2})-\xi^2} \\ \frac{\sigma_i^{-2}\xi}{(\omega+\sigma_i^{-2})(\eta+\sigma_\varrho^{-2})-\xi^2} & \frac{\sigma_\varrho^{-2}(\omega+\sigma_i^{-2})}{(\omega+\sigma_i^{-2})(\eta+\sigma_\varrho^{-2})-\xi^2} \end{pmatrix} \\
P_{21} &= -\begin{pmatrix} \frac{(\eta+\sigma_\varrho^{-2})}{(\omega+\sigma_i^{-2})(\eta+\sigma_\varrho^{-2})-\xi^2} & \frac{\xi}{(\omega+\sigma_i^{-2})(\eta+\sigma_\varrho^{-2})-\xi^2} \\ \frac{\xi}{(\omega+\sigma_i^{-2})(\eta+\sigma_\varrho^{-2})-\xi^2} & \frac{(\omega+\sigma_i^{-2})}{(\omega+\sigma_i^{-2})(\eta+\sigma_\varrho^{-2})-\xi^2} \end{pmatrix} \begin{pmatrix} -\mu^T Q_\phi^{-1} & \mu^T Q_p^{-1} \\ e_j^T Q_\phi^{-1} & e_j^T Q_p^{-1} \end{pmatrix} \\
P_{22} &= \begin{pmatrix} \frac{\omega(\eta+\sigma_\varrho^{-2})-\xi^2}{(\omega+\sigma_i^{-2})(\eta+\sigma_\varrho^{-2})-\xi^2} & -\frac{\sigma_\varrho^{-2}\xi}{(\omega+\sigma_i^{-2})(\eta+\sigma_\varrho^{-2})-\xi^2} \\ -\frac{\sigma_i^{-2}\xi}{(\omega+\sigma_i^{-2})(\eta+\sigma_\varrho^{-2})-\xi^2} & \frac{\eta(\omega+\sigma_i^{-2})-\xi^2}{(\omega+\sigma_i^{-2})(\eta+\sigma_\varrho^{-2})-\xi^2} \end{pmatrix}
\end{aligned}$$

$$\boxed{Q^{-1}_{y(i)} P^{\perp}_{A_{II}(i)} = \begin{bmatrix} S_{11} & S_{21}^T \\ S_{21} & S_{22} \end{bmatrix} \otimes Q(i)^{-1} P^{\perp}_{\mathcal{D}(i)}} \text{ with:}$$

$$\begin{aligned}
S_{11} &= \begin{pmatrix} Q_\phi^{-1} & \\ & Q_p^{-1} \end{pmatrix} - \frac{\omega+\sigma_i^{-2}}{(\omega+\sigma_i^{-2})(\eta+\sigma_\varrho^{-2})-\xi^2} \begin{pmatrix} Q_\phi^{-1} e_j e_j^T Q_\phi^{-1} & Q_\phi^{-1} e_j e_j^T Q_p^{-1} \\ Q_p^{-1} e_j e_j^T Q_\phi^{-1} & Q_p^{-1} e_j e_j^T Q_p^{-1} \end{pmatrix} - \frac{\xi}{(\omega+\sigma_i^{-2})(\eta+\sigma_\varrho^{-2})-\xi^2} \begin{pmatrix} -Q_\phi^{-1} e_j \mu^T Q_\phi^{-1} & Q_\phi^{-1} e_j \mu^T Q_p^{-1} \\ -Q_p^{-1} e_j \mu^T Q_\phi^{-1} & Q_p^{-1} e_j \mu^T Q_p^{-1} \end{pmatrix} \\
&\quad - \frac{\xi}{(\omega+\sigma_i^{-2})(\eta+\sigma_\varrho^{-2})-\xi^2} \begin{pmatrix} -Q_\phi^{-1} \mu e_j^T Q_\phi^{-1} & -Q_\phi^{-1} \mu e_j^T Q_p^{-1} \\ Q_p^{-1} \mu e_j^T Q_\phi^{-1} & Q_p^{-1} \mu e_j^T Q_p^{-1} \end{pmatrix} - \frac{\eta+\sigma_\varrho^{-2}}{(\omega+\sigma_i^{-2})(\eta+\sigma_\varrho^{-2})-\xi^2} \begin{pmatrix} Q_\phi^{-1} \mu\mu^T Q_\phi^{-1} & -Q_\phi^{-1} \mu\mu^T Q_p^{-1} \\ -Q_p^{-1} \mu\mu^T Q_\phi^{-1} & Q_p^{-1} \mu\mu^T Q_p^{-1} \end{pmatrix} \\
S_{21} &= -\begin{pmatrix} \frac{\sigma_i^{-2}(\eta+\sigma_\varrho^{-2})}{(\omega+\sigma_i^{-2})(\eta+\sigma_\varrho^{-2})-\xi^2} & \frac{\sigma_i^{-2}\xi}{(\omega+\sigma_i^{-2})(\eta+\sigma_\varrho^{-2})-\xi^2} \\ \frac{\sigma_\varrho^{-2}\xi}{(\omega+\sigma_i^{-2})(\eta+\sigma_\varrho^{-2})-\xi^2} & \frac{\sigma_\varrho^{-2}(\omega+\sigma_i^{-2})}{(\omega+\sigma_i^{-2})(\eta+\sigma_\varrho^{-2})-\xi^2} \end{pmatrix} \begin{pmatrix} -\mu^T Q_\phi^{-1} & \mu^T Q_p^{-1} \\ e_j^T Q_\phi^{-1} & e_j^T Q_p^{-1} \end{pmatrix} \\
S_{22} &= \begin{pmatrix} \frac{\sigma_i^{-2}\omega(\eta+\sigma_\varrho^{-2})-\xi^2}{(\omega+\sigma_i^{-2})(\eta+\sigma_\varrho^{-2})-\xi^2} & -\frac{\sigma_\varrho^{-2}\sigma_i^{-2}\xi}{(\omega+\sigma_i^{-2})(\eta+\sigma_\varrho^{-2})-\xi^2} \\ -\frac{\sigma_\varrho^{-2}\sigma_i^{-2}\xi}{(\omega+\sigma_i^{-2})(\eta+\sigma_\varrho^{-2})-\xi^2} & \frac{\sigma_\varrho^{-2}\eta(\omega+\sigma_i^{-2})-\xi^2}{(\omega+\sigma_i^{-2})(\eta+\sigma_\varrho^{-2})-\xi^2} \end{pmatrix}
\end{aligned}$$

Table C.4. Closed-form expressions for matrices in the geometry-free *ionosphere-float* model (part 1).

$A_{II}(i)$	$\left[\begin{array}{c} \left[\begin{array}{c} \left(\begin{array}{cc} C_j & \\ & I_j \end{array} \right) \\ \left(\begin{array}{cc} 0 & 0 \end{array} \right) \end{array} \right] \otimes \mathcal{D} \end{array} \quad \begin{array}{c} \left[\begin{array}{c} \left(\begin{array}{cc} -\mu & e_j \\ \mu & e_j \end{array} \right) \\ \left(\begin{array}{cc} 0 & 1 \end{array} \right) \end{array} \right] \otimes I_{nm} \end{array} \right]$
$Q_{y(i)}$	$\text{blkdiag}\left[(Q_\phi,\ Q_p)\,,\ \sigma_\varrho^2 \right] \otimes Q(i)$
$A_{II}(i)^T Q_{y(i)}^{-1}$	$\left[\begin{array}{c} \left[\left(\begin{array}{cc} C_j^T Q_\phi^{-1} & \\ & Q_p^{-1} \end{array} \right) \left(\begin{array}{c} 0 \\ 0 \end{array} \right) \right] \otimes \mathcal{D}^T Q(i)^{-1} \\ \left[\left(\begin{array}{cc} -\mu_j^T Q_\phi^{-1} & \mu^T Q_p^{-1} \\ e_j^T Q_\phi^{-1} & e_j^T Q_p^{-1} \end{array} \right) \left(\begin{array}{c} 0 \\ \sigma_\varrho^{-2} \end{array} \right) \right] \otimes Q(i)^{-1} \end{array} \right]$
$A_{II}(i)^T Q_{y(i)}^{-1} A_{II}(i)$	$\left[\begin{array}{cc} \left(\begin{array}{cc} C_j^T Q_\phi^{-1} C_j & \\ & Q_p^{-1} \end{array} \right) \otimes \mathcal{D}^T Q(i)^{-1} \mathcal{D} & \left(\begin{array}{cc} -C_j^T Q_\phi^{-1} \mu & C_j^T Q_\phi^{-1} e_j \\ Q_p^{-1} \mu & Q_p^{-1} e_j \end{array} \right) \otimes \mathcal{D}^T Q(i)^{-1} \\ \text{symm.} & \left(\begin{array}{cc} \omega & -\xi \\ -\xi & \eta + \sigma_\varrho^{-2} \end{array} \right) \otimes Q(i)^{-1} \end{array} \right]$

$$\left[A_{II}(i)^T Q_{y(i)}^{-1} A_{II}(i) \right]^{-1} = \left[\begin{array}{cc} D_{11} & D_{12} \\ D_{12}^T & D_{22} \end{array} \right], \text{ with:}$$

$$\begin{aligned}
D_{11} &= \left[\left(\begin{array}{cc} \left[C_j^T Q_\phi^{-1} C_j \right]^{-1} & \\ & Q_p \end{array} \right) + \frac{\bar{\omega}}{\bar{\omega}(\bar{\eta}+\sigma_\varrho^{-2})-\bar{\xi}^2} \left(\begin{array}{cc} F_\phi e_j e_j^T F_\phi^T & F_\phi e_j e_j^T \\ e_j e_j^T F_\phi^T & e_j e_j^T \end{array} \right) - \frac{\bar{\xi}}{\bar{\omega}(\bar{\eta}+\sigma_\varrho^{-2})-\bar{\xi}^2} \left(\begin{array}{cc} F_\phi \mu e_j^T F_\phi^T & F_\phi \mu e_j^T \\ -\mu e_j^T F_\phi^T & -\mu e_j^T \end{array} \right) \right. \\
&\quad \left. - \frac{\bar{\xi}}{\bar{\omega}(\bar{\eta}+\sigma_\varrho^{-2})-\bar{\xi}^2} \left(\begin{array}{cc} F_\phi e_j \mu^T F_\phi^T & -F_\phi e_j \mu^T \\ e_j \mu^T F_\phi^T & -e_j \mu^T \end{array} \right) + \frac{\bar{\eta}+\sigma_\varrho^{-2}}{\bar{\omega}(\bar{\eta}+\sigma_\varrho^{-2})-\bar{\xi}^2} \left(\begin{array}{cc} F_\phi \mu \mu^T F_\phi^T & -F_\phi \mu \mu^T \\ -\mu \mu^T F_\phi^T & \mu \mu^T \end{array} \right) \right] \otimes \left(\mathcal{D}^T Q(i)^{-1} \mathcal{D} \right)^{-1} \\
D_{12} &= \left[\frac{-\bar{\xi}}{\bar{\omega}(\bar{\eta}+\sigma_\varrho^{-2})-\bar{\xi}^2} \left(\begin{array}{c} F_\phi e_j \\ e_j \end{array} \right) - \frac{\bar{\eta}+\sigma_\varrho^{-2}}{\bar{\omega}(\bar{\eta}+\sigma_\varrho^{-2})-\bar{\xi}^2} \left(\begin{array}{c} -F_\phi \mu \\ \mu \end{array} \right), \frac{-\bar{\omega}}{\bar{\omega}(\bar{\eta}+\sigma_\varrho^{-2})-\bar{\xi}^2} \left(\begin{array}{c} F_\phi e_j \\ e_j \end{array} \right) - \frac{\bar{\xi}}{\bar{\omega}(\bar{\eta}+\sigma_\varrho^{-2})-\bar{\xi}^2} \left(\begin{array}{c} -F_\phi \mu \\ \mu \end{array} \right) \right] \otimes \left(\mathcal{D}^T Q(i)^{-1} \mathcal{D} \right)^{-1} \mathcal{D}^T \\
D_{22} &= \left(\begin{array}{cc} \frac{\bar{\eta}+\sigma_\varrho^{-2}}{\bar{\omega}(\bar{\eta}+\sigma_\varrho^{-2})-\bar{\xi}^2} & \frac{\bar{\xi}}{\bar{\omega}(\bar{\eta}+\sigma_\varrho^{-2})-\bar{\xi}^2} \\ \frac{\bar{\xi}}{\bar{\omega}(\bar{\eta}+\sigma_\varrho^{-2})-\bar{\xi}^2} & \frac{\bar{\omega}}{\bar{\omega}(\bar{\eta}+\sigma_\varrho^{-2})-\bar{\xi}^2} \end{array} \right) \otimes Q(i) - \left\{ \left(\begin{array}{cc} \frac{\bar{\eta}+\sigma_\varrho^{-2}}{\bar{\omega}(\bar{\eta}+\sigma_\varrho^{-2})-\bar{\xi}^2} & \frac{\bar{\xi}}{\bar{\omega}(\bar{\eta}+\sigma_\varrho^{-2})-\bar{\xi}^2} \\ \frac{\bar{\xi}}{\bar{\omega}(\bar{\eta}+\sigma_\varrho^{-2})-\bar{\xi}^2} & \frac{\bar{\omega}}{\bar{\omega}(\bar{\eta}+\sigma_\varrho^{-2})-\bar{\xi}^2} \end{array} \right) - \left(\begin{array}{cc} \frac{\eta+\sigma_\varrho^{-2}}{\omega(\eta+\sigma_\varrho^{-2})-\xi^2} & \frac{\xi}{\omega(\eta+\sigma_\varrho^{-2})-\xi^2} \\ \frac{\xi}{\omega(\eta+\sigma_\varrho^{-2})-\xi^2} & \frac{\omega}{\omega(\eta+\sigma_\varrho^{-2})-\xi^2} \end{array} \right) \right\} \otimes P_{\mathcal{D}(i)}^{\perp} Q(i)
\end{aligned}$$

$$\left[A_{II}(i)^T Q_{y(i)}^{-1} A_{II}(i) \right]^{-1} A_{II}(i)^T Q_{y(i)}^{-1} = \left[\begin{array}{c} K_1 \\ K_2 \end{array} \right], \text{ with:}$$

$$K_1 = \left[\left(\begin{array}{ccc} -\frac{1}{\mu_1} e_{j-1} & I_{j-1} & 0_{(j-1)\times j} \\ \frac{1}{\mu_1} e_j & 0_{j\times(j-1)} & I_j \end{array} \right), \quad -\left(\begin{array}{c} -\frac{1}{\mu_1} \bar{\mu} + e_{j-1} \\ \frac{1}{\mu_1} \mu + e_j \end{array} \right) \right] \otimes \left(\mathcal{D}^T Q(i)^{-1} \mathcal{D} \right)^{-1} \mathcal{D}^T Q(i)^{-1}$$

Table C.5. Closed-form expressions for matrices in the geometry-free *ionosphere-float* model (part 2).

$$
\begin{aligned}
K_2 \;=\; & \left[\left(\begin{array}{ccc} -\frac{1}{\mu_1} & 0_{1\times(j-1)} & 0_{1\times j} \\ 0 & 0_{1\times(j-1)} & 0_{1\times j} \end{array} \right) \otimes I_{nm} \;+\; \left\{ \left[\left(\begin{array}{ccc} \frac{1}{\mu_1} & 0_{1\times(j-1)} & 0_{1\times j} \\ 0 & 0_{1\times(j-1)} & 0_{1\times j} \end{array} \right) \;+\; \ldots \right. \right. \\
& \left. \left. \left(\begin{array}{cc} \frac{\eta+\sigma_\varrho^{-2}}{\omega(\eta+\sigma_\varrho^{-2})-\xi^2} & \frac{\xi}{\omega(\eta+\sigma_\varrho^{-2})-\xi^2} \\ \frac{\xi}{\omega(\eta+\sigma_\varrho^{-2})-\xi^2} & \frac{\omega}{\omega(\eta+\sigma_\varrho^{-2})-\xi^2} \end{array} \right) \left(\begin{array}{cc} -\mu^T Q_\phi^{-1} & \mu^T Q_p^{-1} \\ e_j^T Q_\phi^{-1} & e_j^T Q_p^{-1} \end{array} \right) \right] \otimes P_{\mathcal{D}(i)}^{\perp} \right\}, \left\{ \left(\begin{array}{c} \frac{1}{\mu_1} \\ 1 \end{array} \right) \otimes I_{nm} \;-\; \left(\begin{array}{c} \frac{1}{\mu_1} - \frac{\sigma_\varrho^{-2}\xi}{\omega(\eta+\sigma_\varrho^{-2})-\xi^2} \\ \frac{\omega\eta-\xi^2}{\omega(\eta+\sigma_\varrho^{-2})-\xi^2} \end{array} \right) \otimes P_{\mathcal{D}(i)}^{\perp} \right\} \right]
\end{aligned}
$$

$$
\boxed{P_{A_{II}(i)}^{\perp} \;=\; \left[\begin{array}{cc} P_{11} & P_{12} \\ P_{21} & P_{22} \end{array} \right] \otimes P_{\mathcal{D}(i)}^{\perp}} \text{ with:}
$$

$$
\begin{aligned}
P_{11} \;=\; & \left(\begin{array}{cc} I_j & \\ & I_j \end{array} \right) - \frac{\omega}{\omega(\eta+\sigma_\varrho^{-2})-\xi^2} \left(\begin{array}{cc} e_j e_j^T Q_\phi^{-1} & e_j e_j^T Q_p^{-1} \\ e_j e_j^T Q_\phi^{-1} & e_j e_j^T Q_p^{-1} \end{array} \right) - \frac{\xi}{\omega(\eta+\sigma_\varrho^{-2})-\xi^2} \left(\begin{array}{cc} -e_j \mu^T Q_\phi^{-1} & e_j \mu^T Q_p^{-1} \\ -e_j \mu^T Q_\phi^{-1} & e_j \mu^T Q_p^{-1} \end{array} \right) - \\
& \frac{\xi}{\omega(\eta+\sigma_\varrho^{-2})-\xi^2} \left(\begin{array}{cc} -\mu e_j^T Q_\phi^{-1} & -\mu e_j^T Q_p^{-1} \\ \mu e_j^T Q_\phi^{-1} & \mu e_j^T Q_p^{-1} \end{array} \right) - \frac{\eta+\sigma_\varrho^{-2}}{\omega(\eta+\sigma_\varrho^{-2})-\xi^2} \left(\begin{array}{cc} \mu\mu^T Q_\phi^{-1} & -\mu\mu^T Q_p^{-1} \\ -\mu\mu^T Q_\phi^{-1} & \mu\mu^T Q_p^{-1} \end{array} \right) \\
P_{12} \;=\; & -\left(\begin{array}{cc} -\mu & e_j \\ \mu & e_j \end{array} \right) \left(\begin{array}{c} \frac{\sigma_\varrho^{-2}\xi}{\omega(\eta+\sigma_\varrho^{-2})-\xi^2} \\ \frac{\sigma_\varrho^{-2}\omega}{\omega(\eta+\sigma_\varrho^{-2})-\xi^2} \end{array} \right) \\
P_{21} \;=\; & -\left(\begin{array}{cc} \frac{\xi}{\omega(\eta+\sigma_\varrho^{-2})-\xi^2} & \frac{\omega}{\omega(\eta+\sigma_\varrho^{-2})-\xi^2} \end{array} \right) \left(\begin{array}{cc} -\mu^T Q_\phi^{-1} & \mu^T Q_p^{-1} \\ e_j^T Q_\phi^{-1} & e_j^T Q_p^{-1} \end{array} \right) \\
P_{22} \;=\; & \frac{\omega\eta-\xi^2}{\omega(\eta+\sigma_\varrho^{-2})-\xi^2}
\end{aligned}
$$

$$
\boxed{Q_{y(i)}^{-1} P_{A_{II}(i)}^{\perp} \;=\; \left[\begin{array}{cc} S_{11} & S_{21}^T \\ S_{21} & S_{22} \end{array} \right] \otimes Q(i)^{-1} P_{\mathcal{D}(i)}^{\perp}} \text{ with:}
$$

$$
\begin{aligned}
S_{11} \;=\; & \left(\begin{array}{cc} Q_\phi^{-1} & \\ & Q_p^{-1} \end{array} \right) - \frac{\omega}{\omega(\eta+\sigma_\varrho^{-2})-\xi^2} \left(\begin{array}{cc} Q_\phi^{-1} e_j e_j^T Q_\phi^{-1} & Q_\phi^{-1} e_j e_j^T Q_p^{-1} \\ Q_p^{-1} e_j e_j^T Q_\phi^{-1} & Q_p^{-1} e_j e_j^T Q_p^{-1} \end{array} \right) - \frac{\xi}{\omega(\eta+\sigma_\varrho^{-2})-\xi^2} \left(\begin{array}{cc} -Q_\phi^{-1} e_j \mu^T Q_\phi^{-1} & Q_\phi^{-1} e_j \mu^T Q_p^{-1} \\ -Q_p^{-1} e_j \mu^T Q_\phi^{-1} & Q_p^{-1} e_j \mu^T Q_p^{-1} \end{array} \right) \\
& - \frac{\xi}{\omega(\eta+\sigma_\varrho^{-2})-\xi^2} \left(\begin{array}{cc} -Q_\phi^{-1} \mu e_j^T Q_\phi^{-1} & -Q_\phi^{-1} \mu e_j^T Q_p^{-1} \\ Q_p^{-1} \mu e_j^T Q_\phi^{-1} & Q_p^{-1} \mu e_j^T Q_p^{-1} \end{array} \right) - \frac{\eta+\sigma_\varrho^{-2}}{\omega(\eta+\sigma_\varrho^{-2})-\xi^2} \left(\begin{array}{cc} Q_\phi^{-1} \mu\mu^T Q_\phi^{-1} & -Q_\phi^{-1} \mu\mu^T Q_p^{-1} \\ -Q_p^{-1} \mu\mu^T Q_\phi^{-1} & Q_p^{-1} \mu\mu^T Q_p^{-1} \end{array} \right) \\
S_{21} \;=\; & -\left(\begin{array}{cc} \frac{\sigma_\varrho^{-2}\xi}{\omega(\eta+\sigma_\varrho^{-2})-\xi^2} & \frac{\sigma_\varrho^{-2}\omega}{\omega(\eta+\sigma_\varrho^{-2})-\xi^2} \end{array} \right) \left(\begin{array}{cc} -\mu^T Q_\phi^{-1} & \mu^T Q_p^{-1} \\ e_j^T Q_\phi^{-1} & e_j^T Q_p^{-1} \end{array} \right) \\
S_{22} \;=\; & \frac{\sigma_\varrho^{-2}\omega\eta-\xi^2}{\omega(\eta+\sigma_\varrho^{-2})-\xi^2}
\end{aligned}
$$

Appendix D
Computation of some receiver/satellite-dependent matrices

In this appendix closed-form expressions are given for some matrices which are a function of the matrix $\mathcal{D}$ in the partial design matrix of the estimable clock parameters in the GPS model based on undifferenced observables. In Chap. 2 this matrix was derived as:

$$\boxed{\mathcal{D} = \underbrace{[C_n \otimes e_m \quad -e_n \otimes I_m]}_{nm\times(n-1+m)}, \quad \text{where } C_n \;=\; \underbrace{\begin{bmatrix} 0_{1\times(n-1)} \\ I_{n-1} \end{bmatrix}}_{n\times(n-1)}} \tag{D.1}$$

In Chap. 5 in the (reduced) normal equations of the geometry and ambiguity parameters of the undifferenced GPS model, matrix $\mathcal{D}$ appears in the matrix product $Q(i)^{-1}P^{\perp}_{\mathcal{D}(i)}$, with $Q(i)$ the vc-matrix of the observables, without the influence of the a priori phase, code, range or ionosphere precision, thus only based on the number of receivers n and satellites m in the network:

$$Q(i) \;=\; \text{blkdiag}\,[Q_1(i),\; \ldots,\; Q_n(i)] \tag{D.2}$$

where $Q_r(i)$ denotes the vc-matrix for each receiver in the network. In this matrix for example satellite elevation-dependent precision can be modelled. The orthogonal projector $P^{\perp}_{\mathcal{D}(i)}$ is defined as follows:

$$P^{\perp}_{\mathcal{D}(i)} \;=\; I_{nm} \;-\; \mathcal{D}\left(\mathcal{D}^T Q(i)^{-1}\mathcal{D}\right)^{-1}\mathcal{D}^T Q(i)^{-1} \tag{D.3}$$

Using the strict expression for vc-matrix $Q(i)$ it is unfortunately very difficult to compute the matrix product $Q(i)^{-1}P^{\perp}_{\mathcal{D}(i)}$ in an analytical way. However, a closed-form expression can be derived with the assumption that all receivers in the network are sufficiently *close* together, such that $Q_1(i) \approx \ldots \approx Q_n(i) \equiv \bar{Q}(i)$. In that case matrix $Q(i)$ may namely be approximated as:

$$\boxed{Q(i) \;=\; I_n \otimes \bar{Q}(i)} \tag{D.4}$$

On basis of this, in Table D.1 closed-form expressions are given for, among others, $Q(i)^{-1}P^{\perp}_{\mathcal{D}(i)}$.

Table D.1. Closed-form expressions for the receiver/satellite-dependent matrices.

$Q(i)$	$I_n \otimes \bar{Q}(i)$
$Q(i)^{-1}$	$I_n \otimes \bar{Q}(i)^{-1}$
$\mathcal{D}$	$\begin{bmatrix} 0 & -I_m \\ I_{n-1} \otimes e_m & -e_{n-1} \otimes I_m \end{bmatrix}$
$\mathcal{D}^T Q(i)^{-1}$	$\begin{bmatrix} 0 & I_{n-1} \otimes e_m^T \bar{Q}(i)^{-1} \\ -\bar{Q}(i)^{-1} & -e_{n-1}^T \otimes \bar{Q}(i)^{-1} \end{bmatrix}$
$\mathcal{D}^T Q(i)^{-1} \mathcal{D}$	$\begin{bmatrix} I_{n-1}\left[e_m^T \bar{Q}(i)^{-1} e_m\right] & -e_{n-1} \otimes e_m^T \bar{Q}(i)^{-1} \\ -e_{n-1}^T \otimes \bar{Q}(i)^{-1} e_m & n\bar{Q}(i)^{-1} \end{bmatrix}$
$\left(\mathcal{D}^T Q(i)^{-1} \mathcal{D}\right)^{-1}$	$\begin{bmatrix} \left(I_{n-1} + e_{n-1} e_{n-1}^T\right) \frac{1}{\left[e_m^T \bar{Q}(i)^{-1} e_m\right]} & e_{n-1} \otimes \frac{1}{\left[e_m^T \bar{Q}(i)^{-1} e_m\right]} e_m^T \\ e_{n-1}^T \otimes \frac{1}{\left[e_m^T \bar{Q}(i)^{-1} e_m\right]} e_m & \frac{1}{n}\bar{Q}(i) + \frac{n-1}{n} \frac{1}{\left[e_m^T \bar{Q}(i)^{-1} e_m\right]} e_m e_m^T \end{bmatrix}$
$\left(\mathcal{D}^T Q(i)^{-1} \mathcal{D}\right)^{-1} \mathcal{D}^T Q(i)^{-1}$	$\begin{bmatrix} -e_{n-1} \otimes \frac{1}{\left[e_m^T \bar{Q}(i)^{-1} e_m\right]} e_m^T \bar{Q}(i)^{-1} & I_{n-1} \otimes \frac{1}{\left[e_m^T \bar{Q}(i)^{-1} e_m\right]} e_m^T \bar{Q}(i)^{-1} \\ -\frac{1}{n} I_m - \frac{n-1}{n} \frac{1}{\left[e_m^T \bar{Q}(i)^{-1} e_m\right]} e_m e_m^T \bar{Q}(i)^{-1} & -\frac{1}{n} e_{n-1}^T \otimes \left(I_m - \frac{1}{\left[e_m^T \bar{Q}(i)^{-1} e_m\right]} e_m e_m^T \bar{Q}(i)^{-1}\right) \end{bmatrix}$
$P_{\mathcal{D}(i)}^{\perp}$	$\underbrace{\left[I_n - \frac{1}{n} e_n e_n^T\right]}_{P_{e_n}^{\perp}} \otimes \underbrace{\left[I_m - \frac{1}{\left[e_m^T \bar{Q}(i)^{-1} e_m\right]} e_m e_m^T \bar{Q}(i)^{-1}\right]}_{P_{e_m}^{\perp}}$
$Q(i)^{-1} P_{\mathcal{D}(i)}^{\perp}$	$\underbrace{\left[I_n - \frac{1}{n} e_n e_n^T\right]}_{P_{e_n}^{\perp}} \otimes \underbrace{\left[\bar{Q}(i)^{-1} - \frac{1}{\left[e_m^T \bar{Q}(i)^{-1} e_m\right]} \bar{Q}(i)^{-1} e_m e_m^T \bar{Q}(i)^{-1}\right]}_{\bar{Q}(i)^{-1} P_{e_m}^{\perp}}$
$\mathcal{C}^T Q(i)^{-1} P_{\mathcal{D}(i)}^{\perp} \mathcal{C}$	$\underbrace{\left[I_{n-1} - \frac{1}{n} e_{n-1} e_{n-1}^T\right]}_{\left(D_n^T D_n\right)^{-1}} \otimes \underbrace{\left[C_m^T \bar{Q}(i)^{-1} C_m - \frac{1}{\left[e_m^T \bar{Q}(i)^{-1} e_m\right]} C_m^T \bar{Q}(i)^{-1} e_m e_m^T \bar{Q}(i)^{-1} C_m\right]}_{\left(D_m^T \bar{Q}(i) D_m\right)^{-1}}$

Appendix E

Ionospheric delay time series as stochastic process

Time series of ionospheric delays may be considered as a continuous-time stochastic process. In this appendix, two types of these stochastic processes are considered, the *random-walk* and the *integrated random-walk* processes. In this appendix for both processes the vc-matrix of the time-varying ionospheric delays is derived.

E.1 Random-walk process

When the ionospheric delay time series is considered as a *random-walk* stochastic process, the *velocity* of the ionospheric delays is assumed as a white-noise process. For this white-noise process *zero-mean* is assumed, and that its auto-covariance function is the *Dirac* or *delta* function with spectral density q_i:

$$E\{i(t_i)\} = 0, \quad \sigma_{ii}(t_i, t_j) = q_i\, \delta(t_i, t_j), \quad \text{where } q_i \text{ has dimension m}^2/\text{s} \tag{E.1}$$

Note that $i(t_i)$ denotes the time-derivative of $\imath(t)$, evaluated at epoch t_i. The discrete-time solution of this process reads [Teunissen, 2001d]:

$$\imath(t_i) = \imath(t_{i-1}) + \underbrace{\int_{t_{i-1}}^{t_i} i(\tau) d\tau}_{d(t_i)} \tag{E.2}$$

Application of the propagation law of variances gives for the variance of $\imath(t_i)$:

$$\sigma_{\imath\imath}(t_i, t_i) = \sigma_{\imath\imath}(t_{i-1}, t_{i-1}) + \underbrace{q_i \Delta t}_{\sigma^2_{d(t_i)}} \tag{E.3}$$

where $\Delta t = t_{i-1} - t_i$ denotes the data sampling interval, which is constant assumed between consecutive epochs. To set up the vc-matrix of the ionospheric delays, the process needs to be initialized. For the ionospheric delay on the first epoch, t_1, it is assumed that it is equal to the white-noise input:

$$\imath(t_1) = d(t_1); \quad \sigma_{\imath\imath}(t_1, t_1) = \sigma^2_{d(t_1)} \tag{E.4}$$

When the correlation between the white-noise input and the ionospheric delays may be neglected, $\sigma_{d\imath}(t_i, t_j) = 0$, it can be proved that the vc-matrix of the ionospheric delays for k epochs reads:

$$D\{\begin{bmatrix} \imath(t_1) \\ \imath(t_2) \\ \imath(t_3) \\ \vdots \\ \imath(t_{k-1}) \\ \imath(t_k) \end{bmatrix}\} = q_i \Delta t \begin{bmatrix} 1 & 1 & 1 & \dots & 1 & 1 \\ 1 & 2 & 2 & \dots & 2 & 2 \\ 1 & 2 & 3 & \dots & 3 & 3 \\ \vdots & \vdots & \vdots & \ddots & \vdots & \vdots \\ 1 & 2 & 3 & \dots & (k-1) & (k-1) \\ 1 & 2 & 3 & \dots & (k-1) & k \end{bmatrix} \tag{E.5}$$

Or, in short-hand notation, $\sigma_{\imath\imath}(t_i, t_j) = q_i \Delta t \min(i, j)$. From this vc-matrix it can be seen that the variances and covariances increase when the number of epochs increases, hence this stochastic process is not *covariance-stationary*. A stationary process can be obtained however, when the following full-rank transformation is applied to the vector of ionospheric delays:

$$\begin{bmatrix} 1 & & & & & \\ -1 & 1 & & & & \\ & -1 & 1 & & & \\ & & \ddots & \ddots & & \\ & & & -1 & 1 & \\ & & & & -1 & 1 \end{bmatrix} \tag{E.6}$$

Applying the propagation law of variances, results in the following transformed vc-matrix:

$$D\{\begin{bmatrix} \imath(t_1) \\ \imath(t_2) - \imath(t_1) \\ \imath(t_3) - \imath(t_2) \\ \vdots \\ \imath(t_{k-1}) - \imath(t_{k-2}) \\ \imath(t_k) - \imath(t_{k-1}) \end{bmatrix}\} = q_i \Delta t \begin{bmatrix} 1 & & & & & \\ & 1 & & & & \\ & & 1 & & & \\ & & & \ddots & & \\ & & & & 1 & \\ & & & & & 1 \end{bmatrix} \tag{E.7}$$

It can be seen that the transformed observables describe a stationary process and are also uncorrelated in time.

E.2 Integrated random-walk process

Instead of the velocity, the *acceleration* of the ionospheric delay may be considered as a white-noise process.

$$E\{\ddot{\imath}(t_i)\} = 0, \quad \sigma_{\ddot{\imath}\ddot{\imath}}(t_i, t_j) = q_{\ddot{\imath}}\, \delta(t_i, t_j), \quad \text{where } q_{\ddot{\imath}} \text{ has dimension } \mathrm{m}^2/\mathrm{s}^3 \tag{E.8}$$

Note that $\ddot{\imath}(t_i)$ denotes the second-order time-derivative of $\imath(t)$, evaluated at epoch t_i. This stochastic process is also known as an *integrated random-walk* process, see

[Herring et al., 1990]. The discrete-time solution of this differential equation reads:

$$\begin{bmatrix} \imath(t_i) \\ i(t_i) \end{bmatrix} = \begin{bmatrix} 1 & (t_i - t_{i-1}) \\ 0 & 1 \end{bmatrix} \begin{bmatrix} \imath(t_{i-1}) \\ i(t_{i-1}) \end{bmatrix} + \underbrace{\int_{t_{i-1}}^{t_i} \begin{bmatrix} (t_i - \tau) \\ 1 \end{bmatrix} w(\tau) d\tau}_{d(t_i)} \quad \text{(E.9)}$$

This solution has the following vc-matrix [Teunissen, 2001d]:

$$D\{\begin{bmatrix} \imath(t_i) \\ i(t_i) \end{bmatrix}\} = \begin{bmatrix} 1 & (t_i - t_{i-1}) \\ 0 & 1 \end{bmatrix} D\{\begin{bmatrix} \imath(t_{i-1}) \\ i(t_{i-1}) \end{bmatrix}\} \begin{bmatrix} 1 & (t_i - t_{i-1}) \\ 0 & 1 \end{bmatrix}^T + \underbrace{\begin{bmatrix} \frac{1}{3}\Delta t^3 & \frac{1}{2}\Delta t^2 \\ \frac{1}{2}\Delta t^2 & \Delta t \end{bmatrix}}_{Q_{d(t_i)}} \quad \text{(E.10)}$$

where $\Delta t = t_{i-1} - t_i$. The process is initialized as follows:

$$\begin{bmatrix} \imath(t_1) \\ i(t_1) \end{bmatrix} = d(t_1); \quad D\{\begin{bmatrix} \imath(t_1) \\ i(t_1) \end{bmatrix}\} = Q_{d(t_1)} \quad \text{(E.11)}$$

When the correlation between the white-noise input and the ionospheric delays is neglected, $\sigma_{di}(t_i, t_j) = 0$, in [Herring et al., 1990] it is proved that the elements of the vc-matrix of the ionospheric delays can be computed as $\sigma_{ii}(t_i, t_j) = \frac{1}{6} q_i \Delta t^3 i^2 [3j - i]$. For example, for $k = 5$, the vc-matrix reads:

$$D\{\begin{bmatrix} \imath(t_1) \\ \imath(t_2) \\ \imath(t_3) \\ \imath(t_4) \\ \imath(t_5) \end{bmatrix}\} = \frac{1}{6} q_i \Delta t^3 \begin{bmatrix} 2 & 5 & 8 & 11 & 14 \\ 5 & 16 & 28 & 40 & 52 \\ 8 & 28 & 54 & 81 & 108 \\ 11 & 40 & 81 & 128 & 176 \\ 14 & 52 & 108 & 176 & 250 \end{bmatrix} \quad \text{(E.12)}$$

Also this stochastic process is *not* covariance-stationary. A stationary process can however be obtained, when the following full-rank transformation matrix is applied to the ionospheric delays:

$$\begin{bmatrix} 1 & & & & & \\ -2 & 1 & & & & \\ 1 & -2 & 1 & & & \\ & \ddots & \ddots & \ddots & & \\ & & 1 & -2 & 1 & \\ & & & 1 & -2 & 1 \end{bmatrix} \quad \text{(E.13)}$$

Applying the propagation law of variances, results in the following transformed vc-matrix:

$$D\{\begin{bmatrix} \imath(t_1) \\ [\imath(t_2)-\imath(t_1)]-\imath(t_1) \\ [\imath(t_3)-\imath(t_2)]-[\imath(t_2)-\imath(t_1)] \\ \vdots \\ [\imath(t_{k-1})-\imath(t_{k-2})]-[\imath(t_{k-2})-\imath(t_{k-3})] \\ [\imath(t_k)-\imath(t_{k-1})]-[\imath(t_{k-1})-\imath(t_{k-2})] \end{bmatrix}\} = \frac{1}{6}q_{\imath}\Delta t^3 \begin{bmatrix} 2 & 1 & & & & \\ 1 & 4 & 1 & & & \\ & 1 & 4 & 1 & & \\ & & \ddots & \ddots & \ddots & \\ & & & 1 & 4 & 1 \\ & & & & 1 & 4 \end{bmatrix} \quad \text{(E.14)}$$

Although the transformed process is stationary, there is still correlation between consecutive epochs.